A First-Principles Study on

BULK AND TRANSFER DOPING OF DIAMOND

Stephen John Sque

Original submission: November 1, 2005
Examination: December 19, 2005
This version: April 1, 2007

Submitted by Stephen John Sque, to the University of Exeter as a thesis for the degree of Doctor of Philosophy in Physics, November 2005.

I certify that all material in this thesis which is not my own work has been identified and that no material has previously been submitted and approved for the award of a degree by this or any other University.

— Stephen Sque

Abstract

Presented herein are the results of theoretical investigations addressing current issues in the doping of diamond. The work has been conducted using first-principles calculations based on density-functional theory under the local-density approximation. Particular emphasis is placed upon two currently problematic aspects of doping diamond: the lack of a suitable shallow donor impurity for *n*-type doping of the bulk, and the need for a stable adsorbate material for *p*-type doping of the diamond surface (*transfer doping*). Since the latter clearly requires an understanding of the properties of the various diamond surfaces, the effects of atomic geometry and surface termination on the electronic structure of the technologically important diamond surfaces have also been investigated.

This study reproduces the experimentally well-known properties of nitrogen and phosphorus defects in diamond, and proceeds to predict that arsenic and antimony will be shallower donors than phosphorus, which is at present the most successful *n*-type dopant. However, the practicality of doping with these larger species may be hindered by the difficulty of incorporating their atoms into the diamond lattice, and by their high likelihood of becoming compensated by forming complexes with vacancies or hydrogen. Meanwhile, the controversial sulphur defect is found to be a deep donor, while the recent experimental observations of shallow-donor behaviour in deuterated, boron-doped diamond samples are not explained by any of the boron-hydrogen complexes modelled in this study. Finally, the N–Si_4 shallow-donor candidate has been critically investigated.

The effects of hydrogen and oxygen termination on the diamond surface are investigated in detail, and both the structural and electronic properties are shown to agree well with experimental observations. An important distinction is made between bulk- and surface-related electronic properties, and the influence of surface states on band bending and electron emission is discussed.

Regarding *p*-type transfer doping of diamond, this study finds that buckminsterfullerene (C_{60}) can effect an electron transfer from hydrogen-terminated diamond, when present in the form of one or more closely packed monolayers on the surface. This work also reports the prediction that the greater electron affinities of *fluorinated* fullerenes (such as $C_{60}F_{36}$) will enhance the effect, to such an extent that individual molecules may extract electrons from a diamond substrate — a finding that has been borne out in recent experiments.

Acknowledgements

First and foremost, I am indebted to Prof. Bob Jones for allowing me to study in his research group, and for being an excellent supervisor over the last three years. His enthusiasm, generosity, and methods of seeking progress are legendary, and deservedly so. I also thank Bob for very kindly helping me to obtain a new position as a Post-Doctoral Research Assistant in his group.

Grants from the U.K. Engineering and Physical Sciences Research Council (EPSRC) have made both my Ph.D. and Post-Doc. possible in the first place, and I am thankful to the board members, despite their anonymity.

I must thank the many colleagues that I have worked with in this fast-changing research group, for making the environment in Exeter an enjoyable and productive one. While the members of the AIMpro family that I have worked alongside are now too numerous to detail, I am especially grateful to James Adey and Thomas Eberlein for using their 'seniority' to help guide me through. I am also grateful to Derek Palmer and G.P. Srivastava for their interest and help, which often provided an alternative look at a problem.

The team in Newcastle deserve a special mention for their work on the AIMpro code, especially Patrick Briddon for his excellent development and maintenance of the program, for which a newer version always seems to be available. Jon Goss deserves special recognition too, for his deft handling of my many naïve questions regarding aspects of the code and condensed-matter physics in general.

Elsewhere, I am very grateful to Sven Öberg for performing many of my calculations on his powerful Swedish supercomputers, and for apparently working at very strange hours to ensure that my results were ready in time for tricky deadlines. Chris Ewels is also thanked for his (sometimes literally) animated help regarding all things nano.

On a more personal level, I gratefully thank my family for supporting me throughout all of my academic endeavours (and for paying for some of them too). Finally, I offer my heartfelt thanks to Susy for being a devoted and wonderful companion for the bulk of my time in Exeter.

List of Publications

First author

- *Structure, electronics, and interaction of hydrogen and oxygen on diamond surfaces*
  S. J. Sque, R. Jones, and P. R. Briddon
  Physical Review B **73 (8)**, 085313 (February 2006)

- *Hydrogenation and oxygenation of the (100) diamond surface and the consequences for transfer doping*
  S. J. Sque, R. Jones, and P. R. Briddon
  Physica Status Solidi (A) **202 (11)**, 2091–2097 (August 2005)

- *First-principles study of C_{60} and $C_{60}F_{36}$ as transfer dopants for p-type diamond*
  S. J. Sque, R. Jones, J. P. Goss, P. R. Briddon, and S. Öberg
  Journal of Physics: Condensed Matter **17 (2)**, L21–L26 (January 2005)

- *Shallow donors in diamond: chalcogens, pnictogens, and their hydrogen complexes*
  S. J. Sque, R. Jones, J. P. Goss, and P. R. Briddon
  Physical Review Letters **92 (1)**, 017402 (January 2004)

- *Shallow donors in diamond: pnictogen and chalcogen hydrogen defects*
  S. J. Sque, R. Jones, J. P. Goss, and P. R. Briddon
  Physica B: Condensed Matter **340–342**, 80–83 (December 2003)

Co-author

- *Vacancy-impurity complexes and limitations for implantation doping of diamond*
  J. P. Goss, P. R. Briddon, M. J. Rayson, **S. J. Sque**, and R. Jones
  Physical Review B **72 (3)**, 035214 (July 2005)

- *Quantum mechanical modeling of the structure and doping properties of defects in diamond*
  J. P. Goss, P. R. Briddon, R. Sachdeva, R. Jones, and S. J. Sque
  Proceedings of the *27th International Conference on the Physics of Semiconductors*, Flagstaff, Arizona, USA, 26–30 July 2004
  AIP Conference Proceedings **772 (1)**, 91–94 (June 2005)

- *Donor and acceptor states in diamond*
  J. P. Goss, P. R. Briddon, R. Jones, and **S. Sque**
  Diamond and Related Materials **13 (4–8)**, 684–690 (April–August 2004)

- *Boron-hydrogen complexes in diamond*
  J. P. Goss, P. R. Briddon, **S. J. Sque**, and R. Jones
  Physical Review B **69 (16)**, 165215 (April 2004)

- *The vacancy-nitrogen-hydrogen complex in diamond: a potential deep centre in chemical vapour deposited material*
  J. P. Goss, P. R. Briddon, R. Jones, and **S. Sque**
  Journal of Physics: Condensed Matter **15 (39)**, S2903–S2911 (October 2003)

Unpublished

- *Transfer doping of diamond: the use of C_{60} and $C_{60}F_{36}$ to effect p-type surface conductivity*
  S. J. Sque, R. Jones, S. Öberg, and P. R. Briddon
  Physica B: Condensed Matter, *in press* (March 2006)

- *Transfer doping of diamond: Buckminsterfullerene on hydrogenated, hydroxylated, and oxygenated diamond surfaces*
  S. J. Sque, R. Jones, S. Öberg, and P. R. Briddon
  submitted to Journal of Materials Science: Materials in Electronics (October 2005)

Contents

List of Tables

List of Figures

Chapter 1

Introduction

1.1 Carbon as diamond

CARBON is arguably the most remarkable and important of the chemical elements. Due to the relatively small size of the C atom and its ability to make strong single, double, and triple chemical bonds with other small atoms and with other atoms of carbon, it forms a great variety of compounds. Indeed, nearly ten million carbon compounds are known, constituting the great majority of chemical compounds. Carbon is key to all of organic chemistry; it is the basis of all life on Earth, and, in a belief known as *carbon chauvinism*, is necessarily the basis of all life in the Universe.

1.1.1 Fundamental properties

As the sixth element in the Periodic Table, carbon's neutral atom adopts a ground-state electronic configuration of $1s^2 2s^2 2p^2$. That is, the isolated atom has two core electrons occupying an s orbital, and four valence electrons: two in an s orbital and two in p orbitals.

When a C atom is threefold coordinated (as in ethene, benzene, graphite, *etc.*), its valence orbitals hybridise to form three equivalent sp^2 orbitals lying in a plane, plus one p orbital with an axis normal to the plane, with one electron in each orbital. Three σ covalent bonds then form with the neighbouring atoms, while the p orbital mixes with any neighbouring p orbitals to form a π bond or part of a delocalised π system.

When a C atom is fourfold coordinated (as in methane, ethane, diamond, *etc.*), four equivalent sp^3 hybrid orbitals are formed, with one electron occupying each. These then make four σ bonds with the surrounding atoms that are preferentially directed toward the four corners of a tetrahedron centred on the C atom.

Diamond is simply an extended network of tetrahedrally coordinated, sp^3-bonded carbon atoms. The incompressibility of the C–C bonds and the three-dimensional stability of the tetrahedral bonding arrangement are responsible for diamond's renowned material hardness. Indeed, natural diamond is used as the maximum for the calibration of the *Mohs (scratch-) hardness scale*, on which it is assigned a value of 10. Although long considered the hardest material known to Man, diamond's position is at present contended by at least *ultrahard fullerite* (three-dimensionally polymerised C_{60}) [1, 2] and *beta carbon nitride* (β-C_3N_4) [3–8].

The small size of C atoms allows them to get close to each other before experiencing net repulsive forces, and so relaxed C–C bonds are considered to be relatively short. The correspondingly large overlap of the orbitals on adjacent C atoms in a C–C bond causes a large energy separation between the occupied bonding orbitals and the unoccupied antibonding orbitals. This effect ultimately gives rise to a very large forbidden energy gap between the valence- and conduction-band states in the electronic structure of bulk diamond. As a result, the material is often considered to be a very large-bandgap semiconductor, if not an insulator. The minimal bandgap is indirect, with a value of ~ 5.47 eV at 300 K [9], which can be compared to corresponding values of 1.12 and 0.66 eV respectively for the more conventional group-IV semiconductors silicon and germanium.

Diamond is also noted for having the highest room-temperature thermal conductivity of any conventional solid. Significant thermal conductivity is unusual amongst semiconductor materials, because at normal temperatures there are very few electrons in conduction band states, free to transfer energy through the crystal. Diamond's large bandgap only serves to exaggerate this lack of room-temperature conduction electrons. However, it is instead the rigid covalent bonds that are responsible for diamond's unusually high thermal conductivity, as they can transfer atomic vibrations through the crystal with great efficiency. Natural diamond's thermal conductivity, measured at 300 K to be between $\sim$ 900–2300 W m^{-1} K^{-1} (Table 1.1), is in fact about two to six times that of metallic copper ($\sim$ 400 W m^{-1} K^{-1} [10]).

The strength of the covalent bonds also renders diamond a material that is considered quite chemically inert, and highly tolerant to irradiation.

Diamond's room-temperature indirect bandgap of 5.47 eV corresponds to pure (defect-free) material absorbing electromagnetic radiation with wavelengths of $\sim$ 227 nm or lower. That is, photons with ultraviolet (UV) or higher energies will create electron-hole pairs. Near-ultraviolet (UV-C) light will be emitted during radiative recombination, when electrons drop from the conduction-band minimum into holes at the top of the valence band. However, the indirect nature of diamond's bandgap means that this recombination must involve a phonon, and the process is inefficient.

Diamond is therefore transparent over a range from the near-ultraviolet, through the visible, to the far-infrared, and even to wavelengths beyond 100 μm. This property makes diamond suitable for use in optical applications such as infrared laser windows.

1.1.2 Crystal structure

The crystal structure that diamond adopts is named after it. The *diamond* structure is equivalent to a face-centred cubic (FCC) lattice, with a basis (or motif) of two atoms at each lattice point: one at (0,0,0) and the other at ($\frac{1}{4}$,$\frac{1}{4}$,$\frac{1}{4}$), where the coordinates are fractions along the cube sides. This is equivalent to two interpenetrating FCC lattices, offset from one another along a body diagonal by one-quarter of its length.

Diamond can also adopt a (2H) *hexagonal* crystal structure in which case it is called *lonsdaleite*. However, this polymorph, discovered in 1967 [11, 12], is extremely rare in Nature. It is found primarily in meteorites, and is believed to form as a result of shock-induced conversion of graphite during impact. Such an impact is also speculated to have formed a new, super-hard crystalline polymorph of carbon [13].

The conventional, cubic unit cell of normal diamond (Fig. 1.1) has a side length a_0 measured to be $\sim$ 3.57 Å (0.357 nm) at room temperature [14]. From this measurement, it is straightforward to derive some further quantities.

The C–C centre-to-centre bond length d is equal to one-quarter of the cubic body diagonal, that is $d = \sqrt{3}a_0/4 \approx 1.54$ Å. The conventional cell contains the equivalent of eight

whole C atoms, and the atomic number density is therefore $8/a_0^3 \approx 1.76 \times 10^{23}$ cm^{-3}. Thus, the concentration of a defect, stated per cm^3, can be converted into parts per million (ppm) by dividing by 1.76×10^{17}.

Multiplying the atomic density by the average atomic mass of the C atom results in a theoretical mass density for diamond $\approx$ 3516 kg m^{-1}. The experimentally measured density of diamond is 3515.25 kg m^{-1}, which is slightly lower than the theoretical value due to the presence in real diamond samples of impurity atoms and crystal imperfections such as voids.

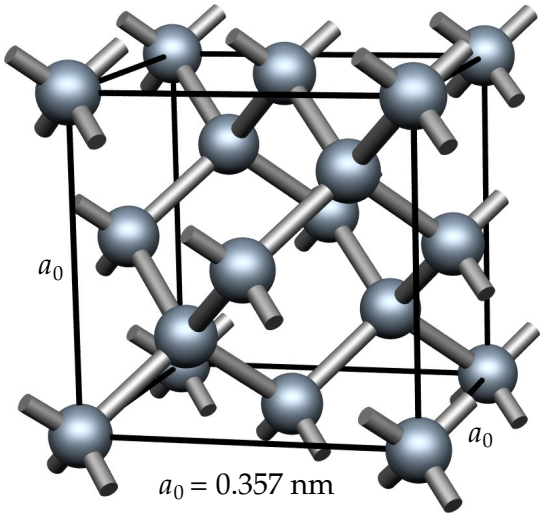

Figure 1.1: Ball-and-stick diagram of the conventional unit cell of diamond, where a_0 is the cubic lattice parameter.

Each C atom can be thought of as a sphere with a radius of one-eighth of the cubic body diagonal, and the packing fraction of the diamond structure is therefore $8 \times (4/3)\pi(\sqrt{3}a_0/8)^3/a_0^3$, which simplifies to $\sqrt{3}\pi/16 \approx 0.34$. This is just less than half of the maximum possible packing fraction of ≈ 0.74 — that of (cubic or hexagonal) close-packed structures. It is interesting to note that while the mass density of diamond is not particularly high — due to this low packing fraction and the low mass of the C atom — its atomic number density is the highest of all terrestrial materials.

1.1.3 Impurities

The dominant impurity atoms in diamond are those of nitrogen and boron (carbon's neighbours on the Periodic Table), and those of the ubiquitous hydrogen. As atoms of hydrogen are very small, they are easily incorporated as interstitials in the bulk diamond. The incorporation of nitrogen and boron atoms as substitutional defects in the diamond lattice is also relatively easy, since their atoms are similar in size to carbon: the covalent radius of nitrogen is 75 pm, that of boron is 82 pm, while that of carbon is 77 pm.

Understandably, nitrogen — with a valence of five electrons — is an electron donor impurity in diamond, while boron — with its valence of three — is an electron acceptor. Nitrogen is considered to be a *deep* donor in diamond, as its activation energy is high, at $\sim$ 1.7 eV; furthermore, this is an appreciable fraction (31%) of the host material's bandgap. However, the boron acceptor is considered quite shallow, since its activation energy is only 0.37 eV. Nevertheless, in the vast majority of diamond samples, the concentration of nitrogen donors far exceeds that of these easily activated boron acceptors, and the latter are therefore fully compensated by the former, leading to highly resistive (and ultimately *n*-type) material.

1.1.4 Classification of diamond

While gemstone diamonds are typically classified according to 'the Four C's' — cut, clarity, colour, and carat (weight) — all samples of diamond can be classified according to their content and type of nitrogen impurities. 'Type I' diamonds contain significant nitrogen impurities and represent the great majority of all natural diamonds, while those of 'Type II' contain so little nitrogen that it is not readily detectable by ultraviolet or infrared absorption measurements. The types are further sub-divided as follows:

- **Type I**: Significant concentrations of nitrogen impurities.
    - **Type Ia**: Nitrogen is present as aggregates of substitutional atoms and can account for up to 0.3% of the material (3000 ppm).
        - **Type IaA**: Nitrogen atoms exist mostly in nearest-neighbour substitutional pairs (the 'A' aggregate) and the material does not tend to show any fluorescence.
        - **Type IaB**: Nitrogen is present in groups of four substitutional atoms that surround a vacancy (the 'B' aggregate) and samples can exhibit moderate to strong blue fluorescence.
        - **Type IaAB**: In addition to A and B centres, groups of three nitrogen substitutionals around a vacancy ('N3' centres) are present. The B centres lead to possible blue fluorescence, while high concentrations of N3 centres can give rise to strong absorption of visible blue light, which leads to yellow colouration of the diamond.

  - **Type Ib**: Nitrogen exists as isolated substitutional impurities. Absorption of light increases toward the blue end of the spectrum, which results in a deep yellow colour for the material. Type Ib diamonds show nitrogen concentrations up to around 500 ppm, although the yellow colouration is supposedly noticeable at a nitrogen concentration of $\sim$ 50 ppm.

- **Type II**: Very low or undetectable amounts of nitrogen.

  - **Type IIa**: These are those that do not show significant electrical conductivity, and are usually colourless. These have no clear nitrogen-related features in the infrared (IR) absorption spectrum in the range 400–1332 cm^{-1} (the single-phonon region).
  - **Type IIb**: Substitutional boron acceptors are uncompensated due to the lack of nitrogen donors, and the material therefore displays a significant *p*-type semiconductivity. The boron impurities also cause absorption of light toward the red end of the visible spectrum, and therefore lend a slight blue colour to the diamond.

1.1.5 Synthesis of diamond

High-pressure, high-temperature synthesis

The high-pressure, high-temperature (HPHT) synthesis of diamond is a technique, developed in the 1950s, that attempts to mimic the conditions under which natural diamonds are formed deep ($\sim$ 200 km) underground on Earth [15]. In the synthesis, an amount of graphite (or glassy carbon [16]) is placed into a large, ceramic, hydraulic press, and is simultaneously heated to a few thousand degrees K (often around 2000 K) and put under pressures of a few (typically 5–6) GPa. With the assistance of a metal catalyst, the graphite is converted over a time period of several hours into single-crystal diamonds, although this conversion can be affected by the presence of impurities [17].

HPHT crystals are typically a few millimetres in size, although the size of the diamonds is in fact only limited by the ability to sustain the same pressure and temperature conditions. As the timescale of their formation is so much less than the millions (or indeed billions) of years that natural diamonds are formed over, most HPHT diamonds are far

too flawed for use as gemstones, but are nevertheless useful for many industrial applications, such as for use on saw blades for cutting asphalt and marble, and to coat the drill bits used in oil and gas drilling.

Chemical vapour deposition

Thin films of (usually polycrystalline) diamond can be grown on suitable substrates by the method of chemical vapour deposition (CVD) at near-atmospheric pressures, and temperatures of less than 1000 °C. The method is based on the decomposition of carbon compounds such as CH_4, diluted in H_2 gas, so that C atoms diffuse down onto a substrate and under the right conditions accumulate to form a film of diamond. The decomposition can be achieved by thermal means (*e.g.* by using a hot filament), by plasma activation (*e.g.* by using microwave, DC, or RF electrical discharges), or by using a combustion flame (*e.g.* an oxyacetylene torch). The activation of the gas also produces atomic hydrogen, which is key to the subsequent gas-phase and surface chemical reactions required to sustain diamond film growth, and which can greatly affect the film morphology and quality [18].

Most diamond films created by the CVD technique can be classified as being of type Ib, due to the fact that atoms of nitrogen (present in the gas mixture) end up in the diamond bulk, and have insufficient time in which to aggregate to form A, B, or N3 centres. The CVD process allows for thin films of diamond to be deposited onto a number of surfaces of different types, shapes, and textures [19–21]. As a result, wear-resistant diamond coatings can be applied to tools in many industrial situations.

Although most diamonds produced by HPHT synthesis and CVD are polycrystalline, at present there are at least two companies that claim to be able to synthesise high-quality, single-crystal diamonds for sale on the general market: *Gemesis*, using HPHT synthesis; and *Apollo Diamond*, who use CVD to produce type IIa diamonds [22]. However, in all cases examined as of 2004, the synthetic diamonds could be identified as being distinct from natural gem diamonds due to their particular fluorescence properties, strain patterns, and characteristic features in IR absorption and photoluminescence spectra [22].

1.2 Applications of diamond

Diamond's material properties are summarised in Tables 1.1 and 1.2.

The large number of extreme properties that diamond exhibits makes it a material with great potential for use in many industrial and commercial applications. Some of these include using diamond for: stone and wood sawing, wear-resistant coatings, polishing other materials, glass grinding, metal cutting, wire drawing, oil and gas drilling, optical and microwave windows, heatspreaders, lining hip joints, surgical blades, radiation detectors, and even for improving the driving performance of golf clubs.

1.2.1 Diamond as a semiconductor material

Diamond represents a material showing great promise for use in semiconductor devices that would be capable of operating in conditions under which traditional semiconductor materials, such as silicon, would fail. In particular, diamond-based devices could provide high power and would function at high frequencies, at high temperatures, and under severe exposure to radiation [34, 35]. These desirable properties are due in part to diamond's high carrier mobility, high thermal conductivity, high breakdown field, low dielectric constant, and wide bandgap.

Basic semiconductor devices

The most basic of the semiconductor devices is the *pn* junction, from which diodes are made. The creation of such a device requires the fabrication of low-resistivity *n*- and *p*-type material by doping diamond with donor and acceptor impurities respectively. As mentioned earlier, the boron acceptor occurs naturally in diamond, and is uncompensated in type-IIb material. In addition, boron has been both grown into and implanted into synthetic diamond. Recall that boron is considered a shallow acceptor, with an activation energy of 0.38 eV.

However, there has been much difficulty in finding a similarly shallow *donor* for diamond to allow the production of *n*-type material. The most successful practical dopant

Table 1.1: Mechanical and thermal properties of diamond. Where available, references are given in square brackets. Some of the unmarked data is taken from references [23] and [24].

Property	**Value**
Crystal structure	Diamond (cubic)
Space group	$Fd\bar{3}m$
Pearson Symbol	cF8
Strukturbericht Designation	A4
Lattice constant (300 K)	3.56683 Å (6.74033 a.u.) [9, 14]
Bond length (300 K)	1.54448 Å (2.91865 a.u.)
Bond angle (the tetrahedral angle)	$2\tan^{-1}(\sqrt{2}) = 109.4712...^\circ$
Packing density (fraction)	$\sqrt{3}\pi/16 = 0.34008738...$
Relative hardness	10 Mohs [exact]
Knoop hardness	8000
Knoop microhardness	79 GPa
(100) face	56–102 GPa
(110), (111) faces	58–88 GPa
Vickers microhardness	
(100) face	88–147 GPa
(111) face	98 GPa
Abrasive hardness	140, 000
Modulus of elasticity	700–1200 GPa
Young's modulus ([111] direction)	1223 GPa [25]
Volume compressibility	18×10^{-10} m^2 N^{-1}
Compressive yield strength	8680–16530 MPa
Poisson's ratio	0.1–0.29
Atomic weight of carbon	$12.0107(8)$ u (a.m.u.)
	$1.9944(1) \times 10^{-26}$ kg
Mass of ^{12}C atom	12 u (a.m.u.) [exact]
	1.992648×10^{-26} kg
Density (300 K)	3515.25 kg m^{-3} [14]
Atomic concentration (300 K)	1.763×10^{23} cm^{-3}
Bulk modulus	442.3 GPa [26]
Linear expansion coefficient (300 K)	1.05×10^{-6} K^{-1}
Melting point	3773 K
	4027 °C
	3850 K [10]
Coefficient of linear thermal expansion (20 °C)	1.18 µm m°C^{-1}
Heat capacity	0.4715 J g^{-1} °C^{-1}
Thermal conductivity	2000 W m^{-1} K^{-1} [9]
(Type-I, 300 K)	895.0 W m^{-1} K^{-1} [10]
(Type-IIa, 300 K)	2300.0 W m^{-1} K^{-1} [10]
(Type-IIb, 300 K)	1350.0 W m^{-1} K^{-1} [10]
Heat of formation	714.4 kJ mol^{-1}
Debye temperature	2067 °C
Raman frequency (first order)	$\sim$ 1332 cm^{-1} [27, 28]

Table 1.2: Optical and electronic properties of diamond. References are given where available.

Property	**Value**
Refractive index	
(546.1 nm)	2.424
(589 nm)	2.419
(591 nm)	2.41 [28]
(visible light range)	$\sim$ 2.40–2.46 [29]
Dielectric constant	
(300 K, 1–10 kHz)	5.70
(25 °C, 1 MHz)	5.5–5.7
Dielectric strength	1000 kV mm^{-1}
Dissipation factor	0.0002
Electronic bandgap (indirect)	
(0 K)	5.48 eV [9]
(300 K)	5.50 eV [14]
	5.47 eV [9]
Direct bandgap	7.3 eV [30–33]
Electron mobility (300 K)	1800 cm^2 V^{-1} s^{-1} [9]
Hole mobility (300 K)	1200 cm^2 V^{-1} s^{-1} [9]
Relative permittivity	5.570 [14]

to date is substitutional phosphorus, and in fact an ultraviolet-light–emitting *pn* junction has been successfully fabricated by using B-doped *p*-type diamond with P-doped *n*-type diamond [36], paving the way for other P-doped–diamond devices [37–39]. However, the activation energy of 0.6 eV for the P donor is still too high for an appreciable fraction of the extra electrons to occupy conduction-band states at room temperature.

Recently, complexes of boron with hydrogen or deuterium appear to have lead to *n*-type conductivity in diamond [40, 41], although the mechanism behind this phenomenon is not understood theoretically [42]. Meanwhile, the status of sulphur as a donor or double-donor in diamond is controversial [43–53].

Electron emitters

Diamond is also renowned for its *electron emission* properties, due to the *negative* electron affinity (NEA) of its hydrogen-terminated surface [54–56]. The conduction-band states in such diamond are higher in energy than the potential of vacuum, and so electrons in the conduction band can be emitted from the surface into vacuum with a net loss in energy.

This property makes diamond very attractive for use in cold cathodes, or field-effect transistors.

Surface-conductive devices

Hydrogen termination of the diamond surface also has the effect of lowering the ionisation potential with respect to that of the clean or oxygenated surfaces. That is, less energy is required to extract electrons from the top of the valence band and take them out into vacuum.

As will be detailed in Chp. 6, this favours the *transfer-doping* effect, wherein a molecule of some foreign chemical species lying on the diamond surface extracts an electron from the bulk diamond and transfers it into one of its unoccupied states [57–59]. This leaves behind a hole in the diamond valence band that is confined to the near-surface region by the attractive potential of the now-negatively charged adsorbate. Repeated extractions lead to an accumulation of holes in a near-surface layer, and a *p*-type surface conductivity is established.

The high *p*-type surface conductivity discovered on various diamond samples [60] is thought to be due to some constituent of the surface wetting layer (formed by exposure to air) extracting electrons via the transfer-doping mechanism [57, 59, 61]. Clearly, finding a suitable *solid-state* adsorbate to *engineer* stable transfer doping of diamond would be preferred over relying on the volatile aqueous layer.

An important problem is that loss of the hydrogen termination or oxidation of the diamond surface destroys both the NEA, and the low ionisation potential that favours the transfer-doping effect [55, 56, 62]. As this would ruin devices based on either property, a good understanding of the interaction between hydrogen and oxygen on the diamond surface is vital.

1.3 Aims of this investigation

The study presented herein is ultimately concerned with improving diamond's suitability as a semiconductor material by working on some of the aforementioned problems in the engineering of its electronic properties. There are three principal aims of this project:

- Continue the search for a suitable **shallow donor for diamond**, evaluate the present suggestions, and investigate the recent claims of shallow donor behaviour.
- Investigate the effect of, and interaction between, **hydrogen and oxygen on the diamond surface** with regard to structural stabilities, and electronic properties such as the electron affinity and ionisation potential.
- Determine a suitably stable adsorbate material for achieving effective **transfer doping of diamond**, to permit the engineering of high *p*-type surface conductivity.

Chapter 2

Theoretical Method

> "Today's scientists have substituted mathematics for experiments, and they wander off through equation after equation, and eventually build a structure which has no relation to reality."
>
> — Nikola Tesla

2.1 The many-body problem

DETERMINING the energy and structure of a specific configuration of atoms involves solving the Schrödinger equation for both the atomic nuclei and the electrons. In the absence of external fields, the Schrödinger equation can be written as

$$\widehat{\mathcal{H}}\Psi_i = E_i\Psi_i, \tag{2.1}$$

where $\widehat{\mathcal{H}}$ is the many-body Hamiltonian, and Ψ_i is the many-body wavefunction describing the i^{th} state, which has an energy of E_i. The Hamiltonian contains the usual kinetic and potential energy terms:

$$\widehat{\mathcal{H}} = \widehat{\mathcal{T}}_{\text{n}} + \widehat{\mathcal{T}}_{\text{e}} + \widehat{\mathcal{V}}_{\text{e-e}} + \widehat{\mathcal{V}}_{\text{e-n}} + \widehat{\mathcal{V}}_{\text{n-n}}, \tag{2.2}$$

in which the subscripts n and e label terms concerned with nuclei and electrons respectively. The system of atomic units (a.u.) will be used, in which $\hbar$, e, m_{e}, and $4\pi\varepsilon_0$ are taken to be unity. Then, 1 a.u. of length is 0.529 Å, and 1 a.u. of energy is 27.211 eV. The

Hamiltonian for a system of N_e electrons in a field due to N_n atomic nuclei can then be written as:

$$\widehat{\mathcal{H}} = -\sum_{\alpha}^{N_\mathrm{n}} \frac{1}{2M_\alpha}\nabla_\alpha^2 - \frac{1}{2}\sum_{\mu}^{N_\mathrm{e}} \nabla_\mu^2 + \frac{1}{2}\sum_{\mu\neq\nu}^{N_\mathrm{e}} \frac{1}{|\mathbf{r}_\mu - \mathbf{r}_\nu|} - \sum_{\mu,\alpha}^{N_\mathrm{e},N_\mathrm{n}} \frac{Z_\alpha}{|\mathbf{r}_\mu - \mathbf{R}_\alpha|} + \frac{1}{2}\sum_{\alpha\neq\beta}^{N_\mathrm{n}} \frac{Z_\alpha Z_\beta}{|\mathbf{R}_\alpha - \mathbf{R}_\beta|}, \tag{2.3}$$

where M_α, Z_α, and $\mathbf{R}_\alpha$ are respectively the mass, charge, and position of the α^{th} atomic nucleus, and $\mathbf{r}_\mu$ is the position of the μ^{th} electron.

The total wavefunction Ψ_i from Eqn. 2.1 is in general a function of the nuclear coordinates, $\mathbf{R}_\alpha$, and the electron position and spin coordinates, $\mathbf{r}_\mu$ and s_μ respectively. That is,

$$\Psi_i \equiv \Psi_i(\mathbf{r}_1, s_1, \ldots, \mathbf{r}_{N_\mathrm{e}}, s_{N_\mathrm{e}}; \mathbf{R}_1, \ldots, \mathbf{R}_{N_\mathrm{n}}). \tag{2.4}$$

For all but the simplest of problems, there is no analytical solution to this problem. In addition, it should be appreciated that the total wavefunction is a function of $3N_\mathrm{n} + 4\sum_\alpha Z_\alpha$ scalar variables, and as such even moderately sized problems are intractable, even with the use of the most powerful supercomputers available at the time of writing. Therefore, a series of approximations must be used in order to reach a compromise between computational expense and accurate output.

2.2 Born-Oppenheimer approximation

As the mass of the electron is ~ 2000 times less than that of a nucleon, the electrons are expected to respond almost instantaneously to motion of the atomic nuclei and achieve the electronic ground state, or rather the electronic wavefunction is modulated *adiabatically* by nuclear motion. Born and Oppenheimer argued that the motion of the electrons and the nuclei can therefore be decoupled [63], and that the substitution

$$\Psi(\mathbf{r};\mathbf{R}) = \chi(\mathbf{R})\psi_\mathbf{R}(\mathbf{r}) \tag{2.5}$$

can be made for the total wavefunction in Eqn. 2.1. Here, χ and ψ are separate wavefunctions for the nuclei and electrons respectively, with $\mathbf{R}$ and $\mathbf{r}$ encompassing all of the respective degrees of freedom for the nuclei and electrons.

Equations for the separate nuclear and electronic problems can then be constructed:

$$\left[\widehat{\mathcal{T}}_{\mathrm{n}} + \widehat{\mathcal{V}}_{\text{n-n}}\right]\chi(\mathbf{R}) = E_{\mathrm{n}}\chi(\mathbf{R}) \tag{2.6}$$

$$\left[\widehat{\mathcal{T}}_{\mathrm{e}} + \widehat{\mathcal{V}}_{\text{e-e}} + \widehat{\mathcal{V}}_{\text{e-n}}\right]\psi_{\mathbf{R}}(\mathbf{r}) = E_{\mathrm{e}}\psi_{\mathbf{R}}(\mathbf{r}), \tag{2.7}$$

where $\widehat{\mathcal{T}}$ and $\widehat{\mathcal{V}}$ respectively include all relevant kinetic and potential terms from Eqn. 2.3. The energy eigenvalues E_{n} and E_{e} can be used in conjunction with Eqn. 2.5 to revise the Schrödinger equation for the complete system:

$$\begin{aligned}\widehat{\mathcal{H}}\chi(\mathbf{R})\psi_{\mathbf{R}}(\mathbf{r}) &= (E_{\mathrm{n}} + E_{\mathrm{e}})\chi(\mathbf{R})\psi_{\mathbf{R}}(\mathbf{r}) \\ &\quad - \sum_{\alpha}^{N_{\mathrm{n}}} \frac{1}{2M_\alpha}\left[\chi(\mathbf{R})\nabla_\alpha^2\psi_{\mathbf{R}}(\mathbf{r}) + 2\nabla_\alpha\psi_{\mathbf{R}}(\mathbf{r})\nabla_\alpha\chi(\mathbf{R})\right].\end{aligned} \tag{2.8}$$

If the second term is considered to be negligibly small due to the large value of M_α, a Schrödinger equation is obtained in which the total energy E is the sum of the independent electronic and nuclear eigenvalues E_{e} and E_{n}, and the Born-Oppenheimer ansatz $\chi(\mathbf{R})\psi_{\mathbf{R}}(\mathbf{r})$ is the eigenstate:

$$\widehat{\mathcal{H}}\chi(\mathbf{R})\psi_{\mathbf{R}}(\mathbf{r}) = (E_{\mathrm{n}} + E_{\mathrm{e}})\chi(\mathbf{R})\psi_{\mathbf{R}}(\mathbf{r}) \tag{2.9}$$

The electron and nuclear motions are then fully decoupled. If the positions of the atomic nuclei are fixed, a stationary state can be obtained for the system following a determination of ψ.

Before continuing, it should be noted that of course the Born-Oppenheimer approximation breaks down when the second term in Eqn. 2.8 is not negligible. This occurs in systems in which electron-nuclear coupling is strong, and $\nabla_\alpha\psi_{\mathbf{R}}(\mathbf{r})$ is therefore very large due to significant overlap of the electronic and nuclear wavefunctions. In such cases a treatment of electron-phonon coupling is required.

When the electrons and nuclei are considered decoupled and the nuclear positions fixed, the purely electronic problem can be considered:

$$\begin{aligned}\widehat{\mathcal{H}}\psi(\mathbf{r}) &= \left[\widehat{\mathcal{T}}_{\mathrm{e}} + \widehat{\mathcal{V}}_{\text{e-e}} + \widehat{\mathcal{V}}_{\text{e-n}}\right]\psi(\mathbf{r}) \\ &= \left[-\frac{1}{2}\sum_{\mu}^{N_{\mathrm{e}}}\nabla_\mu^2 + \frac{1}{2}\sum_{\mu\neq\nu}^{N_{\mathrm{e}}}\frac{1}{|\mathbf{r}_\mu - \mathbf{r}_\nu|} - \sum_{\mu,\alpha}^{N_{\mathrm{e}},N_{\mathrm{n}}}\frac{Z_\alpha}{|\mathbf{r}_\mu - \mathbf{R}_\alpha|}\right]\psi(\mathbf{r}) \\ &= E_{\mathrm{e}}\psi(\mathbf{r}).\end{aligned} \tag{2.10}$$

2.3 Variational principle

Instead of choosing to integrate the Schrödinger equation of Eqn. 2.10 over a discrete grid, one could instead make use of the variational principle. In this method, a subspace $\{\phi_1, \ldots, \phi_M\}$ of the associated Hilbert space is chosen to span an approximation Ψ_{app} of the total ground-state wavefunction Ψ_0 in the form of

$$\Psi_0 \approx \Psi_{\text{app}} = \sum_i^M c_i \, \phi_i. \tag{2.11}$$

An approximation for the total energy E can then be given by the expectation value of E, which can be written as a functional of the approximated wavefunction Ψ_{app}. That is,

$$\begin{aligned} E_{\text{app}} \;=\; E[\Psi_{\text{app}}] \;&=\; \frac{\langle \Psi_{\text{app}} | \widehat{\mathcal{H}} | \Psi_{\text{app}} \rangle}{\langle \Psi_{\text{app}} | \Psi_{\text{app}} \rangle} \\ &=\; \frac{\sum_{i,j}^M c_i^* c_j \langle \phi_i | \widehat{\mathcal{H}} | \phi_j \rangle}{\sum_{i,j}^M c_i^* c_j \langle \phi_i | \phi_j \rangle} \\ &=\; \frac{\sum_{i,j}^M c_i^* c_j H_{ij}}{\sum_{i,j}^M c_i^* c_j S_{ij}}, \end{aligned} \tag{2.12}$$

where H_{ij} and S_{ij} are the so-called *Hamiltonian* and *overlap* matrix elements respectively. The derivative of E_{app} with respect to c_i must vanish in order to lead to stationary states, and so

$$\sum_{j=1}^M \left(H_{ij} - E_{\text{app}} S_{ij} \right) c_j = 0 \quad \text{for} \quad i = 1, \ldots, M, \tag{2.13}$$

which can be generalised to a matrix eigenvalue equation with the form

$$\mathsf{H} \cdot \mathbf{c} = E_{\text{app}} \, \mathsf{S} \cdot \mathbf{c}. \tag{2.14}$$

According to the Rayleigh-Ritz variational principle [64], the lowest eigenvalue found from this equation will always be higher than or equal to the *true* ground-state energy E_0. The inclusion of more basis functions ϕ_i into the set (*i.e.* increasing the value of M) will serve to enlarge the subspace, lowering the value of E_{app} asymptotically toward E_0.

Theorem 1 (Variational principle) *The energy E_{app} calculated from an approximate wavefunction Ψ_{app} is an upper bound to the true ground-state energy E_0. Full minimisation of the functional $E[\Psi]$ with respect to all of the allowed basis functions will give the true ground-state wavefunction Ψ_0 and corresponding energy $E_0 = E[\Psi_0]$. That is,*

$$E_0 = \min_{\Psi} E[\Psi]. \tag{2.15}$$

The variational principle in this form is used in almost all calculations that attempt to determine the ground-state electronic structure of an assembly of atoms.

2.4 Hartree-Fock method

In the Hartree-Fock (HF) method [65–68], the variational principle is used in which the many-electron wavefunction Ψ is taken to be the product of one-electron wavefunctions. The product must be antisymmetric in order to account for the fermionic nature of electrons. This is conveniently achieved by writing Ψ as a Slater determinant (SD) [69]:

$$\Psi_{\mathrm{SD}}(\mathbf{x}_1, \ldots, \mathbf{x}_{N_\mathrm{e}}) = \frac{1}{\sqrt{N_\mathrm{e}!}} \begin{vmatrix} \psi_1(\mathbf{x}_1) & \cdots & \psi_{N_\mathrm{e}}(\mathbf{x}_1) \\ \vdots & \ddots & \vdots \\ \psi_1(\mathbf{x}_{N_\mathrm{e}}) & \cdots & \psi_{N_\mathrm{e}}(\mathbf{x}_{N_\mathrm{e}}) \end{vmatrix}. \tag{2.16}$$

Here, $\mathbf{x}_i$ includes both the spatial *and* spin coordinates for the i^{th} electron, and ψ_j are one-electron *spin-orbitals*, taken to be orthonormal, which are products of spatial orbitals $\phi_j(\mathbf{r}_i)$ and spin functions $\omega_j(s_i) = \alpha(s_i)$ or $\beta(s_i)$. The antisymmetric property of Ψ_{SD} and its compliance with the Pauli exclusion principle is apparent, since exchanging any two electrons changes the sign of the determinant, while if two electrons were to share the same coordinates, Ψ_{SD} would have a value of zero.

By using Ψ_{SD} as a solution to the electronic eigenvalue equation (Eqn. 2.10), an expectation value for the total energy E is obtained as

$$E_{\mathrm{HF}} = \sum_{i}^{N_\mathrm{e}} H_i + \frac{1}{2} \sum_{i,j=1}^{N_\mathrm{e}} \left(J_{ij} - K_{ij} \right), \tag{2.17}$$

where H_i is a one-electron integral taking the form

$$H_i = \int \psi_i^*(\mathbf{x}) \left[-\frac{1}{2}\nabla_i^2 - \sum_{\alpha=1}^{N_\mathrm{n}} \frac{Z_\alpha}{|\mathbf{r}_i - \mathbf{R}_\alpha|} \right] \psi_i(\mathbf{x}) \, \mathrm{d}\mathbf{x}, \tag{2.18}$$

while J_{ij} and K_{ij} are respectively the *Hartree* and *exchange*, two-electron integrals:

$$J_{ij} = \iint \psi_i(\mathbf{x}) \psi_i^*(\mathbf{x}) \frac{1}{|\mathbf{r} - \mathbf{r}'|} \psi_j(\mathbf{x}') \psi_j^*(\mathbf{x}') \, \mathrm{d}\mathbf{x} \, \mathrm{d}\mathbf{x}' \tag{2.19}$$

and

$$K_{ij} = \iint \psi_i(\mathbf{x}) \psi_j^*(\mathbf{x}) \frac{1}{|\mathbf{r} - \mathbf{r}'|} \psi_i(\mathbf{x}') \psi_j^*(\mathbf{x}') \, \mathrm{d}\mathbf{x} \, \mathrm{d}\mathbf{x}'. \tag{2.20}$$

Clearly then, the total energy from Eqn. 2.17 contains terms describing: single-electron kinetic energies, electron-proton attraction, electron-electron repulsion, and an electron-exchange term that accounts for spin-correlation effects. Note that since $J_{ii} = K_{ii}$, the two-electron summation in Eqn. 2.17 can include the $i = j$ term. The total energy is then minimised — bearing the orthogonality condition $\langle\psi_i|\psi_j\rangle = \delta_{ij}$ in mind — to give the *Hartree-Fock equations* [70, 71], which can be written compactly as

$$\widehat{\mathcal{F}}\psi_i(\mathbf{x}) = \sum_{j=1}^{N_e} \epsilon_{ij}\ \psi_j(\mathbf{x}). \tag{2.21}$$

Here, $\widehat{\mathcal{F}}$ is known as the *Fock operator*, and is defined as

$$\widehat{\mathcal{F}} = \widehat{h} + \widehat{j} - \widehat{k}, \tag{2.22}$$

where $\widehat{h}$ comes from $\langle\psi_i|\widehat{h}|\psi_i\rangle = H_i$ (of Eqn. 2.18), while $\widehat{j}$ and $\widehat{k}$ are defined for an arbitrary function $f(\mathbf{x})$ as

$$\widehat{j}(\mathbf{x})f(\mathbf{x}) = \sum_{k=1}^{N_e} \int \psi_k^*(\mathbf{x}')\psi_k(\mathbf{x}')\frac{1}{|\mathbf{r}-\mathbf{r}'|}f(\mathbf{x})\ \mathrm{d}\mathbf{x}' \tag{2.23}$$

and

$$\widehat{k}(\mathbf{x})f(\mathbf{x}) = \sum_{k=1}^{N_e} \int \psi_k^*(\mathbf{x}')f(\mathbf{x}')\frac{1}{|\mathbf{r}-\mathbf{r}'|}\psi_k(\mathbf{x})\ \mathrm{d}\mathbf{x}'. \tag{2.24}$$

The matrix ϵ is populated by Lagrange multipliers, found from the minimisation procedure — its diagonal elements are obtained by integrating the Fock operator, through

$$\epsilon_i \equiv \epsilon_{ii} = \langle\psi_i|\widehat{\mathcal{F}}|\psi_i\rangle \tag{2.25}$$

$$= H_i + \sum_{j=1}^{N_e} \left(J_{ij} - K_{ij}\right). \tag{2.26}$$

By comparing this with Eqn. 2.17, the total energy can be written as

$$H_{\mathrm{HF}} = \sum_{i=1}^{N_e} \epsilon_i - \frac{1}{2}\sum_{i,j=1}^{N_e} \left(J_{ij} - K_{ij}\right). \tag{2.27}$$

The method described so far is known as the *open-shell* or *unrestricted* HF method. In systems containing an even number of electrons, the alternative *closed-shell* or *restricted* HF (RHF) method can be used. Here, the N_e spin-orbitals with spin functions $\omega_j(s_i)$ are replaced by $N_e/2$ orbitals with the form $\phi_j(\mathbf{r}_i)\alpha(s_i)$ and $N_e/2$ orbitals of the form $\phi_j(\mathbf{r}_i)\beta(s_i)$. The total energy then becomes

$$E_{\mathrm{RHF}} = 2\sum_{i=1}^{N_e/2} H_i + \sum_{i,j=1}^{N_e/2} \left(2J_{ij} - K_{ij}\right), \tag{2.28}$$

in which the spin dependence in H_i, J_{ij}, and K_{ij} can now be ignored, with integration being performed over $\mathbf{r}$ instead of over $\mathbf{x}$. The matrices involved in the RHF method are only one-quarter of the size of those in the unrestricted method, since the summations in Eqn. 2.28 only go up to $N_\mathrm{e}/2$.

The spin-orbitals ψ are typically expanded as linear combinations of atomic-type orbitals, such that they can be defined using

$$\psi_j(\mathbf{x}) = \sum_i^M c_{ij}\,\phi_i(\mathbf{x}). \tag{2.29}$$

The HF equations (Eqn. 2.21) can then be written using matrices to give a generalised eigenvalue equation called the *Roothaan(-Hall) equation* [66]:

$$\mathsf{F}\cdot\mathbf{c}_j = \epsilon_j\,\mathsf{S}\cdot\mathbf{c}_j, \tag{2.30}$$

in which S is the overlap matrix with $M \times M$ elements of the form $S_{ij} = \langle\phi_i|\phi_j\rangle$. This equation must be solved *self-consistently* until convergence of the total energy is considered satisfactory. The physical significance of the eigenvalues ϵ_j in the Roothaan equation was realised by Koopmans [72]:

Theorem 2 (Koopmans' theorem) *Assuming that the eigenstates $\mathbf{c}_j$ do not vary after removal of one electron from the system, the ionisation energy I_m of the m^{th} electron is given by $I_m = -\epsilon_m$.*

An important consequence of Koopmans' theorem is the ability of the HF method to calculate the energy of excited states. However, the HF method has one major drawback in that electron correlation is not included; that is, the spin-orbitals do not show a functional dependence on $\mathbf{r}_i - \mathbf{r}_j$. This leads, for example, to a zero density of states at the Fermi energy for the homogeneous electron gas. This problem can be overcome by expressing Ψ as a linear *combination* of Slater determinants in a technique known as the *configuration interaction* (CI) method. In principle, the CI method gives exact many-electron eigenstates and eigenvalues, however the computational effort required is extremely large and renders the method unsuitable at present for application to any system with more than a few tens of atoms.

2.5 Density-Functional Theory

The application of the all-electron HF method, even without CI included, is computationally prohibitive in systems containing many atoms, such as the extended systems used to model the bulk of solid materials. Most modern calculations of the electronic structure of solids instead make use of *density-functional theory* (DFT) [73, 74], since it is far less computationally demanding. Here, the total energy of the system E is a functional of the *electronic charge density* $n(\mathbf{r})$ (*i.e.* $E \equiv E[n]$), rather than of the all-electron wavefunction as in the HF method.

In the HF method, all properties of the ground state of a system are determined by the number of electrons N_e and an external potential v_ext. Hohenberg and Kohn sanctioned the use of the charge density as the basic variable [73] instead of N_e and v_ext:

Theorem 3 (First Hohenberg-Kohn theorem) *The external potential is determined, to within a trivial additive constant, by the electron density* $n(\mathbf{r})$.

Hence, as both the number of electrons and the external potential are uniquely defined by the charge density, so too is the system's ground-state wavefunction and therefore its total energy.

The *second* Hohenberg-Kohn theorem [73] states that for all charge densities n,

$$E[n] = F[n] + \int v_\mathrm{ext}(\mathbf{r})\, n(\mathbf{r})\, \mathrm{d}\mathbf{r} \tag{2.31}$$

$$\geq E[n_0], \tag{2.32}$$

where F is a universal (*i.e.* system-independent) functional that accounts for electronic kinetic energy, electron correlation, and exchange correlation, while n_0 is the ground-state density.

Theorem 4 (Second Hohenberg-Kohn theorem) *For a trial density* $\tilde{n}(\mathbf{r})$, *such that* $\tilde{n}(\mathbf{r}) > 0$ *and* $\int \tilde{n}(\mathbf{r})\, \mathrm{d}\mathbf{r} = N$,

$$E[\tilde{n}] \geq E_0. \tag{2.33}$$

This equation is similar to that of the Rayleigh-Ritz variational principle, hence in this case

$$E_0 = \min_{\tilde{n}} E[\tilde{n}]. \tag{2.34}$$

Now, although the adoption of the charge density as the basic variable has greatly simplified the calculational method, no approximations have been made in order to achieve this. However, the exchange-correlation contribution to the universal functional F remains — as in the HF method — a non-local quantity.

If a set of orthonormal spin-orbitals $\psi_\lambda(\mathbf{r}, s)$ are defined such that the charge density

$$n(\mathbf{r}) = \sum_{\lambda=1}^{N} |\psi_\lambda(\mathbf{r}, s)|^2, \tag{2.35}$$

then the total energy for the many-electron system, as a functional of the charge density, is given [75] by

$$E[n] = T_\mathrm{e}[\psi_\lambda] + V_\mathrm{e\text{-}e}[n] + V_\mathrm{e\text{-}n}[n] + E_\mathrm{xc}[n], \tag{2.36}$$

where the component parts are: the electron kinetic energy

$$T_\mathrm{e}[\psi_\lambda] = -\frac{1}{2} \sum_{\lambda,s} \int \psi^*_\lambda(\mathbf{r}, s) \nabla^2 \psi_\lambda(\mathbf{r}, s) \, \mathrm{d}\mathbf{r}, \tag{2.37}$$

the *Hartree energy*

$$V_\mathrm{e\text{-}e}[n] = \frac{1}{2} \int \frac{n(\mathbf{r})\, n(\mathbf{r}')}{|\mathbf{r} - \mathbf{r}'|} \, \mathrm{d}\mathbf{r} \, \mathrm{d}\mathbf{r}', \tag{2.38}$$

the external potential imposed on the electrons by the nuclei

$$V_\mathrm{e\text{-}n}[n] = -\int n(\mathbf{r}) \sum \frac{Z_\alpha}{|\mathbf{r} - \mathbf{R}_\alpha|} \, \mathrm{d}\mathbf{r}, \tag{2.39}$$

and the exchange-correlation functional E_xc, the form of which is generally unknown but will be discussed later.

2.5.1 Kohn-Sham equations

By making use of the variational principle, and the fact that the spin-orbitals $\psi_\lambda(\mathbf{r}, s)$ are orthonormal, the quantity

$$E - \sum_{\lambda,s} \epsilon_{\lambda,s} \left(\int |\psi_\lambda(\mathbf{r}, s)|^2 \, \mathrm{d}\mathbf{x} - 1 \right) \tag{2.40}$$

can be minimised with respect to ψ_λ^* and $\epsilon_{\lambda,s}$. This leads to a set of one-electron Schrödinger equations:

$$\left[-\frac{1}{2}\nabla^2 + \int \frac{n(\mathbf{r}')}{|\mathbf{r}-\mathbf{r}'|}\,\mathrm{d}\mathbf{r}' - \sum_\alpha \frac{Z_\alpha}{|\mathbf{r}-\mathbf{R}_\alpha|} + \frac{\delta E_{\mathrm{xc}}[n]}{\delta n(\mathbf{r})}\right]\psi_\lambda(\mathbf{r}) = \epsilon_\lambda \psi_\lambda(\mathbf{r}), \tag{2.41}$$

in which the charge density is obtained by summing over all of the N occupied spin-orbitals [74]. Thus,

$$n(\mathbf{r}) = \sum_{\lambda=1}^{N}\sum_s |\psi_\lambda(\mathbf{r},s)|^2\,. \tag{2.42}$$

The charge density in this case be considered as being composed of spin-up ($\uparrow$) and spin-down ($\downarrow$) charge densities; that is, $n(\mathbf{r}) = n_\uparrow(\mathbf{r}) + n_\downarrow(\mathbf{r})$.

Together, Eqns. 2.41 and 2.42 are known as the *Kohn-Sham equations* [74], and are solved in a *self-consistent* manner: First, a trial charge density is chosen and used to solve Eqn. 2.41. The results are used with Eqn. 2.42 to generate a new, improved charge density, which is then fed back into Eqn. 2.41. This process (the *self-consistency cycle*) is repeated until the difference between input and output charge densities becomes negligible. A plot of the corresponding input/output energy difference as a function of iteration number is shown for a typical system in Fig. 2.1.

2.5.2 The exchange-correlation functional

As stated earlier, the form of the non-local exchange-correlation functional $E_{\mathrm{xc}}[n]$ is unknown in the general case. Several approaches have been taken to overcome this problem, the most common of which is the invocation of the *local density approximation* (LDA), or the *local spin-density approximation* (LSDA) in the case of systems with a net spin [74, 76, 77]. Here, it is assumed that the exchange-correlation energy is *local*, and can be considered as separate exchange and correlation parts. In the LDSA notation,

$$E_{\mathrm{xc}}[n_\uparrow, n_\downarrow] = E_{\mathrm{x}}[n_\uparrow, n_\downarrow] + E_{\mathrm{c}}[n_\uparrow, n_\downarrow], \tag{2.43}$$

where the 'up' and 'down' spin-densities are respectively given by

$$n_\uparrow(\mathbf{r}) = \sum_{\lambda=1}^{N} |\psi_\lambda(\mathbf{r},\uparrow)|^2 \quad \text{and} \quad n_\downarrow(\mathbf{r}) = \sum_{\lambda=1}^{N} |\psi_\lambda(\mathbf{r},\downarrow)|^2\,. \tag{2.44}$$

Now, the *exchange* functional is known exactly for the case of the homogeneous electron gas [77], where it is given by

$$E_{\mathrm{x}}[n_{\uparrow}, n_{\downarrow}] = -\frac{3}{2}\left(\frac{3}{4\pi}\right)^{\frac{1}{3}}\left(n_{\uparrow}^{4/3} + n_{\downarrow}^{4/3}\right), \tag{2.45}$$

which is linear with respect to n.

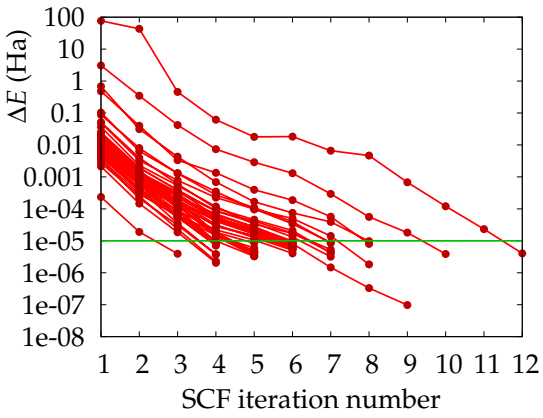

Figure 2.1: Plot of energy changes ΔE during the several self-consistency cycles involved in a typical structural relaxation of a defect in diamond. Each energy is considered converged when $\Delta E < 1 \times 10^{-5}$ Ha, although for the final total energy it is continued until $\Delta E < 1 \times 10^{-7}$ Ha.

However, the *correlation* part is more complicated. Perturbation theory gives rise to an expression for E_{c} that is valid for high charge densities [76], while in the low-density regime, a Green-function quantum-Monte-Carlo method yields a different expression [78, 79]. Nevertheless, it is possible to fit a simple parameterised form to the numerical results of these two expressions, and several parameterisations have been given [76, 80, 81].

An alternative to the L(S)DA is the *generalised gradient approximation* (GGA) [82–84], which involves a first-order expansion of E_{xc} in the density that includes terms in ∇n, and hence carries additional computational expense. The GGA is suitable for accurate studies of molecules, while the L(S)DA is more appropriate for the larger-scale modelling of solids.

2.6 Pseudopotentials

The core electrons in an atom are highly localised and do not take part in chemical reactions, and it is therefore only the *valence* electrons that determine the atom's chemical properties. The modelling of core electrons in a calculation is difficult to perform accurately, since in order to satisfy orthogonality, their wavefunctions must oscillate strongly near to the core, and the number of basis functions required to fit all states accurately becomes prohibitively large. In addition, full-electron calculations give large total energies, with correspondingly large errors introduced when comparing the energies of similar systems.

For these reasons, it is desirable to remove the core electrons from electronic structure calculations. This can be done by considering that, due to the presence of the core electrons nearer to the nucleus, the valence electrons in an atom experience an effective, screened nuclear potential — a *pseudo-potential*. The core electrons are therefore removed, and their influence and that of the nucleus is replaced with a pseudopotential [68, 85–88], as follows.

The pseudopotential is constructed by removing the valence electrons from a neutral atom, leaving an *ionic pseudopotential* [87], such that

$$\widehat{\mathcal{V}}^{\mathrm{ps}}_{\mathrm{ion}}(\mathbf{r}) = \widehat{\mathcal{V}}^{\mathrm{ps}}(\mathbf{r}) - \int \frac{n^{\mathrm{ps}}(\mathbf{r}')}{|\mathbf{r}-\mathbf{r}'|}\,\mathrm{d}\mathbf{r}' - \widehat{\mathcal{V}}_{\mathrm{xc}}[n^{\mathrm{ps}}(\mathbf{r})], \tag{2.46}$$

where the valence-states charge density

$$n^{\mathrm{ps}}(\mathbf{r}) = \sum_{\lambda} \left|\psi^{\mathrm{ps}}_{\lambda}(\mathbf{r})\right|^2, \tag{2.47}$$

in which the sum is performed over the occupied valence eigenstates of the pseudopotential $\widehat{\mathcal{V}}^{\mathrm{ps}}$.

Several approximations/assumptions must be made when making use of pseudopotentials, namely that:

- The all-electron Coulomb operator can be decomposed into two separate parts: one that deals with the core states, and the other that takes care of the valence states. This permits the removal of matrix elements concerned with the core electrons.
- The core states are unaffected by changes in the local environment of the atom. This is called the *frozen-core approximation*.
- There is negligible overlap between the core and valence states, hence the approximation $E_{\mathrm{xc}}(n_{\mathrm{core}} + n_{\mathrm{valence}}) = E_{\mathrm{xc}}(n_{\mathrm{core}}) + E_{\mathrm{xc}}(n_{\mathrm{valence}})$ is valid. This is not always justified, and the *non-linear core correction* [89] is sometimes used to improve the situation.

A practical pseudopotential must also give rise to pseudo-wavefunctions that, outside of a certain 'cut-off' radius from the core, are identical to those derived from an all-electron calculation. This is known as *norm conservation*, and one example of a set of norm-conserving pseudopotentials is that of Bachelet, Hamann, and Schlüter (BHS) [90, 91].

The quality of a given pseudopotential can be assessed by investigating its *transferability*. That is, a transferable pseudopotential is one that will reproduce the properties of an atom's valence electrons sufficiently well in a wide range of different local environments. For example, a high-quality pseudopotential for the carbon atom would give accurate results when used in diamond, graphite, or in fullerenes.

The calculations presented in this thesis have made use of the relativistic, separable, dual-space Gaussian pseudopotentials devised by Hartwigsen, Goedecker, and Hutter (HGH) [92].

2.7 The AIMpro implementation of DFT

The computer code used to perform the calculations presented within this thesis is known as the *Ab-initio Modelling Program*, or AIMpro for short. AIMpro makes use of a real-space, Gaussian-type basis set [93–95] and can perform both *cluster* and *supercell* calculations.

In the cluster method, a collection of atoms is modelled in infinite vacuum, and typical solid-state calculations use between $\sim$ 100–200 atoms in order to represent a small region of bulk material. In most cases, the atoms on the surface of the cluster have their dangling bonds tied up by atoms of hydrogen. Defects can be modelled near the centre of the cluster, although care must be taken to understand the effects of interaction between the defect and the cluster's bounding surface [93].

2.7.1 Supercell AIMpro

The supercell method uses periodic boundary conditions in order to simulate infinite bulk material and therefore avoid surface effects. Nevertheless, supercells can be used to model surfaces by using the *slab* method, which will be discussed later. When a defect is modelled in a supercell representing infinite bulk material, its location in the cell is not important due to the periodicity. However, images of the defect will appear in every repeated supercell, and the defect's interaction with its own repeated images becomes a cause for concern. Supercells must therefore be sensibly shaped and large enough to minimise defect-image coupling arising through Coulombic, dipolar, and quadrupolar

interactions. When modelling a *shallow* defect, its donor or acceptor wavefunction will be considerably delocalised — significantly spread out over a large region of the supercell. Defect-image interaction (overlap of the wavefunction with those originating in repeated cells) is especially important to consider in these cases.

2.7.2 Sampling of the Brillouin zone

In the supercell formalism, one has to perform Brillouin-zone (BZ) integration in order to calculate physical quantities (such as the total energy), and wavefunctions must therefore be expanded in reciprocal space. AIMpro achieves this by using Fourier transformation [96].

The integrand function $f(\mathbf{k})$ used in BZ integration is periodic in reciprocal space, although in general it has no simple analytical form. Numerical integration could be performed over a suitably dense mesh, although this would be computationally expensive and inefficient. One alternative scheme, devised by Monkhorst and Pack (MP) [97, 98], is not computationally expensive, and its convergence as the sampling accuracy is increased can be easily verified.

Integrating f over a BZ with volume $(2\pi)^3/\Omega$ yields an average value $\bar{f}$, which is given by

$$\bar{f} = \frac{\Omega}{(2\pi)^3} \int f(\mathbf{k})\, \mathrm{d}\mathbf{k} \tag{2.48}$$

$$\approx \frac{1}{N} \sum_{n=1}^{N} f(\mathbf{k}_n), \tag{2.49}$$

where the function f is evaluated over a $I \times J \times K$ grid of points in reciprocal space, whose values are given by

$$\mathbf{k}(i,j,k) = \frac{2i-I-1}{2I}\mathbf{g}_1 + \frac{2j-J-1}{2J}\mathbf{g}_2 + \frac{2k-K-1}{2K}\mathbf{g}_3, \tag{2.50}$$

and I, J, and K are integers ≥ 1. Schemes in which $I = J = K$ are said to make use of MP-I^3 grids.

In a supercell of high symmetry, some of the $\mathbf{k}$-points may become equivalent, in which case the redundant $\mathbf{k}$-points can be eliminated provided that the remaining $\mathbf{k}$-points are

weighted with factors ω_n equal to the number of equivalent **k**-points at each **k**-point n. Then, the average $\bar{f}$ from the integral of f over the BZ can be given by

$$\bar{f} = \frac{\Omega}{(2\pi)^3} \int f(\mathbf{k})\, \mathrm{d}\mathbf{k} \tag{2.51}$$

$$\approx \frac{\sum_n \omega_n f(\mathbf{k}_n)}{\sum_n \omega_n}, \tag{2.52}$$

where the sums are performed over the remaining, unique **k**-points only.

2.7.3 Basis functions

AIMpro uses a set of Bloch basis functions $B_{\mathbf{k}i}(\mathbf{r})$ that are themselves built from a set of Cartesian Gaussian functions ϕ_j centred at the atomic sites (with positions $\mathbf{R}_\alpha$), and N_L lattice vectors $\mathbf{L}_n$. The basis functions are defined using

$$B_{\mathbf{k}\alpha}(\mathbf{r}) = \frac{1}{\sqrt{N_\mathrm{L}}} \sum_n^{N_\mathrm{L}} \sum_j \phi_j(\mathbf{r} - \mathbf{R}_\alpha - \mathbf{L}_n)\, \mathrm{e}^{\mathrm{i}\mathbf{k}\cdot\mathbf{L}_n}, \tag{2.53}$$

where **k** is a vector in reciprocal space. The localised, Gaussian orbitals have the form

$$\phi_j(\mathbf{r} - \mathbf{R}_\alpha) = (x - R_{\alpha,x})^{l_1} (y - R_{\alpha,y})^{l_2} (z - R_{\alpha,z})^{l_3} \times \mathrm{e}^{-\beta(\mathbf{r}-\mathbf{R}_\alpha)^2}, \tag{2.54}$$

in which l_i are integers, each ≥ 0. By choosing different values of l_i, different types of orbitals can be constructed that resemble those found in a hydrogenic atom:

- When $\sum_i l_i = 0$, all l_i must be equal to zero, and the single orbital thus formed is spherically symmetric, decaying away from the atom's position $\mathbf{R}_\alpha$. This orbital is said to be *s-like*.
- To satisfy $\sum_i l_i = 1$, one of the l_i must equal 1 while the other two are zero. In each case, the orbital will have a cylindrical axis of symmetry along one of the Cartesian directions, and mirror symmetry about the plane defined by the position $\mathbf{R}_\alpha$ and the two remaining directions. This condition therefore gives rise to three, *p-like* orbitals.
- For the case of $\sum_i l_i = 2$, there are six possible solutions. In three of these, two of the l_i equal 1 while the remaining one is zero, and in the other three solutions, one of the l_i has a value of 2, while the other two are zero. Linear combinations of these solutions can be taken to give five orbitals that are *d-like*, and one orbital that is s-like.

The Kohn-Sham orbitals $\psi_{\mathbf{k}\lambda}$ can then be expanded in terms of these $B_{\mathbf{k}i}$ basis functions, such that

$$\psi_{\mathbf{k}\lambda}(\mathbf{r}) = \sum_{\alpha} c^{\mathbf{k}}_{\lambda\alpha}\, B_{\mathbf{k}\alpha}(\mathbf{r}), \tag{2.55}$$

from which the charge density can be obtained as

$$n(\mathbf{r}) = \sum_{\alpha,\gamma,\mathbf{k}} b_{\alpha\gamma}(\mathbf{k})\, B^{*}_{\mathbf{k}\alpha}(\mathbf{r})\, B_{\mathbf{k}\gamma}(\mathbf{r}), \tag{2.56}$$

in which

$$b_{\alpha\gamma}(\mathbf{k}) = \sum_{\lambda} f_{\mathbf{k}\lambda}\, c^{*}_{\mathbf{k}\lambda,\alpha}\, c_{\mathbf{k}\lambda,\gamma}, \tag{2.57}$$

where $f_{\mathbf{k}\lambda}$ is the occupancy of the $\mathbf{k}\lambda$ state. This should be equal to 2 for a completely filled state (and zero for an empty state) in a spin-averaged calculation, or 1 for a completely filled state in a spin-polarised calculation. If a finite temperature is used to model the filling of the electronic levels, smearing around the Fermi level is achieved by using non-integer values for $f_{\mathbf{k}\lambda}$. In a system in which *metallic* filling is required, $f_{\mathbf{k}\lambda}$ is made independent of $\mathbf{k}$.

The use of Gaussian functions has the advantage that their integrals have analytical forms, which can be calculated easily. Furthermore, they can be chosen to decay away from $\mathbf{R}_{\alpha}$ rather quickly [93], whereas to achieve this with oscillating functions would require the combination of very many plane waves. Although Gaussian orbitals have radial parts of the form $e^{-\beta\mathbf{r}^2}$ while 'true' electronic orbitals are proportional to $e^{-\mathbf{r}}$, the advantage in their use is that the product of two Gaussian orbitals is itself a Gaussian function. This means, for instance, that four-centre integrals are reduced to two-centre integrals that are much faster to evaluate. However, the Gaussian functions used here are not orthogonal, and in addition, using too many can result in *over-completeness*, which introduces numerical instabilities. For more information on the use of Gaussian basis functions in AIMpro, consult Ref. [94].

2.7.4 Basis functions in reciprocal space

Although the Kohn-Sham orbitals are constructed using a real-space basis set, the periodic boundary conditions present in the supercell formalism make representation of the charge density using Fourier series an obvious move. Indeed, the Hartree energy is most simply determined from such a representation. The exchange-correlation energy can then

be found by Fourier transforming the charge density to real space, and then applying the exchange-correlation functional directly. The Fourier transformation is performed using a set of reciprocal-lattice vectors **g**. The accuracy of the transformation is naturally determined by the density of the grid of **g**-vectors. In practice, a uniform grid is used inside of a sphere whose radius g_{cut} defines a *cut-off energy*

$$E_{\text{cut}} = \frac{1}{2} g_{\text{cut}}^2, \tag{2.58}$$

which is increased until the total energy is seen to converge.

2.8 Calculation of observables

AIMpro is capable of calculating many physical properties that are observable in principle or in some way experimentally measurable on real samples. The observables that will be discussed here are those that are relevant to the investigation presented in this thesis.

Firstly, it should be noted that Kohn-Sham density-functional theory is strictly a *ground-state* theory. Excited-state properties cannot be easily determined, owing to the fact that the Kohn-Sham eigenstates are not true one-electron wavefunctions, but rather form a set of basis functions that — when combined and occupied as described in this chapter — will give rise to the correct *ground-state* electronic charge density. However, the energy of the highest-occupied KS state is in fact directly comparable with the ionisation potential of the system [99].

Nevertheless, and as will be seen in Chp. 5, while ground-state properties can be calculated with high accuracy, excited-state properties can be estimated with decent accuracy provided that suitable corrections are made.

2.8.1 Atomic geometry

The ground-state atomic geometry of a system can be determined by minimising the forces acting on each atom in the set. First, a self-consistent charge density is found for the given atomic positions. From this, the total energy E is obtained, and the force $\mathbf{F}_\alpha$

acting on each atom α can be found using

$$\mathbf{F}_\alpha = -\nabla_\alpha E. \tag{2.59}$$

Each atom is then moved by a calculated amount along the direction of the force acting on it. The process is then repeated using the new atomic positions. This continues until the forces acting on the atoms fall beneath a given threshold. The determination of the forces makes use of the Hellmann-Feynman theorem [100, 101]:

Theorem 5 (Hellmann-Feynman theorem) *Let ξ be a parameter in the Hamiltonian $\widehat{\mathcal{H}}$ and Ψ_ξ an eigenvalue of $\widehat{\mathcal{H}}$. Then,*

$$\frac{\partial E}{\partial \xi} = \left\langle \Psi \left| \frac{\partial \widehat{\mathcal{H}}}{\partial \xi} \right| \Psi \right\rangle. \tag{2.60}$$

Using this algorithm to find the ground-state atomic geometry is known as *relaxing* the system.

The movement of each atom by a *calculated* amount along its force vector is performed using the *conjugate gradient algorithm*. In essence, this method provides a quick way to find the (nearest local) minimum of a function given that the gradient of the function can be calculated. Using this technique, AIMpro moves the atoms into a minimum of potential energy. This technique, whilst being fast, has the drawback that the minimal-energy structure found from a given initial atomic configuration might be that corresponding to only a *local* energy minimum, rather than the structure with the *global* minimum energy. Therefore, the choice of initial atomic positions should receive careful attention, and the use of several different starting structures can help in assuring that the global minimum has been achieved.

Symmetry breaking and the Jahn-Teller effect

The presence of high symmetry in the atomic geometry of a system will greatly reduce the amount of computational effort required to calculate its properties, since it decreases the number of unique **k**-points required to sample the BZ (given the specified grid). Furthermore, Nature tends to adopt configurations of high symmetry, since these often result in a balance of forces and correspond to minima in the associated energy surface. Therefore, atomic geometries with high symmetry are very often the most stable.

However, calculations performed with initial atomic coordinates of high symmetry will have artificial constraints imposed on atomic relaxation, due to forces that are exactly equal and opposite. This may lead to the discovery of 'relaxed' structures that are in fact held in unstable equilibrium by symmetry.

Another important consideration is the *Jahn-Teller effect*, wherein a symmetry-lowering distortion of the atomic geometry leads to a lowering of the *electronic* energy, enough to result in a reduction of the total energy. This effect occurs when an electronic state is degenerate (due to the high symmetry of the system), although only partially occupied. A distortion of the atomic geometry to a configuration of lower symmetry will split the degenerate state into states of higher and lower energy. As the electron(s) will naturally occupy the state(s) of lower energy, the total electronic energy is reduced. In general, provided that this energy saving is greater than any rise in energy accompanying the movement in nuclear positions, the total energy has been reduced and the system is more stable.

For example, a defect with T_d symmetry may possess a triply degenerate t_2 level that is only occupied by one electron. A distortion to the lower C_{3v} symmetry can split this level into a doubly degenerate e state of higher energy and a single a_1 state of lower energy (although this ordering is not actually dictated by symmetry), with the single electron occupying the latter.

For these reasons, it is very important to repeat geometry-optimisation calculations after applying symmetry-breaking displacements to the initial atomic coordinates, so as to allow the system the freedom to relax to structures that may exhibit less symmetry but possess lower total energies.

An important practical consideration is that the energy saving of a Jahn-Teller distortion may be quite small, and/or the energy barrier between equivalent distorted structures may be low. The system might then show a different time-averaged symmetry in practice, since at appropriately high temperatures it will rapidly reorient between the different configurations. This is called the *dynamic* Jahn-Teller effect, and is known to occur in the case of the neutral vacancy in diamond [102].

2.8.2 Formation energies

In determining which of several defects in a material is the most energetically stable, it is only valid to directly compare the calculated total energies of the relaxed systems when they each contain the same number and types of atoms, or rather the systems are simply different arrangements of the same set of atoms. When this is not the case, the *formation energy* of each defect is a suitable quantity to compare across systems.

Firstly, the *chemical potential* μ_x of a particle of type x is defined as the derivative of the Gibbs free energy G (for a given phase) with respect to the number n_x of particles of that type [103, 104]. That is, $\mu_x = \partial G/\partial n_x$, where the Gibbs free energy is defined as

$$G = E + pV - TS, \tag{2.61}$$

in which E is the total energy, p and V are the pressure and volume respectively, and T and S are respectively the temperature and entropy of the system. However the last two terms in G can often be neglected, since in most solid-state calculations p and T are both negligibly small. Hence, $G \approx E$, and so

$$\mu_x = \frac{\partial G}{\partial n_x} \approx \frac{\partial E}{\partial n_x} \quad \Rightarrow \quad E = \sum_x n_x \mu_x. \tag{2.62}$$

Furthermore, when in thermodynamic equilibrium, μ_x must be the same for all phases that are in contact. Hence the chemical potential can be thought of as the free energy per particle in its standard (reference) state.

The formation energy $E_A^{\mathrm{f}}(0)$ of a particular system A is then given by the expression

$$E_A^{\mathrm{f}}(0) = E_A(0) - \sum_x n_x \mu_x, \tag{2.63}$$

where $E_A(0)$ is the total energy of the system comprised of n_x particles of type x. Hence, it is the energy difference between the particular configuration A of the particles, and the sum of their free energies when they are in their reference states. In other words, $E_A^{\mathrm{f}}(0)$ is the energy liberated (or expended if it is negative) when one 'builds' the system A using particles taken from reservoirs in which they are in their standard states.

When modelling defects in condensed matter, the appropriate 'particles' are the neutral atoms that form the system, where x is each chemical *species*. The reference state for each atom must be carefully chosen. For instance, the reference state of a C atom might

be diamond or graphite, while that for hydrogen could be the isolated atom or the H_2 molecule. Often, one considers the real origin of each atom in some experiment; for example, the P defect in diamond is grown into CVD material from phosphine (PH_3) gas.

If one wishes to calculate the formation energy of a charged system, the chemical potential μ_e of the extra/fewer electrons must be taken into account, and the expression becomes

$$E_A^f(q) = E_A(q) - \left(\sum_x n_x \mu_x\right) + q\mu_e, \tag{2.64}$$

where q is the charge state of the system (*e.g.* -1, $+2$, *etc.*). The electron chemical potential μ_e is identical to the Fermi energy E_F in the ground state at absolute zero. One must take care to be consistent in defining a reference energy for E_F when using Eqn. 2.64; often, the energy of the valence band maximum E_{VBM} is taken to be the zero of E_F, in which case this extra term is written $q\,(E_{VBM} + E_F)$.

However, in the supercell method, errors arise because of electrostatic and multipole interactions in such charged systems due to the periodic nature of the calculations and the compensating background charge applied [105]. Therefore, an extra term $\kappa_A(q)$ is sometimes included to correct for these effects (although this approach is not universally accepted, especially since it involves approximating the charge to a point), and the formation energy becomes

$$E_A^f(q) = E_A(q) - \left(\sum_x n_x \mu_x\right) + qE_F + \kappa_X(q), \tag{2.65}$$

where the last two terms disappear in the case of $q = 0$.

2.8.3 Complex binding energies

The energy that binds a complex A–B, formed from combining separate defects A and B, can be found by comparing formation energies, as follows. In general, the binding energy $E_{AB}^b(q_{AB})$ of the A–B complex in charge state q_{AB} is given by

$$E_{AB}^b(q_{AB}) = \left[E_A^f(q_A) + E_B^f(q_B)\right] - E_{AB}^f(q_{AB}), \tag{2.66}$$

where the separated components A and B have been modelled in charge states q_A and q_B respectively. If the $E_{AB}^b(q_{AB})$ found from this equation is positive, then the complex is bound with respect to its separated constituents (at least for the charge states considered).

The binding energy has the useful property that it does not depend on the chemical potentials μ_A and μ_B of the impurity species, since these terms cancel, but only on the chemical potential of the host species (*e.g.* carbon). The latter is easily found from separate calculations, as the total energy of a supercell of bulk material, divided by its number of atoms. This value should be independent of supercell size (*e.g.* 2-atom, 8-atom, 64-atom, *etc.*) if the calculations are sufficiently converged.

If the charge states considered with Eqn. 2.66 are non-zero, for example when calculating the energy change in the dissociation reaction $(A\text{–}B)^0 \rightarrow A^+ + B^-$, then potentially large contributions may arise from the correction terms $\kappa_A(q_A)$ and $\kappa_B(q_B)$ in the formation energies. For the pertinent case of charged defects in diamond, the correction terms can include contributions as large as q^2 eV for a 64-atom supercell [42].

When all of the systems being compared are considered in the neutral charge state, the last two terms from Eqn. 2.65 in each formation energy will be zero, and Eqn. 2.66 reduces to a comparison of supercell total energies. The binding energy is then

$$E^{\mathrm{b}}_{AB} = [E_A + E_B - n_C\,\mu_C] - E_{AB}, \tag{2.67}$$

where E_X is the total energy of a neutral supercell containing X in the host material C. In general, there will be more atoms of the host material in the sum of the two systems in the square brackets than in the A–B complex system. Therefore, the extra term $n_C\,\mu_C$ is present to balance the number of host atoms across the systems being compared, where μ_C is the chemical potential of the host species, and n_C is the number of surplus host atoms.

2.8.4 Donor and acceptor levels

Equation 2.65 permits the calculation of several thermodynamic properties, including defect solubilities, concentrations, and occupancy levels [106–108]. The (single) *donor level* of a defect is often denoted using $E(0/+)$, while a single *acceptor* level is written as $E(\text{-}/0)$. In this notation, the slash represents the electrical level, while the two symbols indicate the charge state that the defect would have if the Fermi level were to lie either above (first) or below (second symbol) the level in energy. A second (or *double*-) donor level is written as $E(+/{+}{+})$, while a double-acceptor level is written $E(\text{-}\text{-}/\text{-})$, and so on.

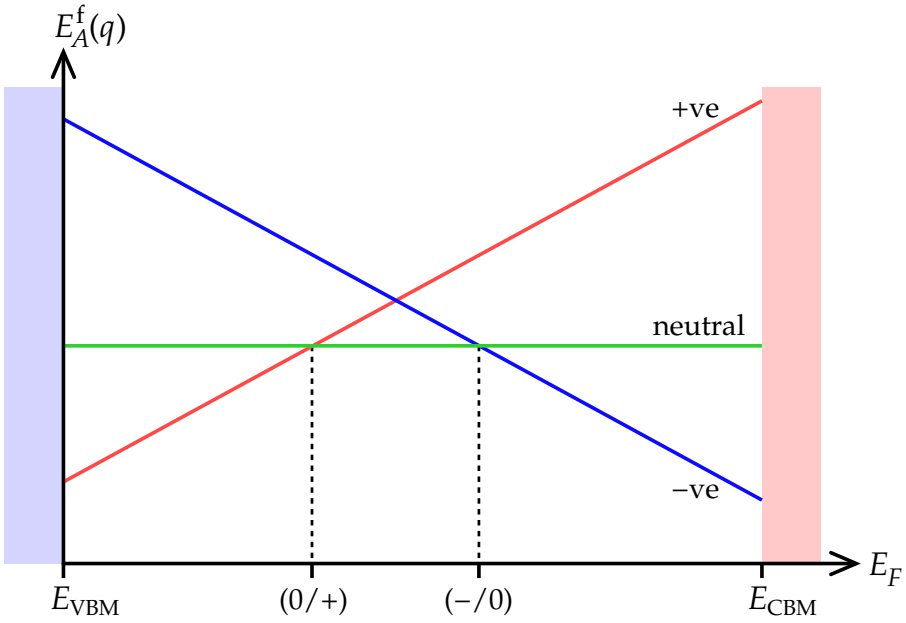

Figure 2.2: Schematic of the formation energy $E_A^{\mathrm{f}}(q)$ for three charge states q of a system A, as a function of the Fermi energy E_F. The bulk valence and conduction bands are shown as shaded regions. The donor level (0/+) is the Fermi energy above which the neutral charge state is lower in energy than the positive charge state, while the acceptor level (-/0) is the value of E_F above which the negative charge state is preferred over the neutral.

Formation energy method (FEM)

Formation energies can be used to calculate the positions of transition levels, since for instance the location of a $(q/(q+1))$ level is given by the Fermi level for which the defect in the q charge state and the defect in the $q+1$ charge state have the same formation energy. That is, the position of the level is the E_F taken from equating $E_A^{\mathrm{f}}(q) = E_A^{\mathrm{f}}(q+1)$.

Clearly, the formation energy $E_A^{\mathrm{f}}(q)$ from Eqn. 2.65 is a straight-line function of the Fermi energy E_F, with the charge state q as the gradient, and the other terms defining the y-axis intercept. One can find three expressions for the lines corresponding to say, $q = -1$, 0, and $+1$, and then plot a graph in the style of Fig. 2.2. Then, the lowest line for each value of E_F describes the preferred charge state for that Fermi energy. The transition levels are then given by the E_F values where the lines cross; that is, where one charge state becomes preferred over another.

The majority of systems produce a formation-energy graph resembling that of Fig. 2.2,

where the donor level is lower in the bandgap than the acceptor level. However, in so-called negative-U systems, this ordering is reversed (that is, the +ve and -ve lines cross below the neutral line). In such systems, the neutral state is never the most stable, and there exists a range of Fermi energies at which both negatively and positively charged defects are present (at least at low temperatures).

Despite the fact that the FEM suffers from the aforementioned problems with calculating the formation energy of charged systems, it is one of the most commonly used, and is discussed for example in Ref. [109].

Marker methods

An alternative approach is the so-called *marker method* (MM), which has a few variations. In what will be referred to as the *defect*-MM, the calculated electrical level of the system under investigation is compared against that calculated for some 'standard' defect (the *marker*) whose donor/acceptor activation energy is experimentally well known [110–113]. This technique requires four calculations, since the test defect X and the marker defect M must both be modelled in the two charge states corresponding to the desired level.

For example, to calculate a donor level, four calculations are performed to find the total energies $E(0)_X$, $E(+)_X$, $E(0)_M$, and $E(+)_M$. Then, a characteristic 'ionisation energy' $E^{\mathrm{i}} = E(+) - E(0)$ can be found for each defect. These E^{i} are proportional to the energy required to remove an electron from each system. It is then argued that the difference in the E^{i} is equal to the difference in the positions of the donor levels — if it is, say, 0.1 eV more difficult to remove an electron from the test system than it is from the marker system, then the test defect has a donor level 0.1 eV below that of the marker. So, as the donor activation energy of the marker E^{a}_M is known from experiment, the donor activation energy of the test defect can be given by

$$E^{\mathrm{a}}_X = E^{\mathrm{a}}_M + (E^{\mathrm{i}}_X - E^{\mathrm{i}}_M). \tag{2.68}$$

The donor level of the defect can then be quoted relative to the conduction band minimum energy E_{c} as being located at $E(0/+)_X = E_{\mathrm{c}} - E^{\mathrm{a}}_X$.

Similar quantities, such as double-donor or acceptor levels, are found in the same way after making the appropriate substitutions.

This method eliminates some of the errors present in DFT calculations, such as where an underestimate in the bandgap may significantly perturb the position of the defect levels, and where systematic errors come from the compensating background present for charged defects [105]. The method has been used with great success in the case of chalcogen defects in silicon, where it corrected errors of the order of 0.5 eV that were encountered when using the formation energy method [111].

The *first-principles* marker method (FPMM) uses four calculations to refer a donor or acceptor level to the bulk band edges, without the need to use any empirical data [114]. To calculate a donor level, one calculates E^{i}_{X} for the defect, and then $E^{\mathrm{i}}_{\mathrm{bulk}}$ for a bulk supercell of the same size. The latter quantity essentially sets the position of the top of the bulk valence band, E_{v}. Then, the donor level of X is located at $E_{\mathrm{v}} + (E^{\mathrm{i}}_{\mathrm{bulk}} - E^{\mathrm{i}}_{X})$. In a similar way, one can calculate acceptor levels from first principles, referring them to E_{c}.

This technique has been used to calculate the donor and acceptor levels of a wide variety of defects in diamond, producing decent agreement with experiment [115, 116].

However, one normally wishes to refer donor levels to E_{c}, and acceptor levels to E_{v}. The underestimation of the bandgap in LDA-DFT calculations means that the experimental bandgap has to be used to convert between the two, in which case the technique is no longer first-principles. The method is then equivalent to the defect-MM, except that here the known 'donor' or 'acceptor' activation energy of the marker is simply the experimental value for the bulk bandgap.

A recent comparison of the various methods concluded the following. While the defect-MM should yield the most accurate predictions, the relative lack of experimental data (markers) in diamond means that the bulk-MM is likely to give the most reliable electrical levels in general for this material. Meanwhile, the FEM yields levels in poorer agreement with experiment, although the lack of a standard double-donor or double-acceptor in diamond for use with the MM renders the FEM the only choice for electrical levels involving higher charge states [115].

2.9 Electronic state characterisation

2.9.1 Mulliken bond population analysis

Mulliken bond population analysis, or simply *Mulliken analysis*, is one technique that can be used to identify which of the atoms in a system are responsible for a particular electronic state. The contribution to the electronic state λ from a basis function ϕ_i can be determined by calculating the Mulliken bond population $p_\lambda(i)$ [117], which is defined as

$$p_\lambda(i) = \frac{1}{N_\mathrm{L}} \sum_{j,\mathbf{k}} c_{\mathbf{k}\lambda,i}\, S^{\mathbf{k}}_{ij}\, c^*_{\mathbf{k}\lambda,j}, \tag{2.69}$$

in which $S^{\mathbf{k}}_{ij}$ are the overlap matrix elements, given by

$$S^{\mathbf{k}}_{ij} = \int B^*_{\mathbf{k}i}\, \mathrm{e}^{-\mathrm{i}\mathbf{k}\cdot\mathbf{r}}\, B_{\mathbf{k}j}\, \mathrm{d}\mathbf{r}, \tag{2.70}$$

and N_L is used to ensure that $\sum_i p_\lambda(i) = 1$. The basis functions $B_{\mathbf{k}i}$ are those defined in Sec. 2.7.3. Now, if a particular state λ has a composition dominated by an orbital ϕ_i centred on a particular atom, then the coefficients $c_{\mathbf{k}\lambda,i}$ will be very large and hence so will the value of $p_\lambda(i)$. That atom can be identified as being mostly responsible for that electronic state, and the hybridisation of the state can be deduced by comparing all of the $p_\lambda(i)$ values for s-, p-, and d-like orbitals.

2.9.2 Wavefunction visualisation

An alternative to Mulliken analysis is now available with the use of the AIMview software. This code allows for two- or three-dimensional visualisation of the KS orbitals around the atoms of a cluster or supercell that has been modelled using AIMpro. This permits a more direct association of energy levels with particular atoms, although it must still be appreciated that the orbitals are in fact solutions to the KS equation, rather than the 'true' one-electron wavefunctions.

To construct a 2D plot, one must first define a plane through the system and choose a particular electronic state ψ_i. Contours are then drawn on this plane to connect points with equal values of ψ_i, and the regions bounded by the contours are coloured according to an appropriate scale. A 3D plot is similarly achieved by defining a *volume* within

the system, and drawing within it curved, coloured iso*surfaces* of equal wavefunction value. Alternatively, contours or isosurfaces of equal $|\psi_i|^2$ can be drawn, so as to give an impression of the spatial distribution of 'charge density' for that particular state.

It is also possible to sum together the wavefunctions of many states and plot the output. This is important when dealing with degenerate energy levels, where the individual wavefunctions must be taken in a linear combination in order to identify the symmetry of the degenerate state.

All plots are appropriate to a given **k**-point in the calculation (typically the Γ point is used), although an average over multiple **k**-points (say the MP sampling grid) can be chosen instead.

2.10 Convergence criteria

Clearly there are many parameters in electronic structure calculations such as these that can be varied to increase the accuracy of the final result, usually at the cost of adding to the computational time required. Each parameter must be varied independently, and usually it is the effect on the total energy of the system that is recorded. The total energy normally converges toward a constant value as the chosen parameter is varied in the direction corresponding to higher simulation accuracy. One then looks for the value of the parameter that corresponds to a short computational time but results in a total energy close to the converged value.

The most important parameters are generally: the size of a supercell (typically the number of bulk-like atoms surrounding a defect); the density of the MP grid of special **k**-points used to sample the BZ; the value of E_{cut} for use in Fourier transformation in reciprocal space; and the number of basis functions on the atoms, and their exponents.

For example, once a supercell of suitable size and a basis set have been chosen, both the value of E_{cut} and the number of **k**-points should be increased independently in a series of calculations, until the total energy of the system changes by less than about 0.001 a.u. per atom. Sometimes, the effect of adding extra basis functions to the system (particularly on any impurity atoms) is then investigated.

There are additional parameters to consider with regard to convergence when modelling more unusual systems such as surfaces, as will be seen in the next section.

2.11 Modelling surfaces

Although the supercell method is normally used to simulate bulk material with infinite extent in all directions, it is possible to model surfaces within the method by constructing so-called *slab* systems. Here, one of the three lattice vectors used to repeat the supercell (typically the third, or $\vec{z}$) is extended in length by a great amount, but the extra supercell volume thus created is not filled with atoms. A large gap of vacuum is opened up between regions of material and their repeated images in this direction. The material repeats as usual in the two remaining directions, hence 'slabs' of material with infinite *planar* extent are created, bounded by the surfaces to be modelled and separated by layers of vacuum.

2.11.1 Convergence criteria

One has to ensure that there is enough vacuum separating repeating slabs to minimise interaction between the upper surface of one slab, and the lower surface of the repeated slab above it. However, increasing the vacuum gap increases the number of plane waves required to model the Fourier-transformed charge density in that region, which adds computational expense. The thickness of the vacuum gap is therefore an additional convergence criterion and a chance for compromise.

Furthermore, the slab of material must also have adequate thickness, so that its innermost atomic layers accurately represent bulk material. This can be checked (to first order) by fully relaxing several slabs with different numbers of atomic layers, and looking for bond lengths between the innermost layers that are negligibly different from those in a supercell of bulk material. A more satisfactory method to check that the central atoms are in a bulk-like environment is to calculate the spatial variation of electrostatic potential across the thickness of the relaxed slab, and compare it with that in a bulk supercell having the same orientation. For a suitably thick slab, the plotted peaks and troughs of potential that correspond to the inner atomic layers will line up well with any of those

taken from in the bulk calculation.

Fortunately, the large real-space dimension needed to accommodate a thick slab and a large vacuum gap corresponds to a small reciprocal-space dimension, and very few **k**-points (often only one) are required for the sampling of the BZ in this direction. In addition, detailed band structures need only be calculated along paths within the plane formed by the other two directions.

2.11.2 Electron affinity, ionisation potential, and work function

Strictly, the *electron affinity* (EA) χ of a substance is the difference between two ground-state total energies: $E(0)$, the energy of the substance in its neutrally charged state, plus a single electron held at infinite distance at the vacuum level; and $E(\text{-})$, the total energy of the system when the electron has been brought in and added to the substance. That is, $\chi = E(\text{-}) - E(0)$. In a similar way, the *ionisation potential* (IP) I is the difference between total energies for: the neutral substance, and the system with one electron removed to infinity, so that $I = E(+) - E(0)$.

For large, extended systems such as solids, the energy difference in both quantities is dominated by the *band structure* term; that is, by the difference between the appropriate KS energy levels. The concern therefore lies with the relative positions of three levels: (i) the (flat) electrostatic potential in the vacuum V_{vac}; (ii) the maximum of the highest occupied electronic level E_{HO}; and (iii) the minimum of the lowest unoccupied electronic level E_{LU}. To first order, the EA is then $\chi = -(E_{\text{LU}} - V_{\text{vac}})$, while the IP is $I = V_{\text{vac}} - E_{\text{HO}}$. Choosing V_{vac} as the zero of the energy scale, these are reduced to $\chi = -E_{\text{LU}}$ and $I = -E_{\text{HO}}$.

A material possesses a *negative* electron affinity (NEA) if its conduction-band states are higher in energy than the vacuum potential. Simple energy-level schemes for positive electron affinity (PEA) and NEA in semiconductor materials are shown in Fig. 2.3.

The *work function* (WF) ϕ of a system is similarly given to first order as the energy difference between the vacuum potential and the Fermi level E_F in the material; that is, $\phi = V_{\text{vac}} - E_F$, or rather $\phi = -E_F$ if the vacuum level has been used as the energy zero. The WF and IP therefore differ by $E_F - E_{\text{HO}}$. In a semiconductor material, it can be dif-

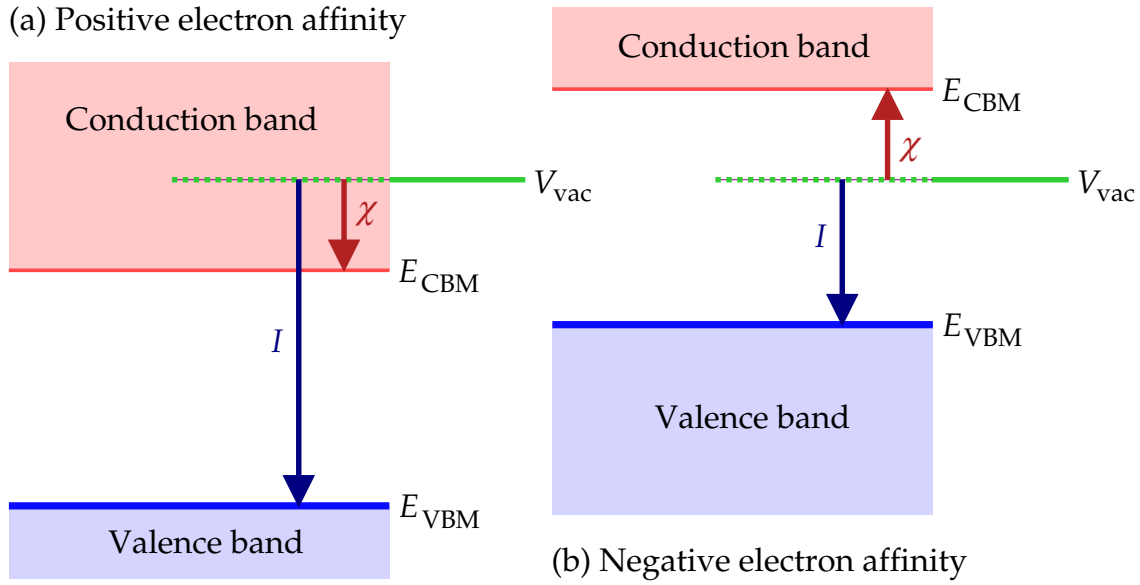

Figure 2.3: Simple energy-level schemes for semiconductor materials with: (a) conventional, positive electron affinity; and (b) negative electron affinity.

ficult to assign a Fermi level, although a level mid-way between the highest occupied and lowest unoccupied levels is often chosen. In a metallic system, the maximum of the highest occupied state, the minimum of the lowest unoccupied state, and the Fermi level are essentially the same thing, hence the EA, IP, and WF are all equal, and are commonly referred to as just the work function.

The EA and IP of an extended material are often measured experimentally as essentially *bulk* properties, since the techniques involved cause electronic transitions deep inside the material that result in electron emission at the surface. In this case, IP is defined as $I = V_{vac} - E_{VBM}$ and EA as $\chi = -(E_{CBM} - V_{vac})$, where E_{CBM} and E_{VBM} are the conduction-band minimum (CBM) and the valence-band maximum (VBM) energies respectively, all measured with respect to the same arbitrary reference level. The IP and EA are related to the bulk bandgap by $E_g = I - \chi$.

In theoretical investigations, while E_{VBM} and E_{CBM} are easily derived from modelling bulk material, V_{vac} can only be determined from a slab calculation, and energies found from the two calculations will not in general share the same reference level. Nevertheless, by ensuring that the surface slab is adequately thick to accurately represent bulk material toward its inner layers, one can align the average electrostatic potential found in the middle of the slab with the average electrostatic potential found in the bulk system, so as

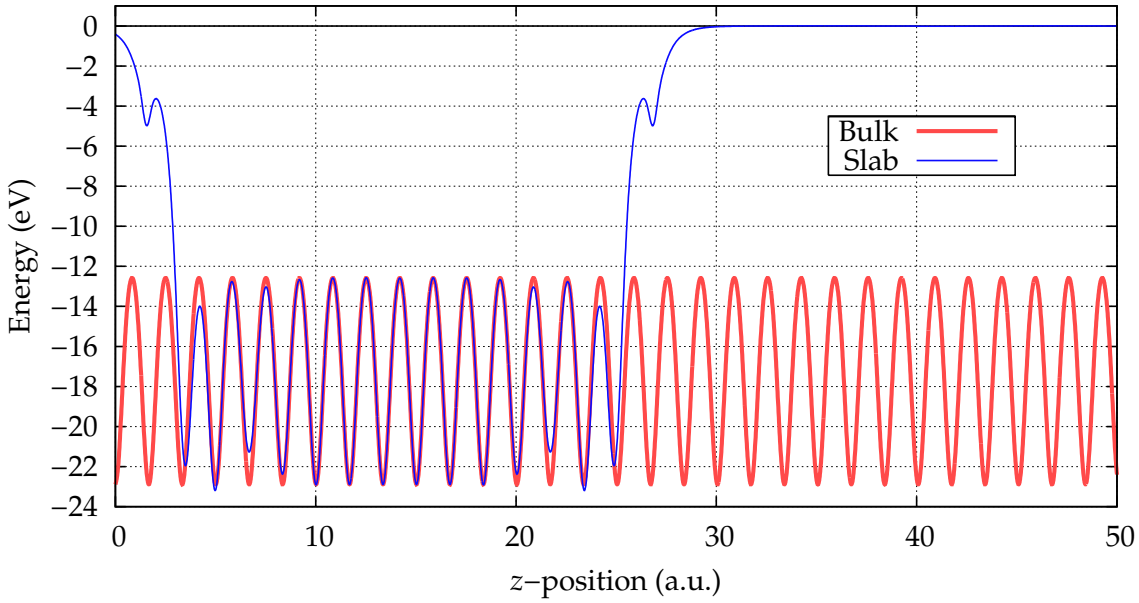

Figure 2.4: Example x, y-averaged electrostatic potentials as a function of z, for a diamond surface slab and continuous bulk diamond. The zero of the energy scale is the vacuum level found from the slab system, and the potential of bulk diamond has been aligned with that found in the middle of the slab system.

to give a common reference level for the vacuum potential and the bulk band edges.

Figure 2.4 shows an example of electrostatic potentials from bulk and slab calculations of diamond. The slab system has the z direction as the surface normal, so that when repeated it forms an infinite surface in the x, y plane. The bulk system is the same, except that the vacuum gap in z has been filled with C atoms to create continuous bulk diamond. For each system, the x, y-plane-averaged potential is plotted as a function of z. It is then straightforward to determine the vacuum potential from the plot of the slab system, and this is set to be the zero of the energy scale. Then, the potential from the bulk system is shifted in energy until it aligns with that found in the middle of the slab system. It can be seen that in this case, the alignment of the plots near the middle few layers of the slab is very good. The same energy shift can then be applied to the electronic band structure found for bulk diamond, in order to refer the bulk energy bands to the vacuum level.

As will be described in Chp. 3, certain experimental techniques can only give information about the near-surface region of a sample, and the IP and EA values reported from such methods are characteristic of *surface-related* electronic states, which arise due to surface reconstruction and adsorbate coverage. Furthermore, in doped material the band edges

may be higher or lower in energy at the surface than in the bulk due to *band bending*, which is discussed further in Sec. 5.1.2. The important distinction between bulk- and surface-related IPs and EAs is emphasised in the work presented in Chp. 5.

2.12 Chapter summary

In this chapter, density functional theory has been presented as a reliable method for determining the ground-state properties of a system of atoms. In essence, DFT takes the charge density as the basic variable, instead of attempting to solve the many-body Schrödinger equation for all electrons. The theory would be exact were it not for the lack of an exact form for the exchange-correlation functional, although by using the local density approximation for this functional, DFT can calculate a wide range of experimentally observable quantities with surprising accuracy.

It is worth noting that most observables are calculated entirely from first principles. The most important failure of the theory is its poor representation of excited states, which leads to an underestimation in the bandgap of semiconductor materials, and encourages the use of empirical quantities (such as in the defect-marker method) in calculating certain electrical properties. Nevertheless, the accuracy often remains remarkably high.

The pseudopotential method helps enormously in speeding up calculations by removing the core electrons of atoms from consideration. Combining this with other time-saving devices such as high symmetry makes it practical for DFT to be used to model large systems of several hundred atoms, while retaining a good level of accuracy. For this and for other reasons, DFT is perceived as a good compromise between capability, accuracy, and computational expense.

Chapter 3

Experimental

Dr. Egon Spengler: There's something very important I forgot to tell you.
Dr. Peter Venkman: What?
Spengler: Don't cross the [plasma] streams.
Venkman: Why?
Spengler: It would be bad.
Venkman: I'm fuzzy on the whole 'good/bad' thing here... what do you mean, 'bad'?
Spengler: Try to imagine all life as you know it stopping instantaneously and every molecule in your body exploding at the speed of light.
Dr. Raymond Stantz: *Total protonic reversal!*
Venkman: That's bad. OK. All right, important safety tip, thanks Egon.

— *Ghostbusters*, 1984

3.1 Introduction

EXPERIMENTAL results are vital to those performing theoretical modelling studies, primarily to give measured values against which the calculated values can be compared. By showing that the model can accurately reproduce quantities that are well known from experiment, the degree of confidence in using the model to predict *unknown* quantities is increased.

In general, theoretical work can help to explain experimental data for which the origin

is unknown, or make predictions that motivate experimental investigations. Likewise, experimental results can expose weaknesses in the theoretical background, or raise new questions that might be answered by subsequent modelling studies.

As mentioned in the preceding chapter, AIMpro can be used to calculate many quantities that are experimentally observable. In this chapter, a brief overview will be given covering some of the experimental techniques that are relevant to the work conducted in this theoretical investigation. The methods will be divided into those that are used primarily for studying bulk properties such as the nature of point defects, and those methods that are used to study surface characteristics such as adsorbate coverage.

3.2 Studying bulk defects

3.2.1 Electron spin/paramagnetic resonance (ESR, EPR)

In most solids, including diamond, electron spins are *paired* in the chemical bonds; that is, there are exactly as many spin-up electrons as there are spin-down, and the material has no net spin. Therefore there is no net electronic magnetic moment, and no interaction between the electron spins and any applied magnetic field. However, if impurity atoms are present, they may introduce unpaired electrons, in which case the material can be expected to show *electron spin resonance* (ESR). In such cases the material will also be paramagnetic, hence ESR is also known as *electron paramagnetic resonance* (EPR).

ESR exploits the *Zeeman effect*: In the presence of an applied magnetic field B, the energy level for an electron in an atom is split into two levels, separated by an amount ΔE given by

$$\Delta E = \frac{gehB}{4\pi m_{\mathrm{e}}} = g\mu_B B, \tag{3.1}$$

where g is the *Landé splitting factor*, e is the charge of the electron, h is Planck's constant, m_{e} is the mass of the electron, and μ_B is the *Bohr magneton*.

By illuminating the material with electromagnetic (EM) radiation of variable frequency, *resonance absorption* can be observed at a frequency $f = \Delta E/h$, corresponding to the energy required to cause electrons to make transitions between the energy levels corresponding to the separated spin states. For a magnetic field of around 0.3 T (the field used

in most ESR spectrometers), resonance absorption occurs when using EM radiation in the *microwave* region. In practice, it is easier to irradiate with EM radiation of a constant frequency (by placing the sample in a microwave cavity), and to then vary the strength of the magnetic field until resonance absorption occurs.

The upper part of Fig. 3.1 shows a schematic absorption peak for an ESR experiment. To help in characterising peaks such as this, most ESR systems run in derivative mode, as shown in the lower part of the figure. The linewidth ΔB is defined as the difference $B_2 - B_1$ between the positions of two peaks in the derivative spectrum, while the amplitude A is the peak-to-peak height. The integrated intensity can then be approximated by $\Delta B \times A$, which is proportional to the concentration of the paramagnetic species present. To get quantitative data from the integrated peak intensities, one must perform a calibration by using a sample for which the concentration of paramagnetic centres is known.

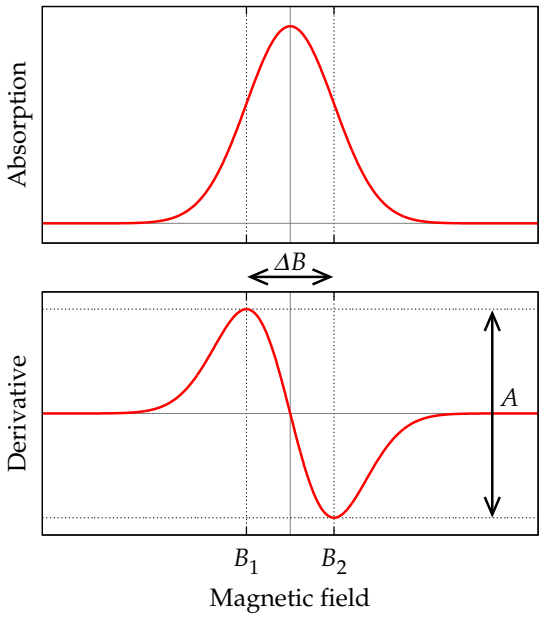

Figure 3.1: Schematic of an absorption peak in an ESR experiment, shown in normal mode (upper plot) and derivative mode (lower plot).

Equation 3.1 indicates that, since μ_B is a constant, the position of the absorption peak in a frequency spectrum for a given B is determined by the value of g, the Landé splitting factor. Comparison of the measured g with the value of 2.0023 for an electron in free space can yield information about the local environment for the unpaired electrons in the material. In addition, coupling between unpaired electrons and nearby nuclei with nonzero net spin can give rise to further energy level splittings, causing *hyperfine structure* in the recorded spectra. This can be carefully analysed to give extra information about the unpaired electron's surroundings.

Furthermore, spin-orbit coupling leads to anisotropy in the measured g-factor; in other words, the value of g varies with the direction of the applied magnetic field. This effect can be exploited to gather information about the symmetry of the unpaired electron

wavefunction, and by extension the symmetry of the defect responsible.

Electron-nuclear double resonance (ENDOR)

The EPR technique can be extended to yield yet more information about the local environment of unpaired electrons, by causing *nuclear magnetic resonance* (NMR) to occur in the sample. That is, *nuclear* energy-level transitions between split spin states in nuclei with nonzero spin can be driven by using an additional source of *radio-frequency* EM radiation. When both electronic and nuclear spin transitions are in resonance, it is known as *electron-nuclear double resonance* (ENDOR), or sometimes as *EPR-detected NMR*.

ENDOR allows for much greater resolution in studying the aforementioned hyperfine interactions between the resonating unpaired electrons and the resonating nonzero-spin nuclei. Careful analysis of the spectra can reveal details of the local atomic structure around paramagnetic centres. However, the technique requires a high degree of control. For instance, since the rates of electronic and nuclear transitions must be similar in order to observe a significant ENDOR effect, the system must be very carefully temperature-controlled, and often kept at a very low temperature such as that offered by liquid helium.

Further details about the ESR technique lie beyond the scope of this thesis; the interested reader should consult, for example, Refs. [118–120].

ESR studies on diamond

The ESR/EPR technique has been used to characterise various defects in diamond. Studies include those on: the phosphorus donor [121–129]; the nitrogen donor and related defects [130–136]; the nitrogen-vacancy centre [137, 138]; vacancy-interstitial pairs [139]; nickel-related defects [140–146]; the boron acceptor [134, 147–150]; co-doping with boron and phosphorus [151]; and hydrogen-related defects [152, 153]. A great many investigations into the structural quality of diamond samples and their defects in general have made use of the ESR method [154–174].

ENDOR has been used, for example, to reveal details about the (excited) neutral vacancy in natural diamond [175], single substitutional nitrogen defects ('P1' centres) [176], and

the combination: nitrogen-vacancy centres [177].

3.2.2 Infrared (IR) spectroscopy

The IR region of the EM spectrum covers wavelengths in the range of about 750 nm to 1 mm, corresponding to photon energies of about 1.2 meV to 1.7 eV. Photons with energies between about 0.05 and 0.50 eV are capable of exciting vibrational modes in typical covalently bonded solids, and so such photons may be absorbed when used to irradiate a sample. By recording a spectrum of absorption against input EM radiation wavelength, the energies of the allowed vibrational modes in a sample can be determined. Absorption or transmission is conventionally plotted against wave*number*, the latter varying over about 400–4000 cm^{-1}.

The allowed vibrational mode frequencies will depend on bond lengths, bond angles (that is, orientation with respect to the surrounding atoms), the masses and interatomic potentials of the atoms involved, and the *type* of vibrational mode. In the context of two bonds that share one parent atom, there are six types of vibrational mode: two types of bond *stretching* (symmetric and asymmetric), and four types of bond *bending* (rocking, scissoring, wagging, and twisting). As with many other spectroscopic techniques, the peaks in a recorded spectrum are compared against those from samples of known composition in order to identify the bond types present.

The key to the absorption process is the fact that the vibrating bond must involve a changing dipole in order to absorb the EM radiation. In general, this means that the two atoms making the bond must be of different chemical species. The inevitable asymmetry in charge distribution between the two types of atom causes an electric dipole, the strength of which will oscillate as the bond vibrates with its natural frequency. The oscillating electric field present in the incident EM radiation can interact with the oscillating dipolar bond, and if the frequencies match, the photon energy will be absorbed, causing the bond to vibrate with greater amplitude.

The result is that, in a monatomic solid such as diamond, the IR absorption process is very sensitive to the presence of defects, and in particular to bonds between atoms of the host material and impurity species.

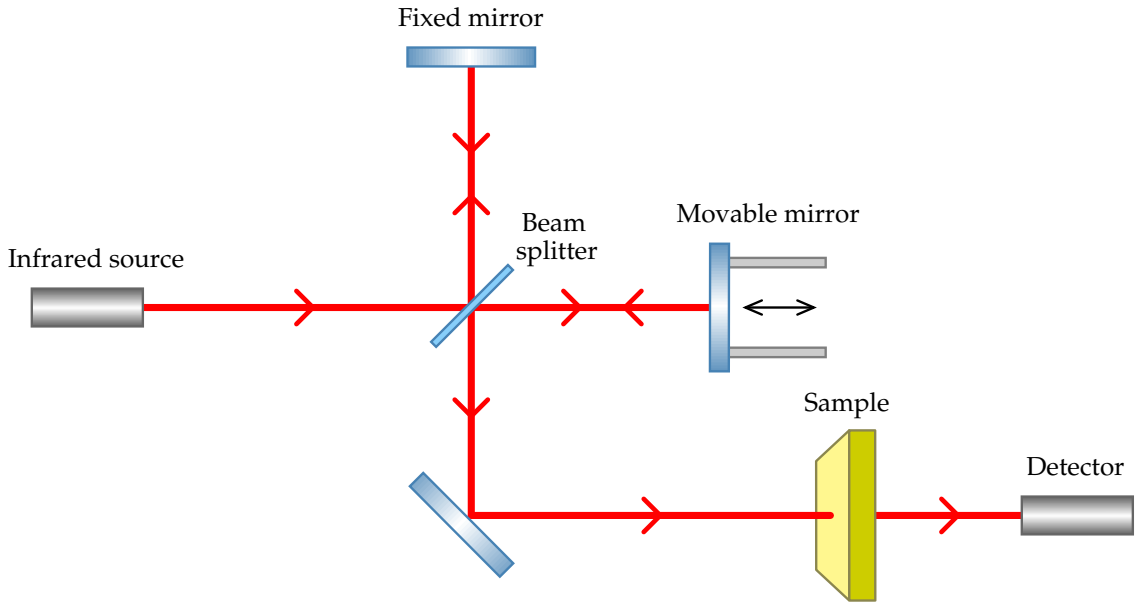

Figure 3.2: Schematic of the apparatus for an FTIR study. A beam of infrared photons with a range of frequencies is directed at a beam splitter, which sends half each to two mirrors. These beams are reflected back and recombine before being directed toward the sample. The transmitted beam is recorded at the detector.

Fourier-transform infrared (FTIR) spectroscopy

In practice, it is more efficient (and cheaper) to irradiate the sample with the full range of frequencies simultaneously, and to then use Fourier transformation to decompose the output into an absorption-frequency spectrum.

The apparatus for an FTIR investigation is based around a *Michelson interferometer* and is shown schematically in Fig. 3.2. First, the many-wavelength IR radiation is directed as a parallel beam toward a beam splitter (a 'half-silvered' mirror). This component reflects about 50% of the radiation down a path toward a fixed mirror, and transmits the remaining 50% down another path toward a second, movable mirror. These (fully silvered) mirrors reflect the beams back normally, to be recombined at the beam splitter. Here, half of the total is transmitted back toward the source and is discarded, and the other half is reflected down a new path, ultimately to be directed at the sample under investigation.

The difference in the length of the paths that the two halves of the split beam traverse as they head from the beam splitter to the mirrors determines whether or not the photons interfere constructively or destructively upon beam recombination. Clearly, there will

be a certain path-length difference that causes (say) destructive interference for each of the particular wavelengths present in the beam. By moving the adjustable mirror, the difference in path length can be linearly varied, and the output beam intensity can be sampled at small intervals. The Fourier transform of this data can be computed to give the *beam profile*, which is the intensity of each wavelength present in the input beam.

Changes in the length of the path to the movable mirror can be measured by reflecting from the mirror a beam from a fixed helium-neon laser. The wavelength of this laser is known with high precision, and so by counting the interference fringes resulting from movement of the mirror, the position of the mirror can be recorded very accurately.

The sample to be tested in then placed in the path of the recombined beam, and the spectrum is recorded. Clearly, by subtracting the beam profile from the recorded spectrum, the absorption spectrum of the sample is obtained. This can then be compared against the spectra from samples of known composition to identify the origin of absorption peaks.

The financial saving in using FTIR over the previous (dispersive) method comes from the fact that it is cheaper to build an interferometer than it is to make an precise monochromator, which would be required to accurately state the frequency as it is swept over the range. Because of this saving, and the several accuracy and efficiency advantages, almost all modern IR studies are performed using the FTIR method.

Once the absorption spectrum for the sample has been constructed, it is often possible to calculate the concentration of the defect responsible for a chosen absorption band. For the case of a non-degenerate vibrational mode with associated effective mass m, the *integrated absorption* (IA) is given by [178]:

$$(IA) = \int \alpha(f)\ \mathrm{d}f = \frac{\pi\eta^2 N}{mn\,c^2}, \tag{3.2}$$

where α is the absorption coefficient varying with the frequency f, N is the sought-for concentration of absorbing defects, n is the refractive index of the material (valid for the frequency range covered), and c is the velocity of light. The quantity $\eta = |\mathrm{d}\mu/\mathrm{d}Q|$ is a measure of the change in dipole moment μ of the defect with respect to changes in its equilibrium configuration Q. Since η has units of electric charge, it is often referred to as the *effective charge* of the defect. The absorption coefficient α is the quantity that is normally measured in the experiments, and is typically stated in cm^{-1}. One can obtain α by comparing the intensity of transmitted IR radiation I_t with that of the input beam I_0

through the equation

$$I_t = \frac{(1-R)^2 \, e^{-\alpha d}}{1 - R^2 \, e^{-2\alpha d}} I_0. \tag{3.3}$$

Here, d is the thickness of the sample, and the *reflection coefficient* R is given by

$$R = \frac{(n-1)^2 + \kappa^2}{(n+1)^2 + \kappa^2}, \tag{3.4}$$

in which n and κ are respectively the refractive index and extinction coefficient for the material.

Effects on the spectrum

The shape and position of a particular absorption peak can be perturbed by many properties of the material. For instance, temperature has an effect in that thermal expansion of the host lattice can affect the local geometry of a defect responsible for absorption, which usually results in a shift in the peak position.

Another major source of shift in peak position comes from isotope effects. Naturally, changes in the nuclear masses of a defect will affect the frequencies with which it can vibrate, and a simple balls-and-springs model for the nuclei and bonds can in many cases provide a good approximation to these isotopic shifts in vibrational mode frequencies. The charge state of a defect will also affect its vibrational modes and therefore its absorption. A lack or surplus of electrons at a defect centre will most noticeably affect the bonding properties. Therefore, while isotopes change the ball masses in the ball-and-springs model, charge states can be thought of as modifying the spring constants, again altering the vibrational frequencies.

Indeed, the balls-and-springs model works well with simple substitutional and interstitial impurity defects, and it has been used to derive some useful results [179–182]. However, it is poor at predicting absolute frequencies, and breaks down when more complex defects are considered.

Electronic IR and the effective mass approximation

Consider a substitutional impurity from group V in a group-IV material such as diamond. Four of the impurity's five valence electrons will participate in bonding with the

four neighbouring atoms of the host material, while the fifth will be loosely bound to the impurity atom. This is due to the impurity nucleus appearing positively charged in comparison to the host-material atoms. At reasonable distances from the impurity nucleus, the potential from this excess of positive charge is approximately Coulombic and is slowly varying. Therefore, the fifth electron experiences a potential not unlike that of the electron in a hydrogen atom. In this case, the effect of interaction with atoms of the host material can be included by using an *effective mass* for this electron. This is known as the *effective mass approximation* (EMA) or theory (EMT) [68, 183–185].

The screened Coulomb potential V of the impurity atom with excess charge Z is therefore approximated by

$$V = -\frac{Z}{\epsilon r}, \tag{3.5}$$

in which ϵ is the permittivity of the material and r is the radial distance from the impurity. An electron moving with effective mass m_e in this potential will have a series of bound states of energies E_n given by

$$E_n = \frac{Z^2 m_e}{2\epsilon^2 n^2} \quad \text{for} \quad n = 1, 2, 3, \ldots, \tag{3.6}$$

which will appear below the host material's conduction band in the electronic structure. These defect excited states are often observed as Lyman (1s→2p, 1s→3p, 1s→4p, ...) or even Balmer series (2s→3p, 2p→3s, 2p→4s, ...) transitions.

The EMT describes an ideal shallow donor, and in diamond the theory puts the associated donor level 0.22 eV beneath the conduction band [186]. Recall that the acceptor level for boron in diamond is about 0.37 eV above the valence band. This will be returned to when investigating potential shallow donors in Chp. 4.

Many FTIR studies have been performed to characterise diamond samples (and to compare diamond with other materials such as diamond simulants [187]). Recent IR-spectroscopy studies on bulk defects in diamond include those on: the phosphorus donor [186, 188–191]; the forms of aggregated nitrogen [192–196]; the boron acceptor [197–199] and its interaction with hydrogen [200, 201]; new defects in HPHT material [202]; and the distribution and concentrations of multiple defects [163, 165, 203].

3.2.3 Photoluminescence (PL)

Luminescence refers to the emission of photons when a system in an excited electronic state relaxes into a state of lower energy, and in *photo*luminescence (PL), the initial excited state is produced by photon irradiation of the sample. Other methods include cathodo-, electro-, and thermo-luminescence, wherein the excited state is produced by respectively using accelerated electrons, electric fields, and heating. For a review of PL, the interested reader should consult, for example, Refs. [102, 204, 205].

During *above-bandgap* PL, the sample is irradiated with photons of energy greater than the material's bandgap, so that electron-hole pairs are created. The electrons rapidly thermalise to the bottom of the conduction band (and the holes to the top of the valence band), and then into any available states of lower energy, such as those offered by defects. These relaxations may proceed via radiative mechanisms, although non-radiative processes are more likely. The electrons eventually recombine with holes in the valence band or in defect states, and this recombination is accompanied by the emission of a photon with an energy equal to the difference in the excited and ground electronic states. In cases where the excited state has a long radiative lifetime, or where the transition to the ground state is forbidden by symmetry, transitions may be instead observed as originating from a higher excited state.

One of the principal differences between the PL and absorption (such as FTIR) techniques is the way in which they reveal the presence of multiple excited states. Absorption methods can in principle detect all excited states (into which the transition from the ground state is allowed by symmetry) by simply illuminating the sample with multichromatic radiation and recording the absorption as the difference between the incident and transmitted spectra. On the other hand, PL reveals excited states in a more indirect manner, as follows.

In *photoluminescence excitation* (PLE), the sample is irradiated with light from a tunable laser, while the luminescence detector is set to record outgoing photons of a specific frequency, say that corresponding to the transition from the lowest (first) excited state into the ground state. The frequency of the incident radiation is gradually increased (starting from a very low value), and peaks in the intensity of the particular luminescence are observed by the detector.

The first peak is due to the first-excited-state → ground-state luminescence itself. As the incident frequency is increased, electrons will be promoted from the ground state into the second excited state, but will relax (most likely non-radiatively) into the first excited state, increasing its population. Therefore, the intensity of the luminescence from the first-excited-state → ground-state transition will increase. At greater incident energies, the third excited state will become occupied, and these electrons will relax (possibly via the second excited state) down into the first excited state, increasing its population and its corresponding luminescence once again. The fourth excited state will be occupied at higher incident energies, and so on. The spectrum of luminescence intensity as a function of incident radiation frequency will therefore contain peaks corresponding to the excited states present.

The PLE technique is suitable for the characterisation of thin samples or those with low defect concentrations, where absorption experiments can be difficult to interpret due to the low signals.

Vibronic coordinate diagram

In general, since an electronic transition changes the distribution of charge density around a defect, there will be an associated change in the allowed vibrational modes (VMs) of that system. Electronic and vibrational transitions are therefore coupled, and known together as *vibronic* transitions.

A generalised *vibronic coordinate diagram* is shown in Fig. 3.3. Here, the total energy of a system is represented as a parabola centred on its equilibrium atomic configuration Q. The ground- and excited-state systems will have different equilibrium configurations (say, bond lengths), giving two total energy curves with minima at Q_{g} and Q_{e} respectively, where the latter curve is higher in energy.

At low temperatures, the ground-state system will initially be in its lowest-energy VM, with higher-energy VMs being separated by the phonon energy $\hbar\omega$. Absorption of a photon in a PL experiment will excite the system into one of the allowed VMs of the excited-state configuration, which will be themselves separated by $\hbar\omega'$. The system is often further idealised at this point by assuming that the forms of the two energy curves are the same, in which case $\hbar\omega' = \hbar\omega$.

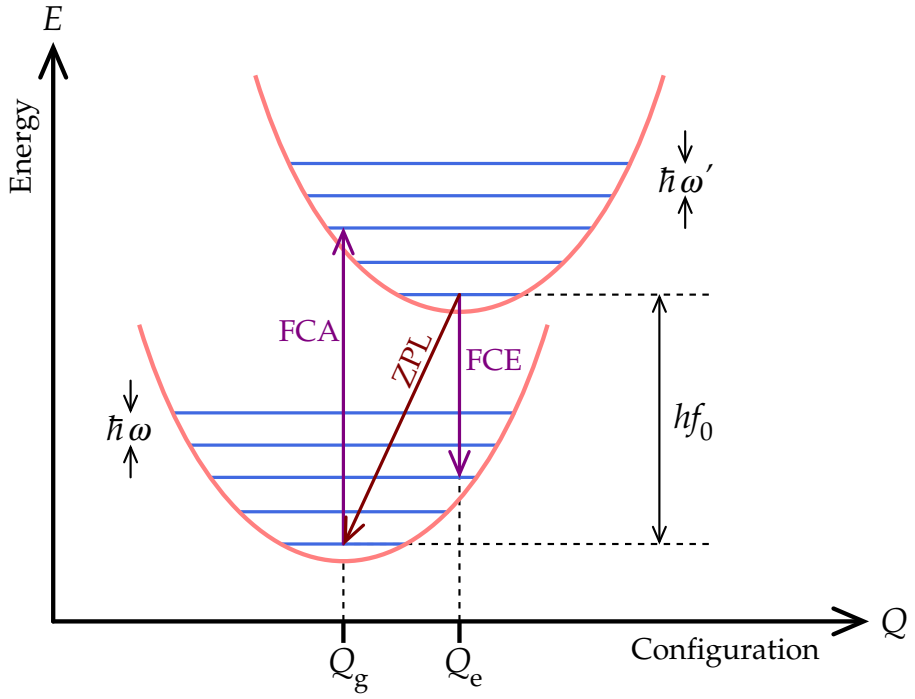

Figure 3.3: Generalised vibronic coordinate diagram for PL, showing Franck-Condon absorption (FCA) and emission (FCE), and the transition responsible for the zero-phonon line (ZPL).

The *Franck-Condon principle* (sometimes *Frank*-Condon principle) states that the likelihood of a transition between two electronic states is proportional to the overlap of their wavefunctions, and it allows for the prediction of intensities for vibronic transitions. The most likely transition from the ground-state configuration to the excited-state configuration is the so-called 'vertical' transition, and this *Franck-Condon absorption* (FCA) is shown in Fig. 3.3. This mechanism can be thought of as related to the Born-Oppenheimer approximation, in that the electronic transition takes place almost instantaneously, while the heavy nuclei take a significant amount of time to move toward their mean positions in the new configuration.

The system will subsequently thermalise into the lowest-energy VM of the excited-state configuration. It can then de-excite back into its ground-state configuration with the emission of a photon and the possible production of a number of phonons, as follows.

Relaxation can take place directly from the lowest-energy VM of the excited-state configuration into the lowest-energy VM of the ground-state configuration, which will not result in the creation of any phonons. In this case, the emitted photon will possess all of

the energy of the de-excitation, hf_0. The signal recorded in the PL spectrum arising from this highest-energy photon is called the zero-phonon line (ZPL).

Franck-Condon emission (FCE) corresponds to a downward vertical transition into one of the high-energy VMs of the ground-state configuration. This will be followed by the creation of a number phonons of energy $\hbar\omega$ as the system relaxes further into the lowest-energy VM of the ground state.

De-excitation may also occur via several other routes in which a photon and a number of phonons are produced in returning the system to the original state, provided that their energies sum to hf_0. This leads to a series of peaks in the PL spectrum with energies below the ZPL, referred to as *vibronic side-bands*. The FCE is simply the most likely of these mechanisms, and corresponds the greatest photon intensity.

Additional considerations

As with other techniques, PL is somewhat sensitive to isotopic effects, since the optical transitions of a defect are slightly different between different isotopes. However, the results must be carefully interpreted, since the energy of a transition is related to the electronic wavefunctions for the ground and excited states, and if these wavefunctions have zero amplitude at one of the impurity atoms, then the transition will show no shift in energy with a change in that atom's isotope.

PL can also be performed when applying uniaxial stress to the sample, in order to infer the symmetry of a defect as well as the symmetries of the electronic states corresponding to the optical transition being monitored. This information can, for example, help to eliminate possible charge states of a defect from consideration.

3.3 Investigating surfaces

3.3.1 Electron diffraction studies

Low-energy electron diffraction (LEED)

LEED can be used to determine the crystallographic structure of a surface by investigating the form of the two-dimensional (2D) electron waves upon it. The diffraction data reveal the type of 2D surface mesh and its dimensions. However, it is often the case that the microscopic region over which measurement is taken contains several types of surface domain, which gives rise to superimposed diffraction patterns that must be carefully separated.

The apparatus for a LEED investigation is composed of two main parts: an electron gun, and a fluorescent screen (Fig. 3.4). The gun directs a beam of electrons toward the crystal under investigation at an angle close to the surface normal. The electron energies are in the range of about 10–200 eV, corresponding to De Broglie wavelengths of about 1–4 Å, which ensures that it is only atoms at or close to the surface that cause electron diffraction.

The reflected electrons will have wave-vectors $\mathbf{k}'$ with the same magnitude as those $\mathbf{k}$ of the incoming electrons, if the assumption is made that electrons are *kinematically reflected*. These electrons are detected on the fluorescent screen and the pattern they form is photographed through a viewport in the apparatus. The key aspect of the reflection is that the vector difference between the wave-vectors of the incoming and outgoing electrons $\mathbf{g} = \mathbf{k}' - \mathbf{k}$ must be a reciprocal lattice vector of the crystal surface. From the complete diffraction pattern it is therefore possible identify the reciprocal lattice type and then reconstruct the real-space lattice of the crystal surface.

LEED diffraction patterns are sharp if the surface under investigation is well ordered (flat) over a distance scale much greater than the wavelength of the probing electrons. Blurring in the pattern spots can therefore indicate surface roughness, or a disordered coverage with impurities. The pattern can also reveal the presence of terraces, steps, and kinks on a surface, and permits calculation of the areal density of such structures.

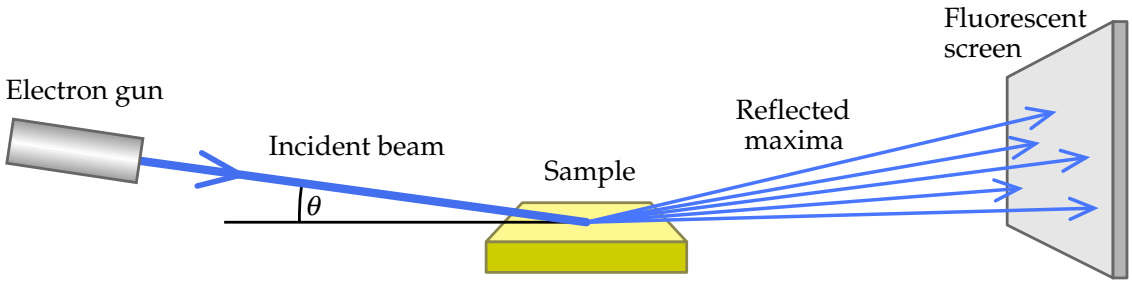

Figure 3.5: Schematic of the apparatus geometry for a RHEED investigation. High-energy electrons are directed at a sample, and the diffraction pattern resulting from reflected electrons is recorded on a fluorescent screen on the far side. The angle θ is typically less than 5 °.

Reflection high-energy electron diffraction (RHEED)

Electrons with higher energies have wavelengths much smaller than the interplanar spacings in most crystals, and so they will penetrate deeper into a specimen, yielding little information about the surface. However, if high-energy electrons are made to impinge on the surface at grazing angles, measurable reflections from the near-surface region can be achieved.

The apparatus geometry for this technique is shown in Fig. 3.5. The angle between the incident beam and the sample surface is typically less than 5 °. The higher electron energies lead to sharper diffraction patterns than those obtained in LEED studies. However, in order to obtain a true representation of the 2D surface, it must be sufficiently flat on the nanometre scale.

RHEED can be used for real-time analysis of the growth of a crystal, as the equipment does not block the path of the species descending vertically onto the growing sample. However, the im-

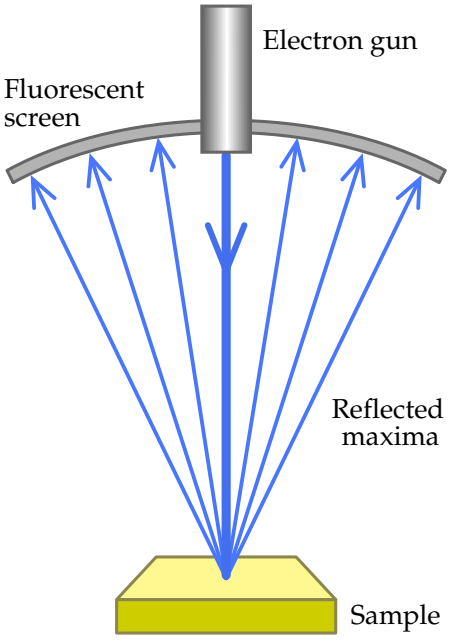

Figure 3.4: Schematic of the apparatus geometry for a LEED investigation. Low-energy electrons are directed at a sample at an angle close to the sample's surface normal. Reflected electrons are detected on a fluorescent screen and form a diffraction pattern.

pact of the high-energy electrons can damage some types of material and disturb their growth. In such situations, MCP-RHEED can be used, wherein the electron beam is lowered in intensity by several orders of magnitude, although the high voltage across a micro-channel plate (MCP) can produce electron multiplication, which is used to amplify the reflected-electron signal. In this way, damage to the crystal can be significantly reduced.

3.3.2 Scanning-probe microscopies

Scanning-probe microscopy refers to a class of techniques in which a very fine needle probe is mechanically moved across the surface of a sample in a series of straight lines (scans). The interaction of the probe with the surface is recorded as a function of position on the surface, hence the nature of the surface is determined in a very direct manner. The techniques are *microscopies* in that direct images are produced, although it is only feasible to probe a very small surface area on the sample. Many different types of probe-surface interaction can be recorded, corresponding to different *modes* of operation. The two most important modes will now be described.

Atomic-force microscopy (AFM)

In AFM apparatus, the probe is mounted on the free end of a very sensitive mechanical cantilever. As the probe is scanned across the sample, the force existing between the atoms at the tip and those of the sample's surface causes deflection of the cantilever, which is typically detected by reflecting a laser beam from the top of the cantilever. In practice, a feedback loop is used to move the cantilever/probe up and down such that a constant force (deflection) is maintained, and the height required is recorded as a function of surface coordinate. This way, one can ensure that only small cantilever deflections occur, which keeps the theoretical calculation of forces accurate. In addition, this prevents damage to the surface which could arise from the large forces of a greatly strained cantilever. As will be seen, one advantage that AFM has over other scanning-probe microscopies is that both electrically conducting and nonconducting surfaces can be investigated.

It is interesting to note that work has recently been undertaken to manufacture AFM

probes out of diamond [206].

Scanning tunnelling microscopy (STM)

Spatial resolution greater than that offered by AFM is possible by using the STM mode. Provided that the surface material is conductive, a voltage can be put across the probe (typically made of platinum-rhodium or tungsten) and the sample, and the weak current due to electrons tunnelling from one side to the other can be recorded during scans. Because the tunnelling current decreases exponentially with distance between the tip of the probe and the atoms of the surface, a very accurate height map can be constructed for the region under investigation. STM is capable of resolving distances of around 2 Å, hence it offers atomic-scale resolution for many conductive substrates.

Other scanning-probe techniques

Other modes of scanning-probe microscopy include: electrostatic-force microscopy (EFM), Kelvin-probe-force microscopy (KFM), magnetic-force microscopy (MFM), near-field scanning optical microscopy (NSOM), and scanning capacitance microscopy (SCM). One advantage of the scanning-probe techniques over the aforementioned LEED and RHEED methods is that the resolution is not diffraction-limited.

Relevance to this investigation

Another use for these techniques, especially STM and AFM, comes from the fact that the probe can significantly perturb the surface structure. This can be used to manipulate adsorbates that are loosely bound to the surface, in order to assemble nanoscale structures. Of direct relevance to the work presented in this thesis is the fact that AFM has recently been used to locally modify the surface structure of diamond in order to create regions of oxygen termination on an otherwise hydrogenated surface [207]; this system then being characterised using the KFM mode. In addition, the resolution and accuracy of Kelvin force microscopy measurements on hydrogenated and oxygenated diamond surfaces have recently been investigated in detail [208].

Experiments have been conducted in which molecules of C_{60} have been moved across the surface of silicon by using STM at room temperature [209]. These studies provide insight into the practical implications of transfer-doping diamond with fullerenes, which is covered in Chp. 6.

STM has been extensively used to study diamond surfaces, most recently by investigating matters such as: the oxidisation process of CVD diamond [210]; the quality of fast-grown diamond intended for surface-conductive devices [211]; the mechanism of field emission from diamond films [212] and particles [213]; the effect of annealing on the surface structure and electronics of single-crystal diamond [214] and CVD material [215, 216]; the ability to desorb hydrogen from diamond surfaces [217]; the photoemission properties of CVD diamond [218]; the extent of damage caused by radiation bombardment [219]; the effect of doping polycrystalline material with boron [220]; and the roughness of HPHT-diamond surfaces exposed to a microwave-assisted hydrogen plasma [221].

3.3.3 Surface spectroscopies

Photoelectron spectroscopy (PES)

Photoelectron spectroscopy — also known as photo*emission* spectroscopy — refers to a class of techniques in which the *photoelectric effect* is exploited in order to characterise materials. Essentially, a monochromatic beam of photons is directed at a test sample, and the *photo*electrons that are ejected from the material as a result are detected and analysed.

When an electron absorbs the energy $E = hf$ from a photon of frequency f, it expends some of it in order to overcome a binding energy E_b and escape from its parent atom, and the rest remains as kinetic energy E_k when the electron is later detected. The binding energy is therefore given by

$$E_b = hf - E_k. \tag{3.7}$$

Photoelectrons do not last long in bulk material before losing the energy required to leave the sample; that is, they have a low *inelastic mean free path*. As a result, it is only photoelectrons created in the near-surface region that manage to escape and which are detected. This small electron *escape depth* means that PES is in general a surface-sensitive technique. In addition, a high level of vacuum must be maintained in order to reduce energy loss by

electrons colliding with molecules in the gas phase.

In a PES study, the flux of emitted electrons across a range of kinetic energies can be recorded, and Eqn. 3.7 can be used to plot this electron intensity against binding energy. Since electron binding energies are dependent on the chemical composition and structure of the material, the peaks in a recorded spectrum can be compared against those seen in spectra from known materials in order to determine the composition of the sample.

Interpretation of photoelectron spectra relies upon Koopmans' theorem (Thm. 2), which states that the binding (or ionisation) energy required to remove an electron from a system is identifiable with the energy ϵ_i of the orbital from which it is ejected, through $B_i = -\epsilon_i$. However, this is only useful as an approximation, as it does not account for the fact that the energy levels of the remaining electrons will be perturbed after the first is removed, which will affect the subsequent ionisation energies.

Furthermore, the ejection of an electron may leave the host atom(s) in a vibrational excited state. In this case, the kinetic energy of the photoelectron will be reduced, and Eqn. 3.7 should be rewritten as

$$E_b = hf - E_k - E^+_{\text{vib}} \tag{3.8}$$

in which E^+_{vib} is the energy used up in exciting the vibration in the ionised host centre. Naturally, the vibrational states are quantised, which gives rise to *vibrational structure* in the photoelectron spectrum.

The two main types of PES are distinguished by the choice of photon energy used for the incident beam.

X-ray photoelectron spectroscopy (XPS)

The energies of 'soft' X-ray photons are in the range of about 100 eV to 10 keV, which is sufficient to excite *core* electrons out of atoms and leave them with appreciable kinetic energies. The binding energies of core electrons are most strongly dependent on the chemical species of their host atoms, and are not greatly affected by the atom's local environment. Therefore, XPS — also known as *electron spectroscopy for chemical analysis* (ESCA) — gives information primarily about the chemical *species* present on a sample's

surface. Furthermore, the measured electron intensities can be used to give the relative concentrations of the surface's constituent species.

However, the small effect that the local environment of the surface atoms has on their core-electron energy levels results in noticeable *chemical shifts* in the positions of the peaks in binding energy. In addition, the *oxidation state* of an atom will affect the binding energies of its electrons; for example, an atom in a highly positive oxidation state will appear very attractive to an electron attempting to escape from it, and that electron's binding energy will be higher than usual. XPS can therefore provide some information about the local environment of the surface atoms and by extension their bonding characteristics.

Ultraviolet photoelectron spectroscopy (UPS)

'Hard' ultraviolet photons have energies in the range of about 5–40 eV, and those emitted by the commonly used helium-discharge lamp have an energy of 21.22 eV, corresponding to the $1s^1 2p^1 \rightarrow 1s^2$ transition in helium. Photons such as these are capable of ejecting only *valence* electrons from the atoms of a sample, hence UPS can be used to study the electronic structure of a surface with regard to the number and types of chemical *bonds* present. In addition, UV photons cannot penetrate as deeply into the sample as can X-ray photons, hence UPS reveals information mainly about the chemical nature of the sample right at the surface.

Angle-resolved (AR) studies involve the recording of many spectra for different angles between the incident photon beam and the surface. Angle-resolved UPS (ARUPS) can be used to map out the surface electronic structure in **k**-space, which is particularly relevant to the parts of this investigation presented in Chp. 5.

Auger electron spectroscopy (AES)

The *Auger effect* is quite commonly exploited in order to obtain information about the chemical species present in a sample. This effect, shown schematically in Fig. 3.6, involves the emission of a *secondary* electron after high-energy irradiation has ejected the first. *Auger electron spectroscopy* (AES) refers to the construction and examination of the energy spectrum of the secondary electrons emitted from a sample under irradiation.

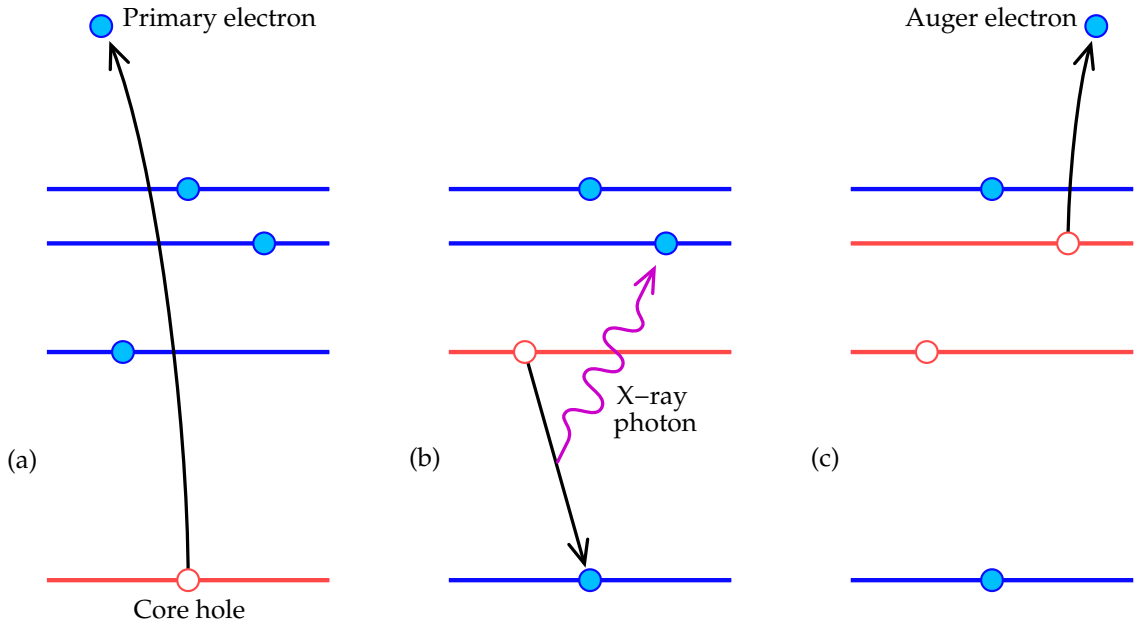

Figure 3.6: Schematic of the electronic transitions occurring in the Auger effect. (a) An electron is ejected from a core state in an atom, leaving behind a core hole. (b) Another electron from a higher-energy orbital falls into the core hole, emitting an X-ray photon that may escape the system as X-ray fluorescence. (c) However, if some other electron absorbs the photon's energy, it will escape the system as a secondary, *Auger* electron.

As in XPS, high-energy radiation can cause an electron to be ejected from a core atomic state, leaving behind a core hole. Another electron from the same atom but occupying an orbital of much higher energy may fall into the core hole and release a photon with X-ray energy. This photon might escape the material and be observed as *X-ray fluorescence*. Alternatively, the photon may be absorbed by yet another electron in the atom, which will receive enough energy to escape the material and be detected as a so-called *Auger electron*. Since the energies of these secondary electrons are related to the allowed electronic transitions in the atoms present in the sample, analysis of the Auger-electron energy spectrum can reveal the composition of the material.

It is clear that the state of the atom after the Auger electron emission (Fig. 3.6(c)) is not the ground state, and subsequent downward electronic transitions will occur in what is known as the *cascade* process. This can cause the ejection of further Auger electrons with lower energies, which leads to a sloping background in the measured electron energy spectrum toward lower energy. In practice, this background is quite uniform, and is largely removed by viewing the spectrum in derivative mode.

The incident radiation used in AES experiments is often an electron beam, containing energies in the range of 1–5 keV. Such electrons have De Broglie wavelengths of 0.2–0.4 Å and so can penetrate fairly deeply into solids such as diamond (having a bond length of 1.54 Å). However, the ejected Auger electrons are of much lower energy (about 10–1000 eV) and it is only those created within around 50 Å of the surface that are able to escape and can be detected. Electron-beam AES has an advantage over XPS in that the beam can be very accurately focused and scanned over the surface, allowing for analysis and imaging of very small surface areas. One disadvantage however is that the electrons will charge the sample, making it difficult to study insulating materials.

A source of X-rays is sometimes used as the incident radiation instead, or from another viewpoint, one could say that Auger electrons are detected in XPS studies. In such a case the technique is sometimes known as *X-ray–induced* (or *-excited*) *Auger electron spectroscopy* (XAES). The 1486.6 eV X-ray photons produced by a typical aluminium Kα source have wavelengths of 8.3401 Å, and so cannot penetrate as deeply as can the aforementioned beam electrons, making this method even more sensitive to the surface.

(X)AES studies are often performed to complement other techniques, and recent studies on diamond have investigated, for example: the change in wettability of diamond surfaces as they are irradiated with ions [222], oxygenated and exposed to hydrogen plasma [223], or doped with phosphorus [224]; the compositional and structural changes of CVD diamond with temperature [225]; co-doping with sulphur and boron [226]; electronic surface states on nanodiamond [227]; caesium adsorption on H-terminated CVD material [228]; the conductivity of the (001)-(2$\times$1) surface [229]; oxygen adsorption and desorption from the (110) and (111) faces of single crystals [230]; and oxidation of the hydrogenated (100) surface [231].

Electron energy-loss spectroscopy (EELS)

A combination of PES and vibrational spectroscopy is *electron energy-loss spectroscopy* (EELS), in which the energy lost by a beam of electrons is measured once they have been reflected from a material's surface. The electrons lose kinetic energy by exciting vibrational modes of the species on the sample's surface, hence the energy spectrum of the reflected electrons can be analysed to determine the modes responsible and infer the composition of the surface.

Typically, the energy spectrum from a sample is recorded and compared against known spectra characteristic of various adsorbate molecules. High-resolution electron-energy-loss spectroscopy (HREELS) is very sensitive to, for example, light chemical elements that X-ray techniques cannot detect. In addition, the technique can identify very small amounts of adsorbate; in some cases only a few tens of atoms on a surface is enough to be reliably detected.

A large proportion of the (HR)EELS studies on diamond are directly relevant to the work conducted in this investigation. Particularly relevant are those that have studied: the structure, stability, and vibrational properties of hydrogen and deuterium on the diamond surface [232–241]; the effects of surface coverage with oxygen [230, 242]; the interaction between hydrogen and oxygen on the surface [231, 243–245]; and the properties of surface-related electronic states [246–249].

3.4 Chapter summary

Overviews of several of the many experimental techniques used to study diamond and other materials have been given in this chapter. The most important techniques as far as this investigation is concerned are as follows.

For the work on bulk doping, which will be presented in the next chapter, electron spin/paramagnetic resonance (ESR/EPR) is a particularly relevant experimental tool, due to its ability to infer the symmetry of point defects, amongst other characteristics. Electronic infrared spectroscopy is also particularly important, owing to the direct way in which it reveals the electronic structure of such defects.

With regard to diamond surfaces, for which the work will be detailed in Chp. 5, the most important techniques are those that most directly investigate the electrical properties, especially with respect to the vacuum level, since it is the electron affinity and work function of the various surfaces that this work is most concerned with. The gross structural properties for the surfaces are (in general) relatively well understood at present, although of course the electrical properties depend critically on the details of the atomic arrangement. Therefore, the surface-spectroscopy techniques such as XPS and UPS are of particular relevance to this work.

Finally, the work on *p*-type doping of the diamond surface will be presented in Chp. 6, and again the PES techniques are important, since these have been used in the relevant experimental studies to characterise the layers of material adsorbed onto the diamond surface. The *p*-type conductivity following such transfer doping of the diamond surface has been quantified using standard conductance measurements.

Chapter 4

Bulk doping of diamond

"Better a diamond with a flaw than a pebble without."

— Confucius

- The work shown in this chapter has been published as Refs. [42, 115, 116, 250–252].

4.1 Introduction

DOPING with acceptor and donor impurities to create both *p*- and *n*-type material is required to build the most basic of the semiconductor devices, the *pn*-junction. Doping *diamond* to achieve *p*-type material is straightforward, as atoms of boron are easily (and sometimes unintentionally) introduced into bulk diamond, and the B acceptors have activation energies that are considered small, at 0.37 eV. However, it is proving much more difficult to create efficient *n*-type diamond by doping with donor impurities, hence the majority of the work on doping diamond concentrates on this problem.

Naturally, one first turns to the group-15 (V) elements (N, P, As, Sb, and Bi) to provide donor electrons in a tetravalent host material such as diamond. Although nitrogen is so readily incorporated that it is the dominant impurity in natural diamond, isolated substitutional N atoms have high donor activation energies, at 1.7 eV.

Phosphorus is the next dopant to consider, although the size of the impurity atom already becomes a concern in such a tight lattice as that of diamond; the covalent radius of the P atom at 106 pm is almost 138% that of a C atom (77 pm). Indeed, theoretical studies have calculated very low solubilities for P in diamond, owing to a large formation energy of $\sim$ 7–11 eV [46, 53, 253, 254]. Nevertheless, experimental doping of diamond with P has been an encouraging success story.

The first reports of the incorporation of P into diamond were published in the early 1990s [255–258], although they did not include sufficient evidence to clearly show *n*-type conduction. Many authors suggest that the first *confirmed* *n*-type doping of diamond with P via growth techniques was achieved in 1996, and published in Ref. [259] in 1997. Initially, an activation energy of 0.43 eV at $\sim$ 400 K, and a $\sim$ 500 K Hall mobility of 23 $cm^2\ V^{-1}\ s^{-1}$ were reported.

Since then, the growth conditions have steadily been optimised [260, 261], with a coincident improvement in the reproducibility and measured mobilities [262]. The most recent measurements of the electrical properties of P-doped diamonds all suggest that the donor level lies $\sim$ 0.6 eV beneath the conduction-band minimum [125, 186, 262–268]. Now that near-100% reproduceability is claimed for P doping of (111)-orientated diamond films, attention is being turned to growing P into the more conventional (001)-orientated films [265]. This will allow for homoepitaxial growth to aid the creation of *pn*-junctions, since B-doped films are normally grown with an (001) orientation.

Meanwhile, several other suggestions have been made for shallow donors [49, 254, 269], including sulphur [51], sulphur-hydrogen centres [270], and more complex defects such as N_2–H [269] and even N–Si_4 [271]. However, the status of these defects is controversial at best [43, 45–53], and the difficulty often encountered in trying to reproduce measured *n*-type activities is a matter of concern [45, 191].

Several recent experimental studies appear to indicate that hydrogenation/deuteration of boron-doped samples gives rise to significant *n*-type conductivity, reversing the *p*-type nature of such samples [40, 41, 272, 273]. However, these findings currently lack a solid theoretical foundation [253, 274–276].

In this chapter, the search for a shallow donor impurity for diamond is continued, and some of the suggestions for shallow donors are investigated, using the AIMpro method.

4.2 Modelling bulk diamond

Naturally, the structure and electronic properties of the host material must be accurately reproduced by the modelling method if one is to be able to reliably calculate the structure and electronic properties of point defects. The accuracy of modelling bulk material is typically assessed by finding the optimum theoretical lattice parameter (and bulk modulus), calculating the corresponding electronic band structure, and by then comparing these to available experimental data.

4.2.1 Lattice parameter and bulk modulus

The effect of the cell volume on the total energy of a supercell of bulk material can be investigated in order to determine both the optimised theoretical lattice parameter a_0 and the corresponding bulk modulus B_0 for the material. The primitive unit cell can be used, and several *one-shot* total energies are performed for different values of the lattice parameter a (and therefore cell volume).

For a solid material, the dependence of the total energy E on the volume V of the system is well described using the *Birch-Murnaghan equation of state* [277]:

$$E(V) = E_0 + \frac{B_0 V}{B_0'}\left(\frac{(V_0/V)^{B_0'}}{B_0' - 1} + 1\right) - \frac{B_0 V_0}{B_0' - 1}, \tag{4.1}$$

in which E_0 is the minimum of the total energy corresponding to the optimised volume V_0, the bulk modulus of the material valid at this minimum is B_0, and B_0' is the (constant-temperature) pressure derivative of the bulk modulus (taken at B_0); that is,

$$B_0' = \left.\frac{\partial B}{\partial p}\right|_{T,B_0}. \tag{4.2}$$

Experimentally, B' is found to change very little with pressure (*i.e.* $B' \approx B_0'$), and furthermore many solid materials exhibit similar values for B_0', around 3.5.

Equation 4.1 can be re-written in the form:

$$E(V) = \alpha V^{\beta} + \gamma V + \delta, \tag{4.3}$$

in which the constants are

$$\alpha = \frac{B_0 V_0^{B_0'}}{B_0'(B_0'-1)}, \tag{4.4}$$

$$\beta = 1 - B_0', \tag{4.5}$$

$$\gamma = B_0/B_0', \tag{4.6}$$

$$\text{and} \quad \delta = E_0 - \frac{B_0 V_0}{B_0' - 1}. \tag{4.7}$$

These can be used as parameters in the fitting of Eqn. 4.3 to the calculated E *vs.* V data, and from their best values one can deduce the optimised volume V_0, the bulk modulus B_0', and the pressure derivative of the bulk modulus. From V_0 it is straightforward to calculate the corresponding optimised lattice parameter a_0.

The modelling of the material is typically considered sufficiently accurate if the optimum theoretical lattice parameter falls within ±1–2% of the experimentally measured value. In most DFT calculations, the calculated a_0 is below the experimental value, and it can be brought closer by adding more basis functions to the atoms. However, a compromise must be made between this increased accuracy and the added computational expense.

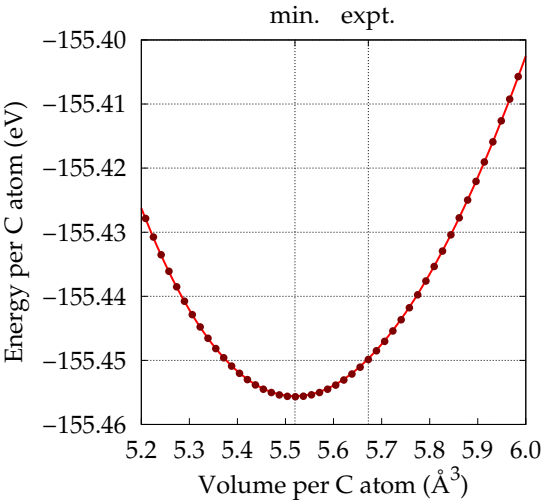

Figure 4.1: Plot of total energy against cell volume (both per C atom) for bulk diamond as modelled using a 'pdpp' basis set. Data points are calculated values, while the solid line is a fitted Birch-Murnaghan equation of state.

When modelling diamond using AIMpro and HGH pseudopotentials, this compromise is best met with the use of a 'pdpp' basis set on each C atom, which provides 22 Gaussian functions of s, p, and d character. This set enables fast calculations, yet it gives sufficiently converged total energies and results in an optimised lattice parameter ≈ 6.679 a.u., which is 99.1% of the experimental value measured at 300 K [14] (Fig. 4.1). The bulk modulus of diamond calculated with this setup is ≈ 462.2 GPa, which is 104.5% of the experimental value of 442.3 GPa [26]. The calculated pressure derivative of the bulk modulus is ∼ 3.67, which is close to the common value of around 3.5.

When these calculations are repeated with the use of the 'PBE96' GGA functional [83] for the exchange-correlation aspect instead of the (default) 'Perdew-Wang 92' LDA functional [81], the optimised lattice parameter is 6.698 a.u. (99.4% experiment), the bulk modulus is 447.8 GPa (101.2% experiment), and the pressure derivative of the bulk modulus is 3.68. However, it is not generally worth the extra computational expense incurred to achieve these slight improvements in accuracy, and unless otherwise stated, all of the work performed in this investigation uses the L(S)DA and a 6.68 a.u. lattice parameter.

4.2.2 Electronic band structure

Experimentally, the (indirect) bandgap in diamond spans from the valence band at the Γ point, to the conduction band at a location just over 70% of the way from Γ to the X point, and has a value in the range of 5.47–5.50 eV at room temperature and below [9, 14]. The *direct* (Γ–Γ) bandgap has a value of around 7.1–7.3 eV [30–33].

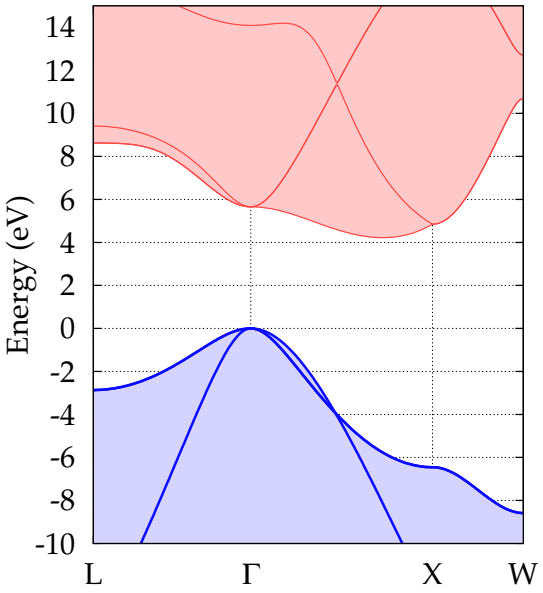

Figure 4.2: Calculated electronic band structure of bulk diamond, using a two-atom unit cell, a lattice parameter of 6.68 a.u., and the 'pdpp' basis set. Occupied and empty electronic states are drawn as thick dark and thin lighter lines respectively. The lower and upper shaded regions represent the valence and conduction bands respectively.

The band structure calculated for diamond as modelled with the LDA method and lattice constant described previously can be seen in Fig. 4.2. The indirect bandgap is calculated to be 4.22 eV, from Γ to 0.73X, while the calculated direct bandgap is 5.66 eV. Comparison of these quantities with the experimental values shows that they are both underestimated by just over 20%. Now, Kohn-Sham density-functional theory is well known to underestimate the positions of excited states (such as the conduction band), with most of the blame being placed upon the local-density approximation [278]. However, these AIMpro values are very close to (101% and 99.6% of) the values of 4.18 and 5.68 eV found in other LDA-DFT calculations [279].

Meanwhile, the maximal energy *width* of the valence band (at Γ) is calculated to be 21.69 eV, which agrees very well with the results of photoemission studies that measure it to be 21 ± 1 eV [280].

The present method therefore reproduces the basic structural and electronic properties of bulk diamond with good accuracy, and so the effects of introducing defects into the system can be investigated with confidence. In the forthcoming electronic band structure plots, the bands of pure bulk diamond are shown as shaded regions in the background, in order to clearly emphasise any defect-related states and the effect that impurities have on the bulk energy bands.

4.3 Chalcogens, pnictogens, and their complexes with hydrogen

Despite the theoretical zero solubility of phosphorus in diamond, it can be successfully grown into CVD material, and significant doping concentrations of $\sim 10^{19}$ cm^{-3} can be achieved [281]. The P atoms exist mainly as substitutional impurities [282]. In the majority of work up until now, the high concentration of P has only been found in $\langle 111 \rangle$ growth sectors. However, P has more recently been grown into (100)-orientated diamond single crystals following optimisation of the growth technique [265]. These results suggest that this super-saturation of P in diamond arises from an effective incorporation at the growing surface [283, 284].

The important implication is that other dopants atoms with large covalent radii might also be grown into diamond, under super-saturation conditions, via a similar mechanism.

Phosphorus in diamond was originally assigned a donor level around $E_c - 0.4$ eV [259], although several more recent measurements are united in placing it ~ 0.6 eV below E_c [125, 186, 262–268]. This value is much lower than the 0.218 eV expected from the effective-mass approximation (EMA) [186], suggesting a large attractive central potential. For a review of P doping in diamond, see Ref. [281].

By comparison, substitutional nitrogen has high solubility in diamond due to a low formation energy [253, 254]. Recall though that N acts as a very deep donor, with an observed activation energy of around 1.6–1.7 eV [285–290].

In this part of the present investigation, the search for shallow donor impurities in diamond is continued by considering two of the other chalcogens, selenium and tellurium, as well as two of the pnictogens, arsenic and antimony (Sb), as substitutional defects. The levels of N and S defects are also examined for comparison with earlier theoretical studies.

The motivation for examining the other chalcogens and pnictogens follows from similar studies in silicon. Here, it is known that the donor level of substitutional Sb (at 0.039 eV below the conduction band minimum energy E_c) is shallower than that of substitutional P ($E_c - 0.045$ eV) [9]. In addition, although S, Se, and Te introduce deep single- and double-donor levels, their complexes with a single H atom possess donor

levels much shallower than the isolated defects [111]. Such defects have been studied by electron-nuclear double resonance [291, 292], Fourier-transform infrared (FTIR) spectroscopy [293], deep-level transient spectroscopy [294, 295], and time-dependent conversion electron Mössbauer spectroscopy [296]. The FTIR data in particular reveal a number of shallow donors associated with S–H having levels around 0.1 eV [293].

The many roles of hydrogen in *diamond* have received much attention in theoretical work. For a recent review, see Ref. [297].

4.3.1 Particulars of the method

The AIMpro calculations were performed in 64- and 216-atom cubic supercells of diamond into which a substitutional impurity atom was placed, along with a hydrogen atom when investigating impurity-hydrogen complexes. Each system was allowed to undergo a full structural relaxation at fixed supercell volume.

Each substitutional defect atom X was investigated sited in at least two positions: (i) X_{latt}, where the X atom lies perfectly on a lattice site and the T_d symmetry of the system is maintained; and (ii) X_{shift}, where X is slightly shifted from the lattice site in $[\bar{1}\bar{1}\bar{1}]$, resulting in a system with C_{3v} symmetry. Those defects that were found to be more stable when shifted from the lattice site were also modelled with an initial shift in $[110]$.

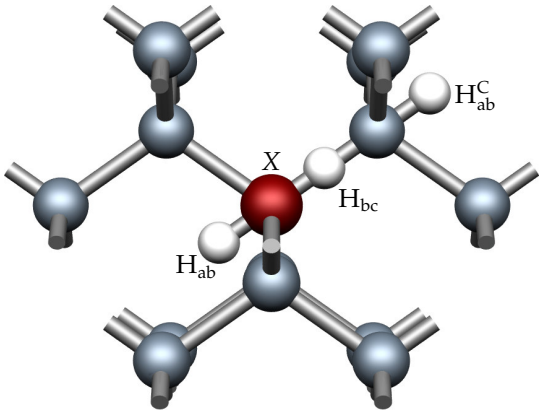

Figure 4.3: Starting positions for the H atom in defect-hydrogen complexes. The sites around the substitutional defect X are: anti-bonded, H_{ab}; at the middle of a X–C bond, H_{bc}; and anti-bonded to a carbon neighbour of X, H^{C}_{ab}.

Three sites for hydrogen bound with X were investigated. These were: (i) X–H_{bc} (bond-centred), where the H atom is at the centre of the bond between the defect X and the nearest C atom in $[111]$, such that there is a X–H–C axis; (ii) X–H_{ab} (X anti-bonding), where the H atom lies behind the impurity atom in $[\bar{1}\bar{1}\bar{1}]$, such that there is a H–X–C axis; and (iii) X–H^{C}_{ab} (C anti-bonding), where the H atom resides behind the $[111]$

C neighbour to the impurity, such that there is a X–C–H axis. These sites are summarised in Fig. 4.3. These complexes all have C_{3v} symmetry.

The most interesting defects were also modelled several times with symmetry-breaking random shifts applied to the initial positions of the key atoms, allowing them to move with greater freedom to find other possible low-energy structures.

The *marker method* (MM), as covered in Chp. 2, was used to calculate the donor levels for the defects investigated in this section. In this case, substitutional phosphorus was used as the marker; that is, each defect's 'ionisation' energy $E^{\mathrm{i}}_X = E(0)_X - E(+)_X$ was compared to that found for substitutional phosphorus, $E^{\mathrm{i}}_{\mathrm{P}}$. The donor activation energy for the defect is then given by $E^{\mathrm{a}}_X = E^{\mathrm{a}}_{\mathrm{P}} + (E^{\mathrm{i}}_{\mathrm{P}} - E^{\mathrm{i}}_X)$, where the activation energy of the phosphorus donor, $E^{\mathrm{a}}_{\mathrm{P}}$, is the experimentally well-known 0.6 eV.

Convergence criteria

The density of the **k**-point sampling mesh was investigated for both 64- and 216-atom supercells, each containing a single substitutional antimony atom on a lattice site. Antimony was chosen as it is the largest atom under investigation and therefore potentially the most disruptive to the surrounding crystal. Total energies were found to converge to within 10 meV for a **k**-point sampling grid of MP-2^3. To ensure adequate convergence, all 64-atom-supercell calculations used at least an MP-3^3 grid, while grids of MP-2^3 or higher were used in all of the 216-atom-supercell work.

The convergence of energies with respect to the value of the plane-wave cut-off energy E_{cut} was also investigated in the same supercells. Total energies $E(0)_{\mathrm{Sb}}$ and $E(+)_{\mathrm{Sb}}$ were converged to 10 meV for $E_{\mathrm{cut}} > 300$ Ry, while energy differences $E^{\mathrm{i}}_{\mathrm{Sb}}$ were sufficiently converged even for very low values of E_{cut}.

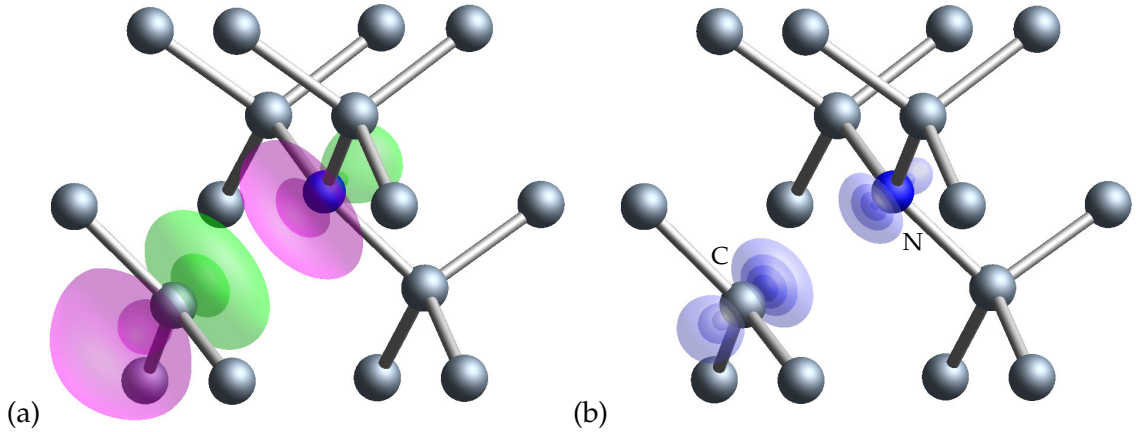

Figure 4.4: Isosurface plots for the orbital of the donor electron of the N substitutional in diamond, as sampled at the Γ point. Plot (a) shows the wavefunction, which confirms that the orbital represents an anti-bonding state between the N atom and the unique $C_{[111]}$ atom. Plot (b) shows the absolute-squared wavefunction, which is analogous to the charge density, and indicates that the majority component lies on the unique $C_{[111]}$ atom.

4.3.2 Substitutional pnictogen defects

Nitrogen

When in the neutral charge state, the trigonal N_{shift} defect was found to be more stable than the tetrahedral N_{latt} by about 0.7 eV, in agreement with previous theoretical studies [254, 298–300], and consistent with the properties of the 'P1' EPR centre attributed to substitutional N [301–303]. The $N^0{}_{shift}$ atom moves away from the lattice site in the $[\bar{1}\bar{1}\bar{1}]$ direction, elongating the unique N–$C_{[111]}$ bond to 129.2% of a normal C–C bond length, while the three other N–C bonds are 95.6% of the normal C–C length. Meanwhile, the unique $C_{[111]}$ atom moves away from the N in [111], almost into the plane of its three C neighbours, and can be considered to become sp^2 bonded.

This is the well-documented chemical re-bonding [254, 298–300, 304] sometimes referred to as the 'pseudo-Jahn-Teller' effect [305]. The N atom prefers to be threefold rather than fourfold coordinated, and its remaining two electrons occupy a lone-pair orbital directed toward the *p* dangling bond on the $C_{[111]}$ atom. As this C dangling bond contains one electron, there is an interatomic repulsion arising from the Pauli principle, and the N and the $C_{[111]}$ atoms mutually move apart.

The wavefunction for the highest-occupied electronic state (that is, for the donor electron) of the neutral N substitutional modelled in a 216-atom supercell is shown Fig. 4.4. The state has character of two p orbitals, one centred on the N atom and the other on the unique $C_{[111]}$ atom, with their axes coincident and directed along the [111] line joining the atomic centres, as required by symmetry. The lobes of the p orbitals facing each other between the atoms are of opposite sign, hence this is an N–C anti-bonding state, consistent with its high energy, and with the results of ESR investigations [301–303].

The positively charged N^+ substitutional relaxed onto the lattice site for all starting positions, yielding equivalent N–C bonds at 100.7% of the bulk C–C length. This T_d symmetry is intuitively expected, as of course the N atom is tetravalent in this charge state.

The donor level found by comparing the energies of the two charge states of the N defect with those of P lies at $E_c - 1.72$ eV in the 64-atom supercell, and at $E_c - 1.65$ eV in the 216-atom supercell. Other *ab initio* work [306] calculates the N donor level to lie 1.92 eV below the conduction band minimum, while the substitutional nitrogen activation energy has been experimentally measured in diamond samples to be around 1.6–1.7 eV [285–290].

This excellent agreement with the known atomic geometry and donor level for substitutional N gives confidence in the modelling and MM used in this work.

Phosphorus

In the 64-atom supercell, all starting structures for P relaxed to systems with approximate T_d symmetry, with total energies no more than a negligible 2 meV lower than that of the perfect T_d structure. However, in the 216-atom supercell, the structure clearly distorted to C_{3v} symmetry, saving 27 meV over the T_d structure. In this form, the unique P–$C_{[111]}$ bond is 112.6% of a bulk C–C length, while the three equivalent P–C bonds are 109.6% of the bulk length.

The orbital of the donor electron is shown in Fig. 4.5, and clearly shows as its main component a lobe attached to the P atom and pointing away from the unique $C_{[111]}$ atom. The second, much smaller component of the wavefunction is on this $C_{[111]}$ atom and points toward the P atom. This picture contrasts that of substitutional N, in that the main component of the donor electron is now on the impurity atom, and the component on the

unique $C_{[111]}$ atom is much smaller.

In the positive charge state, all initial geometries relaxed to the on-site T_d configuration, with P–C bond lengths 109.9% of the bulk length in the 216-atom supercell.

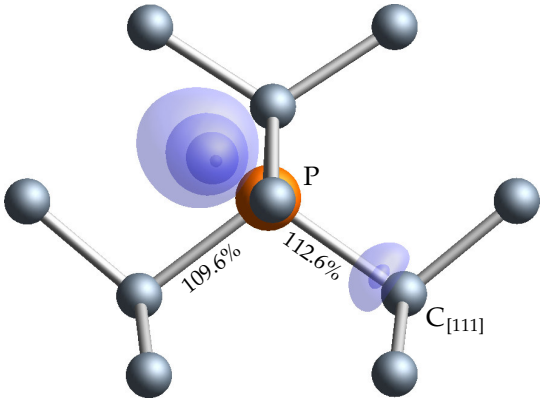

Figure 4.5: Atomic geometry and donor electron wavefunction for substitutional P in diamond. Bond lengths are relative to the bulk C–C length. Isosurfaces of the absolute-squared wavefunction are drawn for the highest occupied electronic state, as sampled at Γ.

In fact, the ground-state symmetry of the neutral P substitutional is currently a matter of contention. Many electron spin resonance studies have been performed to examine P-related defects in diamond [121–129], and while some studies assign a C_{3v} symmetry to the defect [124], more recent ESR work presents evidence for a P-related centre with tetragonal symmetry [125]. On the theoretical side, some studies (such as the present work) support a C_{3v} configuration [49, 307], while others predict T_d symmetry [53, 270, 308].

Recently, the symmetry of the P substitutional in diamond has been investigated using AIMpro in great detail, using supercells of up to 512 atoms [309]. The results indicate that in the large supercells, C_{2v}, C_{3v}, and D_{2d} symmetries are all metastable forms of the centre.

Nevertheless, it appears that the energy differences between the different symmetries of the P substitutional are all very small, and that the effect on the electronic structure is negligible. Therefore, the status of P as a reliable marker for use in the current calculations is unaffected.

Arsenic

Substitutional As appears to follow the N→P trend in that as the impurity atom gets larger, any distortion from the T_d lattice site becomes much smaller. In the 64-atom supercell, all initial geometries for the neutral As defect relaxed to final systems with T_d

symmetry and exactly the same energy.

However, in the 216-atom supercell, a very small distortion to C_{3v} symmetry was identified, with an energy saving of 8 meV over the T_d form. Nevertheless, this may well lie within the error of the modelling method. In terms of bulk C–C bond lengths, the three equivalent As–C bonds were 114.3%, while the unique As–$C_{[111]}$ bond was 116.3%. By comparison, all As–C bonds in the T_d structure were 114.7% of the bulk length. In both supercells, T_d symmetry was adopted by As in the +1 charge state.

Although all of the relaxed As–C bonds are significantly longer than bulk C–C bonds, they are comparable with those of Ni–C, which can occur in large concentrations of around 60–70 ppm [310]. Furthermore, implantation experiments have shown that over half of the implanted As atoms reside at substitutional sites [311–314], although the electrical properties were difficult to examine or have not been reported.

The wavefunction for the donor electron is highly delocalised, with significant magnitude over all parts of the supercell, consistent with the shallow donor behaviour. The absolute-squared wavefunction is of course more localised, and a plot is shown in Fig. 4.6, together with a plot for the first excited state of the system. The donor electron orbital has its largest component adjacent to the As atom, although there is a component of around half the size located next to the neighbouring unique $C_{[111]}$ atom. These orbital lobes are slightly triangular in shape when viewed along the [111] direction. The first excited state is twofold degenerate, and the sum of its two orbitals forms a ring around the As atom, with three concentrated regions next to the three equivalent C neighbours of the As atom, and three larger regions in the spaces between them. It is clear to see how both the highest occupied and first excited states share the subtle C_{3v} symmetry of the defect.

The calculated donor level for As lies at $E_c - 0.32$ eV and at $E_c - 0.39$ eV in the 64- and 216-atom supercells respectively, and it can be concluded that the substitutional As centre will possess a donor activation energy of ~ 0.4 eV. The electronic band structures have been calculated in 216-atom supercells for the three cases of: pure bulk diamond; diamond with As; and diamond with P, and a comparison of the electronic levels is shown in Fig. 4.7. Indeed, the highest occupied level for the As defect lies closer to the bulk diamond conduction-band states than does the highest occupied level of the P defect, throughout **k**-space.

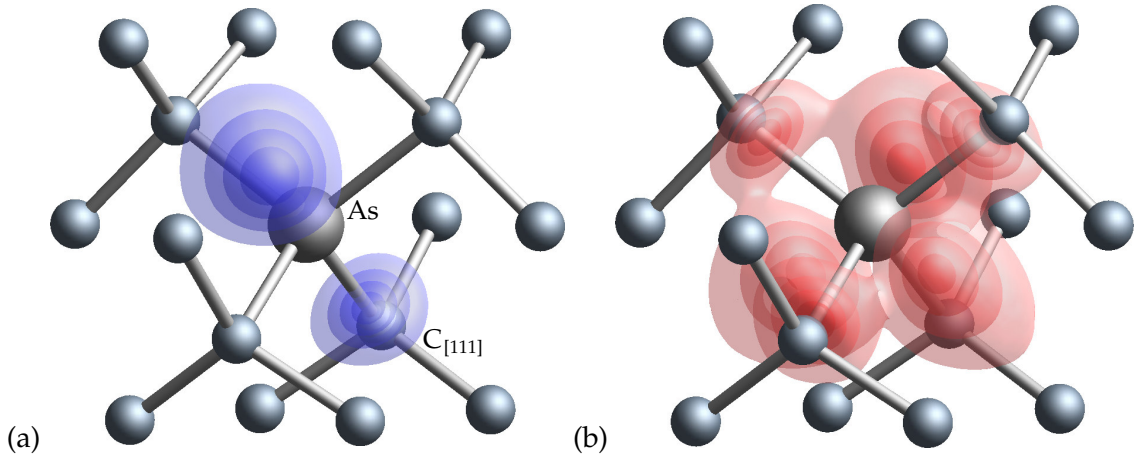

Figure 4.6: Isosurface plots of the absolute-squared wavefunction, sampled at Γ, for the As substitutional in diamond. Plot (a) shows the highest occupied electronic state (the donor electron), while (b) shows the lowest unoccupied (first excited) state.

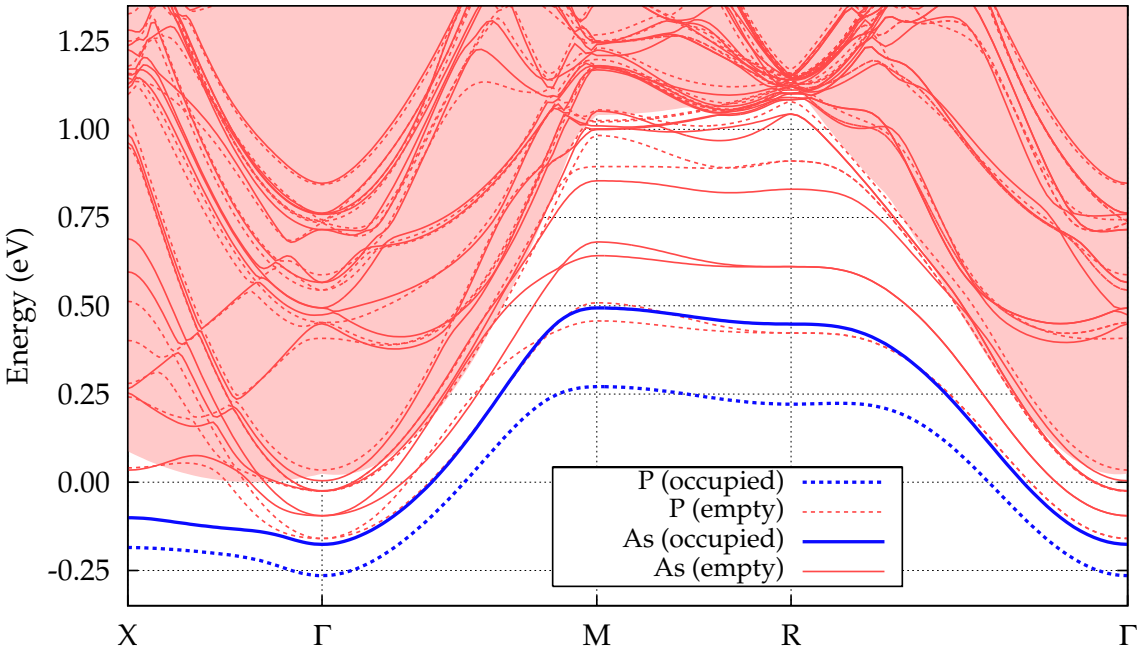

Figure 4.7: Band structure comparison showing the states near the conduction band for substitutional As and P defects in a 216-atom diamond supercell. The band structures are shown superimposed and have been aligned by their valence band maxima at the Γ point. The conduction band of bulk diamond is shown as the shaded region, while the zero of the energy scale corresponds to its minimum. Occupied and empty defect states are indicated by thick and thin lines respectively, while solid and dashed lines respectively show the states of the As and P defects.

The band structures also show that, even in the 216-atom supercell, there is significant dispersion of the defect levels. Since this dispersion is due to overlap between the electron wavefunctions of the defect and those of its images in repeated supercells, the delocalised nature of the donor electrons is evident. The peak-to-peak dispersion of the As donor electron level is 0.67 eV, while that of the P level is less, at 0.54 eV.

All signs therefore point to arsenic representing a donor that is shallower than substitutional phosphorus.

Arsenic-vacancy centres

Since the As atom is a large impurity in diamond, there is concern over its likelihood of binding strongly to vacancies. For this reason, arsenic-vacancy (As–V) centres have also been modelled in this work. A substitutional As atom with a $C_{[111]}$ vacancy as a first neighbour has the freedom to move in [111] toward the vacancy, in which case it can of course also be considered as an interstitial As atom at the middle of a C–C divacancy (As_i–V_2). This system has been placed in both 64- and 216-atom supercells, and relaxed with perfect symmetry and with random initial displacements.

In both supercells, all starting structures relaxed to the axial V–As_i–V configuration, which has D_{3d} symmetry, and is shown in Fig. 4.8(a). This was found to be true of both the neutral and positive charge states. In the relaxed 216-atom supercell, the nearest C neighbours to the As atom are 130.2% of a bulk C–C bond length distant when the system is neutral (and 130.9% when it is positively charged). In the neutral supercell, these C atoms have been displaced by 0.13 Å from their bulk lattice positions, although the displacement is not radially outward from the As atom, and in fact the As–C bond lengths have increased by only 3.5% during the relaxation. Comparison with the bond-length increases of $\sim$ 15% for substitutional arsenic gives an idea of how comfortable the As atom is at this divacancy site.

The binding energy $E^{\mathrm{b}}_{\mathrm{As}-V}$ of the neutral As–V complex can be calculated using

$$E^{\mathrm{b}}_{\mathrm{As}-V} = [E_{\mathrm{As}} + E_V - n_{\mathrm{C}}\,\mu_{\mathrm{C}}] - E_{\mathrm{As}-V}, \tag{4.8}$$

where E_X is the total energy of a neutral supercell containing the relaxed system X. The $n_{\mathrm{C}}\,\mu_{\mathrm{C}}$ term takes care of the surplus number of C atoms in the sum of the two separated

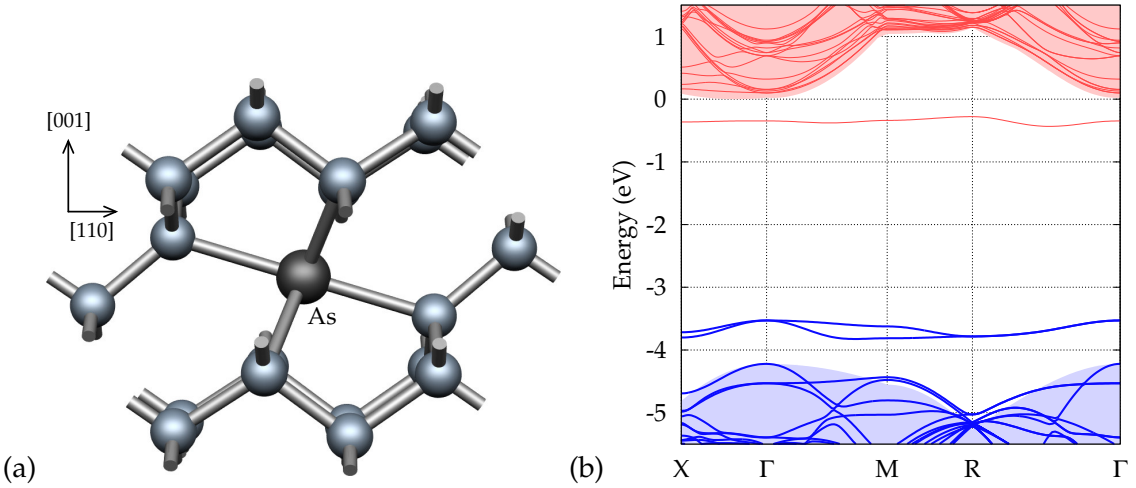

Figure 4.8: (a) Relaxed atomic geometry for the neutral As–V complex in a 216-atom supercell, and (b) its corresponding electronic band structure. The shaded regions represent the aligned bands of bulk diamond, while occupied and empty states from the As–V system are shown as thick and thin lines respectively.

systems, and is described in Sec. 2.8.3.

The results indicate that the complex is bound by 10.15 eV in the 64-atom supercell, and 10.19 eV in the 216-atom supercell. First, the fact that the difference in these figures is very small again suggests that the As is comfortable at the divacancy site and does not exert much strain on the surrounding material. Most importantly, this figure of $\sim$ 10 eV is very large, and suggests that As atoms bind extremely strongly to vacancies. However, there is likely to be significant error in this calculation, since the multiplet energies of the neutral vacancy are notoriously difficult to calculate [315], leading to a large error in the E_V of Eqn. 4.8.

The calculated binding energy of the As–V complex can be improved by using the formation energies, through

$$E^{\mathrm{b}}_{\mathrm{As}-V} = \left[E^{\mathrm{f}}_{\mathrm{As}} + E^{\mathrm{f}}_{V}\right] - E^{\mathrm{f}}_{\mathrm{As}-V}, \tag{4.9}$$

as described in Sec. 2.8.3, where the formation energy for the neutral vacancy $E^{\mathrm{f}}_{V} = 5.96$ eV is taken from recent quantum diffusion Monte Carlo calculations [315]. This results in revised As–V binding energies of 9.05 eV (64-atom) and 8.93 eV (216-atom). Hence, it can be concluded that the As–V complex is bound by around 9 eV.

The calculated electronic band structure for the As–V complex is shown in Fig. 4.8(b).

Clearly, it only has very deep levels. The highest occupied defect states lie within 1 eV of the bulk VBM, and an unoccupied level appears within about 0.5 eV of the CBM, while the rest of the bandgap is empty.

Using the MM with the P substitutional resulted in a donor level for the As–V complex at $E_c - 4.68$ eV in the 64-atom supercell, and at $E_c - 4.55$ eV in the 216-atom supercell. These values are likely to have high errors, since the P substitutional is quite a different defect to the As–V complex, and so the MM will not be very effective in cancelling the systematic errors present in both calculations. Furthermore, both of the calculated donor levels are larger than the DFT bandgap (4.22 eV), yet the highest occupied level seen in Fig. 4.8(b) is not embedded in the valence band. Nevertheless, it is plain to see that As–V is an extremely deep donor.

Antimony

Antimony continues the N→P→As trend in atomic geometry, in that there is now very little difference between the relaxed T_d and C_{3v} structures in terms of bond lengths, and in fact the two systems have essentially the same total energy. Meanwhile, the positively charged defect adopts T_d symmetry as expected.

Now, Sb is a very large atom (with a covalent radius almost 180% that of C), and the impurity causes a large distortion to the surrounding material, in that the Sb–C bonds are around 22% longer than the bulk C–C length. However, the distances to the second-nearest C neighbours of the Sb atom are increased by only 3.5%, and third-nearest neighbours are only 0.5% further away than in bulk. Therefore, the strain exerted by the Sb impurity — while high — is quite local, which is testament to the high incompressibility of diamond. However, it should perhaps be noted that these calculations were performed at a fixed supercell volume.

Substitutional antimony has a calculated donor level at $E_c - 0.33$ eV in the 216-atom supercell, while the 64-atom-supercell result of $E_c - 0.2$ eV is likely to have a large error with such a big impurity. Thus, it is likely that the Sb substitutional is only marginally shallower than the As defect.

Table 4.1 shows the trends in structural parameters and donor activation energy with

Table 4.1: Summary of data for neutral pnictogen defects in the 216-atom diamond supercell. Recall that the covalent radius of the neutral C atom is 77 pm. The P donor level is the reference for the others and is taken from experiment.

Property	**N**	**P**	**As**	**Sb**
Covalent radius of the neutral atom (pm)	75	106	119	138
$T_d \rightarrow C_{3v}$ energy saving (meV)	701	27	8	0
Unique X–$C_{[111]}$ bond length (% of bulk length)	130.3	112.6	116.3	122.7
Length of three equivalent X–C bonds (%)	95.5	109.6	114.3	121.5
Ratio of unique:equivalent bond lengths	1.36	1.03	1.02	1.01
Donor activation energy (eV)	1.65	(0.60)	0.39	0.33

impurity-atom size as one moves down the pnictogen group.

4.3.3 Pnictogen-hydrogen complexes

Complexes of the pnictogens with single H atoms have also been investigated, although in every case they exhibited very deep donor levels. This is in agreement with previous studies on N–H and P–H defects [253], and with the basic argument that the electron of the H atom will pair up with the donor electron of the pnictogen impurity, forming an X–H bonding orbital of very low energy. These passive centres are of no further interest to this study.

Furthermore, since the neutral pnictogen-hydrogen complexes introduce two extra electrons into the crystal, each defect could exist in either the spin-0 or spin-1 electronic configuration. However, a spin-1 state is not compatible with the formation of an X–H bond, and it is certain to be unstable with respect to the spin-0 configuration.

4.3.4 Substitutional chalcogen defects

First, it should be pointed out that since the chalcogen defects have six valence electrons, their substitutional impurities in diamond can adopt either spin-0 or spin-1 states when neutral. This extra factor has been included in this study by modelling all of the chalcogen defects in states with either zero or two unpaired electrons.

Oxygen

Substitutional oxygen in diamond has previously been investigated using AIMpro, and the results are reported in detail in Ref. [116]. To summarise, relaxed structures for the spin-0 oxygen substitutional with small off-site displacements in $\langle 111 \rangle$ and $\langle 100 \rangle$ (giving C_{3v} and C_{2v} symmetry respectively) had essentially the same energy as an on-site T_d configuration. In addition, the particular spin-1 defect with C_{2v} symmetry was found to have the same energy as these spin-0 forms. Therefore, the ground-state symmetry and spin state of the substitutional O defect is ambiguous.

In any case, substitutional oxygen has mid-gap donor and acceptor levels, and the bare defect is not a candidate for a shallow donor.

Sulphur

The status of S as a donor in diamond is still a matter of debate [43–53]. Experimentally, initial findings of shallow donor behaviour due to S — with an activation energy of 0.38 eV [51] — were subsequently attributed to p-type conduction due to contamination by boron [45], a problem that has arisen in other experiments [191]. Meanwhile, other measurements indicate that only a small fraction of incorporated S atoms are electrically active [44].

The present calculations agree with previous theoretical studies [46, 49, 53], in finding the trigonal S_{shift} arrangement as the most stable form of the defect. In the 64-atom supercell, the neutral, spin-0 C_{3v} structure is 0.3 eV more stable than the T_d form, although this energy difference increases to 0.6 eV in the 216-atom calculations.

However, while C_{3v} symmetry and the spin-0 configuration corresponds to the most stable neutral defect found, this form is only 0.1–0.2 eV more stable than the C_{2v} form when the defect is in the spin-1 configuration.

The 216-atom-supercell results indicate that the spin-1 C_{3v} defect is 0.4 eV higher in energy than the spin-0 C_{3v} form, although when the system is constrained to C_{2v} symmetry, the spin-1 configuration is slightly (0.1 eV) more stable than the spin-0 defect. With a T_d

symmetry constraint, spin-1 is again slightly more stable than spin-0, by 0.2 eV. Nevertheless, spin-0 and C_{3v} symmetry appears to be the most stable combination overall.

In the +1 charge state, C_{3v} was also found to be the most stable symmetry, with energy savings over the C_{2v} and T_d structures of 0.1 and 0.3 eV respectively (in the 216-atom supercell). This could be anticipated, since this group-16 (VI) defect still has one unpaired electron in this charge state, and can be viewed as somewhat like a group-15 (V) impurity.

The donor level found for the sulphur defect by comparing its C_{3v} forms lies at $E_c - 1.32$ eV in the 64-atom supercell, and at $E_c - 1.44$ eV in the 216-atom supercell. This is fairly close to the previous estimate of $E_c - 1.63$ eV from LDA-DFT calculations [49], and clearly represents a deep donor.

However, other DFT work predicts a shallow donor level for S [43], although this is only based on the positions of the KS levels, and the use of relatively small diamond clusters. Another early theoretical study, using 64-atom supercells, predicted an extremely shallow donor level for S, at $E_c - 0.15$ eV [50], although again it appears that this comes from inspection of KS levels alone (however, this is not clear). Furthermore, a 2^3 MP grid was used, while the present calculations find that MP-3^3 is required to ensure the convergence of total energies for 64-atom supercells. This is especially likely to be true in the case of a shallow donor, where the delocalised donor wavefunction causes significant defect-image interaction, leading to high dispersion in its energy level, and requiring a high MP-grid density for accurate sampling (although this is acknowledged in Ref. [50]).

Selenium

Owing to the size of the impurity, selenium was modelled in diamond in just the larger (216-atom) supercells. The results with regard to the optimised structure are fairly similar to those found for substitutional sulphur. In the spin-0 state, a C_{3v} configuration is most stable, being 0.6 eV lower in energy than the T_d form, although it is only 0.05 eV more stable than a C_{2v} distortion. In the spin-1 state, it is the C_{2v} geometry that is preferred over the T_d and C_{3v} forms, by 0.3 and 0.1 eV respectively. Overall, the most stable combination for the neutral defect is (spin-0, C_{3v}), which is 0.5 eV lower in energy than the (spin-1, C_{2v}) defect. Therefore, the ground state is almost certainly spin-0 with an off-site distortion, although there is some ambiguity in the direction of this displacement.

In the +1 charge state, a C_{3v} distortion is preferentially adopted over T_d and C_{2v} symmetries, with associated energy savings of 0.3 and 0.2 eV, respectively.

The donor level found by comparing the most stable forms lies at $E_c - 1.56$ eV. Surprisingly, this is deeper than that found for sulphur. The origin of this discrepancy is at present unknown.

Tellurium

The 216-atom supercell results for Te appear to follow the trends set by sulphur and selenium. The neutral, spin-0 defect distorts to C_{3v} symmetry with a saving of 0.5 eV over the T_d structure. However, the C_{2v} distortion is only 0.02 eV higher in energy than C_{3v}. With a spin-1 electronic configuration, C_{2v} represents a saving of 0.3 and 0.2 eV over the T_d and C_{3v} forms respectively. The (spin-0, C_{3v}) defect is more stable than (spin-1, C_{2v}) by 0.4 eV. Again, the neutral ground state is a structurally distorted spin-0, and now the off-site distortion is truly ambiguous.

Once again, C_{3v} symmetry appears to be preferred when the defect is in the +1 charge state, in which case it saves 0.2 eV over a T_d configuration. However, the C_{2v} form is less stable by only 0.03 eV, which means that the nature of the off-site distortion is uncertain in the positive charge state as well. This is most likely a size effect: as the size of the impurity atom increases, the freedom to move away from the T_d lattice site is reduced.

The donor level found for substitutional Te is located at $E_c - 1.26$ eV, about 0.2 eV shallower than the level predicted for sulphur. Still, it appears that none of these isolated chalcogen defects behaves as a notably shallow donor.

4.3.5 Chalcogen-hydrogen complexes

Oxygen-hydrogen complexes

The interaction of hydrogen with substitutional oxygen in diamond has previously been studied using AIMpro supercell calculations [115]. The H atom is found to prefer a bond-centred site, H_{bc}. The electrical levels were calculated using both the formation energy

method (FEM, see Sec. 2.8.4) and the *first-principles* marker method (FPMM, *i.e.* where bulk diamond is used as a marker). Both methods suggest that the defect is a deep donor, with the FEM putting the donor level at $E_v + 2.0$ eV, and the FPMM placing it at $E_v + 3.0$ eV. Therefore, the complex has an approximately mid-gap donor level.

Sulphur-hydrogen complexes

The 64-atom-supercell calculations identified the S–H_{ab} form as the most stable configuration of the S–H complex. That is, the H atom preferentially bonds to the S substitutional, in agreement with other studies [47, 307]. In both the neutral and positive charge states, this arrangement was $\sim$ 1 eV lower in energy than the S–H^{C}_{ab} form, and close to 2 eV more stable than the S–H_{bc} configuration.

Furthermore, preliminary 64-atom-supercell calculations found the latter S–H_{bc} arrangement to be less stable than a 'separated' form in which the S atom is a bare substitutional and the H atom is lying distant, at the middle of a C–C bond. The separated form was $\sim$ 0.5 eV more stable than S–H_{bc} in the neutral charge state, and $\sim$ 0.2 eV more stable when positively charged. These values also show that the S–H^{C}_{ab} and S–H_{ab} forms are stable *against* forming the separated arrangement.

A more rigorous determination of the binding energy in the stable S–H_{ab} complex was conducted by comparing the total energies of diamond supercells containing: the S–H_{ab} complex; the bare S substitutional; and the isolated H atom. Hydrogen is known to prefer a bond-centred interstitial site in diamond [253, 316, 317], where in the neutral charge state it lies exactly at the C–C mid-point, exhibiting D_{3d} symmetry. This form was therefore used in these calculations, and indeed, random displacements confirmed that this is the site of lowest energy.

The 64-atom-supercell results suggest that the S–H_{ab} complex is bound with respect to its separated neutral components by 3.02 eV, with 216-atom supercells giving a very similar figure of 3.03 eV. These values are quite high, although the calculations included a low-energy form of the S–H_{ab} complex, which will now be described.

The relaxed atomic geometry of the neutral S–H_{ab} complex was surprising, and is shown in Fig. 4.9. While the symmetry might be expected to be C_{3v} (with a straight H–S–C axis),

all of the calculations performed with randomised initial positions relaxed to a geometry in which there was a slight off-axis distortion of the S and H atoms. In this structure, the two impurity atoms are displaced off the [111] axis in roughly the $[11\bar{2}]$ direction, reducing the symmetry elements to just one mirror plane (C_{1h}). The H–S–C bond angle has changed from 180 ° to $\sim$ 175 °. Repeating the calculations with a shift in exactly the $[11\bar{2}]$ direction applied to the S and H atoms (from the C_{3v} structure) resulted in the same distorted structure and total energy as in the 'randomised' calculation. The energy saving over the trigonal structure is 0.20 eV, which is certainly significant at this level of accuracy. By comparison, all starting structures in the +1 charge state relaxed to the C_{3v} configuration.

The 216-atom-supercell calculations on the distorted S–H_{ab} complex were repeated with the MP sampling grid increased from 2^3 to 3^3. This resulted in no change in structure, and a negligible change in total energy of $\sim$ 4 meV in both charge states.

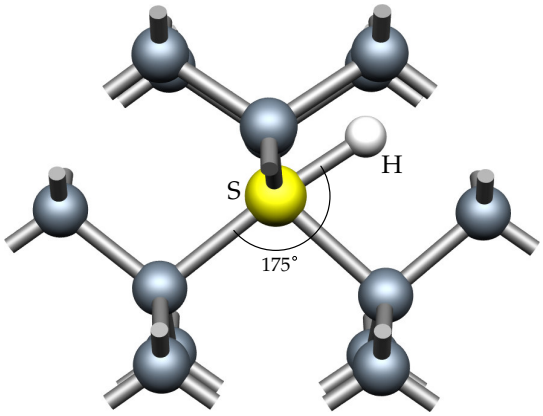

Figure 4.9: Relaxed atomic geometry for the neutral S–H_{ab} complex in a 216-atom supercell, showing the slight off-[111]-axis distortion of the S and H atoms.

Inspection of the electronic structure reveals the mechanism responsible for the distortion. In the C_{3v} geometry, the highest occupied electronic state is twofold degenerate (at least for Γ–R in these supercell calculations — defect-image interaction causes dispersion and splitting of the level elsewhere in **k**-space), although in the neutral charge state this level is occupied by only one electron. The system is therefore a candidate for the Jahn-Teller effect, and indeed, when the symmetry-breaking distortion is allowed in the calculation with randomised initial coordinates, this electronic level splits into a lower, singly occupied level, and an unoccupied level that mixes with the higher excited states.

The electronic band structures for both the C_{3v} and C_{1h} symmetries of the defect are shown in Fig. 4.10, where it is clear to see that the highest occupied level drops in energy by around 0.3 eV following the symmetry-lowering distortion of the structure.

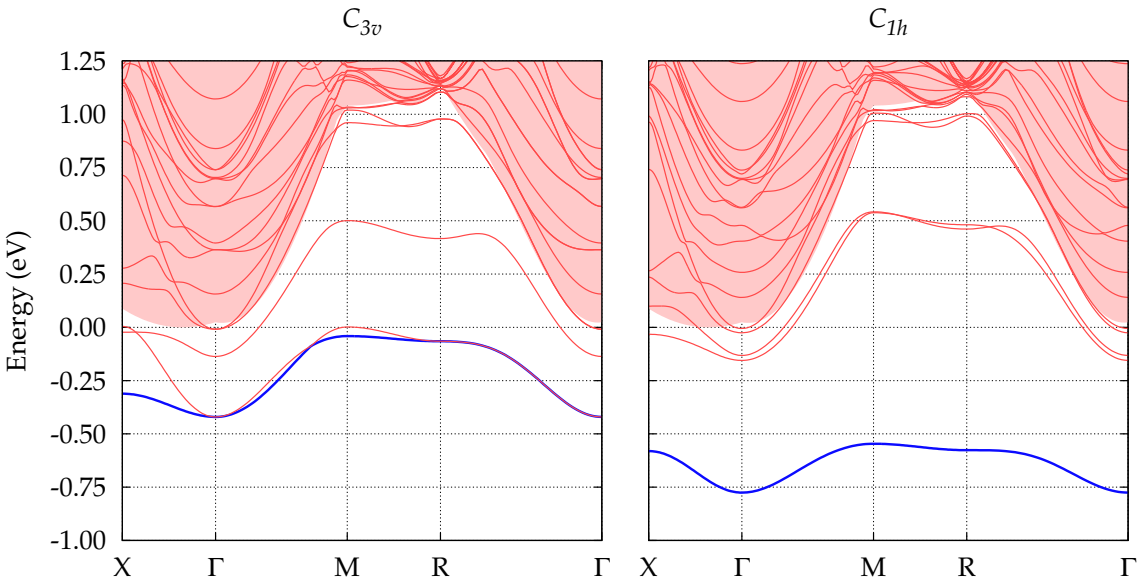

Figure 4.10: Calculated electronic band structures for the S–H_{ab} complex in a 216-atom diamond supercell. In the left panel the defect has C_{3v} symmetry, while in the right panel it has C_{1h} symmetry. The shaded regions represent the aligned conduction band of bulk diamond, while the zero of the energy scale is its minimum. Occupied and empty levels from the defect systems are shown as thick and thin lines respectively.

Of course, this Jahn-Teller distortion has negative implications for the formation of a shallow donor. The donor level for the S–H_{ab} complex in its C_{3v} form is calculated in the 216-atom supercell to lie at $E_c - 1.00$ eV, while after the distortion to C_{1h} symmetry, it lies at $E_c - 1.20$ eV.

Comparison with the $E_c - 1.44$ eV donor level for the bare S_{shift} defect confirms that the presence of anti-bonding hydrogen makes the defect a significantly shallower donor, although it remains much deeper than the bare P substitutional.

The findings for the C_{3v} form of the S–H_{ab} complex are in line with a previous study that places the donor level of S–H at $E_c - 1.07$ eV [306], and they also agree qualitatively with the electrical properties of the corresponding defects in silicon.

However, these results disagree with a recent, similar theoretical study [270], in which the S–H^C_{ab} form was found to be the most stable, and presented a donor level at $E_c - 0.61$ eV, very close to that of the bare P substitutional. It should be noted that in the present work, the 64-atom-supercell calculations suggest that the metastable S–H^C_{ab} complex has a donor level lying at $E_c - 1.03$ eV.

The discrepancy in stability and donor levels may be due to the fact that the cluster formalism was used in Ref. [270], whereas the supercells used in the present investigation not only contained a greater number of C atoms, but also did not require H termination. Furthermore, no symmetry-lowering distortion is reported in Ref. [270]. In any case, it is difficult to model a shallow donor in the cluster formalism, since its correspondingly delocalised donor wavefunction might be unrealistically confined to within the boundaries of the cluster (and also undergo interaction with the terminating H atoms), elevating its energy level.

Selenium-hydrogen complexes

Preliminary 64-atom-supercell calculations identified Se–H_{ab}^{C} as the most stable form of the neutral Se–H complex. With systems restricted to C_{3v} symmetry, Se–H_{ab}^{C} was 1.97 eV lower in energy than Se–H_{bc}, but only 0.16 eV more stable than the defect–anti-bonded Se–H_{ab}. Both of the anti-bonded forms underwent slight off-axis distortions when the initial coordinates were randomised, although Se–H_{ab}^{C} remained the lowest-energy arrangement, by 0.11 eV.

In the +1 charge state, no off-axis distortion was found for either anti-bonded arrangement (which is consistent with the distortions being of a Jahn-Teller nature similar to that of S–H) and Se–H_{ab}^{C} was found to be 0.16 eV lower in energy than Se–H_{ab}.

The stable Se–H_{ab}^{C} defect was transferred to the 216-atom supercell for further relaxation and investigation. For the neutral defect, the energy saving of the off-axis distortion was calculated in this supercell to be 0.21 eV, which is very similar to that seen in the distortion of the sulphur-hydrogen complex. The mechanism responsible is also likely to be similar, although this has not been explicitly investigated.

The donor level found for the Se–H_{ab}^{C} complex lies at $E_c - 0.75$ eV in the 64-atom supercell, and at $E_c - 0.91$ eV in the 216-atom calculations. Therefore, the complex is ~ 0.3 eV shallower than S–H, and over half an eV shallower than the bare selenium substitutional.

Tellurium-hydrogen complexes

Te–H_{ab}^{C} was found to be the most stable Te–H complex in both the neutral and positive charge states, in both supercells. The defect causes significant outward distortion to the surrounding material, which is not surprising given that the covalent radius of a Te atom is some 175.3% that of a C atom. The neutral defect shows a slight off-axis distortion as seen with S–H_{ab}, most likely due to a similar Jahn-Teller mechanism, although with the great strain on the surrounding crystal, this distortion is very small; the energy saving over the on-axis (C_{3v}) structure was negligible in the 64-atom supercell, and only 32 meV in the larger supercell.

The donor level for the Te–H_{ab}^{C} defect lies at $E_c - 0.51$ eV in the 64-atom supercell, and at $E_c - 0.76$ eV in the 216-atom supercell. These estimates are either side of the P donor level, although of course the value from the larger supercell is likely to be more accurate. Indeed, the significant discrepancy in these figures suggests that a very large supercell is required to adequately contain the defect. The basic conclusion is that Te–H_{ab}^{C} represents a donor with a level close to that of P, although the extremely large size of the impurity presents a formidable obstacle to its formation in a crystal as tight as that of diamond.

4.3.6 Section summary

The trends in atomic geometry and electrical activity as one considers the pnictogens as substitutional defects in diamond are quite clear, with the larger impurities showing less off-site distortion and shallower donor levels. All of the results on substitutional arsenic in diamond indicate that it is a shallower donor than substitutional phosphorus. Now, while the theoretical bulk solubility of As in diamond is most likely negligible, the impurity may perhaps be introduced into the material via the same mechanism of favourable surface chemistry that leads to the incorporation of (theoretically insoluble) phosphorus, despite this mechanism not being fully understood at present. However, donor activity could be compensated by the formation of defects such as arsenic-vacancy centres. The larger antimony substitutional exhibits slightly shallower donor behaviour than does As, although the incorporation of Sb into diamond is likely to be extremely difficult. Meanwhile, the controversial sulphur defect appears to be a deep donor.

The chalcogen-hydrogen complexes are indeed shallower donors than the bare double-donor chalcogen impurities, with the donor level becoming shallower as the size of the chalcogen impurity increases. However, they are all still quite deep when compared to bare P, let alone As or Sb. Even the hydrogen complex of the largest chalcogen considered (tellurium) has a donor level only around the same as that of P. The hydrogen complex of sulphur exhibits a noticeable symmetry-lowering distortion that can be explained by the Jahn-Teller mechanism. This is somewhat significant, given the disagreement over the structure of this complex, although the defect is almost certainly a deeper donor than phosphorus.

4.4 Boron-hydrogen complexes: shallow donor behaviour?

4.4.1 Introduction

Recently, the electrical properties of heavily boron-doped and deuterated diamond have been investigated using a range of experimental techniques [40, 41, 272, 273]. The surprising results have been interpreted as shallow donor behaviour, due to the formation of B–D complexes. Hall effect measurements indicate that the conduction is *n*-type, although such measurements are notoriously difficult to obtain [45]. Electronic infrared absorption measurements do not show the features at 2450 and 2800 cm^{-1} characteristic of substitutional boron, suggesting that the deuterium has passivated this impurity [41]. The boron concentration in the heavily doped samples, [B] $\sim 10^{19}$ cm^{-3}, is similar to the measured concentration of electrons, suggesting that the B acceptors have been efficiently converted into easily ionised donors through deuterium complex formation.

The donor level is measured to lie at $E_c - 0.23$ eV, which is extremely close to the EMA value of 0.22 eV [186], although in samples with lower boron concentration (where [B] $\sim 10^{17}$ cm^{-3}), the donor level drops slightly to $E_c - 0.34$ eV [40]. However, it remains to be seen just how easily reproducible this shallow donor behaviour is. Indeed, very recent experiments using Hall-effect measurements and secondary ion mass spectroscopy have not found any evidence for *n*-type electrical activity following deuteration of boron-doped CVD diamond, but rather indicate a highly resistive state [318].

The results of secondary ion mass spectroscopy (SIMS) measurements indicate the presence of more than one D atom per B acceptor, and therefore B–D_2 complexes have been suggested as being responsible for the shallow donor behaviour [41]. Indeed, recent experiments using ion-beam analysis of such samples indicate that the D:B ratio must be ≥ 2 in order for the *n*-type conductivity to arise [272]. Furthermore, the concentrations of other impurities in these samples are very low, which strongly suggests that the defect responsible for the high carrier concentration must contain B and D constituents.

The *n*-type conductivity appears to be stable at room temperature, as required for device applications, although the effect is lost at elevated temperatures. The concentration of free electrons drops severely when the sample is annealed to 520 °C, while the activity is removed altogether by annealing at 600 °C for 15 minutes. The *p*-type nature of the B-

doped sample is recovered at even higher temperatures (750 °C), presumably when the D is lost from the sample. This hole conductivity has a very low activation energy of 90 meV [41], which is likely due to impurity-band conduction arising from the very high boron concentration.

B–H complexes

From a simple chemical argument, boron-hydrogen (or boron-deuterium) pairs are expected to be passive, with the H donating its electron to the B acceptor, and then this H^+ (bare proton) being strongly bound to the charged B^-. Indeed, electronic IR absorption [319] and capacitance-voltage [320] measurements have shown the passive nature of B-doped diamond subsequent to hydrogenation. Meanwhile, theoretical work predicts a corresponding lack of bandgap levels for the B–H pair [253, 274–276].

The structure of the B–H pair has previously been calculated by DFT to have the H atom situated roughly in the (say) [001] direction from the B atom, although with a slight displacement in [110] toward a C neighbour of the B atom [253, 275, 321]. This structure has been reproduced for this investigation, and indeed the system is stable, with the relaxed atomic geometry shown in Fig. 4.11. The theoretical binding energy for the B–H pair appears to vary strongly with the method used, although the DFT estimates are in reasonable agreement with experiment [253, 274, 275].

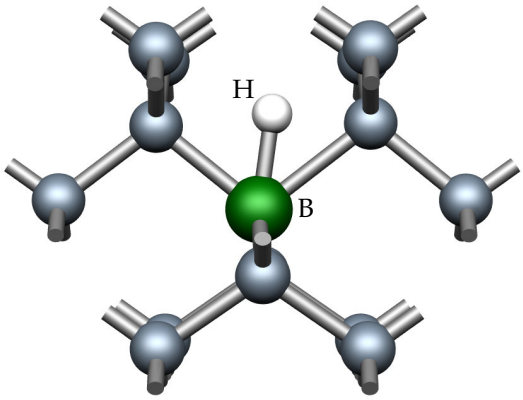

Figure 4.11: Relaxed atomic geometry for the the B–H defect in a 64-atom diamond supercell. The [001] direction is vertical in the plane of the image.

B_2–H_2 complexes

AIMpro has also been used to model complexes involving two B and two H atoms [274]. However, all of the complexes considered behaved as acceptors with levels in the lower

half of the bandgap, or as passive centres, with no indication of any shallow donor behaviour. Furthermore, these can be ruled out of this particular study, since they are incompatible with the results of the aforementioned SIMS measurements [41].

B–H_2 complexes

Recent DFT calculations using the cluster method have predicted the structure for B–H_2 to comprise a H atom at a buckled B–C bond centre, with the second H atom close to a C–C bond centre whose atoms are second and third neighbours of the substitutional B atom (excluding the C atom involved in the B–H–C bond) [275]. However, the binding energy of this complex suggested that it is highly unstable with respect to dissociating into B–H and a distant interstitial H atom. In addition to being unstable, the complex possessed only very deep occupied levels in the bandgap. Furthermore, the effect of charge on the structure and stability of the B–H_2 complex was not investigated.

Shallow donor behaviour for the B–H_2 complex might be expected if one uses the co-doping argument. This scheme, related to the work in the next section on the N–Si_4 complex, explains how the combination of two or more impurities can cause level repulsion that elevates the level of a donor impurity, making it shallower. For instance, the N-Al-N complex is expected to have a shallower donor level than the isolated N impurity due to such a mechanism [322]. So, since H is theoretically a donor in diamond [53, 253, 307, 323], the effect of the nearby B–H pair in the B–H_2 complex may be to raise its donor level. However, bond-centred H is a very deep donor, with a level in the lower half of the bandgap [253], and even with significant level repulsion it is hard to imagine it as being responsible for the very shallow donor level seen in experiment.

Nevertheless, the B–H_2 complex appears to be the most promising candidate for the shallow donor behaviour in light of the results of the SIMS measurements. In addition, it is easier to model B–H_2 than B complexes of higher H content, due to the runaway number of possible configurations. The B–H_2 complex has therefore been studied in more detail.

4.4.2 Particulars of the method

First, it should be noted that the structural optimisation routine in AIMpro does not involve the masses of the atoms concerned, and so the structures derived from modelling H in diamond are equally valid for deuterium.

Several starting structures were considered for the addition of a H atom to the stable B–H pair. This approach is likely to be the most appropriate, since the experimental studies indicate that the shallow donors are formed in a two-step process: first, passive B–D complexes are formed, and then further exposure to the D plasma creates a layer of material containing roughly twice as many D atoms as B atoms, and it is this second step that creates the *n*-type activity [273].

In general the starting structures formed by adding H to B–H can be categorised as: (i) H anti-bonded to the B atom, in the same plane as the B–H pair (this for instance represents two sites due to the off-[001]-axis distortion of the first H atom); (ii) H in a B–C bond centre; (iii) H in a nearby C–C bond centre; and (iv) H anti-bonded to a first-B-neighbour C atom.

The structure of B–H_2 found in silicon was also included, wherein the two H atoms are located near to bond centres in two of the B–C bonds. However, this structure was very high in energy, most likely due to the difference in lattice parameters between silicon and diamond, and would relax to other structures given changes in the starting positions.

In addition, H_2^* (the stable form of the hydrogen dimer in diamond) was modelled close to the B substitutional. The H_2^* defect represents one H atom at a C–C bond centre, and the second H atom anti-bonded to one of these C atoms, along a $\langle 111 \rangle$ direction. However, in the vicinity of the B atom, this relaxed into a range of structures of lower energy after perturbing the starting coordinates.

Finally, the H_2 molecule was placed in interstitial space in the neighbourhood of the B substitutional, although this always corresponded to high-energy structures.

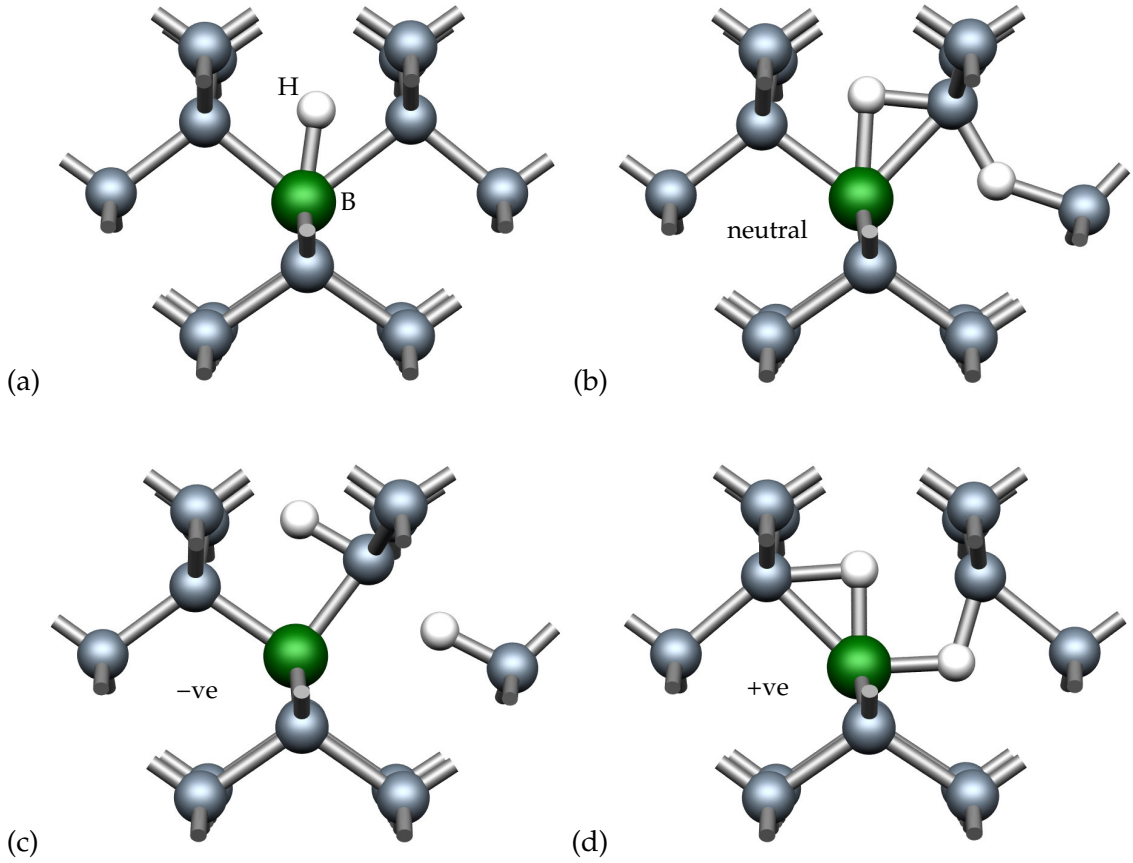

Figure 4.12: Relaxed atomic geometries for the B–H_2 complex, where panel (a) shows the relaxed B–H pair for comparison. The most stable structure is shown for the complex as: (b) neutral, (c) negatively charged, and (d) positively charged.

4.4.3 Results on B–H_2

Structure

The most stable form of the B–H_2 complex was found to depend quite significantly on the charge state of the system. In the neutral state, the first H atom remains close to its position in the B–H pair, while the second H atom lies in a nearby C–C bond. This bond is buckled, with a C–H–C angle of around 138 °, and this structure agrees qualitatively with that found in the earlier cluster DFT study [275].

In the negative charge state, the structure can be regarded as containing H_2^* close to the B substitutional. That is, the first H atom is further away from the B atom in $[001]$ than when the system is neutral, while the second H atom also moves away from the B substi-

Table 4.2: Summary of calculated binding energies for the creation of B–H_2 complexes. B atoms are substitutional, while H_i refers to interstitial hydrogen. Systems are in the neutral state unless otherwise indicated.

Reactants	→	**Product**	**Binding (eV)**
$B^- + H_2^*$	→	$(B–H_2)^-$	-0.1
$B–H + H_i^-$	→	$(B–H_2)^-$	2.1
$B + H_2^*$	→	$B–H_2$	0.8
$B–H + H_i$	→	$B–H_2$	0.5
$B–H + H_i^+$	→	$(B–H_2)^+$	0.7

tutional, and closer to the mid-point of its C–C bond, reducing the buckling such that the C–H–C is now 162 °. The particular C atom that is involved with the B atom and both H atoms is significantly displaced from its bulk lattice site, and essentially lies in the plane defined by its C neighbours and the B atom.

In the positive charge state, the structure is significantly different. The first H atom remains close to its position in the neutral system, although it has moved in $[\bar{1}\bar{1}0]$, away from one C atom and toward another. Most importantly, the second H atom has moved from a nearby C–C bond to a very strongly buckled B–C bond, such that it lies roughly in the [110] direction from the B atom.

The effect of going from the positive → neutral → negative charge states can then be summarised as movement of the H atoms away from the B substitutional, with the first moving in roughly [001], and the second moving in approximately [110].

Binding and dissociation-activation energies

The various binding energies associated with the B–H_2 complex and its possible separated components have been calculated using the full formation-energy-based method described in Eqns. 2.65 and 2.66 of Chp. 2, so that the effects of charge states are included. The calculated binding energies are summarised in Table 4.2.

The first finding is that the negatively charged $(B–H_2)^-$ complex is unstable with respect to dissociating into ionised B^- and the stable neutral H_2^* dimer, since the binding energy is negative. However, the value is small, and the problems in calculating the formation energies of charged systems may have introduced large errors into this quantity.

However, the largest binding energy (of 2.1 eV) is against this $(B–H_2)^-$ complex dissociating into the neutral B–H pair and a negatively charged interstitial H atom. The large difference with the previous result exists primarily because B is a shallow acceptor, while the acceptor level of H_i is very deep. This means that the dissociation of $(B–H_2)^-$ into components including B^- is likely to require less energy than dissociation into components that include H^-.

The other binding energies, for the neutral and positively charged $B–H_2$ complex, are all quite small. Furthermore, the values associated with the neutral complex and neutral components do not suffer from the aforementioned charge-state problems, and are likely to be more reliable.

The *activation* energies for dissociation of the $B–H_2$ complex can be estimated by adding the migration barriers of the components to the binding energies. For example, the binding energy of H_2^* in diamond is around 2.5 eV, while the migration barrier of the neutral H interstitial is close to 1.6 eV, and so the dissociation of H_2^* into neutral H atoms will have an activation energy of about 4.1 eV [253].

The migration barrier for the proton H^+ in diamond is calculated to be $\sim$ 0.2 eV [253], and so the activation energy E_{act} for the loss of H^+ from the $(B–H_2)^+$ complex is expected to be 0.9 eV. As it will now be shown, this low value is not compatible with the measured stability of the shallow donor behaviour.

The thermal stability of a defect can be estimated as follows. If a system at temperature T attempts (with frequency ω) to surmount a barrier of height E_{act}, the rate ν at which it will be successful (neglecting entropy contributions) is given by the Arrhenius equation:

$$\nu = \omega \exp\left(\frac{-E_{\text{act}}}{k_B T}\right), \tag{4.10}$$

where k_B is Boltzmann's constant. That is, the rate of successful barrier hops is a fraction of the attempt rate, where this fraction is the proportion of 'systems' that have enough energy to jump the barrier, as determined by the Maxwell-Boltzmann distribution.

Choosing ω to be a typical C–H vibration frequency of $\sim$ 90 THz, the 0.9 eV barrier to dissociation of the $(B–H_2)^+$ complex could be surmounted once per second at a temperature of only $\sim$ 52 °C. Alternatively, at the stability temperature of 520 °C, the same 1 Hz dissociation rate for this complex could be achieved with an attempt frequency as

low as 5.2×10^5 Hz. From yet another point of view, to prevent 1 Hz dissociation up to a temperature of 520 °C, the activation barrier would have to be over twice as high, at 2.2 eV.

The choice of ν and ω can be altered somewhat without a large effect on these calculated quantities. The Raman 'frequency' of diamond is 1332 cm^{-1} [27, 28], which corresponds to a frequency of 3.99×10^{13} Hz, or around 40 THz, and this is often taken as a typical attempt frequency ω. The 600 °C annealing experiments at which the shallow donor behaviour is completely lost were performed for 15 minutes, and so each centre can be expected to surmount the barrier once (*i.e.* dissociate) in these 900 seconds, or rather $\nu = 1/900$ Hz. Using these values in the same equation suggests that the barrier to dissociation would have to be 2.9 eV to be consistent with these findings.

Therefore, it can be concluded that the B–H_2 complex is almost certainly much less stable than the measured electrical conductivity.

Electrical properties of B–H_2

From the formation energy method (FEM), as described in Sec. 2.8.4 of Chp. 2, the donor level for the B–H_2 complex is calculated to lie at $E_v + 1.65$ eV, when taking the most stable form of the complex for each charge state. This level is ~ 3.9 eV beneath the CBM using the experimental bandgap, or 2.6 eV beneath the underestimated DFT E_{CBM}, and so the complex is certainly not a shallow donor. The FEM also reveals an acceptor level at $E_v + 1.50$ eV (*i.e.* below the donor level in the gap), which makes B–H_2 a negative-U defect.

The marker method (MM, Sec. 2.8.4) has also been used to calculate the donor and acceptor levels of B–H_2. For the donor level, the first-principles MM (using bulk as a marker) places it at $E_v + 2.6$ eV, while using the N substitutional as an empirical marker places it at $E_c - 3.0$ eV. Incidentally, using substitutional P as the marker also results in a calculated donor level at $E_c - 3.0$ eV, because — as seen in the previous section — the MM using P reproduces the donor level for N very accurately. Bearing in mind the experimental bandgap of 5.5 eV, these MM estimates are clearly within 0.1 eV of each other, although they predict the level to be about 1 eV closer to the CBM than does the FEM. Nevertheless, the system is still a very deep donor.

With regard to the acceptor level, the first-principles MM places it at $E_c - 3.6$ eV, while using the B acceptor as an empirical marker suggests that it lies at $E_v + 1.8$ eV. Again, these are within 0.1 eV of each other when considering the experimental bandgap. They are not too far from the estimate given by the FEM, and confirm the negative-U character of the system.

Taking the lowest-energy structure for each charge state in these level calculations implicitly assumes that the atoms can easily move between the ground-state structures. If this is not the case, the level has to be estimated by relaxing the positively charged system with its initial coordinates taken from the ground-state neutral structure. However, it was found that doing this made the donor shallower by only a few tenths of an eV.

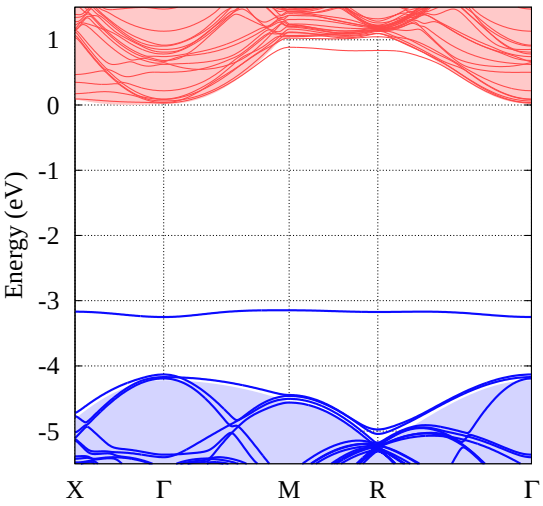

Figure 4.13: Electronic band structure for the neutral B–H_2 complex in a 216-atom supercell. The energy zero is the bulk diamond conduction-band minimum.

The electronic band structure for the most stable form of the neutral B–H_2 complex is shown in Fig. 4.13, as calculated in a 216-atom supercell. Clearly, the only defect-related level appearing in the band gap lies over 3 eV below the position of the bulk CBM, hence the picture is that of a very deep donor.

By contrast, another *ab initio* theoretical study on B–H_2 complexes in diamond (in which the cluster formalism was used) finds occupied defect-related states located only 1–2 eV below the conduction band, suggesting that B–H_2 is (qualitatively at least) a shallow donor [324]. The validity of this result can be called into question when considering that only very small, 35-C-atom clusters were used in the study — in fact, this cluster is known as the diamondoid molecule *superadamantane* — and so bulk diamond (and its conduction band) was most likely not modelled realistically. Furthermore, AIMview calculations on (pure) superadamantane performed for the present investigation indicate that the lowest unoccupied states in the system are mainly due to the surface C–H bonds, and not the 'bulk' diamond, casting doubt on the identification of the conduction band.

However, the most striking fault of the work of Ref. [324] is that the simple B–H defect is found to be an *acceptor*, even shallower than isolated substitutional boron. This finding is in stark contrast to the experimentally well-known passivation of boron acceptors by single atoms of hydrogen, hence the other results of the study may well be in error.

4.4.4 Other boron-hydrogen defects

The results presented here are part of a larger AIMpro study on boron-hydrogen complexes in diamond, detailed fully in Ref. [42]. Higher degrees of hydrogenation were considered, as well as the interaction of B and H with native defects, and the main findings of this further work will be summarised here.

B–H_3 and B–H_4 complexes

The first B–H_3 structures considered were all found to be much higher in energy than their potential separated components B–H and H_2^*, with even the lowest-energy form of B–H_3 being unstable with respect to this separation by around 4 eV.

However, a rather more stable form for B–H_3 was found by considering replacing a C–H pair with B in the stable H_4 complex predicted by previous AIMpro work [325]. The most likely dissociation path for the neutral B–H_3 structure so derived was found to be that into B–H_2 and H_i^+, although the activation barrier for this is large, at $\sim$ 4 eV.

Nevertheless, all of the B–H_3 complexes exhibited Kohn-Sham eigenvalues consistent with only very deep donor behaviour.

The results of modelling B–H_4 complexes were very similar. Firstly, the most stable arrangement of four equivalent H atoms around the B substitutional was found to be approximately 4 eV less stable than separated B–H_2 + H_2^*. Secondly, the most stable B–H_4 complex was obtained by replacing a C atom in the H_4 structure with boron. However, the 'fourth' H atom in this system is very weakly bound, since the (positively charged) complex can dissociate into B–H_3 and H_i^+ with an activation energy of only 0.9 eV.

Once again, the B–H_4 complex acts as a very deep donor, with the first-principles MM

suggesting that it has a (0/+) level at $E_v + 1.8$ eV (about $E_c - 3.7$ eV). Therefore, all of the B–H_3 and B–H_4 complexes considered were found to be deep donors, and most showed significant instability.

Boron-hydrogen complexes with native defects

It is possible that, in samples of high boron concentration, some of the boron may be present as interstitial atoms, or complexed with C (self-) interstitials or vacancies. Furthermore, the dangling bonds present in such centres are likely to interact with atoms of hydrogen.

The lowest-energy form of B interstitial was found to be that of a B–C split-interstitial aligned along [001], although a C interstitial adjacent to fourfold-coordinated *substitutional* B was found to be 0.25 eV lower in energy when neutral. The donor level of the latter was calculated using the first-principles MM to lie at $E_v + 2.2$ eV, with the former having a similarly deep donor level. Furthermore, the latter B–C_i defect has a very high formation energy, around 9 eV higher than that of isolated substitutional B.

When adding hydrogen to either form of the complex, it was found in all cases that the first H atom prefers to saturate a dangling bond on a C atom rather than attach to the B atom. For the lowest-energy, single-H structure found, there appears to be *no* donor level, and an acceptor level at $E_c - 1.9$ eV.

The addition of a second H atom is also most energetically favourable when it binds to the C interstitial rather than to the substitutional B atom. The binding energy for the reaction B–(C_iH) + H $\rightarrow$ B–($C_i H_2$) is calculated to be 2.4 eV. The complex so formed has only an acceptor level in the bottom half of the bandgap, which can be interpreted as the B acceptor level, perturbed by the presence of the C_i and H atoms.

The boron-vacancy complex has also been investigated, and it was found that the intimate B–V centre is bound by ~ 1.8 eV with respect to separated B and V. The defect appears to have an electronic structure similar to that of the well-studied N–V centre. From the bulk MM, B–V has an acceptor level at $E_c - 3.8$ eV and a donor level at $E_v + 1.1$ eV; the N–V complex has an acceptor at $E_c - 3.3$ eV and a donor at $E_v + 1.5$ eV [115].

As with the interstitial-related defects, H prefers to saturate the C dangling bonds rather than those of B. With either one or two H atoms added, the B–V complex has mid-gap acceptor levels, and donor levels only very close to the valence band. With three H atoms, all three dangling bonds of the vacancy are saturated, and the B–V–H_3 defect does not have a donor level, although a mid-gap acceptor level due to B remains. The binding energy per H atom in these complexes is very high at 6 eV, making them particularly thermally stable.

The binding of a fourth H atom to B–V–H_3 is much less favourable, at around 2 eV, and this B–V–H_4 defect has only very deep donor and acceptor levels.

4.4.5 Section summary

A wide range of complexes containing boron and several interstitial hydrogen atoms have been investigated using AIMpro. The most promising candidate for shallow donor behaviour, B–H_2, is not found to have shallow donor levels in any of the forms considered, and furthermore its stability is not consistent with the results of annealing experiments. Boron defects with three or four H atoms appear to be either passive or to exhibit only very deep levels. The same is true of complexes containing interstitial B or C with hydrogen, and similar defects containing a vacancy.

There is therefore no evidence from this modelling study that complexes of boron and hydrogen in diamond can give rise to shallow donor activity, and the results of additional experimental studies are required in order to get a better understanding of the apparent p-type to n-type conversion of certain samples.

4.5 Nitrogen-silicon complexes: Isovalent-donor coupling

In a theoretical work of 2003, the suggestion was made that a complex of N and Si substitutionals in diamond would be energetically stable, and give rise to a very shallow donor level [271]. The defect is composed of a N substitutional, surrounded by four Si substitutionals as its first neighbours. The shallow donor behaviour supposedly arises from level repulsion, whereby the occupied levels of the Si atoms increase the energy of the donor level on the N atom, making it a shallower donor.

In this section, the results of modelling this N–Si_4 complex with AIMpro are reported and compared against those from the original work. The calculations were all performed with the standard lattice parameter, sampling grid, *etc.* as described in previous sections.

4.5.1 Results

Structure

In the 64-atom supercell, the neutral complex adopted T_d symmetry from all of the starting positions, including one with a large initial off-site distortion for the N atom. In this supercell, the relaxed N–Si bond lengths were 107.1% of the bulk C–C length, while the Si–C bonds to second-nearest neighbours of the N substitutional were 111.0% of the bulk length.

However, in the 216-atom supercell, the randomised starting positions led to the discovery of a structure with lower energy than the T_d system, possessing approximate D_2 symmetry. A repeated calculation with 'exact' D_2 symmetry given to the initial coordinates underwent a relaxation to the same total energy.

In the N–Si_4 complex, one can define two planes as those containing: (i) the N atom and the 'upper' two Si atoms, and (ii) the N atom and the 'lower' two Si atoms. In the T_d structure, these planes are at 90 ° to each other, and are mirror planes. In the D_2 structure, these planes are slightly twisted toward each other, forming an angle $< 90\,°$, and are therefore no longer mirror planes. However, the three C_2 symmetry axes of the T_d structure remain. Nevertheless, the energy saving of this D_2 structure over the T_d

structure is small, at 20 meV. The relaxed D_2 structure is shown in Fig. 4.14.

The N–Si bonds in the D_2 structure are still equivalent, and relaxed to 107.3% of the bulk length. The three Si–C bonds on each Si atom are no longer equivalent: one is 113.1% of the bulk length, while the other two are 111.6%. The slightly longer bond lengths in the 216-atom supercell reflect the large strain that the complex exerts on the surrounding material, and the need for a large supercell to adequately contain such a defect.

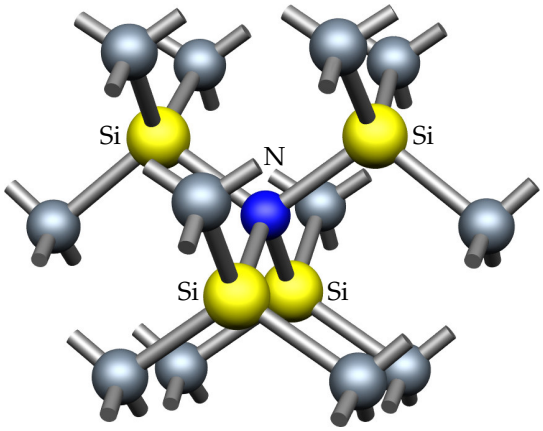

Figure 4.14: Relaxed atomic geometry for the N–Si_4 complex, from a 216-atom supercell. The symmetry-lowering distortion is not discernible.

Repeating the calculation once more with the symmetry of the initial coordinates *raised* from D_2 to D_{2d} gave rise to a structure with exactly the same total energy (to within the accuracy of the code) as the final D_2 structure. This suggested that the structure given initial D_2 symmetry in fact relaxed to a D_{2d} arrangement. A proper analysis using a brute-force symmetry-determination routine confirmed that it had indeed relaxed from D_2 to D_{2d} symmetry.

Minor structural changes aside, it appears that the compressive strain on the N substitutional arising from its four Si neighbours has prevented the atom from undergoing the pseudo-Jahn-Teller distortion to C_{3v} symmetry, as seen with the bare N substitutional. This has prevented its extra electron from lowering its energy and the centre from becoming a deep donor.

In the +1 charge state, the T_d symmetry was maintained, as intuitively expected, in both supercells. In terms of bulk C–C lengths, the N–Si bonds were 107.4% and the Si–C bonds were 110.8% in the 64-atom supercell, while in the 216-atom supercell the corresponding values were 108.4% and 111.7%.

Binding energy

The binding energy E_b of the N–Si_4 complex in diamond can be calculated using

$$E_\mathrm{b} = [E(\mathrm{N}) + 4E(\mathrm{Si}) - n_\mathrm{C}\,\mu_\mathrm{C}] - E(\mathrm{N\text{–}Si_4}), \tag{4.11}$$

where $E(\mathrm{N\text{–}Si_4})$ is the total energy of the diamond supercell containing the N–Si_4 defect, $E(\mathrm{N})$ is that of a similarly sized supercell containing the bare N substitutional, and $E(\mathrm{Si})$ is the same for the Si substitutional. μ_C is the chemical potential of a C atom in diamond, and in this case, the multiplier n_C is equal to four times the number of atoms in the supercells being used. Hence, the $n_\mathrm{C}\,\mu_\mathrm{C}$ term is equivalent to four times the total energy of a bulk supercell of the same size as those used in the defect calculations.

The results from the 64-atom supercells indicate that the N–Si_4 complex is bound by 3.04 eV, while those from the 216-atom calculations give a binding of 3.69 eV. The authors of the original paper quote a binding of 3.17 eV, from using a 128-atom supercell [271]. The significant difference in these figures exposes the shortcomings of using small supercells to model such a large defect. Nonetheless, the complex is strongly bound with respect to isolated substitutional species.

Electronic properties

The electronic band structure was calculated for the N–Si_4 complex with both T_d and D_{2d} symmetry in the 216-atom supercell, and a comparison in the region of the conduction band is shown in Fig. 4.15. In the T_d system, the highest occupied state is clearly degenerate with the lowest unoccupied state (at least at Γ, a point close to M, and for most of R $\rightarrow$ Γ), while in the D_{2d} system, the distortion has split the occupied and unoccupied levels by at least $\sim$ 0.1 eV throughout the BZ.

In both cases, the defect states lie very close to the conduction band (within 0.5 eV), and the highest occupied level shows about 0.4 eV of (peak-peak) dispersion. The only perturbation to the valence band states (not shown) occurs around the R point of the BZ, and is presumably due to the isoelectronic Si atoms.

The marker method with P was used to infer the donor level of the N–Si_4 complex. The 64-atom supercell results suggest that the level lies at $E_\mathrm{c} - 0.28$ eV, corresponding to an

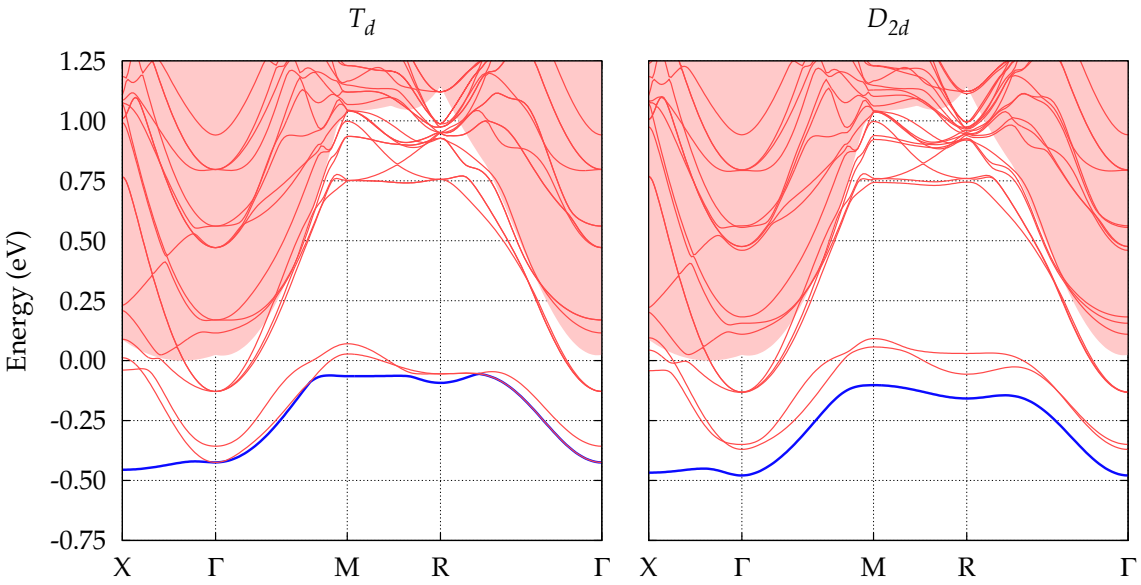

Figure 4.15: Calculated electronic band structures for the N–Si_4 complex in a 216-atom diamond supercell. In the left panel the defect has T_d symmetry, while in the right panel it has D_{2d} symmetry. The shaded regions represent the aligned conduction band of bulk diamond, while the zero of the energy scale is its minimum. Occupied and empty levels from the defect systems are shown as thick and thin lines respectively.

activation energy of around half that of P. However, in the 216-atom supercell, the donor level is much deeper, and very close to that of P, at $E_c - 0.62$ eV. Again, this discrepancy shows the weakness of using a 64-atom supercell for this defect.

These calculated donor levels are significantly deeper than the $E_c - 0.09$ eV predicted in the original work [271]. That result is perhaps compatible with regarding the defect as a nano-inclusion of (3C-) SiC in diamond, containing a substitutional N donor. The donor level of N in SiC is very shallow, at about $E_c - 0.05$ eV [326]. However, this 'inclusion' is diamond is very highly strained, as is evidenced by the expansion of the Si–C bonds (and the bond-length mismatch of $\sim$ 20% between 3C-SiC and diamond), hence it does not represent a bulk-SiC-like local environment for the N donor, and it should not be expected to show the same behaviour as substitutional N at a C site in bulk SiC.

Furthermore, the calculational method used in the original work is seen to underestimate the activation energies of the well-known defects P and N (respectively 0.38 and 1.59 eV, compared to the experimental 0.6 and 1.7 eV), whereas the present work has been shown previously to avoid this problem. It is therefore quite likely that the quoted 0.09 eV for N–Si_4 is also underestimated.

The N–Si_3 complex

The complexity of the N–Si_4 defect raises questions about its formation. It is therefore interesting to examine the properties of the 'partially formed' N–Si_3 version of the complex, where one of the first neighbours of the N atom is a normal C atom. When perfect (on–lattice-site) initial coordinates are used, this complex has C_{3v} symmetry, and it is envisioned that the N atom will distort along the N–C axis, most likely lowering the energy of its extra electron and becoming a deeper donor.

The N–Si_3 complex has been modelled in the 216-atom supercell, and the results of structural optimisation are shown in Fig. 4.16. As expected, the N atom is repelled by the large Si atoms and moves away from them in [111], toward the unique C atom. For the neutral complex, the N–C bond length is quite short, at 90.8% that of a bulk C–C bond, while the three equivalent N–Si bonds are elongated, at 111.2%. In the positive charge state the structure is very similar, although the distortion is not so dramatic, in that the N–C and N–Si bond lengths are respectively 93.9% and 110.6% of a bulk C–C length. In both charge states, random displacements of the initial coordinates did not lead to the formation of any other structures.

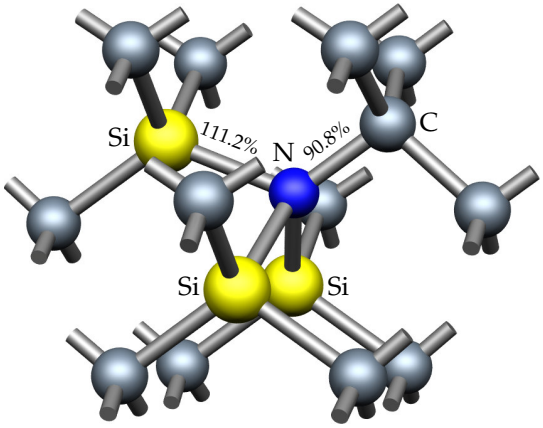

Figure 4.16: Relaxed atomic geometry for the N–Si_4 complex in a 216-atom supercell. The defect has C_{3v} symmetry, hence all N–Si bond lengths are equivalent.

Despite sharing the same symmetry, this distortion is significantly different to that of bare substitutional N in diamond, in that there the N atom moves away from a single C neighbour toward interstitial space (Fig. 4.4), while here it is pushed toward its unique C neighbour, shortening the N–C bond.

The calculated band structure for the C_{3v} N–Si_3 complex is shown in Fig. 4.17, and suggests that its donor level is quite deep. Comparison of total energies with those of substitutional P indicates that this donor level is located at $E_c - 1.11$ eV. This is about half an

electron-volt deeper than that of the complete N–Si_4 defect, and about half an electron-volt shallower than the level calculated for the bare N substitutional, placing the N–Si_3 level mid-way between these extremes.

4.5.2 Section summary

The N–Si_4 defect is a genuine donor in diamond, although it is not unambiguously a shallower donor than substitutional P. The defect is large, and causes considerable expansion of the diamond lattice, hence very large supercells are required to accurately model it within bulk-like material. The defect is expected to be stable, since it is bound by more than 3 eV, although its complexity means that it is not clear how it might be formed in large concentrations in practice. The 'partially formed' N–Si_3 defect appears to possess a deep donor level, and furthermore the 'empty' Si_4 component (where a C atom lies at the core instead of a N atom) is predicted to be unstable by itself [271].

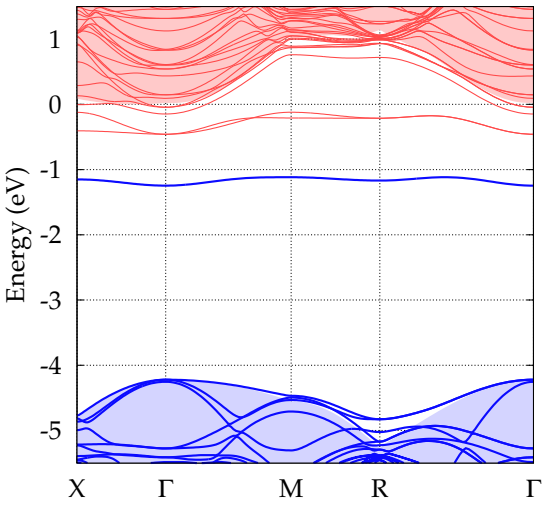

Figure 4.17: Electronic band structure for the N–Si_3 complex in a 216-atom supercell. The zero of the energy scale is the bulk diamond conduction-band minimum.

The results of the original work have most likely underestimated the activation energy of the N–Si_4 donor, by using supercells of insufficient size, together with a calculational method that consistently underestimates activation energies.

4.6 Chapter summary

The results of modelling a variety of point defects in diamond have been presented in this chapter. After confirming that the theoretical method accurately reproduces the structural and electronic properties of bulk diamond, defects that are currently considered to be candidates for shallow-donor behaviour were investigated.

First, the chalcogens, pnictogens, and their hydrogen complexes were studied, since these include defects that are known to behave as shallow donors in silicon. The results suggest that arsenic and antimony impurities can act as donors shallower than phosphorus, which is currently the most favoured dopant used in practice. While the size of the antimony atom may render its incorporation into diamond impossible, it may be that the smaller arsenic impurity could be introduced via the same mechanism of favourable surface chemistry by which phosphorus is grown into diamond. However, arsenic is likely to bind strongly to vacancies, which would remove its shallow-donor behaviour. Meanwhile, the chalcogen-hydrogen complexes only appear to behave as donors similar to, or deeper than substitutional phosphorus.

Next, the interaction of hydrogen with boron was studied with a view to explaining the shallow-donor behaviour recently observed in experiments on deuterated, boron-doped diamond samples. However, none of the many forms of boron-hydrogen complex modelled exhibited any signs of shallow-donor activity, while the stability of the most promising candidate does not match the experimental findings. Furthermore, no shallow donors were found by modelling interstitial boron and its complexes with hydrogen or vacancies. Therefore, the experimental results remain without a theoretical understanding.

Finally, a nitrogen-silicon defect suggested as a potential shallow donor has been critically studied. The most reliable results of the present modelling indicate that this complicated defect could only represent a donor with an activation energy comparable to that of the simple phosphorus substitutional. Indeed, the complexity of this defect raises serious doubts with regard to its formation in real material.

Chapter 5

Diamond surfaces

> "Nothing is rich but the inexhaustible wealth of Nature.
> She shows us only surfaces, but she is a million fathoms deep."
>
> — Ralph Waldo Emerson

- The work presented in this chapter has been published as Refs. [327, 328].

5.1 Introduction

SURFACES can be said to be the largest defects present in *every* real material. The transition from bulk material to vacuum, gas, or liquid overlayer inevitably introduces dangling bonds, impurity-atom termination, atomic reconstructions, electric dipoles, or at the very least unusual coordination of the atoms at the surface [329–332]. An understanding of the nature of a material's surface and its effect on the properties of the bulk is of great importance to those wishing to exploit that material's characteristics. In particular, the effect of the ambient atmosphere on surface properties — especially over time — is a factor to consider in the design of devices in many fields.

For diamond, the most technologically important surfaces are those with {001} and {111} orientations, as a consequence of the way that diamond crystals grow during the CVD process. Figure 5.1 shows a cross-section through a single diamond crystal during growth.

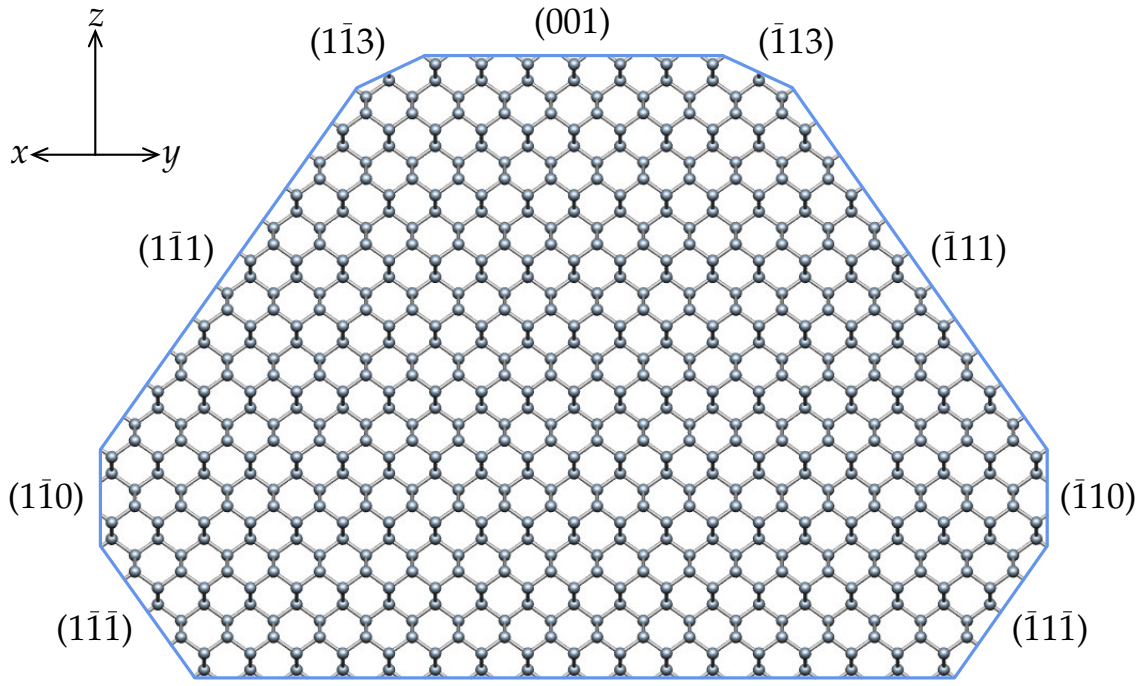

Figure 5.1: Schematic vertical cross-section through a single diamond crystal during the CVD growth process, with a magnified atomic structure shown within it. The x, y, and z directions are those of the conventional unit cell, and here z is the primary growth direction.

The exposed faces are those of {111}, {001}, {110}, and {113} sectors, with their surface areas decreasing in that order. The dominance of the {111} and {001} faces is due to the fact that these are the slowest-growing faces [333, 334], hence they remain behind once the faster-growing surfaces have grown themselves out of existence. For the same reasons, the randomly orientated crystallites in polycrystalline diamond films have predominantly {111} and {001} faces exposed. Another reason for the importance of {111} surfaces is the fact that *fracture* of diamond is dominated by cleavage on the {111} planes.

5.1.1 Surface dipoles

When diamond is terminated by an impurity species X, differences in electronegativity between atoms of C and X will lead to polarisation of the C–X groups on the surface. Thus $C^{\delta+}$–$X^{\delta-}$ or $C^{\delta-}$–$X^{\delta+}$ dipoles can be present, with the strength and sense depending on the relative electronegativities. Such dipoles essentially present either 'upward' or 'downward' ramps in electrostatic potential to charged species that approach the surface.

$C^{\delta-}$–$X^{\delta+}$ dipoles represent a downward ramp in potential that aids electrons attempting to escape from the bulk diamond out into vacuum, whereas $C^{\delta+}$–$X^{\delta-}$ groups on the surface serve to prevent electrons from being emitted. From an energy-level point of view, the strength and sign of the surface dipoles will determine a systematic *shift* in the energy bands for electrons in the material, with $C^{\delta-}$–$X^{\delta+}$ dipoles moving the energy levels upward with respect to the vacuum level (meaning that less energy is required to reach the vacuum states), and $C^{\delta+}$–$X^{\delta-}$ dipoles pushing the energy bands down.

5.1.2 Band bending

The phenomenon of *band bending* has important implications for the technological use of diamond in applications that exploit surface properties, such as electron emission. It refers to changes in the position of the electronic energy levels in the material as a function of distance from the surface.

In general, the presence of defect states in the bulk material and surface states at the edges promotes electron transfer and the creation of electric fields. Such fields will either encourage or discourage electrons from approaching the surface, in other words lowering or raising the energy bands toward the surface. The mechanisms are described more fully in Figs. 5.2 and 5.3.

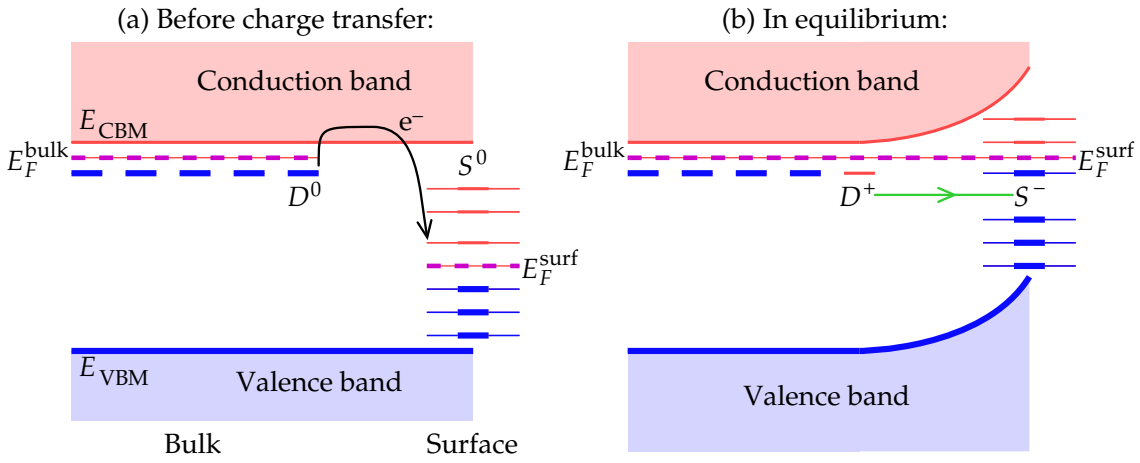

Figure 5.2: Schematic of the mechanism for band bending in n-type material. (a) The Fermi energies E_F of the bulk and surface regions of a material do not typically coincide, encouraging electron transfer from neutral donor impurities (D^0) to unoccupied surface-related states (S^0). (b) During charge transfer, an electric field is created between ionised donors (D^+) and the negatively charged surface (S^-), which causes the energy bands to bend upward toward the surface. This process continues until the bulk and surface Fermi levels are aligned and the system is in equilibrium (pictured).

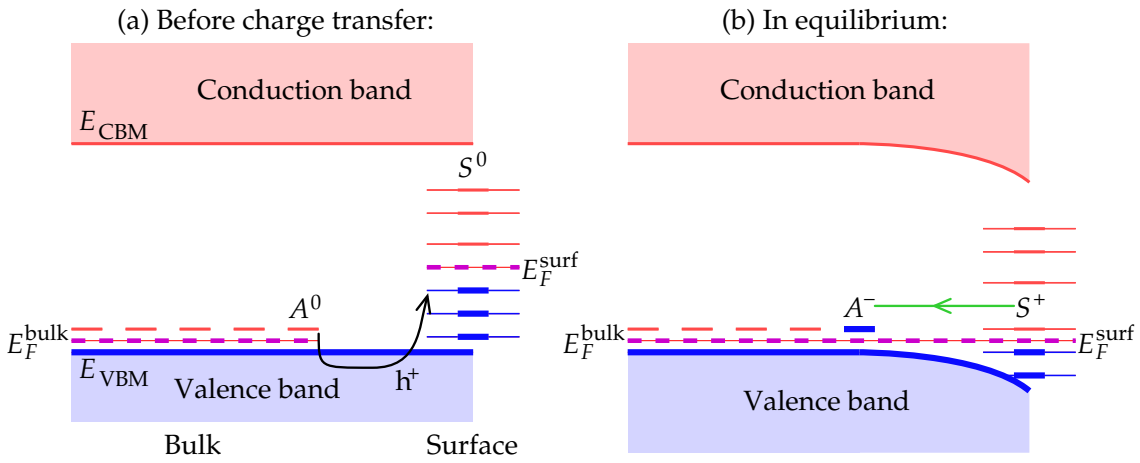

Figure 5.3: Schematic showing band bending in p-type material, which can be thought of as the 'mirror image' of the mechanism in n-type material. (a) Non-alignment of the bulk and surface Fermi energies causes multiple electronic transitions, equivalent to holes being transferred from neutral acceptor impurities (A^0) into occupied surface-related states (S^0). (b) During charge transfer, an electric field points from the positively charged surface (S^+) to the negatively charged acceptors (A^-) in the bulk, causing *downward* band bending to occur toward the surface. This continues until the bulk and surface Fermi levels come into alignment.

5.2 The effect of hydrogen and oxygen on diamond surfaces

It is well known that diamond surfaces can exhibit the phenomenon of *negative* electron affinity (NEA, Fig. 2.3(b)) [335–338] and possess low ionisation potentials (IPs), provided that they are covered by a layer of chemisorbed hydrogen. This property makes diamond a promising material for applications requiring electron emission, such as cold cathodes.

Hydrogen termination is also understood to be a prerequisite for the high *p*-type surface conductivity observed [60] on many diamond samples — a phenomenon that can be explained by the *transfer doping* model [57, 339–341]. In this scheme, the diamond valence-band maximum (VBM), raised in energy by the effect of the H termination, is close in energy to an unoccupied electronic state offered by an adsorbate material, such as the aqueous layer that forms on surfaces exposed to atmosphere. Electrons then flow from the diamond to the adsorbate, leaving behind a layer of accumulating holes that are responsible for the planar *p*-type conductivity. This mechanism is described in more detail in Sec. 6.1.2 of the next chapter of this thesis.

However, diamond surfaces terminated with *oxygen* exhibit large *positive* electron affinities (PEAs) and very large ionisation potentials [54, 55, 336]. Furthermore, photoemission spectra suggest that molecular oxygen is easily adsorbed onto any isolated carbon dangling bonds on a partially hydrogenated diamond (001)-(2×1) surface [342]. Therefore, knowledge of the interaction of oxygen and hydrogen on diamond surfaces is crucial for the effective manufacture of devices exploiting NEA or the transfer-doping effect, and in estimating the operational lifetimes of such devices.

In this part of the present investigation, the electronic and structural properties of the low-index surfaces of diamond with various terminations have been investigated using AIMpro, and the results are compared against those from other modelling work, and the results of experimental studies. The clean and hydrogen-terminated surfaces have been investigated for the (001), (110), and (111) surface orientations, while the effect of oxygen termination and its interaction with hydrogen have been investigated in detail on the technologically important (001) surface. First, the basic nature of the diamond surfaces will be discussed.

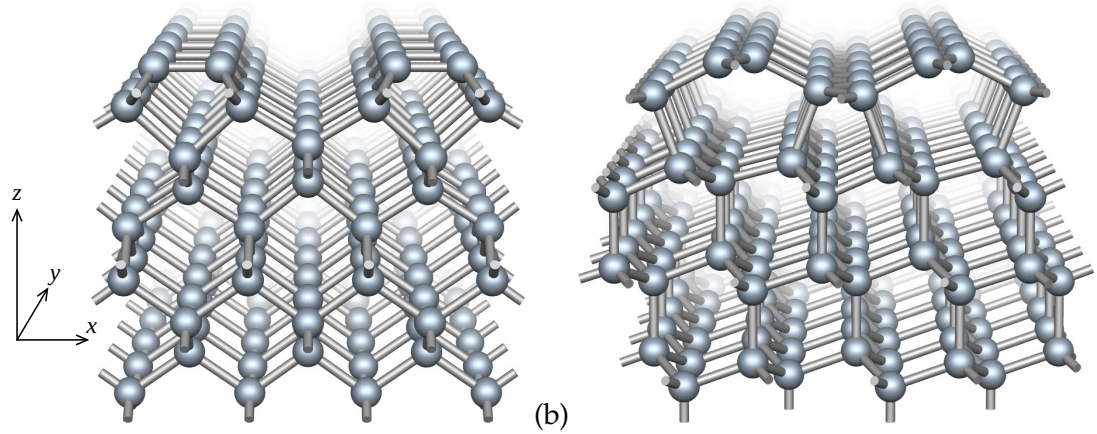

Figure 5.4: Perspective views of the atomic geometries for the most stable clean (001) and (111) diamond surfaces: (a) the (001)-(2×1) surface, where the uppermost C atoms form isolated dimers; and (b) the (111)-(2×1) Pandey-chain surface, in which the top two rows of C atoms form zig-zag chains extending into and out of the plane of the diagram. The axes in (a) refer to both diagrams.

5.2.1 Clean surfaces

On the clean (001) surface, neighbouring C atoms come together to form double-bonded (C=C) dimers, as shown in Fig. 5.4(a), which introduce occupied π and unoccupied π^* states into the bandgap of the electronic structure. Perpendicular to the bonds, the dimers are separated from one another by $1/\sqrt{2}$ of the conventional lattice parameter (*i.e.* by about 2.5 Å), and this (001)-(2×1) surface is non-metallic.

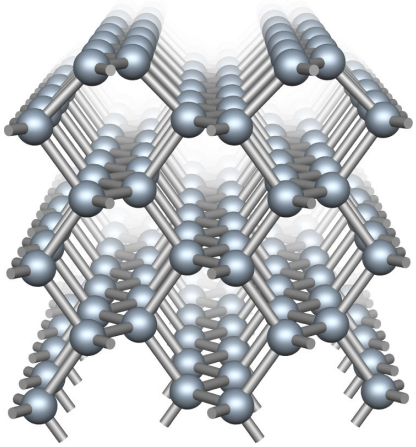

Figure 5.5: Perspective view of the stable atomic geometry for the clean (110) diamond surface, upon which no atomic reconstruction is required.

The clean (110) surface is notable in that it does not undergo any reconstruction, since the single dangling bond on each C atom simply contributes to the formation of a delocalised π network that extends along the zig-zag chain of bonded C atoms on this surface. This (110)-(1×1) surface, shown in Fig. 5.5, therefore shows semi-metallic behaviour.

To create surfaces with a (111) orientation, it is clear that bulk diamond can be cleaved in two distinct ways to expose two types of (111) surface: one in which each C atom possesses a single dangling bond (SDB) pointing exactly normal to the surface, and another in which each C atom is left with three dangling bonds (triple dangling bond, TDB). As intuitively expected, it requires less energy to break one bond per C atom than three, and so the SDB (111) surface has a lower surface energy than the TDB surface, hence it appears much more often in practice. This is the so-called *bond-scission* argument for surface stability.

The clean, SDB (111) surface is well known to exhibit a dramatic reconstruction to the *Pandey-chain* structure [343, 344] (Fig. 5.4(b)), in which it becomes more like that of the clean (110) surface. The exposed C atoms form upper and lower zig-zag chains that run in parallel across the surface. Since the uppermost of these atoms are only threefold coordinated, they share a delocalised π network running along the chain, causing this (111)-(2$\times$1) surface to exhibit semi-metallic properties.

The TDB form of the (111) surface undergoes a similar reconstruction, to *Seiwatz chains* [345, 346], which are equivalent to Pandey chains with the uppermost (π-bonded) C atoms removed (although doing this causes the new uppermost atoms to become π-bonded). However, even with reconstruction, this surface has a higher surface energy than the SDB Pandey-chain surface, and is therefore formed much less often in practice.

5.2.2 Hydrogenated surfaces

The mono-hydrogenated, (001)-(2$\times$1):H surface is widely accepted to be the most stable form of the hydrogen-covered (001) surface under normal conditions [347–349], and so this was the form studied in this work. The addition of hydrogen removes the π and π^* states from the electronic structure, as the surface dimers change from double (π) to single (σ) bonds.

Hydrogenation of the clean (110) surface is similarly straightforward: an H atom is simply attached to each of the uppermost C atoms, increasing their coordination from three to four, and thus removing the extended π network and the associated semi-metallic behaviour. This surface is denoted by (110)-(1$\times$1):H.

For the (111) orientation, mono-hydrogenation of both the (SDB) bulk-terminated and the Pandey-chain–reconstructed surfaces was investigated, these becoming respectively the (111)-(1×1):H and (111)-(2×1):H surfaces. Again, this hydrogenation will remove the semi-metallic nature of the reconstructed clean surface.

5.2.3 Oxygenated (001) surface

There are two most plausible configurations for oxygen on the (001) surface, neither of which involve surface reconstruction. These are: (a) the 'ketone' form, in which the O atom is double-bonded to a single surface C atom, with the axis of this carbonyl group normal to the surface; and (b) the 'ether' arrangement, in which the O atom bridges two surface C atoms and makes a single bond to each. The relaxed structures for these (001)-(1×1):O forms are shown later, in Fig. 5.18.

5.2.4 Hydroxylated (–OH-terminated) (001) surface

The presence of hydroxyl groups (–OH) on diamond surfaces has been demonstrated by organic chemical reactions, wetting angle measurements, and XPS [350]. The hydroxylated (001) diamond surface has been theoretically modelled before [56, 351], although the exact atomic geometry was not reported. In the present investigation, this surface has been investigated by attaching –OH groups to the (2×1) reconstructed (001) surface (in analogy to H termination), and performing relaxations with several initial coordinates for the O and H atoms.

5.3 Particulars of the method

5.3.1 General

The three surface orientations were modelled using a slab-supercell geometry (as mentioned in Sec. 2.11). Orthorhombic unit cells were devised such that when repeated by orthogonal $\vec{x}$, $\vec{y}$, and $\vec{z}$ lattice vectors (given in Table 5.1), slabs of diamond with infinite extent in the x, y-plane are formed, separated by layers of vacuum at least 25 Å thick in z.

Table 5.1: Orthogonal $\vec{x}$ and $\vec{y}$ lattice vectors along which unit cells of diamond are repeated to form infinite slabs with the z direction as the desired surface normal. a_0 is the lattice parameter of the conventional (cubic) unit cell for diamond, and the vector lengths from using $a_0 = 6.68$ a.u. are also given. Finally, the density of dangling bonds (DBs) for each clean, unreconstructed surface is shown.

Surface	$\vec{x}$	$\lvert\vec{x}\rvert$	$\vec{y}$	$\lvert\vec{y}\rvert$	**DBs: per atom**	**per area** a_0^2
(001)	$a_0\,(1,1,0)$	5.00	$a_0\left(\frac{\bar{1}}{2},\frac{1}{2},0\right)$	2.50	2	4.00
(110)	$a_0\,(0,0,1)$	3.53	$a_0\left(\frac{1}{2},\frac{\bar{1}}{2},0\right)$	2.50	1	2.83... $(2\sqrt{2})$
(111)	$a_0\left(\frac{\bar{1}}{2},\frac{\bar{1}}{2},1\right)$	4.33	$a_0\left(\frac{1}{2},\frac{\bar{1}}{2},0\right)$	2.50	1	2.31... $(4/\sqrt{3})$
					3	6.93... $(12/\sqrt{3})$

The supercells for all surface slabs contained 28 C atoms (forming 14 planes of diamond), plus any required atoms of H or O for modelling the various surface terminations.

This number of diamond layers and the thickness of the vacuum region are both larger than those used in many similar studies [56, 351–356], and gave well-converged total energies. In all cases, the 'upper' and 'lower' surfaces of the slab were reconstructed and terminated identically, in order to add either inversion or reflection symmetry to the system. Also, any modification made to the atomic geometry (such as changing the initial coordinates for structural relaxations) was the same on the upper and lower surfaces. This scheme helps to speed up the calculations, and also to avoid any spurious effects that might arise from the presence of C–H dipoles if the dangling bonds on the underside of the slab were to be saturated using H atoms.

Monkhorst-Pack grids [97] of special **k**-points were generated for sampling the Brillouin zone (BZ) of each system. Grid parameters were varied independently for each supercell until its total energy was converged to within 1×10^{-5} Ha ($\sim 3 \times 10^{-4}$ eV), and a grid of $8{\times}16{\times}1$ **k**-points was found to be more than sufficient to give converged total energies for all of the slab systems modelled. A grid of at least this density was used in all of the calculations.

System charge densities were Fourier-transformed using plane waves, as per usual. Total energies for all of the slab systems were converged to within 1×10^{-5} Ha when using a plane-wave energy cut-off of 300 Ha.

Atomic relaxations were performed via a conjugate-gradient scheme until the energy

change between subsequent iterations of structural optimisation became less than 1×10^{-5} Ha. In all cases, this criterion corresponded to the maximum force acting on any atom in the final iteration being less than 1×10^{-3} Ha/a.u.

For each system, the x, y-plane-averaged electrostatic potential was calculated as a function of position along the z axis (the normal to the surface planes), as described in Sec. 2.11.2. The value of the flat potential V_{vac} in the vacuum region was thus determined for each system, so that the electrical levels of different systems could then be compared by aligning their respective values of V_{vac}.

For all surface orientations, the plane-averaged potential was also calculated for a supercell of the same dimensions but containing only bulk diamond. The potentials were then compared with the corresponding potentials from the slab/vacuum system, so as to ensure that enough layers were present in the diamond slab to adequately represent bulk material toward the middle layers. Figure 2.4 of Chp. 2 in fact shows the potential plot for the (001)-(2×1):H surface, compared against that for bulk diamond filling a supercell of the same dimensions.

5.3.2 Electron affinity and ionisation potential

The method used for calculating the electron affinity (EA), ionisation potential (IP), and work function (WF) for each of the various diamond surfaces has been described previously, in Sec. 2.11.2. It is important to note that in practice, each of these quantities can be given as a surface-related or a bulk-related property, depending on whether the experimental method used probes surface-related electronic states, or the bulk energy bands deep in the material.

To first order, the EA for a semiconductor solid is the energy difference between the vacuum level and the lowest unoccupied bulk or surface state, while the IP is the difference between the vacuum level and the highest occupied (bulk or surface) state. In order to differentiate between the bulk/surface definitions, electron affinities χ and ionisation potentials I will be given as χ_{surf}, χ_{bulk}, I_{surf}, and I_{bulk}, where the surface quantities are calculated using the energies E_{HO} and E_{LU} taken from the band structure of the slab system, and the bulk quantities are determined using E_{VBM} and E_{CBM} derived from modelling bulk material and aligning electrostatic potentials (see Sec. 2.11.2 and Fig. 2.4).

5.3.3 Treatment of the vacuum region

Since this work makes use of localised (Gaussian) basis functions, which decay rapidly away from the atoms on which they are centred, it could be argued that the vacuum region in a slab calculation is incorrectly treated, as there are no basis functions available to model any electronic state that should exist in that region. This issue does not occur in simulations that use plane-wave basis functions, since such functions are not localised but rather extend over the whole supercell. Nevertheless, the treatment of electronic states in vacuum is not normally a matter of concern when modelling semiconductor surfaces, since the vast majority of materials have considerable positive electron affinities; that is, their conduction-band minima lie well below the vacuum level, and one is not typically concerned with states high above the CBM.

However, in the case of diamond, a negative electron affinity is expected for some surfaces, and it must therefore be ensured that there are sufficient basis functions present to model any unoccupied surface states having energies above or around the vacuum level, as they may extend significantly into the vacuum region in real space. Extra basis functions have been added into the vacuum region in these calculations by means of *ghost atoms*. These are atom-like entities that have zero nuclear charge and zero (*i.e.* flat) pseudopotentials, but that provide Gaussian basis functions centred on their coordinates. The ghost atoms used in this study were given 16 s- and p-like functions (with four exponents), and a cubic array of ghost atoms was created in the vacuum region of each surface slab. The exponents of the ghost-atom functions were adjusted so that a system containing just the cubic array of ghost atoms displayed a free-electron–like band structure; that is, a set of parabolic energy levels with the lowest starting from zero (the vacuum level) at the Γ point. The

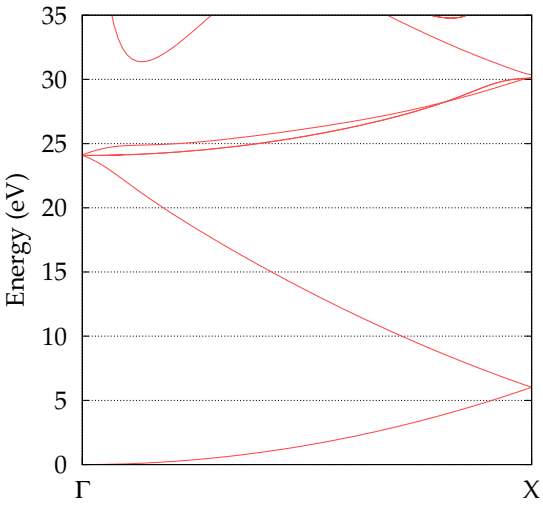

Figure 5.6: Calculated electronic band structure for an infinite cubic array of ghost atoms, created using one ghost atom in a cubic supercell of side length $a_0/\sqrt{2}$, where a_0 is the conventional lattice parameter of diamond.

calculated band structure for the purely ghost-atom system is shown in Fig. 5.6, and confirms that they provide free-electron states that are accurate (*i.e.* parabolic) over at least the first 20 eV above the vacuum level.

5.3.4 Correction to the calculated electron affinities

The use of Kohn-Sham density-functional theory is well known to lead to an underestimation in the energies of a system's excited states. As shown earlier in Sec. 4.2, band structure calculations performed for pure bulk diamond give an indirect bandgap of 4.22 eV, while experimentally this is measured to be 5.48 eV at low temperatures [9]. In addition, the calculated *direct* bandgap with this set-up is 5.66 eV, and experimentally it is around 7.3 eV [30–33].

It is apparent then that both experimental bandgaps can be recovered if the theoretical bandgaps are multiplied by a factor of around 1.3. Since both gaps involve the position of the diamond VBM (at the Γ point), this correction is equivalent to scaling the theoretical unoccupied states upward in energy, with reference to the VBM. It is also clear that a systematic upward *shifting* of the unoccupied states by a constant amount would not be as effective a correction. Furthermore, the upward shifting, or 'scissors operator', has been shown to be considerably less effective in correcting the band structure for diamond than in the case of other semiconductor materials [278].

Therefore, estimated surface electron affinities χ_{surf} have been calculated in this investigation by scaling the lowest unoccupied state in each surface system upward in energy, with reference to the bulk VBM, by a factor of 1.297. However, the electronic band structures are plotted without this correction.

In several other theoretical studies regarding the EA of diamond, the calculated conduction-band states are discarded rather than corrected, and the experimental bulk bandgap is added to the calculated VBM in order to give the position of the bulk CBM [56, 343, 351, 354]. This gives the same value for bulk electron affinities χ_{bulk} as the method used in this investigation, although it says nothing about the energies of any surface states and hence the value of the surface electron affinity χ_{surf}.

5.3.5 Surface dipole moments

A simple electrostatic dipole model can be used to calculate the difference in surface dipole moment Δp between two different surface terminations, once the difference in their bulk electron affinities $\Delta\chi$ is known [351].

The change in electrostatic potential $\Delta\phi$ when crossing from one side of an infinite sheet of electric dipoles to the other can be given by the relation

$$\Delta\phi = \frac{q_\mathrm{e}\, p}{\epsilon_0 A}, \tag{5.1}$$

where q_e is the charge on the electron, ϵ_0 is the electric constant, and p/A is the dipole moment per unit area of the sheet.

When considering two surfaces (say a and b) of the same material, that differ only in their reconstruction and termination, the difference between their values for $\Delta\phi$ will be the same as the difference in their bulk electron affinities, since all other sources of change in potential (such as the transition from bulk to vacuum) can be considered identical and will cancel. Hence, $\Delta\chi = \Delta\phi_b - \Delta\phi_a$, which gives

$$\Delta p = \frac{\epsilon_0 A}{q_\mathrm{e}}\Delta\chi, \tag{5.2}$$

in which $\Delta p = p_b - p_a$ is the sought-for difference in dipole moment between the two surfaces. The notional area A is necessarily the same in systems a and b, and in this work using the supercell x, y-area is appropriate.

In this way, the change in dipole moment Δp relative to that of the clean surface with the same orientation has been calculated for each surface termination. For the (001) surfaces the unit cell area A is 12.50 Å^2, for the (110) surfaces it is 8.84 Å^2, and for the (111) surfaces $A = 10.82$ Å^2 (see Table 5.1).

5.4 Results

The electronic band structure for each surface system has been calculated along a route in its BZ connecting the **k**-points defined in Fig. 5.8. Since in each case the $\vec{z}$ lattice vector is so large, its reciprocal lattice vector is small enough to remove the need to explore this

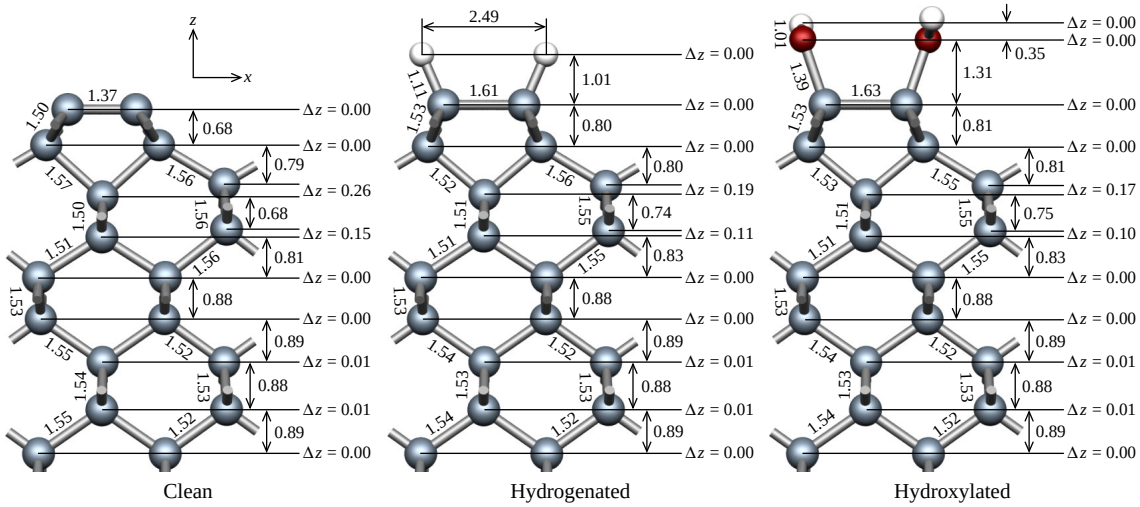

Figure 5.7: Optimised atomic geometries for the clean, hydrogenated, and hydroxylated (001)-(2×1) diamond surfaces, where the –OH surface is in its stable 'anti' configuration. Structural parameters include bond lengths, layer separations (with arrows), and layer bucklings (Δz), all given in Å. Unmarked bonds are symmetrically equivalent to other, marked bonds. Atoms are separated from their repeated images in the orthogonal y direction by 2.50 Å.

dimension in **k**-space. Note that the **k**-point labels are not appropriate to the conventional unit cell of diamond, nor do they refer to the same **k**-point across slabs of different surface orientation.

5.4.1 (001)-(2×1) clean surface

The most characteristic property of the standard structure for the clean (001) surface is the dimer bond length, and in these calculations it has a value of 1.37 Å (Fig. 5.7). This matches exactly the value found in other LDA-DFT calculations [354, 357]. Another notable feature of the structure is the *buckling* of the atomic layers. The buckling can be quantified by measuring differences in z coordinate (Δz) for the pairs of atoms that form each layer. Counting the C=C dimer as the first layer, only the third and fourth atomic layers show significant buckling, having Δz values of 0.26 and 0.15 Å respectively. This also means that the surface dimers are not tilted to any degree, unlike on the surfaces of silicon and germanium; again, this is standard.

The electronic band structure for the surface supercell can be seen in Fig. 5.8, where it is

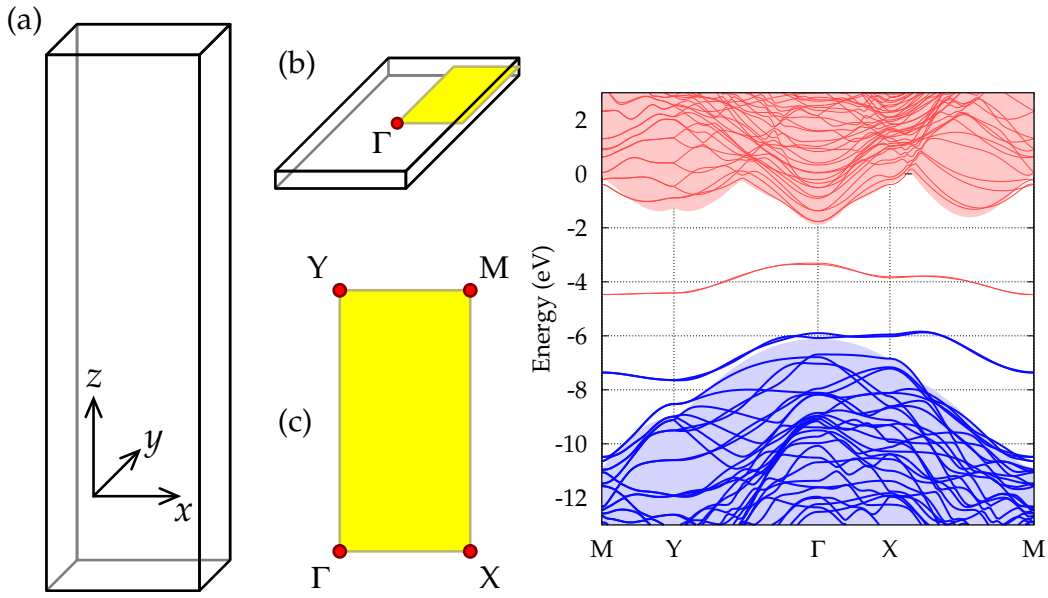

Figure 5.8: The labelling of **k**-points in band structure diagrams, and the appropriate plot for the clean (001) surface. The box in (a) represents the real-space supercell for a surface slab, and (b) shows its corresponding Brillouin zone. The irreducible portion is shown in (c) with **k**-point labels. On the right is the electronic band structure calculated for the clean (001) diamond surface. The zero of the energy scale is the vacuum level of the system. Occupied and unoccupied electronic levels are indicated by thick and thin lines respectively. The shaded regions represent the aligned band structure for a similar supercell containing only bulk diamond.

shown superimposed upon the band structure calculated for a supercell of bulk diamond. The π and π^* states arising from the double bond in the dimer of the surface system are conspicuous in the bandgap of the bulk material. The occupied π state rides along the top of the bulk conduction band at the Γ point, where the lower, bulk-like levels of the slab system have been perturbed downward in energy somewhat. The emergence of the occupied surface state into the bandgap and its heavy dispersion in regions away from the zone centre are in good qualitative agreement with results from angle-resolved photoelectron spectra [347].

From the bulk VBM, a value of $I_{\text{bulk}} = 6.11$ eV is obtained, while the maximum of the highest occupied *surface* state corresponds to a lower IP of $I_{\text{surf}} = 5.85$ eV. The CBM lies well below the vacuum potential, and when the upward scaling correction is applied, it corresponds to $\chi_{\text{bulk}} = +0.64$ eV. This value is very close to the 0.69 eV obtained in previous theoretical work in which 10-layer slabs were used [351]. The minimum of the lowest unoccupied slab state (on the π^* state at the M point) lies much lower than the

CBM, and gives rise to a large EA of $\chi_{\mathrm{surf}} = +3.99$ eV for this surface, after correction.

5.4.2 (110)-(1×1) clean surface

Since the clean (110) surface does not undergo any reconstruction, the only atomic relaxation that occurs is movement of the uppermost C atoms (since they are not tetrahedrally coordinated, but rather support the delocalised π network running along the zig-zag chain), and shifting of the top few layers of material in the z direction (normal to the surface).

In the plane of the surface, the C–C bond length on the uppermost layer (*i.e.* along the zig-zag chain) contracted to 1.42 Å, or 92.9% that of a bulk C–C length, while on the second layer (in which the C atoms are approximately tetrahedrally coordinated), the bond length along the chain is 1.49 Å, or 97.6% of a bulk length. The corresponding bonds in the third, fourth, and fifth layers from the surface are respectively 99.8%, 99.9%, and 100.0% of a bulk C–C length.

In the direction normal to the surface, the uppermost C atoms have moved downward (toward the bulk material) by 0.17 Å relative to their initial (perfect bulk) positions, while the atoms of the second layer have in fact moved upward, by about 0.03 Å. The third and deeper layers have essentially remained in their bulk-like positions.

To investigate the possibility of *dimerisation* on the clean (110) surface, the atomic coordinates from the relaxed system were taken, and a symmetry-breaking dimerisation was created by moving the uppermost (and lowermost) C atoms in $\pm y$ so that alternating C–C bond lengths along the zig-zag chains were 1.33 and 1.52 Å rather than the aforementioned 1.42 Å. All atoms in the system were then allowed to relax. However, no evidence for dimerisation was found, since the atoms relaxed back to their original positions (giving equivalent 1.42 Å bonds in the chain), while the final total energy was identical to that of the previous calculations.

This test was repeated with a greater degree of dimerisation given to the initial coordinates (bond lengths of 1.15 and 1.71 Å), and the results were the same, in that the bonds relaxed to 1.42 Å, and the total energy was exactly the same as before. Therefore, this model does not support dimerisation on the clean (110) surface.

The electronic band structure for this clean (110) surface is shown in Fig. 5.9. The energy bands of bulk diamond align very well with the levels from the surface slab, and the VBM corresponds to $I_{\text{bulk}} = 6.68$ eV. When corrected for the underestimated bandgap, the bulk electron affinity $\chi_{\text{bulk}} = 1.21$ eV.

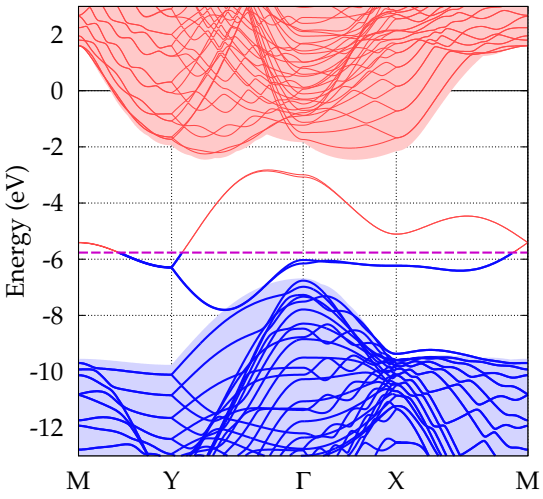

Figure 5.9: Electronic band structure calculated for the clean (110) diamond surface. The zero of the energy scale is the vacuum level, while the Fermi level is shown as a horizontal dashed line.

The semi-metallic nature of this surface is immediately apparent, since the π and π^* states meet at the Y and M points, and are degenerate along the M→Y portion of the route around the BZ. Since this surface is semi-metallic, the surface ionisation potential and electron affinity are equal, and equivalent to the work function. This is given by the position of the Fermi level with respect to the vacuum potential, and in these calculations $I_{\text{surf}} = \chi_{\text{surf}} = 5.77$ eV.

5.4.3 (111)-(2×1) clean surface

The Pandey-chain–reconstructed (111) surface (Fig. 5.10(a)) was found to be lower in energy than the unreconstructed (1×1) surface by 0.80 eV per surface C atom, in good qualitative agreement with experiment. Further calculations showed that the unreconstructed clean surface was metastable, although with the barrier to reconstruction to the Pandey chains being very small; random displacements of the C atoms on the (1×1) surface by as little as 0.1 Å proved enough to cause reconstruction to the (2×1) structure. This agrees well with other DFT calculations that do not find a significant energy barrier to this reconstruction [343]. However, the finer details of the structure of the Pandey-chain surface are still a matter of debate, hence they deserve further attention.

The uppermost zig-zag chain of threefold-coordinated C atoms shows a very small degree of dimerisation; alternate C–C bonds along the chain have lengths of 1.428 and 1.429 Å. However, these differences are most likely to be remnants of the aforementioned random initial displacements and the tolerance for stopping structural optimisation, and

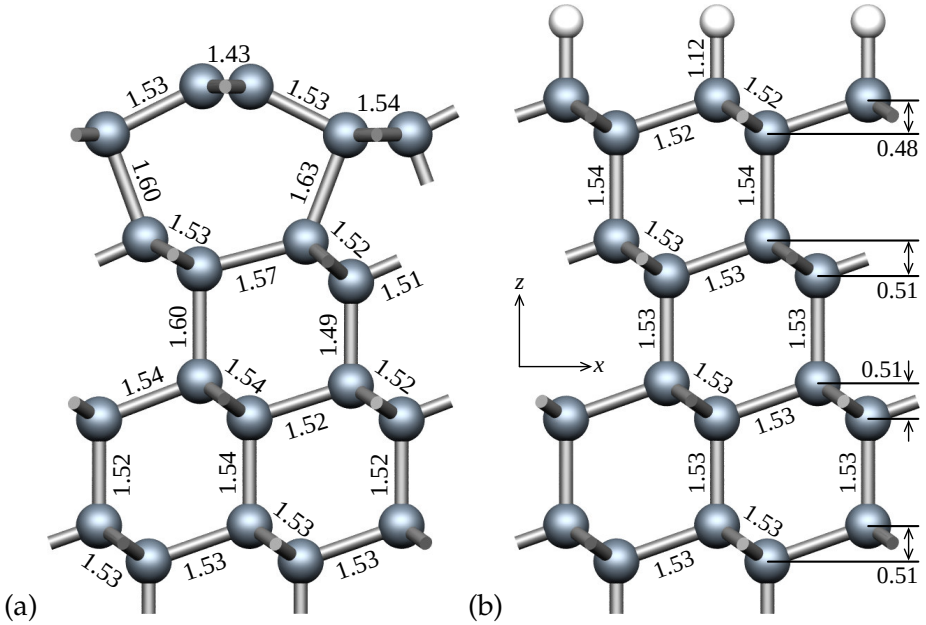

Figure 5.10: Relaxed atomic geometries for the (111) diamond surface, with: (a) no adsorbate coverage and the Pandey-chain reconstruction; and (b) hydrogen termination without reconstruction. Bond lengths and layer separations are in Å.

are not significant. By comparison, the fourfold-coordinated C atoms along the lower surface chain are equally separated, by 1.54 Å; this being very close to the bulk bond length of 1.53 Å found in these calculations. These chain bond lengths are in complete agreement with the corresponding values of 1.43 and 1.54 Å found in other theoretical work [343], and are essentially the same as the 1.44 and 1.55 Å given in another study [352].

To check for the possible formation of dimers, the calculation was repeated by adding a deliberate dimerisation to the relaxed chains and relaxing the system again, as was done with the (110) surface. The given initial coordinates corresponded to alternating bond lengths of 1.16 and 1.71 Å along the upper zig-zag chain. The system immediately relaxed to yield upper-chain bond lengths of 1.427 and 1.429 Å, with a total energy essentially identical to the previous, non-dimerised result. Therefore, no evidence for dimerisation in the Pandey chains has been found, in accordance with several other theoretical studies on this surface [343, 358, 359].

The upper and lower zig-zag chains of the relaxed system are not significantly tilted, in that the pairs of atoms have very similar z coordinates. However, at least one experimen-

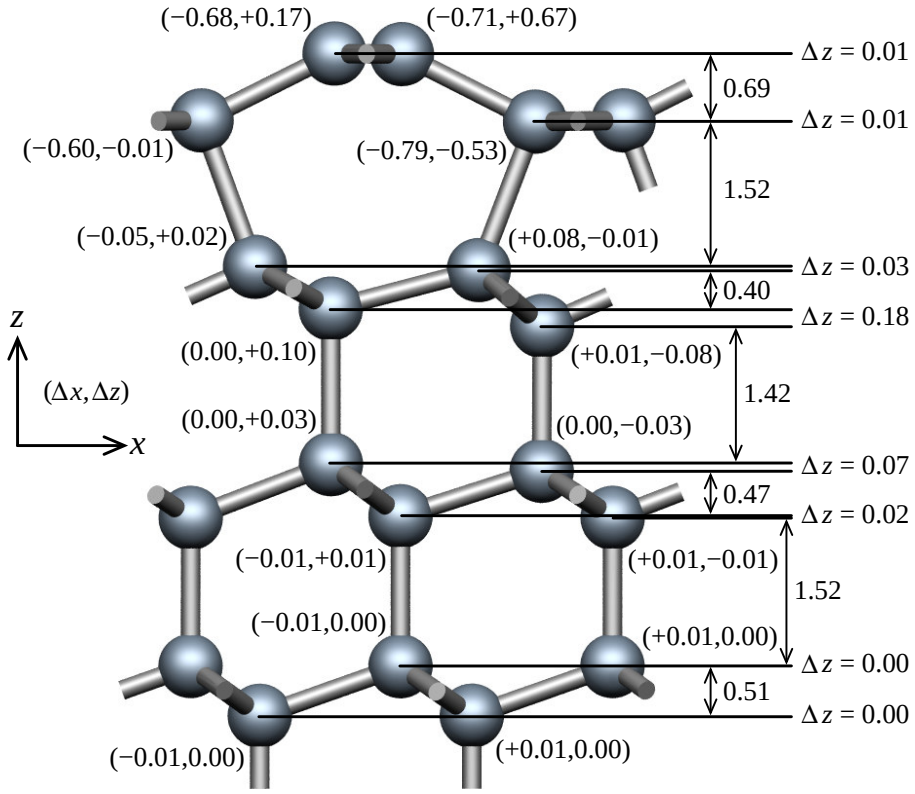

Figure 5.11: Structural parameters for the clean (111) diamond surface. The labels in parentheses indicate how far each atom has moved from its ideal (bulk) position in the x and z directions. Interlayer separations are marked with arrows. On the right, differences in z-position for pairs of atoms are given to indicate buckling in the layers. All distances are given in Å.

tal study using X-ray diffraction has presented evidence for tilting of these chains [360]. In the model given as a best fit to the experimental data, the C atoms of the upper chain are separated by $\sim$ 0.3 Å in the z direction, while those of the lower chain differ in z-height by about 0.1 Å. To explicitly check for the presence of any tilting, the present calculations were repeated using the best-fit model from the experimental study [360] as starting coordinates. However, the system relaxed back to the same, non-tilted atomic geometry as found previously, and essentially the same total energy. The present study therefore supports the several other theoretical investigations that find these chains to be flat [343, 352, 358, 359].

The degree of buckling in the monolayers of this system is also of interest. Where the upper and lower zig-zag chains are counted as the first two layers, it is the buckling in the fourth and fifth layers that is the most controversial. The results of the present investiga-

tion are reported in Fig. 5.11, where it can be seen that the buckling in the fourth and fifth layers is significant, corresponding to Δz values of 0.18 and 0.07 Å respectively. These compare very well with the values of 0.17 and 0.06 Å given in other DFT work [343]. All other layer bucklings are small, with $\Delta z \leq 0.03$ Å, while the seventh and eighth layers are almost perfectly bulk-like. It should be noted though that these are the middle two layers of the slab, which are symmetrically equivalent. However, even though all atoms in the system were allowed to relax, the most distorted C–C bond across these two central layers is still 100.3% of a bulk length.

The calculated electronic band structure (Fig. 5.12) shows the expected semi-metallic nature of the clean (111) surface, with gap states existing throughout the BZ, and the Fermi level intersecting the surface states about 0.8 eV above the bulk diamond VBM. The very small dimerisation of the upper chain is thought to be responsible for the small energy splitting in the surface state, just above the Fermi level, around the M point of the BZ. From the bulk VBM, the ionisation potential $I_{\text{bulk}} = 5.83$ eV, while the scaled bulk CBM corresponds to $\chi_{\text{bulk}} = +0.35$ eV. Since the surface is semi-metallic, the surface IP and EA are equal and equivalent to the work function: $I_{\text{surf}} = \chi_{\text{surf}} = 5.01$ eV.

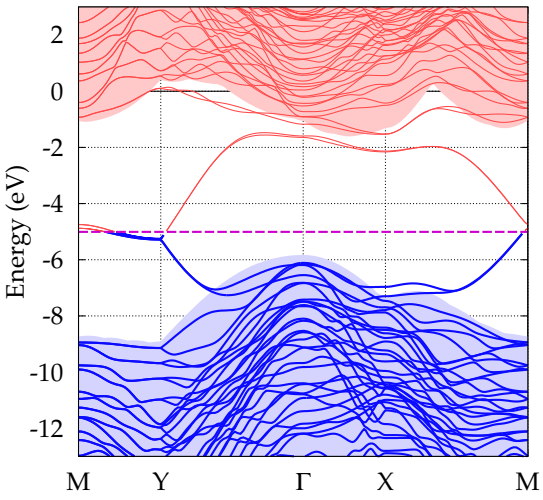

Figure 5.12: Electronic band structure calculated for the clean (111) diamond surface, with Pandey-chain reconstruction. The zero of the energy scale is the vacuum level, while the Fermi level is shown as a horizontal dashed line.

5.4.4 (001)-(2×1):H surface

The relaxed bond length of the *hydrogenated* C–C dimer is 1.61 Å, and the difference with the 1.37 Å of the clean-surface dimer reflects the change in the nature of the dimer bond. This value agrees very well with other theoretical work [354] and the value of 1.60 ± 0.05 Å determined by low-energy electron diffraction [349]. Comparison of total energies suggests that this hydrogenated (001) surface is favoured over the clean surface plus distant gas-phase H_2 molecules, by 2.1 eV per surface C atom. This is in excellent

agreement with the 2.05 eV calculated in other work [354].

Electronically, hydrogen termination has caused the bulk energy bands to move upward by about 2.5 eV from their positions with the clean surface (Fig. 5.13). It is this effect that corresponds to a low IP and a NEA for the hydrogenated surface. The highest occupied state in the hydrogenated surface slab has been perturbed near the zone centre so that it lies just below the bulk VBM. AIMview analysis reveals that this state has a wavefunction with maximum amplitude in the bulk-like region (Fig. 5.14(a)). This perturbation of the valence band at the surface corresponds to $I_{\text{surf}} = 3.97$ eV, while $I_{\text{bulk}} = 3.57$ eV.

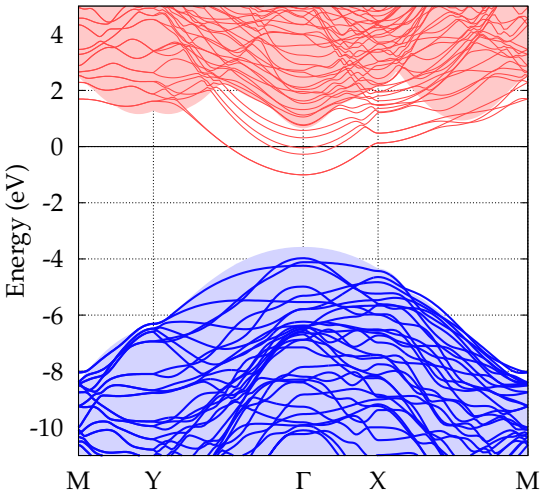

Figure 5.13: Electronic band structure calculated for the hydrogen-terminated (001) diamond surface.

However, the most striking feature of the band structure is the collection of unoccupied states that swoop below the bulk conduction band around the Γ point. The minimum of the lowest unoccupied surface state is nearly 2 eV below the bulk-diamond CBM. Note that while the CBM of bulk diamond is observed just over 70% of the way from Γ to the X point, it appears at the Γ point (sometimes denoted the $\overline{\Gamma}$ point) of this *surface* BZ due to folding.

Analysis of the wavefunction for this state at Γ (Fig. 5.14(b)) indicates that it is composed of *p*-like orbitals centred on the C atoms of the surface dimer. The axes of these orbitals coincide with the axes of the C–H bonds, and their lobes on the bulk side of the dimer show significant overlap. Therefore, this state is characteristic of σ C–H bonds with a small degree of π bonding along the C–C dimer. These findings support those of other *ab-initio* DFT calculations performed on the hydrogenated (001) diamond surface [354]. By scaling this state upward with respect to the VBM, the surface-related electron affinity χ_{surf} is estimated to be $+0.24$ eV.

The second-lowest unoccupied state has a wavefunction with its greatest magnitude in

the vacuum region of the supercell (Fig. 5.14(c)), although there is also a small component located on the hydrogenated dimer. This state is therefore free-electron–like, although some mixing with the surface states has lowered its energy, enough to bring its minimum below the vacuum level. The next three unoccupied states higher in energy also show wavefunctions with mostly free-electron character and small components along the C–H bonds.

The next unoccupied surface state at higher energy lines up with the conduction band from the bulk system almost perfectly, and indeed wavefunction analysis (Fig. 5.14(d)) confirms that it is due to atoms in the bulk-like region of the slab. The corrected value for the bulk electron affinity $\chi_{\text{bulk}} = -1.90$ eV, which is close to the values around -2 eV found in other theoretical work [56, 351], in which the experimental bandgap was added to the position of the VBM. It is interesting to note that since the lowest unoccupied *bulk-related* state is higher in energy than several vacuum-related states, the negative-electron-affinity nature of this surface has been demonstrated without having to refer to the vacuum level.

These results are in decent qualitative agreement with the NEA measured on the (001)-(2×1):H diamond surface by means of ultraviolet photoelectron spectroscopy [361], which probes the near-surface region.

5.4.5 (110)-(1×1):H surface

The effects of hydrogen termination on the structure of the clean (110) surface are mainly a change in the length of the uppermost C–C bonds and movement of the atomic layers in the z direction.

The C–C bond length in the first layer changes from 1.42 to 1.51 Å after H atoms are attached, again reflecting the change in nature of the C–C bonding. The C–C bonds in the second layer are now 1.53 Å in length, or 99.8% of a normal bulk bond length, whereas on the clean surface, this value was 97.6%.

The relaxation of the layers in the z direction almost brings the atoms back to their positions in ideal bulk material. The surface C layer is only 0.02 Å below its position in bulk material, while the displacement of the second layer from its bulk position is a fac-

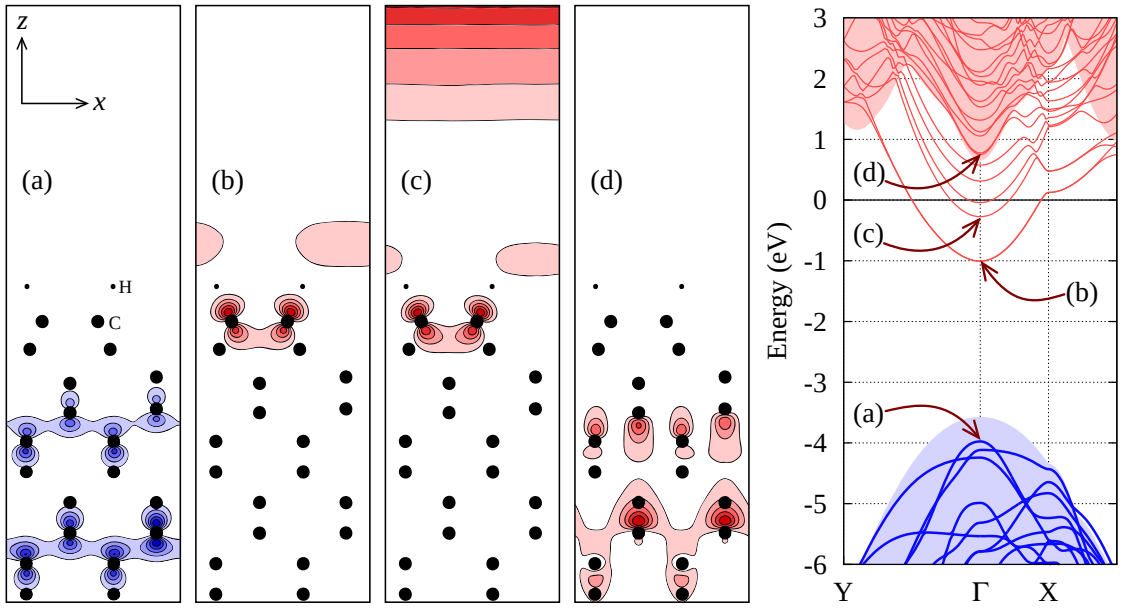

Figure 5.14: Wavefunction visualisation for the (001)-(2×1):H diamond surface. (a) Plot of the absolute-squared value of the wavefunction ($|\psi|^2$) at the Γ point for the highest occupied electronic state in the slab system. Carbon and hydrogen atoms are represented by large and small black circles respectively, and the view is the same as that in Fig. 5.7. Black contours join points of equal $|\psi|^2$ value and enclose regions in which greater shading intensity represents higher value. (b) Similar plot for the lowest unoccupied state in the system. (c) Plot for the second-lowest unoccupied state, which shows a large wavefunction component in the vacuum region. (d) Plot for the lowest *bulk-like* unoccupied state, which is about 1 eV higher in energy than the lowest vacuum-related state. On the right, the band structure around Γ is displayed without any corrective scaling, and the points corresponding to the wavefunction plots are indicated. The zero of the energy scale is the calculated vacuum level for the system.

tor of ten smaller. The atoms in the third and lower layers are essentially in their ideal positions.

This structure is the most bulk-like of all of the surface systems studied, and the alignment of its electrostatic potential with that of bulk diamond is correspondingly excellent (see Fig. 5.15). Furthermore, the potential in the vacuum region converges quickly with distance from the surface and is notably flat. Therefore, the accuracy in calculating the EA and IP of this surface is likely to be particularly high.

The calculated electronic band structure for the (110)-(1×1):H surface is shown in Fig. 5.16(a). The features immediately resemble those seen in Fig. 5.13 for the hydrogen-terminated (001) surface: the valence band states are perturbed only slightly in the slab system, while

many new unoccupied states appear beneath the bulk conduction band, with these having approximately parabolic forms around the zone centre. As with the (001)-(2×1):H surface, AIMview analysis confirms that the highest occupied level is bulk-like, while the lowest unoccupied level is due to the surface C–H bonds; see Fig. 5.16(b) and (c). The parabolic levels between the unoccupied C–H-related state and the CBM are once again vacuum-related states, formed with the help of the ghost atoms.

The slab and bulk valence bands are very similar, and correspond to ionisation potentials of $I_{\text{surf}} = 3.11$ eV and $I_{\text{bulk}} = 3.04$ eV; the small difference reflecting the minimal disturbance that hydrogen termination causes to the structure of this system. These values are significantly smaller than the respective values of 3.97 and 3.57 eV found for the hydrogen-terminated (001) surface, which suggests that the z-component of the $C^{\delta-}$–$H^{\delta+}$ dipole layer is greater on the (110)-(1×1):H surface than it is on (001)-(2×1):H. This is consistent with the fact that the exposed surface area is smaller in the (110) supercell than in the (001) supercell, hence the dipole density is greater on (110):H. On the hydrogen-terminated (001) surface, there is one $C^{\delta-}$–$H^{\delta+}$ dipole per 6.25 Å^2 of surface area, while on (110):H there is one dipole per 4.42 Å^2 of area.

Furthermore, in the relaxed structures the C–H bonds are orientated at 66.6 ° to the surface plane on the (001) surface, but at only 56.5 ° on the (110) surface; that is, the C–H bonds are closer to the surface normal on (110), which serves to increase the z-component of the dipole. However, this argument assumes that the degree of $C^{\delta-}$–$H^{\delta+}$ polarisation is the same on both surfaces (although the C–H bond length is indeed the same, at 1.11 Å).

Despite the fact that the ionisation potential is low on (110)-(1×1):H (*i.e.* the energy bands are high with respect to the vacuum level), the unoccupied C–H-related surface state extends deep below the CBM, and as far as mid-gap (although of course it is surely underestimated by the theory), and so the *surface* electron affinity is still significantly positive; even with the scaling correction, the minimum of this state remains below vacuum, and $\chi_{\text{surf}} = +0.42$ eV. By comparison, the scaled bulk CBM lies well above vacuum, and corresponds to the largest NEA found in this investigation, at $\chi_{\text{bulk}} = -2.43$ eV.

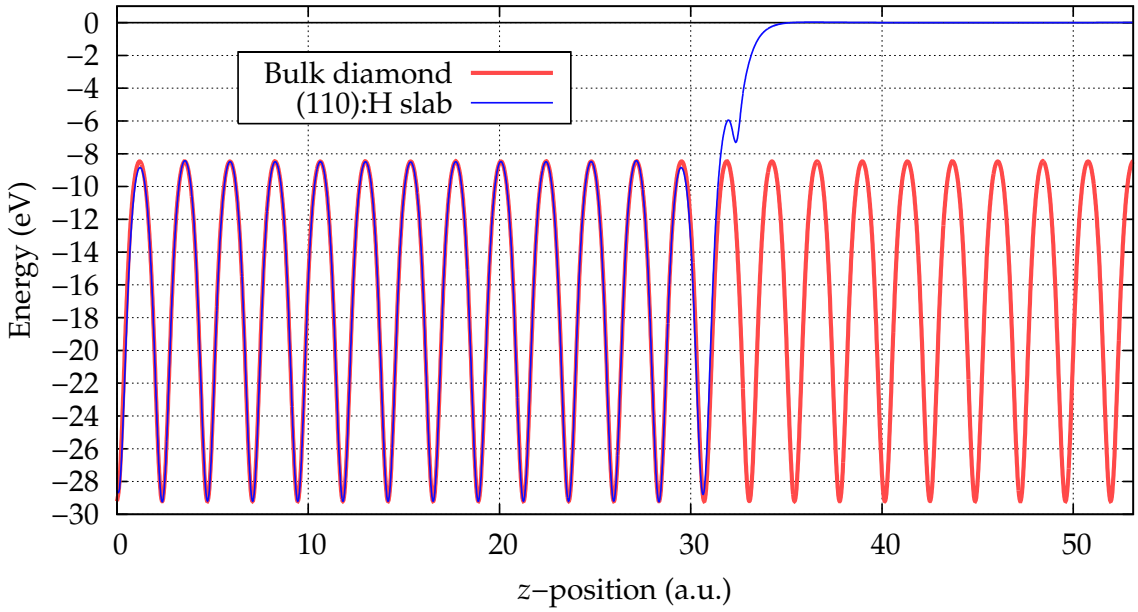

Figure 5.15: Plane-averaged electrostatic potentials for the (110)-(1×1):H diamond surface and bulk diamond. The zero of the energy scale is the vacuum level found from the surface system, while the potential of bulk diamond has been aligned with that found in the middle of the slab. Only half of the vacuum region is shown.

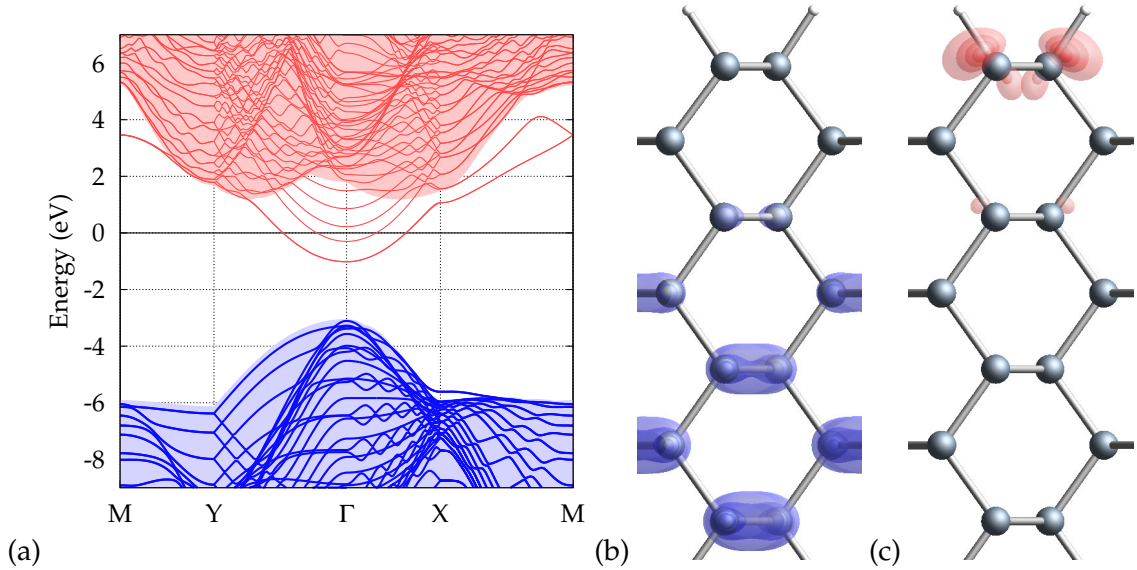

Figure 5.16: Properties of the hydrogen-terminated (110) diamond surface. Plot (a) shows the electronic band structure with the energy zero as the vacuum level, and the relaxed atomic geometry is shown together with isosurfaces of the absolute-squared wavefunction for: (b) the highest occupied electronic state, and (c) the lowest unoccupied state, both as sampled at the Γ point.

5.4.6 (111)-(1×1):H surface

Hydrogen saturating the single dangling bonds on the unreconstructed (111) surface (Fig. 5.10(b)) was found to be more energetically stable than H bonding to the topmost atoms on the Pandey-chain reconstruction, by 0.70 eV per surface C–H pair; this being in very good agreement with the 0.694 eV calculated in other work [343], and with experiment [362]. The hydrogen termination and lack of reconstruction means that there is very little disturbance caused to the lower layers of diamond, as shown in Fig. 5.10(b); only the uppermost double layer of C atoms appears to be perturbed. As a result, the electrostatic potential of this system lines up particularly well with that of bulk diamond, hence there is a very low error in aligning the band structure of this surface with the bulk bands.

The electronic structure of the (111)-(1×1):H surface (Fig. 5.17) is very similar to that of the the hydrogenated (001) and (110) surfaces, in that H coverage removes the bandgap states of the clean surface and introduces unoccupied states that pass below the conduction band around the Γ point. Analysis of the wavefunctions for the surface states confirms that the situation is very similar to that seen in Figs. 5.14 and 5.16, in that: the highest occupied electronic state exists in the bulk diamond; the lowest unoccupied state is formed from p orbitals on the surface C atoms with axes along the C–H bonds; the next four unoccupied states higher in energy exist mainly in the vacuum region but have small components on the C–H bonds; and the next state up exists almost entirely in the bulk-diamond region of the slab. Again, the character of these states and their ordering in energy confirms the NEA of the hydrogenated surface without the need to refer to a vacuum level.

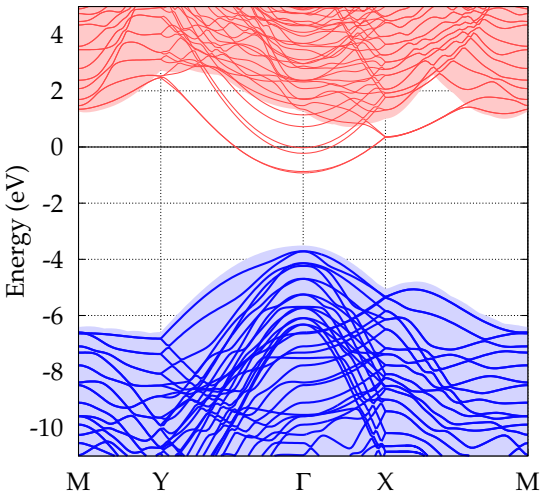

Figure 5.17: Electronic band structure calculated for the (111)-(1×1):H system, which is the most stable monohydrogenated (111) surface.

The bulk bands correspond to $I_{\text{bulk}} = 3.51$ eV and $\chi_{\text{bulk}} = -1.97$ eV, while the extrema of

the surface states correspond to $I_{\mathrm{surf}} = 3.71$ eV and $\chi_{\mathrm{surf}} = +0.15$ eV. With the exception of the surface IP, these are all within 0.1 eV of the corresponding values calculated for the hydrogen-terminated (001) surface. The $C^{\delta-}$–$H^{\delta+}$ dipole density on this surface is in-between those of the hydrogenated (001) and (110) surfaces, at one $C^{\delta-}$–$H^{\delta+}$ dipole per 5.41 Å^2 of surface area.

5.4.7 (001)-(1×1):O surface

The relaxed atomic geometries for the 'ketone' and 'ether' forms of oxygen termination on the unreconstructed (001) surface are shown in Fig. 5.18. The 'ether' arrangement was found to be more stable than the 'ketone' configuration by 0.61 eV per O atom. While this ordering in stability would not follow from a simple chemical argument based on bond enthalpies, the result agrees with the ordering and 0.50 eV difference calculated in other theoretical studies [56, 351].

On the relaxed 'ether' surface, the plane of oxygen atoms lies 0.80 Å above the surface carbon layer (Fig. 5.18(b)), which is in decent agreement with low-energy electron diffraction studies favouring the 'ether' arrangement and a C–O layer separation of 0.72 Å [349]. For comparison, the layer separation found on the 'ketone' surface (that is, the C=O bond length) in the present work is 1.19 Å (Fig. 5.18(a)). The 'ether' oxygen termination causes very little disruption to the underlying diamond, with all but the uppermost atomic layers containing bulk-like C–C bond lengths of 1.53 Å (Fig. 5.18); this is primarily due to the lack of surface reconstruction.

To study conversion between the two configurations for the oxygenated (001) surface, and to determine the stability of each form, calculations based on two diffusion techniques were performed. In the first, 'drag' method, each oxygen atom was stepped along a vector pointing from its 'ketone' coordinates to its 'ether' coordinates, and at each step a structural relaxation was performed in which the O atoms were constrained to lie in planes perpendicular to their movement vectors, while the other atoms were allowed to relax with complete freedom.

The second diffusion method used was the 'improved tangent nudged elastic band' (NEB) technique. This is described in detail in the original work [363], and has previously been used within AIMpro to investigate the diffusion of nitrogen dimers in silicon,

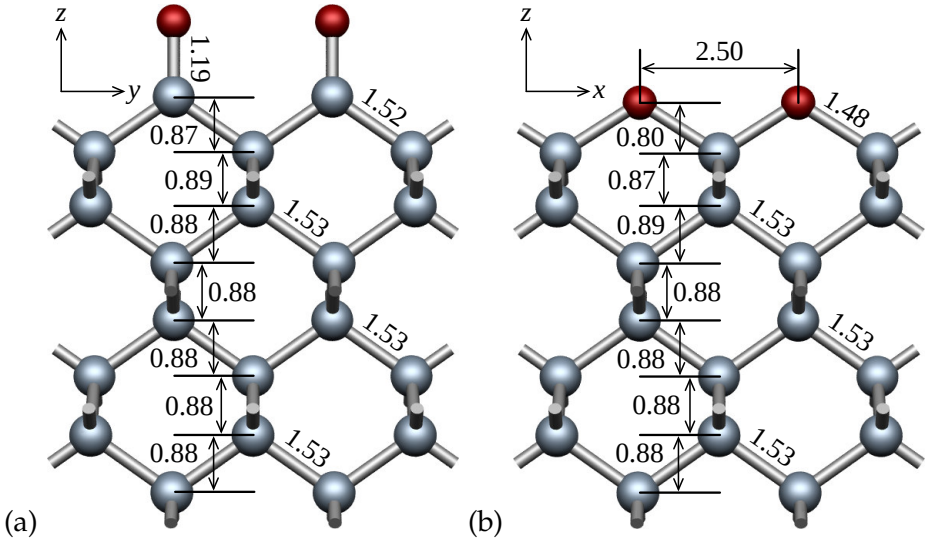

Figure 5.18: Relaxed atomic geometries for monolayer oxygen coverage on the (001)-(1×1) diamond surface. (a) 'Ketone' (C=O) configuration. (b) 'Ether' (C–O–C bridge) configuration. Interatomic distances are given in the plane of the figure in Å. Atoms are separated from their repeated images in the direction orthogonal to the plane of the figure by 2.50 Å. There is no layer buckling in either of the systems.

with much success in reproducing experimental results [364]. The method essentially proceeds as follows. First, several sets of atomic coordinates intermediate between the initial and final structures are created by linear interpolation. Then, the atomic positions in each one of these 'images' is relaxed, wherein each atom is subject to the normal interatomic forces plus 'spring' forces that couple it to its coordinates in the adjacent images. In this way, the minimum-energy route between the initial and final structures is determined. This is analogous to stretching an elastic band (where the spring forces provide the tension) over the configuration-energy surface connecting the initial and final structures, and 'nudging' it until it settles into the path of minimum energy.

In both methods, the four C atoms corresponding to the central two layers of the slab were held fixed, in order to prevent translation of the whole arrangement of atoms during the structural optimisations. Nine intermediate structures were created between the 'ketone' and 'ether' geometries in both diffusion techniques.

The results from the two methods are plotted in Fig. 5.20. There appears to be no significant energy barrier between the two oxygen arrangements, since the drag method finds only a negligible rise in energy as the system moves away from the 'ketone' coordinates, while the NEB method gives no energy rise and hence finds the 'ketone' arrangement to

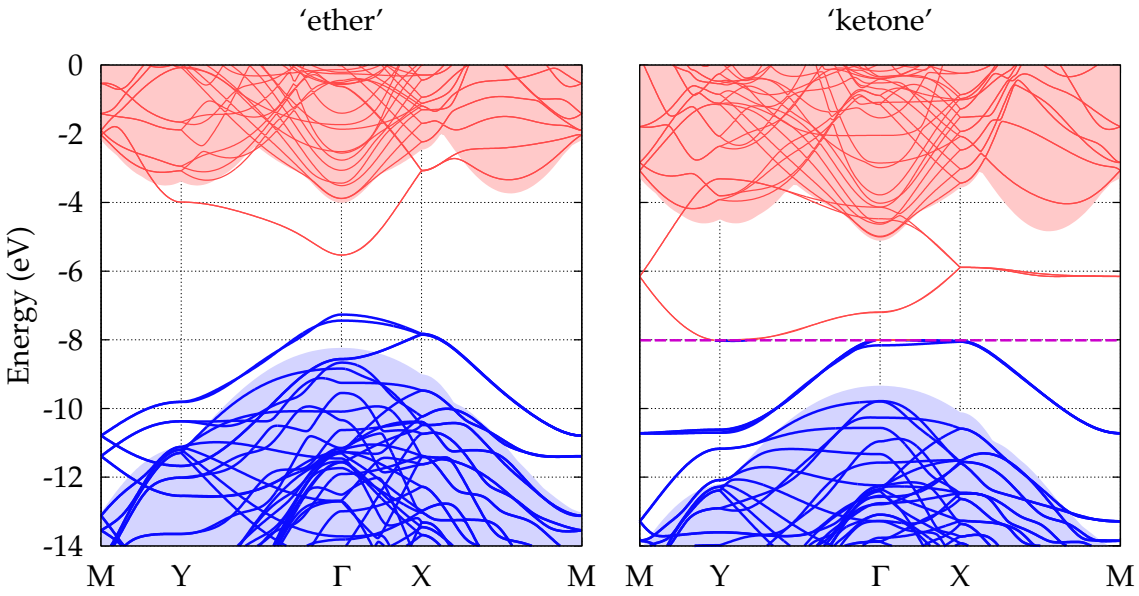

Figure 5.19: Calculated electronic band structures for the 'ether' and 'ketone' forms of the (001)-(1×1):O diamond surface. The zero of the energy scale is the vacuum potential. For the 'ketone' form, the Fermi level is indicated by a horizontal dashed line.

be unstable.

The results of the two methods are in general agreement, but differ significantly around a point at which it could be argued that the strained double bond of the 'ketone' is broken and the second single C–O bond of the 'ether' is created. However, the NEB results are likely to be the most reliable, since the spring forces involved prevent it from finding a discontinuous reaction pathway, while this is not assured when using the drag method.

The electronic band structures for the two forms of oxygenated (001) diamond surface are shown in Fig. 5.19. Both surfaces show occupied and unoccupied states in the bandgap, which persist for most of the sampled region of the BZ.

The picture for the 'ether' surface is entirely consistent with the results of experimental probing of oxygen-related surface states using photoemission techniques [365]. In particular, the presence of occupied states about 1 eV above the bulk VBM at Γ agrees very well with the high density of surface states measured on field-effect transistors based on oxygen-terminated diamond [366]. This is also consistent with KFM measurements on oxygenated regions of a (001) diamond surface, which place the Fermi level 0.7–2.0 eV above the VBM [208].

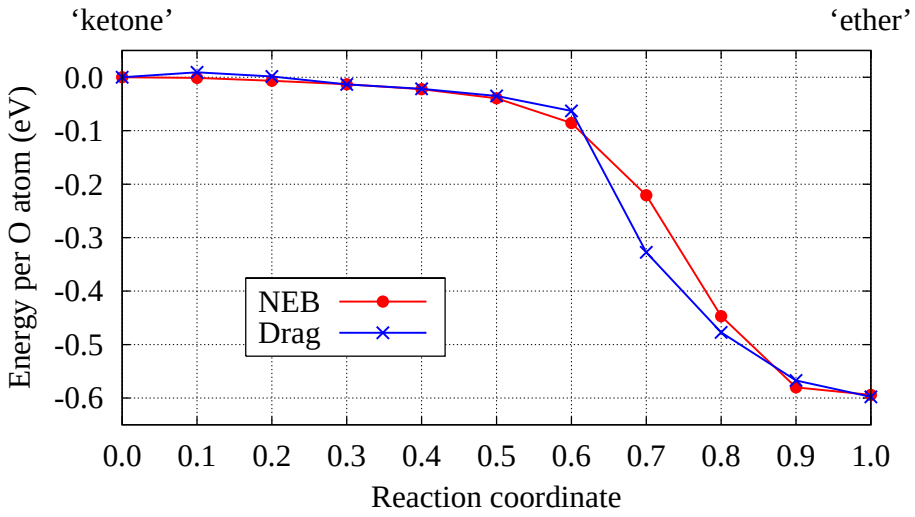

Figure 5.20: Relative energy per oxygen atom as the oxygenated (001) diamond surface is stepped between its 'ketone' and 'ether' configurations, as calculated using the 'nudged elastic band' (NEB, circles) and 'drag' (crosses) diffusion techniques.

Oxygen coverage has caused a downward shift in the band structure (relative to that of the clean surface) of about 2.1 eV, which is slightly smaller than the upward shift caused by hydrogen termination. The calculated bulk IP for this surface $I_{\text{bulk}} = 8.23$ eV, while from the gap states, $I_{\text{surf}} = 7.26$ eV, both of which are very large, as expected. The bulk EA is correspondingly highly positive, at $\chi_{\text{bulk}} = +2.76$ eV, which is close to the 2.70 eV calculated in an earlier study [351]. The surface-related EA is even greater (due to the deep gap state), at $\chi_{\text{surf}} = +4.73$ eV. Both EA values are in general agreement with theoretical and experimental studies that find the oxygenated surface to have a very large PEA [55, 56, 62].

The most notable aspect of the band structure for the 'ketone' surface is that the maximum of the highest occupied state and the minimum of the lowest unoccupied state occur at essentially the same energy, although they are located at different points in **k**-space. Therefore, this surface might display (indirect) semi-metallic behaviour, or rather if the underestimate of unoccupied states is taken into account, it might be better described as having the properties of a small-bandgap indirect semiconductor. However, the unstable nature of this geometric configuration must be appreciated. Considering this system as semi-metallic, the surface EA and IP are the same and equivalent to the work function, which is 8.01 eV. With a scaling correction applied to the unoccupied states, the surface EA decreases to 7.64 eV. Meanwhile, the bulk bands correspond to $I_{\text{bulk}} = 9.36$ eV and $\chi_{\text{bulk}} = +3.88$ eV.

The larger downward shift of the energy bands for the 'ketone' surface compared to the 'ether' surface is consistent with the difference in atomic geometry. If it is assumed that the amount of charge transferred from C to O atoms (forming the $C^{\delta+}$–$O^{\delta-}$ dipoles) is about the same in both systems, it is clear from Fig. 5.18 that the 'ketone' surface will have a greater z-component of the surface dipole, causing larger values for the bulk EA and IP (see Sec. 5.1.1).

Γ-point AIMview analysis performed on the 'ether' system reveals that the highest occupied state has a wavefunction with p-like orbitals centred on the oxygen atoms. The axes of these orbitals lie in the plane of the surface, and are directed perpendicular to the line of oxygen 'bridges'; that is, they are aligned with the y axis of Fig. 5.18(b). The lowest unoccupied state in the 'ether' system also has a wavefunction consisting of p-like orbtials, although these are centred on the uppermost C atoms, and are directed normal to the surface (*i.e.* along z). Furthermore, the orbital lobes on the vacuum side of the surface are significantly larger than those on the bulk side, which is consistent with the large z-asymmetry of the environment at the surface.

Similar Γ-point analysis for the 'ketone' surface shows that the highest occupied state again consists of p-like orbitals centred on the oxygen atoms, with their axes lying in the plane of the surface. Specifically, the orbital axes are directed parallel to the zig-zag line of bonds linking the uppermost C atoms; that is, in the $\pm y$ direction of Fig. 5.18(a). The lowest unoccupied state also has a wavefunction consisting mainly of p-like orbitals centred on the oxygen atoms, lying in the surface plane, although these are perpendicular to the orbitals of the highest occupied state; that is, they are aligned with the x axis. In addition, this state also has significant p-like components centred on the uppermost C atoms, with the orbital axes essentially parallel to those of the p-like orbitals on the O atoms above.

5.4.8 (001)-(2×1):OH surface

In this system, an –OH group is attached to each of the C atoms in the dimer of the clean surface. Structural relaxations were performed with slightly randomised initial atomic coordinates for the O and H atoms, which helped to identify two distinct relative orientations for the two O–H bonds corresponding to one C–C dimer: (a) the 'para' configuration, in which the two O–H bonds are pointing in similar directions and are therefore

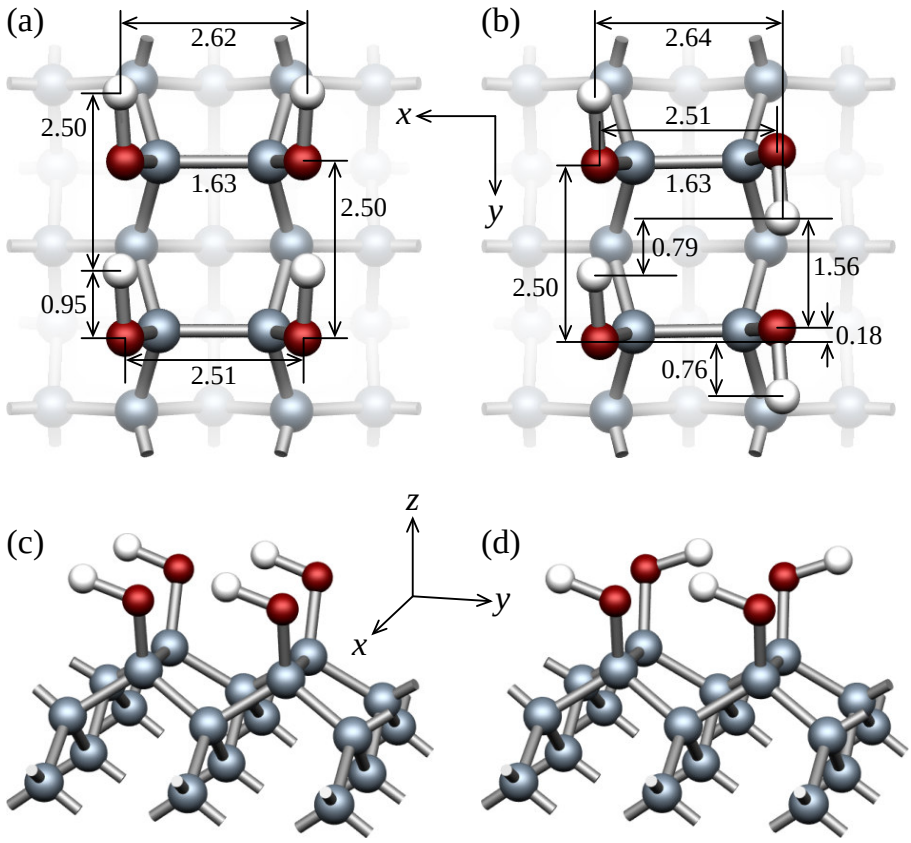

Figure 5.21: Relaxed atomic geometries for two stable forms of the (001)-(2×1):OH diamond surface. The 'para' configuration is shown in plan view in (a) and in perspective in (c). The slightly lower-energy 'anti' arrangement is shown in (b) and (d). All interatomic separations are given in Å.

almost parallel; and (b) 'anti', in which the O–H bonds point in opposite directions and are exactly anti-parallel. In both cases, the O–H bonds are almost orthogonal to the underlying C–C bond of the surface dimer. These two configurations are shown in Fig. 5.21.

The 'anti' configuration supercell was found to be 85.2 meV lower in energy than the 'para' supercell, which is equivalent to 21.3 meV per surface O–H group. Although this difference is small, it is understandable, since the H atoms are slightly further apart when in the 'anti' configuration, and so too are the regions of high electronic charge density in the O–H bonds.

The electronic structure of the (001)-(2×1):OH 'anti' surface is shown in Fig. 5.22, while the band structure for the 'para' configuration looks extremely similar. Occupied states emerge from the bulk valence band and exist in regions of the bandgap away from the

zone centre, although they do not rise higher than the VBM. There is also an unoccupied surface state about 0.5 eV below the conduction band around the CBM. The overall shift of the bands relative to the clean surface is upward, by about 1.2 eV. The bulk VBM corresponds to $I_{\mathrm{bulk}} = 4.92$ eV, while a downward perturbation of the corresponding states in the slab system causes a larger $I_{\mathrm{surf}} = 5.27$ eV. In the raw band structure (Fig. 5.22), the conduction band lies just below the vacuum level, hence there are no vacuum-related states appearing in the bandgap. However, applying the correction to the excited states raises the conduction band above the vacuum level (Fig. 5.25), and so this system is estimated to have a negative bulk EA, of about -0.55 eV. The minimum of the lowest unoccupied surface-related state is almost coincident with the vacuum level after correction, hence the surface EA is almost zero, at $\chi_{\mathrm{surf}} = +0.03$ eV.

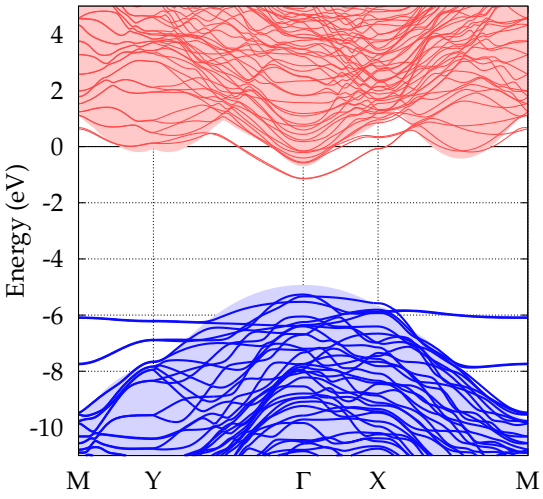

Figure 5.22: Electronic band structure for the 'anti' form of (001)-(2×1):OH surface.

5.4.9 Interaction of oxygen and hydrogen

Hydrogen bonding on (001)-(2×1):OH

The hydrogen atom has an electronegativity of 2.20 on the Pauling scale, while that for atoms of oxygen is much greater, at 3.44. Therefore, the O–H bonds on this surface are likely to be strongly $O^{\delta-}$–$H^{\delta+}$ polarised. Considering that the O atoms have exposed lone pairs, this suggests that there may be significant *hydrogen bonding* in the manner of O–H$\cdots$O–H occurring on this surface. Of course, this would help to stabilise the hydroxylated surface.

There are two main ways in which hydrogen bonding could occur on this surface: (i) between O–H groups located on different C–C dimers (as in either of the forms shown in Fig. 5.21), or (ii) between O–H groups attached to C atoms of the same surface dimer. The first is no doubt present to some degree in the stable 'anti' and 'para' forms, since

the H and O atoms across neighbouring O–H groups are separated by about 1.6 Å, and the typical length of a hydrogen bond in water is about 2 Å. The second possibility for hydrogen bonding has been investigated separately, as follows.

The initial atomic coordinates for modelling interaction (ii) were devised by taking the relaxed structure for the 'anti' surface, and rotating the O–H groups on the C–C dimer so that they both point in the same direction ($+x$ of Fig. 5.21). The O atoms lie slightly out of the x, z-plane (which contains the C–C dimer and the vertical), and so the atoms are not constrained by symmetry. All atoms in the system were then allowed to relax.

This did indeed result in a stable hydrogen-bonding structure, in which all of the H and O atoms lie in the same plane as the C–C dimer. This is despite the fact that the previous relaxations from randomised initial coordinates only gave rise to either the 'anti' or 'para' configurations. The optimised structure is shown in Fig. 5.23. The O$\cdots$H hydrogen bond formed above the C–C dimer is 1.68 Å in length, while the O$\cdots$H bond formed across dimers has a length of 1.57 Å. The former is longer due to a significant upward relaxation of the H atom above the C–C dimer bond. Both of these bond lengths are close to the aforementioned 1.6 Å of the O$\cdots$H bonds on the 'anti' and 'para' surfaces. Comparison of Fig. 5.23 with Fig. 5.7 shows that this new arrangement of the O–H bonds does not significantly affect the structure of the underlying diamond.

However, this structure is slightly less stable than the 'anti' and 'para' forms; the energy per O–H group is 70 meV higher than that with the most-stable 'anti' –OH termination, which makes it about 50 meV higher than that of the 'para' form. Still, these energy differences are small, and so a mixture of these forms is likely to be found on a hydroxylated surface at moderate temperatures in practice.

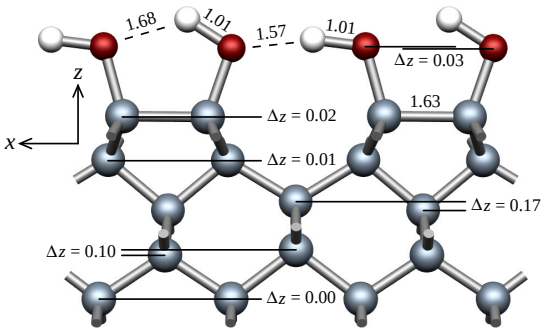

Figure 5.23: Atomic geometry for a metastable form of the –OH-terminated (001) diamond surface. The O–H groups and C–C dimers all lie in the plane of the figure. Bond lengths and layer bucklings are given in Å.

To further investigate the stability of this new arrangement, the H atoms in the relaxed structure were displaced in opposite directions in the plane of the surface ($\pm y$) by a significant amount (~ 0.6 Å), and the sys-

tem was relaxed again. After many iterations of structural optimisation, the structure settled into the familiar 'anti' form and had a total energy within 8 meV of that of the earlier 'anti' calculations.

While the hydrogen bonding is an interesting aspect of this surface, and although these findings are most likely to be chemically sensible, it must be noted that the local-density approximation is often found to result in a relatively poor description of such interactions. For instance, the LDA is seen to overestimate the hydrogen bonding (and therefore underestimate the H-bond lengths) in studies on the interaction of water molecules [367–369]. Therefore, to obtain a quantitatively more accurate model of the hydrogen bonding on this surface, one should turn to higher levels of theory, for instance by invoking the generalised-gradient approximation [370–372].

Hydrogen desorption

On the surface of silicon, there is a very low energy barrier to rotation of terminating O–H groups. That is, an O–H bond can easily rotate around the axis defined by its corresponding Si–O bond. However, on the diamond surface, the O–H groups are closer together due to the smaller lattice parameter. The resulting stronger interaction of the H atoms hinders free rotation of the O–H groups about their C–O axes, although one might be concerned that opposing H atoms could form H_2 molecules that desorb from the surface. To simulate this interaction, the surface H atoms from the relaxed 'para' simulation (Fig. 5.21(a) and (c)) were rotated toward each other about their C–O axes, and brought to within a hydrogen-molecule bond length of one another. The system geometry was then allowed to relax. The H atoms were repelled from one another, and the O–H bonds rotated back into their relaxed positions from the 'para' configuration, resulting in the same final structure and energy as found previously. This result is not surprising if one considers the $H^{\delta+}$ charge state of these atoms.

The likelihood of formation of the –OH-terminated surface can be estimated by comparing its total energy against the total energy of a purely oxygenated surface plus distant, gas-phase H_2 molecules. H_2 was modelled in a very large (30 Å-side) cubic vacuum supercell, in order to obtain an energy for an isolated molecule, while the total energy for the purely oxygenated surface is already known.

In another calculation, molecules of H_2 were added into the supercells of the relaxed 'ketone' and 'ether' oxygenated surfaces and placed as far away from the surfaces and their own repeated images as possible. When the system was allowed to relax, there was no significant movement of any of the atoms, which indicates that the components are sufficiently separated. Furthermore, the difference in the total energies of the 'ketone-O-surface + H_2' and 'ether-O-surface + H_2' systems was the same as found in the earlier O-surface calculations without the H_2 molecules present; that is, only the energy difference between the 'ketone' and 'ether' arrangements remained.

However, due to the periodic boundary conditions, each of the supercells containing an O-surface plus a distant H_2 molecule actually represents an infinite diamond slab plus what could be considered as an infinite sheet of H_2 molecules, and interaction between the molecules in this sheet could render these simulations unrealistic.

Nevertheless, the energy difference between that of the 'ether-O-surface + H_2' system and the energy sum of the plain 'ether-O-surface' and 'isolated H_2' systems was a negligible 1.4 meV, confirming that there is very little interaction in the infinite H_2 sheet of the combined system.

Comparison of total energies for these systems indicates that the (001)-(2×1):OH 'anti' surface is more stable than the separated 'ether-O-surface + H_2' system by 1.17 eV per surface C atom (or O–H group), or equivalently by 2.34 eV per H_2 molecule. While this suggests that reaction of molecular hydrogen with an oxygenated diamond surface is ultimately energetically favourable, nothing can be said about the energy barrier to such a reaction. However, it should noted that the aforementioned possibility of an overestimate in the strength of hydrogen bonding in these calculations might mean that the stability of the hydroxylated surface is slightly overestimated.

Combination of H and O terminations

Results have also been obtained in this investigation for a (001) surface terminated with a simultaneous combination of –H, –O–, and –OH groups. The structure was obtained by relaxing the atomic coordinates of a system in which a molecule of H_2 was placed very close to the 'ether' oxygenated (001) surface. The relaxed geometry and corresponding band structure are shown in Fig. 5.24. This structure is more stable than the separated

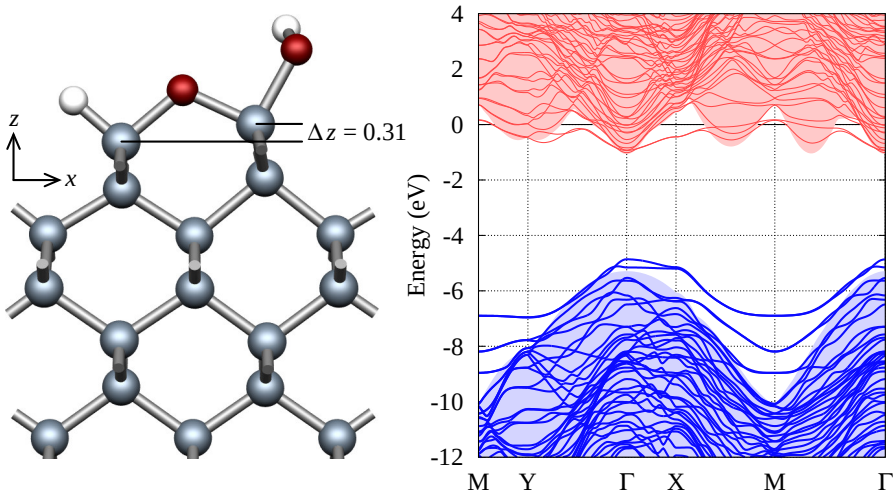

Figure 5.24: Relaxed atomic geometry and electronic band structure for the (001)-(1×1):(H,O,OH) diamond surface. The zero of the band-structure energy scale is the system's vacuum potential.

'ether' (001) surface and H_2 molecules, by 0.46 eV per O–H pair, which makes it 0.71 eV *less* stable than the fully hydroxylated (001) surface.

The band structure for this combination surface shows occupied surface states emerging from the conduction band away from the zone centre, although the highest occupied state lies above the valence band throughout the BZ. These states are similar to those seen in the oxygenated and –OH-terminated (001) surfaces, although the most notable aspect of the electronic structure of this system is that there are no unoccupied surface states significantly below the bulk CBM.

The absolute position of the band structure with respect to the vacuum potential is similar to that in the clean and –OH-terminated surface systems. It appears that while the C–O–C component of this system tends to lower the energy bands and encourage PEA, the C–H (and to some extent the C–O–H) dipole tends to raise the bands, and the effects cancel to a large degree. The calculated IPs for this system are $I_{\text{bulk}} = 5.29$ eV and $I_{\text{surf}} = 4.86$ eV, while the corrected excited states start just above the vacuum level, such that $\chi_{\text{bulk}} = -0.19$ eV and $\chi_{\text{surf}} = -0.26$ eV. It is interesting to note that this is the only surface under investigation with a clear negative *surface* electron affinity; that is, it possesses no unoccupied surface-related states that lie below the vacuum level.

5.4.10 Photoemission threshold and band bending

Recent studies on the hydrogenated (001) diamond surface have made use of total photoelectron yield spectroscopy (TPYS) to investigate the material's surface electronic structure [373]. The results show that the same threshold energy of 4.4 eV is required for photoelectron emission from both boron- and phosphorus-doped diamond, as well as from type-IIa material. This 4.4 eV threshold was attributed directly to hydrogen termination, as it was not observed when using oxidised surfaces. Its independence on the Fermi energy rules out mechanisms based on transitions between occupied bulk or surface defect states and the conduction band. The suggestion was made that the threshold was therefore due to transitions directly from the VBM at the surface to the vacuum states [373].

As described previously, the present calculations demonstrate that for the (001)-(2×1):H surface, an empty hydrogen-related band lies (when corrected) $\sim$ 3.7 eV above the surface VBM. However, transitions to this band would not contribute to photoemission. It is clear from Figs. 5.13 and 5.14 that vacuum states lie just above this band, and that the aforementioned photoemission threshold is related to I_{surf} at 3.97 eV, which is in reasonable agreement with the observed threshold. The fact that a similar TPYS threshold was not observed for the oxygenated surface is also consistent with the present calculations.

In addition, the experimental photoyield resulting from input energies above the bandgap energy was suppressed in both types of doped material, compared to that in chemically pure IIa diamond; that is, something is preventing conduction band electrons from escaping the doped material. The suppression in the case of boron-doped diamond was attributed to the use of a thin sample, while in the phosphorus-doped material the suppression was suggested as being due to an *upward* band bending, which represents a barrier to electron emission [373].

The mechanism for band bending in *n*-type material was shown schematically in Fig. 5.2 and is based upon an electric field existing between ionised donors in the bulk material and a negatively charged surface region. Band bending is expected to occur when unoccupied surface states lie below impurity donor levels; however, the surface states must also lie below vacuum in order to bind the electrons and establish the electric field. This field presents an additional barrier to conduction-band electrons attempting to escape

the material, and this is reflected in the TPYS results on *n*-type diamond in which greater photon energies are required to eject electrons than in samples where there is little band bending [373, 374].

The most common donor in diamond is nitrogen, and the single substitutional N defect has a donor level around 1.7 eV below the CBM [285–290]. Therefore, the condition for band bending is that an unoccupied surface state lies more than 1.7 eV below the CBM, or rather $\chi_{\mathrm{surf}} - \chi_{\mathrm{bulk}} > 1.7$ eV.

This condition is satisfied by all of the clean and hydrogenated surfaces considered in this investigation, and possibly by the oxygenated (001) surface, but certainly not by the (001) surface when –OH terminated or with the (H,O,OH) combination of terminations.

The donor level of phosphorus, which is appropriate to the samples used in the pertinent TPYS study, is known to lie around 0.6 eV below the CBM [186, 262, 264, 266–268]. The condition for band bending with P-doped material is again satisfied by all of the surfaces modelled in the present work, except the –OH- and (H,O,OH)-terminated (001) surfaces.

It should be noted that if electrons donated by P impurities indeed go on to occupy the C–H-related surface state suggested in the present calculations, the measured threshold for photoemission should be only $\sim$ 0.2 eV; that is, the energy by which the (now-occupied) surface state lies below the vacuum level. However, such a low threshold might lie outside of the range that can be detected experimentally.

5.5 Data summary

The calculated bulk- and surface-related ionisation potentials and electron affinities for the various surface systems studied in this part of the investigation are given in Table 5.2, and are summarised visually in Fig. 5.25.

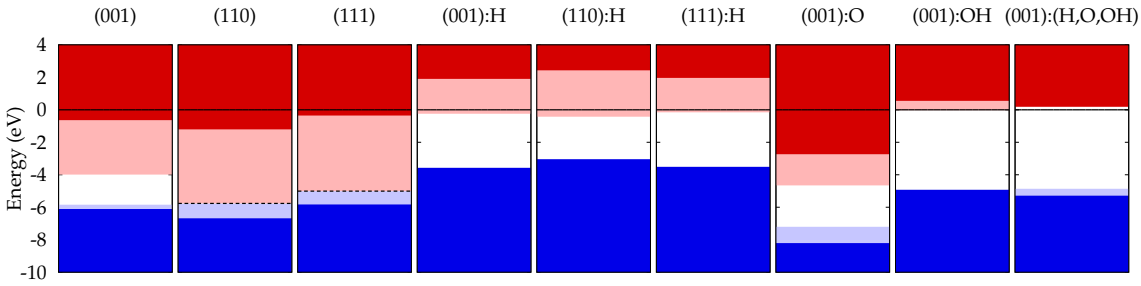

Figure 5.25: Simplified electronic band schemes for the most stable configurations of the surfaces considered in this work (see text). The zero of the energy scale is the vacuum potential for each system and is shown as a solid black line. The darker shaded regions represent the valence and conduction bands of bulk diamond, while the lighter shaded regions show the extent of occupied and unoccupied surface states. For the semi-metallic (110) and (111) clean surfaces, the Fermi level is shown as a dashed black line. All unoccupied states include the first-order correction to their underestimation by the method.

Table 5.2: Summary of calculated bulk- and surface-related ionisation potentials I and electron affinities χ for the most stable surface structures considered in this investigation, with values given in eV. Note that for the semi-metallic clean (110) and (111) surfaces, the surface ionisation potential and electron affinity are the same, and are equivalent to the work function. Also given for each surface is its difference in dipole moment Δp (in eÅ per unit cell) with that of the clean surface of the same orientation.

Diamond surface	I_{bulk}	I_{surf}	χ_{bulk}	χ_{surf}	Δp
(001)-(2×1)	6.11	5.85	+0.64	+3.99	(ref.)
(110)-(1×1)	6.68	5.77	+1.21	+5.77	(ref.)
(111)-(2×1) (Pandey)	5.83	5.01	+0.35	+5.01	(ref.)
(001)-(2×1):H	3.57	3.97	−1.90	+0.24	−0.18
(110)-(1×1):H	3.04	3.11	−2.43	+0.42	−0.18
(111)-(1×1):H	3.51	3.71	−1.97	+0.15	−0.14
(001)-(1×1):O ('ether')	8.23	7.26	+2.76	+4.73	+0.15
(001)-(2×1):OH ('anti')	4.92	5.27	−0.55	+0.03	−0.08
(001)-(1×1):(H,O,OH)	5.29	4.86	−0.19	−0.26	−0.06

5.6 Chapter summary

In this chapter, the results of modelling the low-index diamond surfaces — both clean and hydrogen terminated — have been presented. The effects of oxygen termination and the interaction of oxygen with hydrogen have also been studied on the technologically important (001) surface.

The hydrogenated surfaces show the large, negative electron affinities expected from experiment, provided that a correction is made to account for the underestimation of the position of the conduction band in calculations of this type. Hydrogen termination also introduces unoccupied surface states, with minima below but close to the vacuum level, which could trap excited electrons that would otherwise escape the material.

The –OH-terminated (001) surface exhibits a small negative bulk electron affinity, and also possesses unoccupied surface states that may lie close to the vacuum level. Meanwhile, the oxygenated (001) surface has a large, positive electron affinity, as has been observed in experiment. A combination of hydrogen and oxygen termination on the (001) surface gives rise to a bandgap relatively clear of surface-related states, and an overall electron affinity close to zero.

The majority of the surfaces modelled are likely to show an upward band-bending effect in *n*-type diamond, due to the presence of unoccupied surface-related states lying below the donor levels of common bulk impurities. These results agree qualitatively with the findings of recent total photoelectron yield experiments on hydrogenated diamond. Furthermore, these calculations reproduce well the measured threshold for photoemission from hydrogenated (001) surfaces.

Transfer doping of the diamond surface will be examined in the next chapter. For efficient electron transfer from diamond to some adsorbed material, the bulk diamond valence band must be as high in energy as possible, while the adsorbate must possess low-energy unoccupied states. Therefore, the suitability of each diamond surface for this task is reflected in its ionisation potential. The H-terminated surfaces, with their low bulk ionisation potentials, clearly represent the most suitable substrates, although the hydroxylated (001) surface might also undergo transfer doping when combined with an adsorbate of very high electron affinity. This premise will be explored in the next chapter.

Chapter 6

Fullerenes as transfer dopants for p-type diamond surfaces

> "Everything you've learned in school as 'obvious' becomes less and less obvious as you begin to study the Universe. For example, there are no solids in the Universe. There's not even a suggestion of a solid. There are no absolute continuums. There are no surfaces. There are no straight lines."
>
> — R. Buckminster Fuller

- The work presented in this chapter has been published as Refs. [375–377].

6.1 Introduction: The surface conductivity of diamond

HIGH surface conductivity was first detected on diamond samples in 1989 [60], and has been found on both natural diamond treated by hydrogen plasma [378] and on diamond films prepared by the chemical vapour deposition (CVD) technique. Interestingly, the electrical resistance near the surface region of diamond films has been observed to decrease by four orders of magnitude within ten minutes of exposure of the sample to air, following its removal from the CVD chamber in which it was deposited [340].

The surface conductivity has been measured to be of the order of 10^{-4}–10^{-5} Ω^{-1} at room temperature [57], while the areal density of the charge carriers lies in the range

of $(1\text{–}5) \times 10^{13}$ cm^{-2} [379] and does not depend greatly on temperature between 150 K and room temperature. The Hall mobility of these carriers also varies little with temperature [339] and has typical values lying in the range of 10–30 cm^2 V^{-1} s^{-1} [379]. A maximum Hall mobility of 70 cm^2 V^{-1} s^{-1} has been reported, for a lower carrier density of 1.2×10^{12} cm^{-2} [380].

Amongst all semiconductors, this high surface conductivity is unique to diamond, and it has been utilised to create several devices, including metal-semiconductor field-effect transistors (MESFETs) on single crystal [381, 382] and polycrystalline diamond [383], metal-oxide semiconductor field-effect transistor (MOSFET) devices [384], single-hole transistors [385], and even a novel type of field-effect transistor [386]. However, these devices are unstable with respect to changes in the ambient temperature and environment [387, 388], hence the surface of hydrogen-terminated diamond must be passivated in some way if devices are to be manufactured to commercial specifications.

Since the measured mobilities are similar to those found in boron-doped (*i.e. p*-type) diamond, initial speculation suggested that the carriers responsible are *holes*, residing in an accumulation layer at the surface [386]. Indeed, the surface conductivity was confirmed to be *p*-type by experiments exploiting the Seebeck effect [378] and by Hall-effect measurements [389–391].

In addition, since the surface conductivity is only observed on hydrogen-terminated diamond surfaces [57] and disappears following dehydrogenation or oxidation of the surface, it is assumed that the role of hydrogen is critical in the formation of any hole accumulation layer [392].

Several models have since been proposed to account for this phenomenon, such as the passivation of deep defects [393], the formation of shallow, hydrogen-related acceptor states [394], and the *transfer doping* model based on a surface layer of adsorbate material [57, 339–341].

6.1.1 The formation of shallow acceptor states

In the *shallow-acceptor* scheme, hydrogen impurities form sub-surface acceptor defects [395], which provide the mobile holes. However, pure hydrogen defects in bulk diamond act as

deep acceptors [253], and such shallow-acceptor defects remain to be identified. Furthermore, hydrogen defects also behave as deep *donors*, and their high concentration in the sub-surface region should lead to compensation of the unknown shallow acceptors [253].

The depth distribution of the acceptors responsible for this hole accumulation is controversial, with different models proposing that they reside close to the surface [339, 386], that they are arranged in layers extending up to 10 nm into the bulk diamond [395], or that they could even reside in a layer lying 30 nm below the surface [396].

This model for the surface conductivity of diamond has other significant weaknesses, such as the following. If the system contains a quasi–two-dimensional acceptor layer at or up to 30 nm below the surface, the measured areal density of holes of 10^{13} cm^{-2} requires a band profile with the Fermi level lying within a few $k_{\mathrm{B}}T$ of the valence band maximum [386]; however, recent studies on Al-based Schottky contacts to hydrogen-terminated diamond have reported capacitance measurements that are much too low to be compatible with such a model [379].

6.1.2 The transfer doping model

Transfer doping refers to the introduction of some foreign species onto the surface of a material so that this adsorbate either adds or extracts electrons from the substrate, effectively doping the material. The transfer doping mechanism has also been suggested as the reason for the high *p*-type surface conductivity on diamond surface exposed to air [57, 339–341].

In this case, it is believed that some constituent of the surface wetting layer (that naturally forms on surfaces exposed to the atmosphere) is responsible for the extraction of electrons from the diamond, leaving behind a layer of holes responsible for the *p*-type conductivity. It is thought that screened protons present in a layer of water on the diamond surface act as the principal adsorbate electron sink. This has been related to the observation of an enhancement in the conductivity following the exposure of the surface to NO_2, while exposure to NH_3 suppresses the effect [339, 340]. However, recent experiments show that while exposure to the atmosphere does lower the resistivity, the initial hydrogenation has a much larger effect in lowering the resistivity, suggesting that a combination of mechanisms is responsible for the surface conductivity [397].

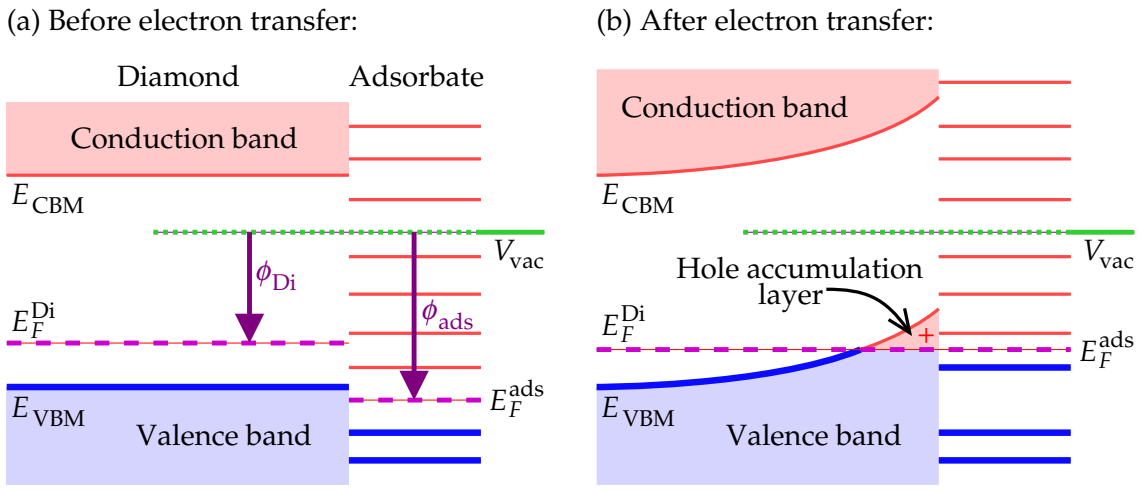

Figure 6.1: Schematic of the energy levels for thermodynamic transfer doping. (a) Before electron transfer has occurred: the Fermi level (E_F) of the adsorbate (ads) is lower than that of the diamond (Di) substrate; in terms of work-functions, $\phi_{ads} > \phi_{Di}$. (b) In equilibrium, after electron transfer from the diamond to the adsorbate: the two Fermi levels are aligned and the diamond has a layer of accumulated holes at its surface.

The transfer-doping mechanism in the sense of substrate-to-adsorbate electron transfer is summarised in Fig. 6.1, and relies upon two properties of the components involved: (i) the semiconductor substrate must have a valence band maximum that lies very high in energy, and (ii) the adsorbate material must possess very low-lying unoccupied electronic states. That is, the substrate must have a small ionisation potential (IP) and the adsorbate must have a high electron affinity (EA), in order to promote an electron transfer. As a result of such charge transfer, an upward band-bending is induced toward the diamond surface, and a narrow hole accumulation layer is created, since the Fermi level lies below the position of the valence-band maximum in the vicinity of the surface.

As detailed in the previous chapter, hydrogen termination of diamond is known to lower its IP, since the $C^{\delta-}$–$H^{\delta+}$ dipoles at the surface present a 'downward' ramp in potential that assists electrons in escaping from the material and out into vacuum states [335–338]. Meanwhile, *oxygen* termination of the diamond surface leads to the formation of $C^{\delta+}$–$O^{\delta-}$ dipoles that present an upward potential ramp, discouraging electron emission and consequently increasing the IP [54, 55, 336]. Oxygen termination is therefore expected to destroy the possibility of transfer doping. However, this effect could be exploited by patterning hydrogen- and oxygen-terminated regions on a diamond surface in order to create channels of high surface conductivity.

In order to confine the holes to the near-surface region, the negatively charged adsorbate must remain on the surface (otherwise, the band bending in Fig. 6.1(b) would disappear), and so the effect is lost after evaporation of the wetting layer [387, 388, 398], although it can be recovered by exposing the sample to the normal atmosphere for an hour. Such a volatile wetting layer cannot be relied upon if one wishes to exploit this high *p*-type surface conductivity for device applications, and so a thermally stable, non-volatile, and easily reproducible surface adsorbate capable of extracting electrons from diamond must be found. There is therefore significant interest in finding a suitable *solid-state* transfer dopant for diamond. Useful adsorbates would be chemically inert and leave the hydrogenated surface intact. Theoretical work on this problem has shown that CO_3H and other adsorbate molecules with large electron affinities will induce a hole in the top of the diamond valence band [397].

The transfer-doping model is gaining acceptance over the other models for the atmosphere-induced surface conductivity, due to the considerable experimental evidence, and it is steadily being refined as research continues [59, 339, 348, 387, 391, 399]. However, it is important to note that whether or not the transfer-doping scheme provides the correct explanation for the high atmosphere-induced surface conductivity, the present investigation assumes that the transfer-doping mechanism itself is sound, and focuses on finding a suitable transfer dopant for deliberately engineering the effect.

6.2 Fullerenes as potential transfer dopants

In a previous AIMpro study on the transfer doping mechanism, several different molecules were individually modelled as adsorbed on the hydrogenated diamond surface, using cluster calculations [397]. This study helped to identify candidate molecules that might extract electrons from the diamond substrate. In particular, molecular C_{60} was found to be capable of such an electron transfer, hence *solid* C_{60} (fullerite) was suggested as a solution to the problem of finding a stable adsorbate material for manufacturing the transfer-doping effect.

The present work represents a more detailed look at C_{60} on diamond. The supercell formalism has been used to approximate solid C_{60} adsorbed on various diamond substrates. Systems of solid C_{60}, molecular C_{60}, and a near-monolayer of C_{60} covering the hydrogenated, hydroxylated, and oxygenated diamond surfaces have been investigated using supercell AIMpro.

It is known both theoretically [400] and experimentally [401] that the *fluorinated* derivatives of C_{60} have greater electron affinities than the 'plain' molecule, and that the EA increases in general as more fluorine atoms are attached [400–402].

$C_{60}F_{36}$ is a particularly stable [403] fluorinated fullerene that has been synthesised [404, 405], studied [401, 406, 407], and modelled theoretically [402, 408–410]. The higher EA of this molecule means that it is expected to be more efficient at extracting electrons from diamond than C_{60}. Therefore, $C_{60}F_{36}$ has also been considered as an adsorbate on the diamond surface as part of this investigation.

Interestingly, a recent study suggests that similar functionalisation of fullerenes can lower their *toxicity* with respect to human cells [411]. This could represent an added advantage in using fluorinated fullerenes in device applications. For a good review of the fluorination of fullerenes, see Ref. [412].

6.3 Particulars of the method

6.3.1 Modelling solid and molecular C_{60}

At room temperature, solid C_{60} is most stable as a face-centred cubic (FCC) packed crystal, with a conventional lattice parameter of 14.16–14.17 Å [413, 414]. Solid C_{60} has been modelled in this work using FCC packing with a lattice parameter of exactly 14.16 Å.

Isolated C_{60} molecules have been approximated by progressively increasing the lattice parameter of the FCC solid, separating the molecules from each other, until the total energy was converged to within 1×10^{-4} Ha.

Solid C_{60} has also been simulated in a slab geometry in order to provide a region of vacuum for obtaining the vacuum potential to assess the material's electron affinity. A supercell was constructed to represent four hexagonally packed C_{60} monolayers (the *abca* layers of a FCC solid), with a vacuum gap of 20 Å separating repeating slabs.

6.3.2 Modelling C_{60} on the (001) diamond surface

The (001) orientation of diamond surface was chosen for the substrate in this investigation, since — as detailed in the previous chapter — it is the most technologically important, and the properties of its hydrogen and oxygen terminations are relatively well known.

A near-monolayer of C_{60} coverage on the hydrogenated, hydroxylated, and oxygenated diamond surfaces was modelled using the supercell-slab method, as follows.

First, an orthorhombic unit cell was devised such that when repeated in the Cartesian directions under the supercell formalism, a slab of diamond with infinite extent in the x and y directions is created and bounded by 'upper' and 'lower' (001) surfaces, where the z direction is the surface normal. The slabs were 14 diamond monolayer planes in thickness, while the $\vec{z}$ lattice vector was made large enough to provide more than 25 Å of vacuum between the facing surfaces of repeating slabs. The chosen surface reconstruction and impurity-atom termination was then added identically to the upper and lower

slab faces. This ensures that there is no net change in electrostatic potential due to the surface dipoles when traversing a route from vacuum, through the slab, and back out into vacuum. This also adds an element of symmetry to the system, which helps to reduce the computational cost. Each surface reconstruction/termination was subsequently optimised, with all atoms being allowed to relax according to the usual method. The detailed results of modelling these diamond surfaces were given in the previous chapter.

Next, the relaxed unit cell for each surface was repeated to form a 'platform' with a 10.00 Å-square surface area upon which a molecule of C_{60} was placed. Now, the planar symmetry in a monolayer of solid C_{60} is of course hexagonal, and not square as with the diamond platform. Therefore, non-orthogonal lattice vectors $\vec{a}$, $\vec{b}$, and $\vec{c}$ were specified so that when this combined system is supercell-repeated, a monolayer of *quasi-hexagonally* packed C_{60} molecules is created above a diamond substrate that tessellates correctly. In the direction normal to the surface, the $\vec{c}$ lattice vector was kept the same as the previous $\vec{z}$ vector, which allows for more than 15 Å of vacuum above the C_{60} molecule before the underside of the repeated diamond slab appears. This supercell scheme is summarised schematically in Fig. 6.2.

Now, the centre-to-centre spacing between adjacent C_{60} molecules in this repeating scheme is 10.00 Å in the a direction, and 11.18 Å in the b direction. Recall that the lattice parameter of FCC solid C_{60} is 14.16–14.17 Å under standard conditions, and so the natural spacing between C_{60} molecules in a hexagonally packed (111) monolayer is about 10.02 Å. By this fortunate coincidence, the quasi-hexagonal C_{60} monolayer in these simulations is not under any significant tension or compression. In any case, C_{60} monolayers are known to adopt quasi-hexagonal packings on certain substrates in order to achieve commensurate structures [415, 416].

Finally, electronic band structures were calculated, and the Kohn-Sham wavefunctions were visually inspected in order to determine the atoms responsible for each electronic level. For each system, the method of comparison of electrostatic potentials was used to align its electronic band structure with that calculated for perfect bulk diamond. From these analyses, it is possible to draw conclusions with regard to electron transfer from diamond to C_{60}.

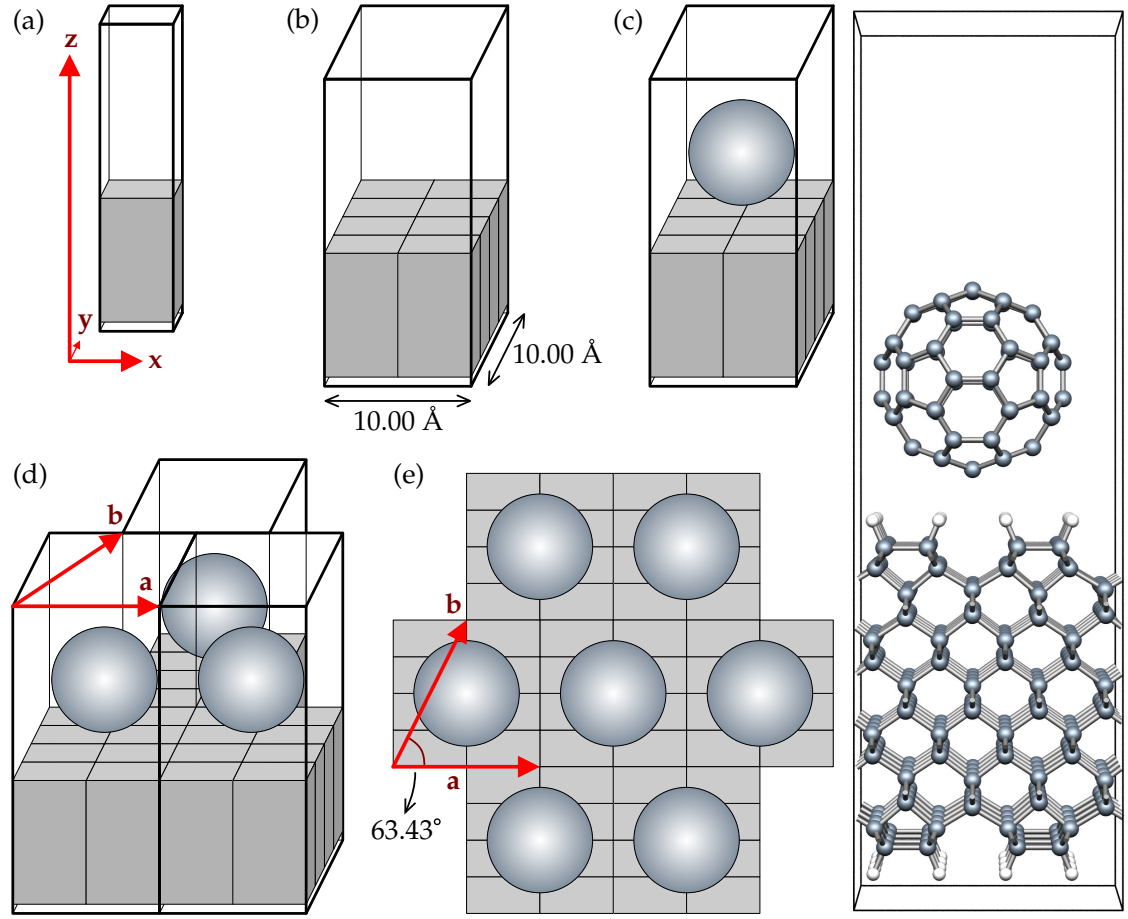

Figure 6.2: Schematic summary of the method used to model a monolayer of C_{60} molecules covering the (001) surface of diamond. The minimal unit cell for the diamond surface slab is represented in (a), where the shaded region indicates diamond and the empty region vacuum. (b) The minimal cell is repeated once in the x direction and three times in y in order to form a surface 'platform', square in plan view. (c) A molecule of C_{60} is placed into the new supercell on top of the platform; the supercell for C_{60} on the hydrogen-terminated (001) surface is shown on the right. (d) The combined system is then modelled using the lattice vectors **a** and **b**. Two repeated images are shown. The third lattice vector **c** is the same as **z** used in the minimal cell. (e) The result, shown in plan view, is that repeated C_{60} molecules form a quasi-hexagonally packed monolayer, while the underlying diamond substrate still tessellates correctly.

6.3.3 Modelling fluorinated C_{60} on diamond

Owing to the larger size of the fluorinated fullerene molecule, $C_{60}F_{36}$ could not be placed upon the same diamond platform as that used with C_{60}, as this would represent a monolayer of $C_{60}F_{36}$ under significant compression. Therefore a larger, 14.14 Å-square area of (001) surface was used as the base. With this increased number of carbon atoms in the

diamond platform, and the 36 extra fluorine atoms, the size of the calculation becomes prohibitive unless the number of layers in the diamond slab is reduced. Therefore, $C_{60}F_{36}$ was placed upon a slab containing 8 rather than 14 monolayers of diamond.

6.3.4 General

The pseudopotentials and basis sets used were the standard ones described in Secs. 2.6 and 2.7.3 of Chp. 2. Atoms of fluorine were treated using 28 basis functions of up to d character. As usual, the Monkhorst-Pack grid of **k**-points was varied for each system until the total energy was converged to within 1×10^{-5} Ha; this was achieved for the C_{60}-on-substrate supercells with a grid of MP-4×4×1. Total energies were similarly converged with a plane-wave energy cut-off of 300 Ha. Atomic relaxations were performed via the normal conjugate-gradient scheme. The vacuum level for each supercell containing such a region was determined using plane-averaged electrostatic potentials.

Electron transfer from the diamond slab to the adsorbate can be expected to take place if the electron affinity (EA) χ of the isolated adsorbate is greater than the ionisation potential (IP) I of the diamond surface. As mentioned earlier, these quantities are given to first order by the energies E_{LU} and E_{HO} of the lowest unoccupied (LU) and highest occupied (HO) levels of the separated adsorbate and diamond slab respectively, referenced with respect to the vacuum potential. The relative position of these levels provides a rough estimate of the likelihood of charge transfer. The *energy gap* is defined as the minimal difference between the HO and LU levels in a system, such that $E_g = E_{\mathrm{LU}} - E_{\mathrm{HO}}$.

However, when the adsorbate is actually placed on top of the diamond surface, the corresponding energy levels may be affected by both charge transfer to surface states and polarisation at the surface. To properly treat these effects, it is essential that a calculation of the levels of the combined system (including a diamond slab, an adsorbate, and a vacuum region) be performed. The character of the HO and LU levels can be then found from a Mulliken bond population analysis or by inspection of the relevant wavefunctions.

The mechanism for charge transfer in electrostatic calculations is presented in Fig. 6.3, which should be compared against Fig. 6.1.

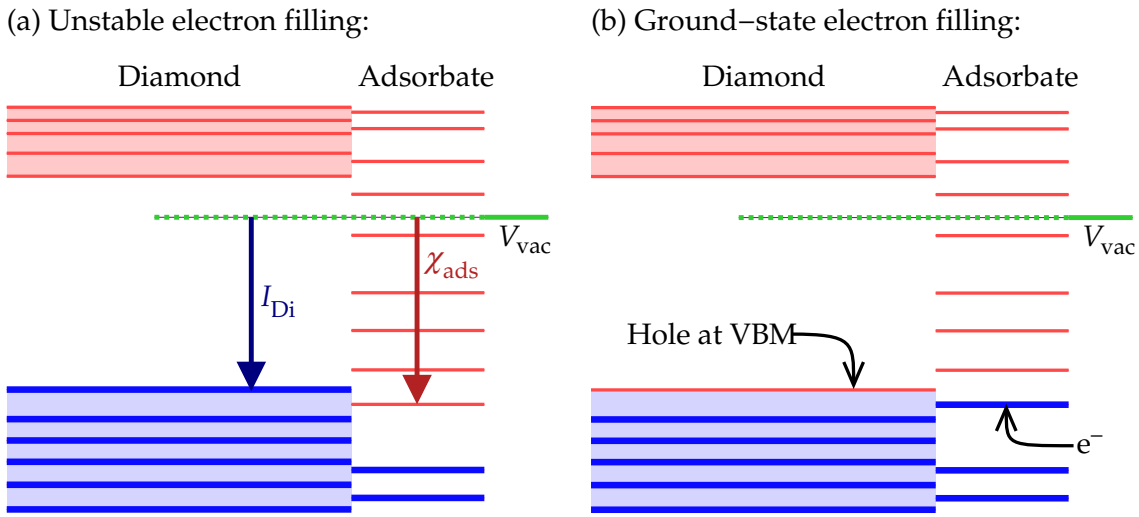

Figure 6.3: Schematic of the energy levels for transfer doping in electrostatic calculations such as those presented in this work. (a) 'Normal' filling of the electronic levels in the diamond and the adsorbate material is unstable in a combined system if the electron affinity of the adsorbate (χ_{ads}) is greater than the ionisation potential of the diamond (I_{Di}). (b) In the ground-state filling, an electron is present in what is normally the lowest unoccupied state in the adsorbate material, and a hole is left behind at the top of the diamond valence band.

6.4 Results

6.4.1 Diamond substrate

The results of calculations on the structure and electronic properties of the (001)-(2×1):H diamond surface were reported in detail in Sec. 5.4.4 of the previous chapter. The most important parameter as far as transfer doping is concerned is the bulk ionisation potential, which was calculated to be 3.97 eV. Therefore, to first order, a candidate adsorbate material is required to have $\chi > 3.97$ eV in order for an exothermic transfer of an electron to occur upon placing it on this diamond substrate.

6.4.2 Isolated and solid C_{60}

The results of varying the lattice parameter of FCC-packed C_{60} are shown in Fig. 6.4. When increasing the separation between molecules, the total energy is converged to within 1×10^{-4} Ha for a lattice parameter of about 16.9 Å, which corresponds to a (centre-

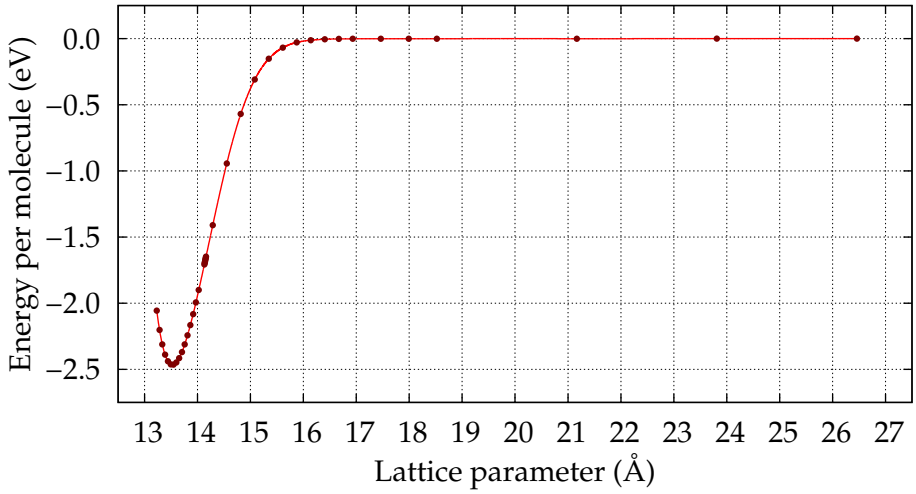

Figure 6.4: Relative energy per C_{60} molecule as a function of FCC lattice parameter. The zero of the energy scale is the converged value for isolated C_{60} molecules.

to-centre) inter-molecular separation of 12.0 Å. The *isolated* C_{60} molecule was therefore modelled by using FCC lattice vectors with a conventional lattice parameter of 35 a.u. (18.5 Å), which represents a separation of 13.1 Å.

The electronic band structure for the isolated C_{60} molecule is shown in Fig. 6.5. Clearly, the energy levels are flat, indicating that the molecule is sufficiently separated from its supercell-repeated images. The calculated HO–LU energy gap E_g is 1.75 eV, which compares very favourably with the experimental value of 1.8 eV [417, 418]. The calculated electron affinity is $\chi = 3.09$ eV, which can be compared to experimental values of around 2.7 eV [417, 419, 420], while the calculated IP for the isolated molecule is 4.84 eV.

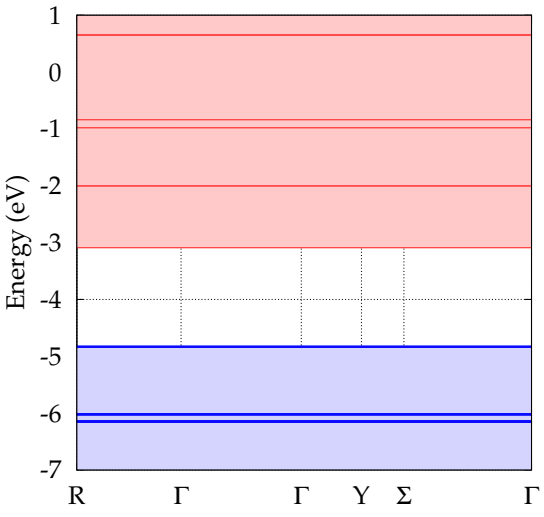

Figure 6.5: Electronic band structure for the isolated C_{60} molecule. The zero of the energy scale is the vacuum level.

It is important to note that the theoretical 'electron affinity' found here for a molecule may be quite different to the electron affinity measured in experiment. This is because in the theoretical work, the EA is simply taken to be the difference in the posi-

tions of the vacuum and LU levels, while strictly the EA is the difference in total energy between the neutral molecule (plus a distant electron) and the molecule in the -1 charge state, and there may be significant structural differences between these two. Furthermore, the LU level is an excited state and may therefore be somewhat underestimated by these LDA-DFT calculations.

Nevertheless, it is actually the position of the LU level of the adsorbate relative to the valence-band maximum (VBM) of the substrate that gives the best indication of the possibility of transfer doping, and so the $\chi = V_{\mathrm{vac}} - E_{\mathrm{LU}}$ definition for EA established in Sec. 2.11.2 gives an appropriate quantity to compare with the IP of the diamond substrate.

The quasi-hexagonally packed *monolayer* of solid C_{60} due to be placed on the diamond substrate has also been modelled in isolation. The resulting electronic band structure shows that the energy bands are strongly affected by inter-molecular coupling. The states in the vicinity of the bandgap exhibit significant dispersion, and the minimal HO–LU gap is now 1.36 eV, which is 77.7% of the value calculated for the isolated molecule. Correspondingly, the electron affinity increases to 3.27 eV, while the IP falls to 4.63 eV.

Modelling fullerite via the four-monolayer (properly hexagonally packed) *slab* system results in another decrease of the bandgap to $E_g = 1.15$ eV. Meanwhile, the extrema of the dispersed LU and HO energy levels correspond to $\chi = 3.43$ eV and $I = 4.57$ eV for the four-layer C_{60} slab.

Inspection of Fig. 6.4 suggests that the optimum lattice parameter that minimises the energy per C_{60} molecule in the solid is about 13.5 Å, which is 95.5% of the experimental value [413, 414]. This underestimation is probably due to two facts: (i) the relative orientation of C_{60} molecules was not investigated (the supercell contained just one C_{60} molecule, which of course repeats periodically); and (ii) the LDA does not give a particularly good description of the van-der-Waals forces responsible for the binding between C_{60} molecules in the solid. However, the present calculated value is certainly in line with the 13.6 Å obtained in another LDA-DFT study (which also used Gaussian basis sets) [421].

The electronic band structure calculated for infinite *solid* C_{60} held at the experimental lattice parameter of 26.76 a.u. is shown in Fig. 6.6. The form of the levels is entirely

consistent with that seen in the aforementioned theoretical study [421], and in particular the system is a *direct* bandgap semiconductor, with the minimal gap occurring at the X edge of the Brillouin zone. The E_g calculated for the FCC solid has decreased further still to 1.08 eV, which is 61.7% of the calculated gap for isolated C_{60} molecules. Since there is no vacuum region in the solid system, χ and I can not be determined from the electronic levels.

These results demonstrate quite clearly that clustering of C_{60} leads to an increase in its electron affinity and decreased values of the ionisation potential, although the position of the centre of the gap remains approximately unchanged. Therefore, high coverages of C_{60} should increase the possibility of charge transfer from diamond. Nevertheless, since even the EA for solid fullerite remains smaller than the IP of diamond, charge transfer would not be anticipated without significant interaction between the adsorbate and substrate components.

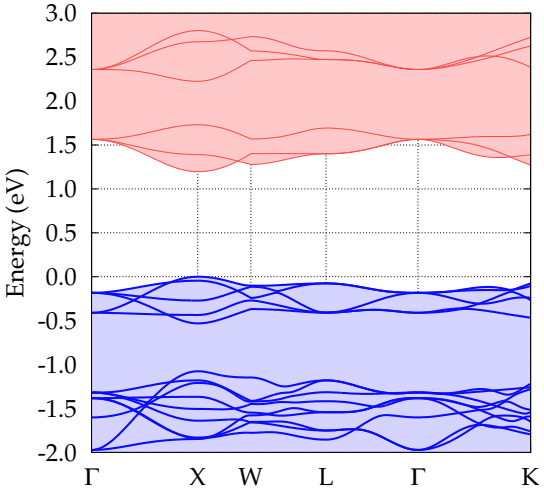

Figure 6.6: Electronic band structure for FCC solid C_{60}. The maximum of the highest occupied level is the energy zero.

6.4.3 C_{60} on the hydrogen-terminated surface

The (001)-(2×1):H form of the hydrogenated surface was used in this study, since it is widely accepted as the most stable under normal conditions [347–349]. This results of studying this surface in detail were reported in the previous chapter (Sec. 5.4.4).

Relaxing the molecule of C_{60} on this surface resulted in negligible disturbance to both the molecule and the surface; the H atoms immediately below the C_{60} molecule were depressed by only 0.01 Å with respect to those H atoms furthest from the C_{60} molecule. The final separation between the lowermost C atoms of the C_{60} and the H atoms below was $\sim$ 1.9 Å in the c direction. The relaxed structure for this system is that shown on the right-hand side of Fig. 6.2.

The electronic band structure for C_{60} on (001)-(2×1):H diamond is shown in Fig. 6.7. The lowest unoccupied level can clearly be seen to cross the highest occupied level near the Γ point. The results of Mulliken analysis confirm the expected: the lowermost empty state is the lowest unoccupied molecular orbital (LUMO) of the C_{60} monolayer, and the highest occupied level is the VBM of the diamond substrate. As a result, there is no energy gap preventing electron transfer from the diamond substrate to the adsorbed layer of C_{60} molecules; that is, the system exhibits semi-metallic behaviour.

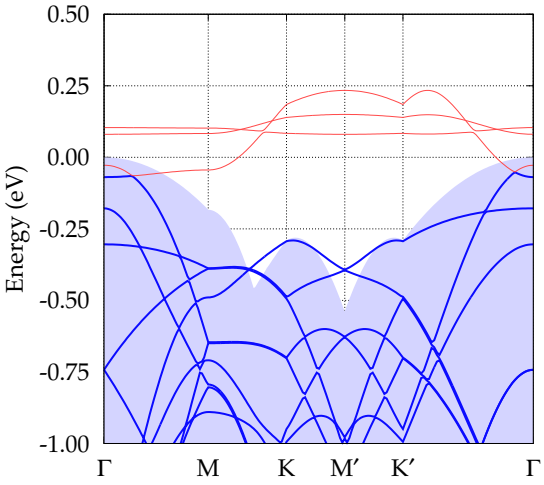

Figure 6.7: Electronic band structure for C_{60} on the (001)-(2×1):H diamond surface. One of the unoccupied states (thin lines) due to the C_{60} can be seen intersecting both the diamond valence band (shaded region) and one of the occupied surface states (thick lines). The zero of the energy scale is the bulk diamond valence-band maximum.

Importantly, the energy levels of C_{60} appear to be a few tenths of an eV lower in this combination system than in the calculations on the isolated C_{60} monolayer, while the energy bands of the diamond slab have been *raised* from their positions in calculations on the isolated diamond substrate, by a similar amount. Therefore, this energy-level crossing appears to be due not only to the dispersion of the C_{60} LUMO, but also to this shifting of the energy levels in the combined system.

This effect is suggestive of polarisation of the C_{60} molecule in the presence of the $C^{\delta-}$–$H^{\delta+}$ dipole layer on the diamond surface. In fact, a similar phenomenon has been observed using photoelectron spectroscopy during the growth of C_{60} on the (001) GeS surface: observations of band bending in the GeS substrate are explained by an effective dipole being induced on the C_{60} molecule as it is adsorbed onto the polar GeS surface [413].

Wavefunction visualisation at the Γ point for the C_{60}-on-diamond system shows that the most energetic electron occupies an orbital localised on the circumference of the C_{60} molecule, while the first hole has a diffuse wavefunction running through the diamond substrate. Plots of the absolute-squared wavefunction for these two states are shown in Fig. 6.8. Most importantly, the hole wavefunction is not localised onto any particular

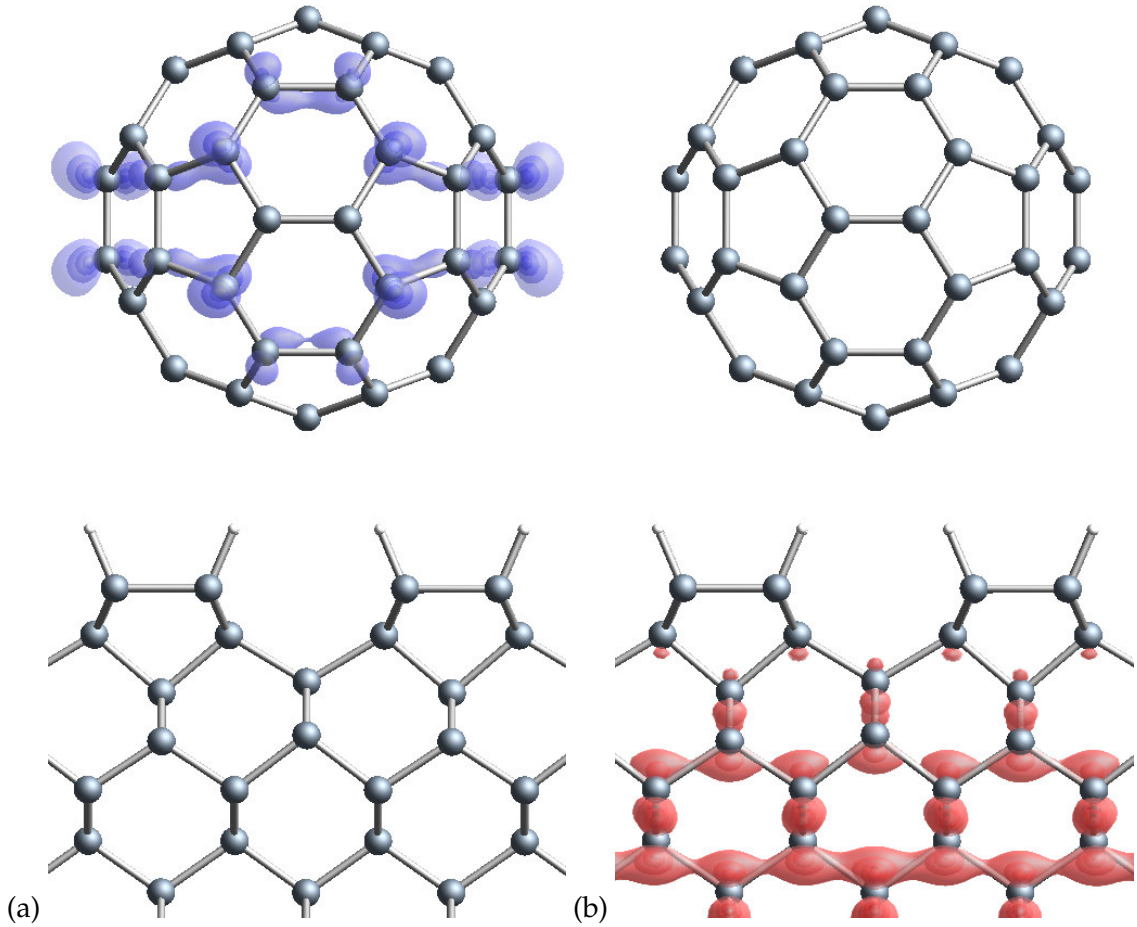

Figure 6.8: Wavefunction visualisation for C_{60} on the hydrogenated diamond surface. Isosurfaces of the absolute-squared wavefunction are shown for: (a) the highest occupied, and (b) the lowest unoccupied electronic states, as sampled at the Γ point of the calculation (see Fig. 6.7).

region (such as the surface C–H bonds), but rather is extended throughout the bulk-like diamond, and so the hole is most likely rather mobile.

It is interesting to note that the second- and third-lowest unoccupied states offered by the C_{60} are only about 0.1 eV above the diamond VBM (Fig. 6.7). However, even if all of these unoccupied states have been underestimated due to the failings of LDA-DFT, there is still a convincing case for the transfer of at least a single electron.

It should be mentioned again that the electron affinity of the bulk-like (four-monolayer) C_{60} slab is higher than the EA of a single monolayer or that of an isolated molecule, hence charge transfer would appear to be more likely with greater C_{60} coverage on the surface.

These predictions have been dramatically borne out in experiment. Fullerene layers have been evaporated onto the surface of plasma-hydrogenated, (001)-orientated diamond samples in ultra-high vacuum, and the surface conductivity was subsequently measured using standard techniques [422, 423]. The results show a clear rise in surface conductivity with C_{60} coverage, with a maximum occurring for a coverage between about 4 and 8 monolayers. In particular, the formation of one or more complete monolayers was required to achieve a significant surface conductivity. This is entirely consistent with the present results from theoretical modelling.

Binding energy

The binding energy $E^{\mathrm{b}}_{\mathrm{CD}}$ of the C_{60} molecule to the diamond surface in these calculations was estimated using

$$E^{\mathrm{b}}_{\mathrm{CD}} = [E_{\mathrm{C}} + E_{\mathrm{D}}] - E_{\mathrm{CD}}, \tag{6.1}$$

where E_{C}, E_{D}, and E_{CD} are respectively the relaxed total energies of the isolated C_{60} monolayer, isolated diamond platform, and the combined system. The resulting value of $E^{\mathrm{b}}_{\mathrm{CD}} = +1.50$ eV indicates that the combined system is bound quite significantly.

For a different approach, the binding energy was found by progressively increasing the separation of the C_{60} monolayer and the diamond slab, and noting the effect on the total energy (without relaxation). Of course, the furthest that the C_{60} molecule could be placed from the diamond surface is half-way between the faces of repeating diamond slabs. However, the total energy appeared to have adequately converged (*i.e.* flattened out with respect to C_{60}–Di separation) before reaching this point.

By this second method, $E^{\mathrm{b}}_{\mathrm{CD}}$ was determined to be 1.52 eV. Hence, both methods suggest that the C_{60} monolayer is bound to the hydrogenated diamond surface by about 1.5 eV per molecule. However, this assumes that the components would separate into neutral entities, which may not be the case.

Basis set superposition error

These estimated binding energies may suffer from *basis set superposition error* (BSSE), in which case they would be overestimated. This phenomenon results from the fact that in

the combined system, atoms belonging to one binding component (say, the C_{60} molecule) might 'borrow' basis functions from close-by atoms of the other component (the hydrogenated surface) in order to better model their own electronic states, in a manner *beyond* the real interaction of these components. Of course, this borrowing of functions is not possible in the isolated systems, and so the total energy of the combined system may be especially low, causing the binding energy to be overestimated.

This problem can be minimised by using basis sets that are as complete as possible; that is, very well converged with respect to adding more basis functions. However, this can lead to great computational expense when modelling systems as large as those in the present study, and in any case, no basis set is ever truly complete.

The BSSE is commonly mitigated somewhat by using the *counterpoise correction* [424, 425]. Here, the basis functions of the combined system are introduced into the isolated systems through the use of ghost atoms, such as those described in the previous chapter. In the present case, one would model three systems: (i) the normal C_{60}-on-diamond combined system; (ii) C_{60} on top of a 'diamond' substrate that is made of ghost atoms; and (iii) a 'C_{60}' molecule, made of ghost atoms, on top of a 'real' diamond substrate.

Unfortunately, the introduction of ghost atoms into the present systems leads to significant problems in obtaining self-consistent charge densities, and the correction to the binding energy is generally not worth the additional computational effort required. Therefore, the calculated 1.5 eV binding energy of the C_{60} molecule to the hydrogenated diamond surface should perhaps be considered as simply an *upper limit* to the correct value.

6.4.4 $C_{60}F_{36}$ on the hydrogen-terminated surface

For the investigation of potential transfer doping using the fluorinated molecule, a low-energy structure of $C_{60}F_{36}$ derived from Hartree-Fock calculations [426] was obtained. The isolated $C_{60}F_{36}$ molecule has been modelled in the present work in a similar way to that of C_{60}, and the calculated energy gap $E_g = 3.65$ eV, while the electron affinity $\chi = 4.94$ eV, and the IP is 8.60 eV. As expected, the electron affinity of the fluorinated molecule greatly exceeds that of molecular and even solid C_{60}.

In the relaxed structure for the combined $C_{60}F_{36}$ and 8-monolayer diamond slab (shown

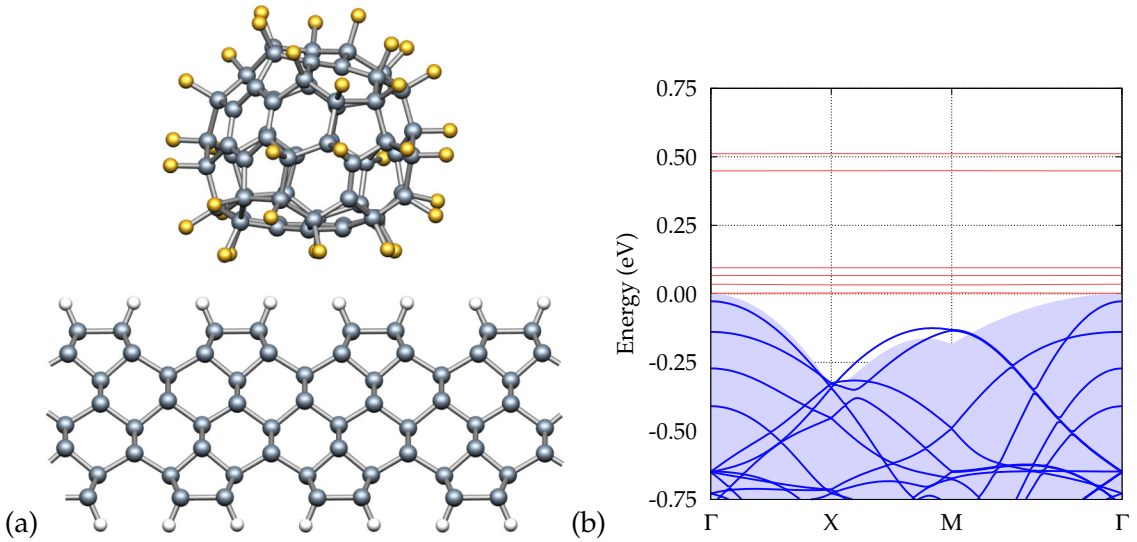

Figure 6.9: (a) Atomic geometry and (b) electronic band structure for $C_{60}F_{36}$ on the hydrogenated (001) diamond surface. The unoccupied states in (b) are due to the $C_{60}F_{36}$ molecule, and clearly come very close to the diamond valence band states at Γ.

in Fig. 6.9(a)), the minimal separation between the surface hydrogen atoms on the diamond and the fluorine atoms on the molecule is 1.76 Å. Therefore, as was seen with the C_{60}–Di system, the $C_{60}F_{36}$ molecule does not significantly disturb the hydrogenated diamond surface, and the molecule is only physisorbed to the substrate.

Electronically, the unoccupied states due to the adsorbate lie *above* the top of the diamond valence band throughout **k**-space, and show no noticeable dispersion. However, the energy gap at the Γ point is a negligible 0.03 eV (see Fig. 6.9(b)), hence electron transfer is expected in practice at room temperature, even for very low coverages of $C_{60}F_{36}$.

This finding is peculiar, since the electron affinity found for the isolated $C_{60}F_{36}$ molecule (4.94 eV) was much greater than the ionisation potential calculated for the (14-layer) hydrogen-terminated diamond substrate (3.97 eV), and so spontaneous electron transfer was expected. This discrepancy is may be due to the failings of using a thin slab for the diamond substrate in this particular combined system.

Nevertheless, this acceptor level 0.03 eV above the VBT represents an improvement in *p*-type doping of over an order of magnitude, when compared against the 0.37 eV acceptor level of substitutional boron defects in the bulk.

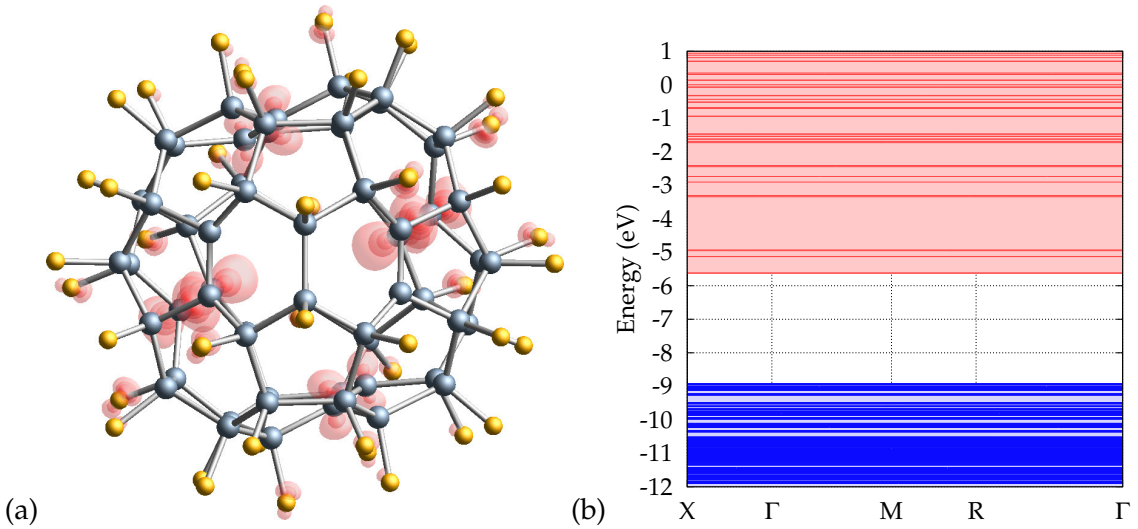

Figure 6.10: Properties of the isolated $C_{60}F_{48}$ molecule. (a) The relaxed atomic geometry, showing isosurfaces of the absolute-squared wavefunction for the lowest unoccupied electronic state. (b) The electronic structure, with the energy zero as the vacuum level.

6.4.5 The $C_{60}F_{48}$ molecule

Subsequent to modelling $C_{60}F_{36}$ on diamond, the more-highly fluorinated $C_{60}F_{48}$ molecule has been modelled in isolation. The relaxed structure and its electronic band structure are shown in Fig. 6.10. Its calculated electron affinity of 5.63 eV is indeed greater than that found for isolated $C_{60}F_{36}$, which suggests that it could be a more efficient transfer dopant for diamond. However, this molecule has not been modelled adjacent to a diamond substrate, since such a system would at present represent a formidable challenge in terms of computational expense.

The suggestions that $C_{60}F_{36}$ could extract electrons from diamond at very low coverages, and that $C_{60}F_{48}$ could represent an even more efficient acceptor have also been confirmed in recent experiments, in which $C_{60}F_{48}$ was used as a transfer dopant for hydrogen-terminated diamond [423]. The surface conductivity induced by $C_{60}F_{48}$ was measured to be much greater than that caused by C_{60} adsorption, for all similar coverages. In particular, the surface conductivity produced by 0.1 monolayers of adsorbate coverage was eight orders of magnitude greater when using $C_{60}F_{48}$ rather than plain C_{60} [423].

The calculated electronic properties for the various fullerenes in different local environments are summarised in Table 6.1.

Table 6.1: Summary of calculated electronic values (in eV) for the fullerenes, with symbols defined as follows. χ: electron affinity; I: ionisation potential; E_g: minimal energy gap between lowest unoccupied and highest occupied electrical levels.

System	χ	I	E_g
C_{60} (isolated molecule)	3.09	4.84	1.75
C_{60} (quasi-hexagonal monolayer)	3.27	4.63	1.36
C_{60} (four-layer fullerite slab)	3.43	4.57	1.15
C_{60} (infinite FCC solid)	–	–	1.08
$C_{60}F_{36}$ (isolated molecule)	4.94	8.60	3.65
$C_{60}F_{48}$ (isolated molecule)	5.63	8.94	3.31

6.4.6 C_{60} on the hydroxylated surface

The form of the –OH-terminated surface chosen was the (001)-(2×1):OH 'parallel' configuration, in which –OH groups replace the –H termination on the dimerised (001) diamond surface, as described in the previous chapter.

Recall that the earlier calculations (Sec. 5.4.8) found an 'anti-parallel' arrangement of the surface O–H groups to be lower in energy than this 'parallel' configuration; however, it is only the 'parallel' surface that tessellates correctly under the quasi-hexagonal supercell scheme used to study C_{60} on the surface. Repeating the 'anti-parallel' surface with the quasi-hexagonal lattice vectors results in –OH groups that oppose each other at the interfaces of repeating supercells, which causes problems with the atomic relaxation. Nevertheless, these two forms of hydroxylated surface have nearly identical electronic band structures, and so this choice is not expected to have any significant consequences. Furthermore, hydroxylated surfaces in practice are likely to have a mixture of these two and other possible forms of –OH-group orientation (see Sec. 5.4.9 for instance).

As with the H-terminated substrate, the C_{60} molecule perturbed the structure of the underlying –OH-surface only very slightly. The H atoms underneath the molecule were pushed downward by 0.11 Å with respect to those furthest from the molecule, while the O atoms nearest the molecule were displaced downward by only 0.08 Å with respect to those furthest away. The *c*-separation between the lowermost atoms of the C_{60} and the closest H atoms on the diamond surface is 1.8 Å in the relaxed structure, which can be seen in Fig. 6.11.

The –OH-terminated diamond surface could be considered as quite chemically reactive, since the strong $–O^{\delta-}–H^{\delta+}$ dipoles are exposed to chemical attack. Nevertheless, no chemical interaction with C_{60} has been seen in the present calculations.

The C_{60} molecule was originally placed so that the minimum c-separation (as defined previously) was 1.5 Å, and during the structural optimisation, the molecule was quickly repelled to the aforementioned 1.8 Å. However, it of course remains a possibility that a chemical reaction could be observed if the molecule were to be initially placed much closer to the substrate, say to within a typical C–H bond length of 1.1 Å.

The plane-averaged electrostatic potential for this system is shown in Fig. 6.12, where it is compared against that found for bulk diamond with the same spatial orientation. The presence of the C_{60} molecule is immediately obvious, although it is clear that the middle layers of the diamond slab remain in an almost-perfectly bulk-like environment.

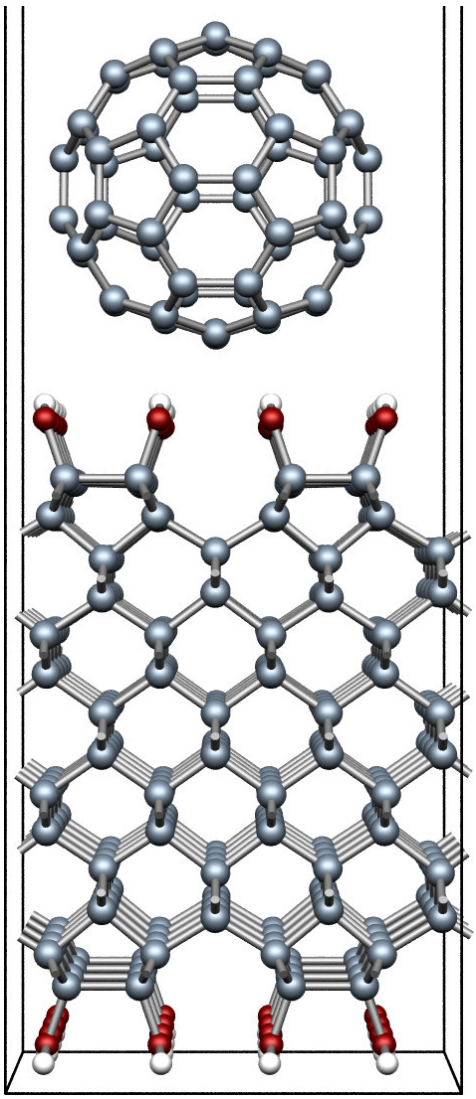

Figure 6.11: Relaxed atomic geometry for C_{60} on top of the hydroxylated diamond (001) surface. The supercell edges are shown as black lines, although it extends much higher than the top of the figure.

It initially proved quite difficult to find a well-converged charge density for this system. This can be seen in Fig. 6.13, which plots energy changes during the self-consistency cycles involved in the first few iterations of structural optimisation. The first cycle was very slow to converge, with large energy differences between the input and output charge densities. However, the convergence in the subsequent cycles was much faster, and the final charge density is not thought to be in error. To improve self-consistency in this system, a filling of $k_B T = 0.04$ eV was used for the electronic energy levels in preliminary calculations, while the 'normal' value of 0.01 eV was used for the final runs.

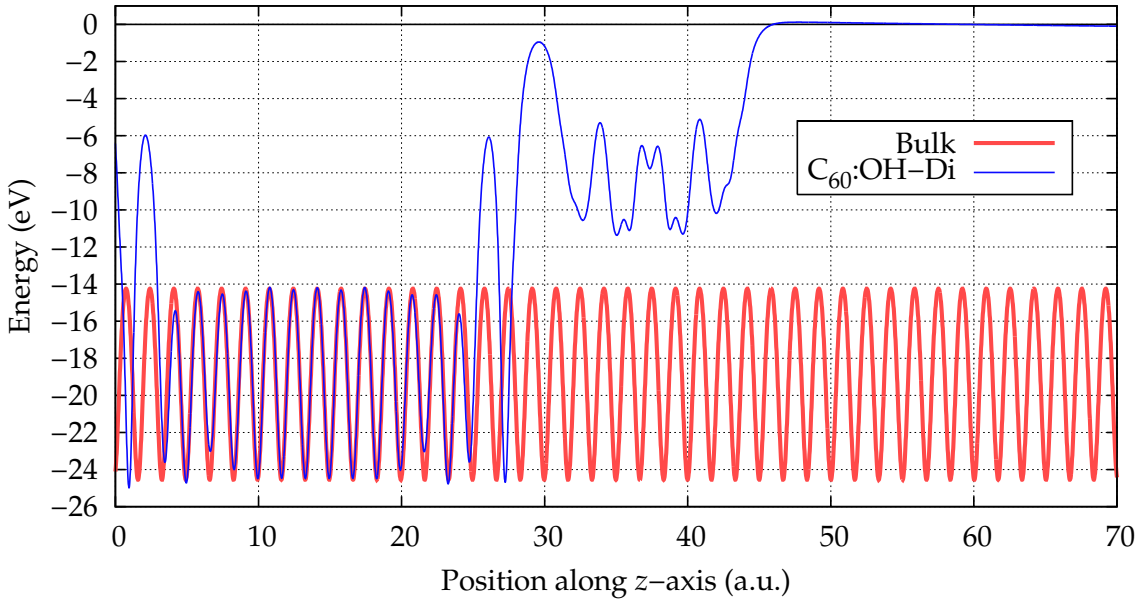

Figure 6.12: Plane-averaged electrostatic potentials for C_{60} on the hydroxylated diamond surface (C_{60}:OH-Di) and bulk diamond. The zero of the energy scale is the vacuum level found from the C_{60}:OH-Di system, while the potential of bulk diamond has been aligned with that found in the middle of the C_{60}:OH-Di diamond slab. The supercell extends in the z direction up to 75.6 a.u.

Furthermore, the first few iterations of structural optimisation were performed using Γ-point sampling of the BZ and a contracted basis set for the electronic orbitals of bulk-like C atoms.

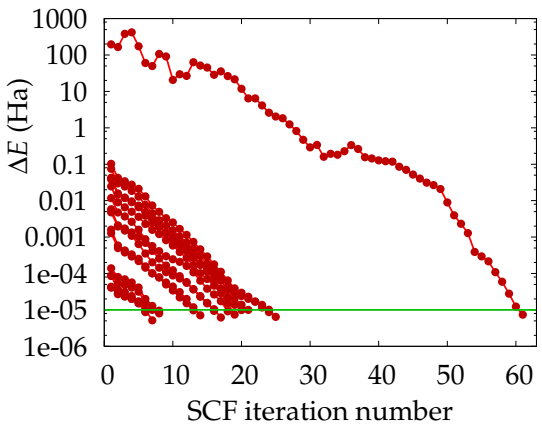

Figure 6.13: Energy changes during the several self-consistency cycles associated with the structural optimisation of C_{60} on the hydroxylated (001) diamond surface.

The electronic band structure for C_{60} on the (001)-(2×1):OH surface is shown in Fig. 6.14. The lowest unoccupied states are due to the C_{60} monolayer, and begin about 0.8 eV above the VBM for bulk diamond. The bulk-diamond-like states in the combined system have been depressed by about 0.2 eV — which is similar to that seen in calculations on the hydroxylated surface alone (Sec. 5.4.8) — and so they are separated from the unoccupied C_{60} states by 1.0 eV. Therefore, the gap to electron transfer in this system appears to be around or just less than 1 eV.

This gap suggests that $C_{60}F_{36}$ (or a more-highly fluorinated fullerene such as $C_{60}F_{48}$) may have an EA high enough to render it capable of extracting electrons from a *hydroxylated* diamond surface. However, such a system has not been explicitly modelled in this work.

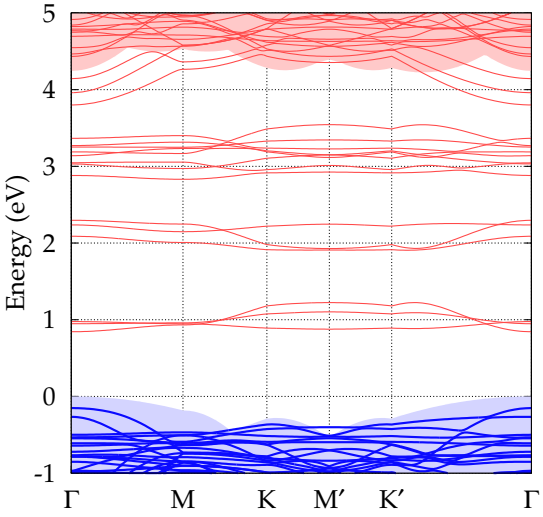

Figure 6.14: Electronic band structure for C_{60} on the (001)-(2×1):OH diamond surface. The valence-band maximum of bulk diamond is the zero of the energy scale.

6.4.7 C_{60} on the oxygenated surface

The 'ether' form of the oxygenated (001) diamond surface has been used in this study, since it is more stable than the alternative 'ketone' configuration, as detailed in the previous chapter. In the combined system containing C_{60} adsorbed on this oxygenated surface, the molecule caused only a very small disturbance to the substrate, as with the other two systems. The (two) oxygen atoms immediately below the molecule were depressed by only 0.06 Å with respect to those furthest from the C_{60}. In the relaxed geometry (shown in Fig. 6.15), the *c*-separation between the underside of the C_{60} and the O atoms below was $\sim$ 2.2 Å.

The electronic band structure for C_{60} on (001)-(1×1):O is shown in Fig. 6.16. Careful wavefunction analysis was required to reveal the origin of the various states, and the results are as follows.

The diamond valence-band states in this combined system were identified and have been perturbed to lie slightly below the VBM of perfect bulk diamond; the latter being set as the zero of the energy scale. Extending up to $\sim$ 1 eV above the bulk VBM are occupied states that are due to the oxygen termination of the surface in the slab system. These states were of course also seen in simulations of the surface without the C_{60} layer present (Sec. 5.4.7). Between about 1–1.5 eV above the VBM, a band of occupied C_{60} states appears, exhibiting some dispersion and a degree of mixing with the oxygen-related surface states. Around 2.5 eV above the VBM lies the uppermost occupied band of states related to the C_{60} monolayer.

The first *unoccupied* states begin about 2.8 eV above the diamond VBM, and are again surface states due to the –O– termination. Just above 4 eV from the VBM, the lowest unoccupied C_{60} states appear, mixed in with some of the aforementioned surface states. Immediately above this empty band of C_{60} states, the bulk diamond conduction band begins; recall however that the bulk diamond bandgap is underestimated at this level of theory, being $\sim$ 4.2 eV rather than the experimental 5.5 eV (Sec. 4.2.2).

Most importantly, the minimum of the C_{60} LUMO lies $\sim$ 4 eV above the diamond valence band maximum, at the Γ point of the calculation; therefore, this is the energy gap for electron transfer and the formation of a mobile hole in the diamond. If the C_{60} excited states are in error due to the method, this gap is most likely to be slightly larger. These results are also consistent with the aforementioned experimental studies, in which no increase in surface conductivity was observed when C_{60} was evaporated onto oxygen-terminated diamond samples [422, 423].

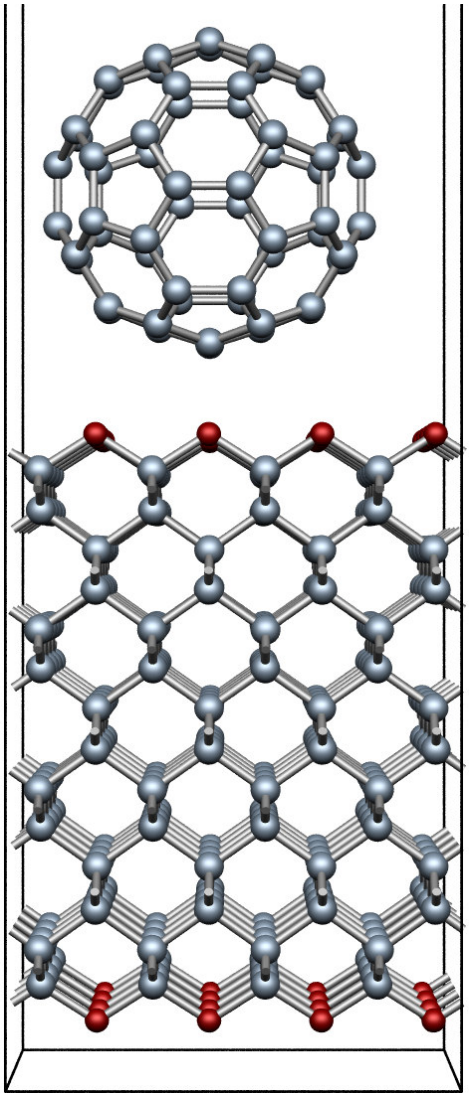

Figure 6.15: Relaxed atomic geometry for C_{60} on the 'ether' oxygenated diamond (001) surface. The supercell extends beyond the top of the figure.

It is also interesting to note that the lowest unoccupied states in the system are those of the oxygenated diamond surface, while the highest occupied states are due to the C_{60}, and that the minimum separation between these is just 0.2 eV. This raises the possibility of *C_{60}-to-diamond* electron transfer at high temperatures. However, an electron so transferred to the diamond would most likely be localised on the C–O–C termination, hence this 'opposite' transfer-doping effect should not give rise to useful *n*-type doping of the diamond. This would be especially true if there were disorder in the oxygen termination, involving for example the presence of both C–O–C and C=O groups. Once in this surface state, the electron would have to jump a further gap of

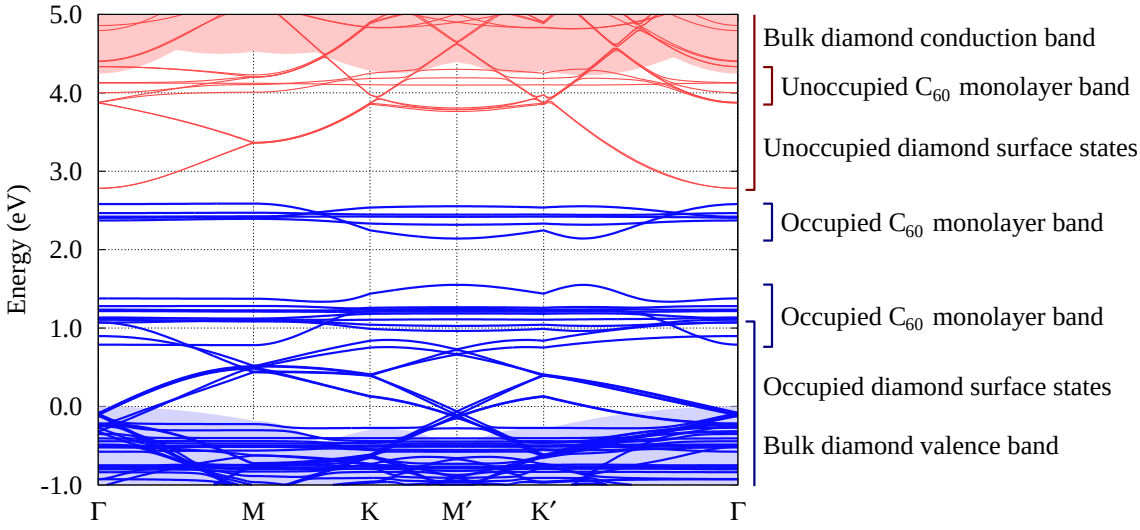

Figure 6.16: Electronic band structure for C_{60} on the (001)-(1×1):O diamond surface. The labels identifying states are the results of wavefunction analysis.

$\sim$ 1.5 eV to occupy a bulk-diamond conduction-band state. Nevertheless, the charging of the C_{60} and the surface due to such an electron transfer would help in binding the molecule to the substrate, and raises further questions about a chemical interaction in this system.

6.5 Chapter summary

To summarise, results have been presented regarding the modelling of: molecular and solid C_{60}; a near-monolayer of C_{60} covering the hydrogenated, hydroxylated, and hydrogenated (001) diamond surfaces; molecular $C_{60}F_{36}$ and $C_{60}F_{48}$; and $C_{60}F_{36}$ molecules on the hydrogenated (001) diamond surface.

Dispersion of the electronic levels in C_{60} as it undergoes a molecule-to-solid transition increases the material's electron affinity, and hence the potential for transfer doping. Clear evidence for spontaneous diamond-to-C_{60} electron transfer is seen for around one monolayer of C_{60} coverage, although the underestimation of the energy gap inherent in the model suggests that such a transfer will occur in practice for greater coverages. Experimentally, appreciable surface conductivity was obtained for a C_{60} coverage of around two monolayers or more [422].

The electron affinity of $C_{60}F_{36}$ is greater than that of C_{60}, and an electron transfer is predicted for $C_{60}F_{36}$ on the diamond surface, even for individual molecules. Individual molecules of $C_{60}F_n$ with $n > 36$ (such as $C_{60}F_{48}$) are likely to spontaneously extract electrons from diamond. Again, this finding was later supported by experiments [423].

With an –OH-terminated diamond substrate, the C_{60} LUMO and the diamond VBM are separated by just under 1 eV, rendering transfer doping with C_{60} unlikely under normal conditions. However, transfer doping may be possible on this surface with the use of a heavily fluorinated fullerene. The fully oxygenated surface effectively forbids electron transfer, since there is a large energy gap of $\sim$ 4 eV between the C_{60} LUMO and the diamond VBM. Interestingly, the gap to a reverse electron transfer may be quite small.

In every case, no chemical interaction is expected between C_{60} and the substrate, although calculation of the reaction barriers lies beyond the scope of the present study.

The results presented in this chapter have potential implications for the creation of surface-conductive channels through patterning the diamond surface with hydrogen- and oxygen-terminated regions.

Chapter 7

Concluding remarks

THE purpose of this thesis has been to report the results of using density-functional-theory calculations to determine the structural and electronic properties of: potential shallow-donor defects in bulk diamond; hydrogen and oxygen on diamond surfaces; and large, fullerene-based transfer-dopant molecules adsorbed on diamond substrates.

7.1 Summary

7.1.1 Bulk doping

First, the AIMpro theoretical method has been shown to accurately reproduce the basic, observed properties of the structure and electronics of bulk diamond, which is essential before calculations on point defects can be performed. The marker method, employed to determine the donor levels of impurity defects, was shown to reproduce the well-known donor level of the common nitrogen substitutional with remarkable accuracy.

In the search for a donor defect with an activation energy less than that of the phosphorus impurity currently used in practice, the pnictogens, chalcogens, and their hydrogen complexes have been modelled as substitutional defects in diamond. The results show the anticipated size effect, in that larger impurities have donor electrons that are more loosely bound. However, the calculations suggest that only arsenic and antimony possess donor levels that are unambiguously shallower than that of phosphorus. As expected, the

chalcogen-hydrogen complexes are found to be shallower donors than the bare chalcogen impurities, although even the most shallow complex obtained (tellurium-hydrogen) has a donor level only comparable with that of the bare phosphorus substitutional.

Unfortunately, the difficulty in incorporating impurities into the tight lattice of diamond is most likely to increase with the increasing size of the atom. Furthermore, large impurities are likely to complex with vacancies, and for instance the arsenic-vacancy complex has been shown to have an extremely deep donor level. Nevertheless, such dire predictions were also made for the phosphorus impurity, yet it is enjoying much success as an uncompensated donor in practice. It is worth noting that the growth procedure by which phosphorus is incorporated is a non-equilibrium process, and is poorly understood at present. Perhaps arsenic could be introduced into diamond via a similar growth mechanism, without complexing with vacancies, and proceed to exhibit shallow-donor behaviour.

In order to investigate the apparent shallow-donor activity arising in experiment for some deuterated, boron-doped diamond samples, several complexes of boron with multiple atoms of hydrogen were modelled. Unfortunately, none of the boron-hydrogen complexes studied were found to act as shallow donors, and neither did any of the complexes of boron with native defects. In addition, the most likely candidate defect for explaining the experimental behaviour (the B–H_2 complex) was shown to have a structural stability inconsistent with the results of annealing experiments. Even in the light of other theoretical investigations, the experimental observations are still lacking a reliable theoretical explanation.

The final investigation with regard to bulk donors concerned the examination of the exotic N–Si_4 defect, suggested in other theoretical work as a potential shallow donor. The present results of AIMpro modelling do not support the conclusion that this centre is a shallow donor; rather they suggest that it should behave similarly to the bare phosphorus impurity. Furthermore, despite the finding that this defect is strongly bound, the relatively complicated atomic arrangement is likely to render its formation in practice extremely unlikely.

7.1.2 Diamond surfaces

An understanding of the nature of a material's surface is important in the manufacture of many practical devices. The common (001) surface of diamond was studied in this investigation, initially to gain an understanding of its electronic properties for later application to the transfer-doping problem. However, the study was extended to include the other low-index diamond surfaces, and to investigate the effect that oxygen has on the hydrogenated diamond surface.

The models that were used were shown to accurately represent bulk diamond beneath the surface, and so the effects of changing the surface termination and orientation were independently investigated. In particular, the structures of the clean and hydrogenated surfaces were presented in enough detail to facilitate comparison with experimental measurements such as those obtained using electron or X-ray diffraction techniques.

The hydrogen-terminated surfaces were confirmed to exhibit the negative electron affinities found in other theoretical work and observed in experiment. However, this and other theoretical works calculate a much larger negative electron affinity than that measured on real samples. This may be explained somewhat by the considerable difficulty in obtaining atomically flat surfaces without contamination in practice. Meanwhile, complete oxygen termination of the diamond surfaces was shown to reproduce the large positive electron affinities found in other work, while a detailed examination of the atomic geometry was also given.

Hydrogen termination introduces unoccupied electronic states into the upper half of the surface bandgap. A method for correcting the underestimation in energy of such states was presented, and the results of applying it indicate that these surface states will lie close to the vacuum level in energy. These states may act as traps for conduction-band electrons that would otherwise escape from the diamond, in which case band bending could occur, having implications for electron emission applications.

The hydroxylated diamond surface was studied in some detail, and is found to be rather stable. However, an overestimate in the strength of hydrogen bonding on this surface might weaken this claim to some degree. This surface termination is shown to largely remove surface-related states from the bandgap and give a small negative electron affinity.

7.1.3 Transfer doping

Following on from a suggestion given in previous theoretical work, C_{60} adsorbed on the diamond surface was modelled with a view to solving the problem of finding a stable transfer dopant for diamond. A near-monolayer of C_{60} was modelled on the hydrogenated, hydroxylated, and oxygenated (001) diamond surfaces, and the electronic levels in each of these systems were carefully examined.

C_{60} was found to spontaneously extract an electron from the hydrogen-terminated surface, as was seen in the earlier study. However, the finding of the previous work may be due to the limitations of using the cluster formalism, whereas in the present, supercell calculations, the formation of a closely packed monolayer of C_{60} is shown to be essential in order to induce the electron transfer. The effect is found to rely on both the dispersion of the electronic levels in C_{60} as it undergoes a molecule-to-solid transition, and the shifting of the energy levels as the monolayer of solid C_{60} interacts with the diamond surface. These findings were later supported by experiments in which several monolayers of C_{60} coverage were required to achieve electron transfer and create significant *p*-type surface conductivity on the diamond.

No electron transfer was found for C_{60} on the hydroxylated surface, although the energy gap to such a transfer is small enough that adsorbate materials with greater electron affinities might be capable of transfer doping a diamond sample having this surface termination. No chemical interaction of C_{60} was seen with this, or indeed the other surface terminations.

On the oxygenated diamond surface, the energy gap to electron transfer is sufficiently large to effectively render it impossible when using C_{60} as the adsorbate. However, it is interesting to note that an electron transfer from C_{60} to the unoccupied, oxygen-related states on this surface may be a possibility.

Since fluorination of fullerenes is known to increase their electron affinities, and hence their potential for extracting electrons from diamond, molecules of $C_{60}F_{36}$ and $C_{60}F_{48}$ were also studied. Modelling $C_{60}F_{36}$ on the hydrogen-terminated diamond substrate suggested that electron transfer could be achieved by individual molecules without having to form monolayer coverages, while the electronic properties of gas-phase $C_{60}F_{48}$

allude to it being even more efficient as a transfer dopant for diamond. These predictions were also subsequently supported by experiments in which molecular $C_{60}F_{48}$ was observed to induce high surface conductivity on diamond.

A further prediction is that $C_{60}F_{48}$ might be capable of extracting electrons from a hydrogenated diamond surface that has been contaminated with oxygen so as to contain –OH terminating groups.

7.2 Outlook

> "I know, for I told me so, and I'm sure each of you quite agrees:
> The more it stays the same, the less it changes."
>
> — Spiñal Tap, 'The Majesty of Rock'

Hopefully, it is clear that studies such as this provoke at least as many new questions as they provide answers for. Regarding the search for a shallow donor in bulk diamond, it remains to be seen whether or not arsenic can be grown into diamond and lead to useful electrical activity. The gradual success of incorporating phosphorus into diamond should provide suitable encouragement, and the author knows of at least one research group that are currently looking into doping diamond with arsenic. Meanwhile, more work on the controversial sulphur-hydrogen complex would certainly be welcomed.

Clearly, many more studies — both theoretical and experimental — need to be undertaken with regard to the supposed *n*-type activity in deuterated, boron-doped diamond samples. While other laboratories purportedly confirm the shallow-donor activity of certain samples, it appears that the reproducibility needs improving. Meanwhile, theoretical investigations could be extended to look at a wider range of boron- and hydrogen-related defects in the search for a complex that fits the experimental observations.

The engineering of high *p*-type surface conductivity on diamond via transfer doping with fullerenes is an exciting area of research. Recent reports submit that the *stability* of the fluorinated fullerenes on the diamond surface is a matter of concern, since the molecules evaporate off rather easily. However, the binding energy of $C_{60}F_{36}$ to the diamond substrate was not explicitly calculated in this investigation.

Furthermore, unpublished observations show the stability of the plain C_{60} monolayers on diamond to *increase* with time. It has been suggested that this effect is due to atmospheric oxygen, activated by the ultraviolet component of sunlight, helping to bind the C_{60} molecules together by covalently bridging between them. This premise could quite easily be investigated using the current theoretical method, which would help to converge the search for a stable transfer dopant for diamond.

It should be mentioned that there are many other possible transfer dopants, including organic molecules, which may exhibit interesting fluorescent properties. Certainly, the complexity of such molecules presents an interesting challenge to the theoretical modelling of their interaction with diamond.

Further work could also include the modelling of carbon *nanotubes* [427] on diamond substrates, to get an insight into how to exploit the remarkable properties of both the substrate and adsorbate in such an interface. Very recently, first-principles calculations have been used to model carbon nanotubes adsorbed on clean and hydrogen-terminated silicon substrates [428, 429, **?**, 429]. The periodicity of nanotubes can easily be exploited in supercell calculations to yield manageable systems.

When the apparently never-ending improvements in computational power are combined with research into more efficient algorithms in the field of computer science, many more problems in atomic-scale computational physics become tractable. While this means that standard calculations can be performed much faster, and so a wider number of configurations for one defect can be studied in the same time period, it also means that larger, more complex systems can be treated at higher levels of theory. These advantages will permit the *ab initio* study of systems with increasing complexity, and eventually those with truly fascinating properties.

Bibliography

[1] V. D. Blank *et al.*, Structures and physical properties of superhard and ultrahard 3D polymerized fullerites created from solid C_{60} by high pressure high temperature treatment, Carbon **36(5–6)**, 665 (1998).

[2] V. Blank, M. Popov, G. Pivovarov, N. Lvova, K. Gogolinsky, and V. Reshetov, Ultrahard and superhard phases of fullerite C_{60}: comparison with diamond on hardness and wear, Diamond and Related Mater. **7(2–5)**, 427 (1998).

[3] A. Badzian, Diamond challenged by hard materials: a reflection on developments in the last decades, Mater. Chem. Phys. **72(2)**, 110 (2001).

[4] A. Badzian, T. Badzian, R. Roy, and W. Drawl, Silicon carbonitride, a new hard material and its relation to the confusion about 'harder than diamond' C_3N_4, Thin Solid Films **354(1–2)**, 148 (1999).

[5] T. Malkow, Critical observations in the research of carbon nitride, Mater. Sci. Eng. A **302(2)**, 311 (2001).

[6] S. F. Matar and M. Mattesini, Ab initio search of carbon nitrides, isoelectronic with diamond, likely to lead to new ultra hard materials, Comptes Rendus de l'Académie des Sciences — Series IIC — Chemistry **4(4)**, 255 (2001).

[7] S. Matsumoto, E.-Q. Xie, and F. Izumi, On the validity of the formation of crystalline carbon nitrides, C_3N_4, Diamond and Related Mater. **8(7)**, 1175 (1999).

[8] L.-W. Yin, M.-S. Li, G. Luo, J.-L. Sui, and J.-M. Wang, Nanosized beta carbon nitride crystal through mechanochemical reaction, Chem. Phys. Lett. **369(3–4)**, 483 (2003).

[9] S. M. Sze, Physics of Semiconductor Devices, 2nd ed. (Wiley-Interscience, New York, 1981).

[10] CRC handbook of chemistry and physics, 75th ed., edited by D. R. Lide (CRC Press, London, 1995).

[11] C. Frondel and U. B. Marvin, Lonsdaleite, a new hexagonal polymorph of diamond, Nature **214**, 587 (1967).

[12] C. Frondel and U. B. Marvin, Lonsdaleite, a hexagonal polymorph of diamond, Am. Min. **52**, 1576 (1967).

[13] A. El Goresy, L. S. Dubrovinsky, P. Gillet, S. Mostefaoui, G. Graup, M. Drakopoulos, A. S. Simionovici, V. Swamy, and V. L. Masaitis, A new natural, super-hard, transparent polymorph of carbon from the Popigai impact crater, Russia, Comptes Rendus Geosciences **335(12)**, 889 (2003).

[14] J. Singh, Physics of semiconductors and their heterostructures (McGraw-Hill, New York, 1993).

[15] J. Siebert, F. Guyot, and V. Malavergne, Diamond formation in metal-carbonate interactions, Earth and Planetary Science Letters **229(3–4)**, 205 (2005).

[16] O. Fukunaga, T. Miyake, and N. Ohashi, Formation of diamond and graphite at high pressure using glassy carbon source, Diamond and Related Mater. **14(2)**, 160 (2005).

[17] Z. Z. Liang, X. Jia, C. Y. Zang, P. W. Zhu, H. A. Ma, and G. Z. Ren, The influences of N and H on diamond synthesized with Ni-Mn-Co catalyst by HPHT, Diamond and Related Mater. **14(2)**, 243 (2005).

[18] C. J. Tang, A. J. Neves, and M. C. Carmo, Characterization of chemical vapour deposited diamond films: correlation between hydrogen incorporation and film morphology and quality, J. Phys.: Condens. Matter **17(10)**, 1687 (2005).

[19] J. G. Buijnsters, P. Shankar, W. J. P. van Enckevort, J. J. Schermer, and J. J. ter Meulen, Adhesion analysis of polycrystalline diamond films on molybdenum by means of scratch, indentation and sand abrasion testing, Thin Solid Films **474(1–2)**, 186 (2005).

[20] J. R. Rabeau, S. T. Huntington, A. D. Greentree, and S. Prawer, Diamond chemical-vapor deposition on optical fibers for fluorescence waveguiding, Appl. Phys. Lett. **86**, 134104 (2005).

[21] M. Rossi, M. L. Terranova, S. Piccirillo, V. Sessa, and D. Manno, Meso- and nano-scale investigation of carbon fibers coated by nano-crystalline diamond, Chem. Phys. Lett. **402(4–6)**, 340 (2005).

[22] W. Wang, T. Moses, R. C. Linares, J. E. Shigley, M. Hall, and J. E. Butler, Gem-quality synthetic diamonds grown by a chemical vapor deposition (CVD) method, Gems Gemol. **39(4)**, 268 (2003).

[23] E. M. Winkler, Stone: Properties, Durability in Man's Environment, Applied Mineralogy, 2nd ed. (Springer-Verlag, New York, 1975).

[24] ASM Engineered Materials Reference Book, 2nd ed., edited by M. L. Bauccio (ASM International, Materials Park, Ohio, 1994).

[25] S.-F. Wang, Y.-F. Hsu, J.-C. Pu, J. C. Sung, and L. G. Hwa, Determination of acoustic wave velocities and elastic properties for diamond and other hard materials, Mater. Chem. Phys. **85(2–3)**, 432 (2004).

[26] H. J. McSkimin and P. Andreatch, Jr., Elastic moduli of diamond as a function of pressure and temperature, J. Appl. Phys. **43(7)**, 2944 (1972).

[27] S. A. Solin and A. K. Ramdas, Raman spectrum of diamond, Phys. Rev. B **1(4)**, 1687 (1970).

[28] Synthetic Diamond: Emerging CVD Science and Technology, Electrochemical Society Series, edited by K. E. Spear and J. P. Dismukes (John Wiley & Sons, Inc., New York, 1994).

[29] D. F. Edwards and H. R. Philipp, in Handbook of Optical Constants of Solids, edited by E. D. Palik (Academic Press, New York, 1985), Vol. 1, p. 665.

[30] Landolt-Börnstein: Numerical Data and Functional Relationships in Science and Technology. Group III: Condensed Matter, edited by O. Madelung, M. Shulz, and H. Weiss (Springer-Verlag, Berlin, 1982), Vol. 17: Physics of Group IV Elements and III-V Compounds. Part A.

[31] S. Logothetidis, J. Petalas, H. M. Polatoglou, and D. Fuchs, Origin and temperature dependence of the first direct gap of diamond, Phys. Rev. B **46(8)**, 4483 (1992).

[32] H. R. Philipp and E. A. Taft, Optical properties of diamond in the vacuum ultraviolet, Phys. Rev. **127(1)**, 159 (1962).

[33] R. A. Roberts and W. C. Walker, Optical study of the electronic structure of diamond, Phys. Rev. **161(3)**, 730 (1967).

[34] G. A. J. Amaratunga, A dawn for carbon electronics?, Science **297**, 1657 (2002).

[35] J. Isberg, J. Hammersberg, E. Johansson, T. Wikström, D. J. Twitchen, A. J. Whitehead, S. E. Coe, and G. A. Scarsbrook, High carrier mobility in single-crystal plasma-deposited diamond, Science **297**, 1670 (2002).

[36] S. Koizumi, K. Watanabe, M. Hasegawa, and H. Kanda, Ultraviolet emission from a diamond pn junction, Science **292**, 1899 (2001).

[37] M. Suzuki, H. Yoshida, N. Sakuma, T. Ono, T. Sakai, and S. Koizumi, Electrical characterization of phosphorus-doped *n*-type homoepitaxial diamond layers by Schottky barrier diodes, Appl. Phys. Lett. **84(13)**, 2349 (2004).

[38] A. Tajani, C. Tavares, M. Wade, C. Baron, E. Gheeraert, E. Bustarret, S. Koizumi, and D. Araujo, Homoepitaxial {111}-oriented diamond pn junctions grown on B-doped Ib synthetic diamond, Phys. Status Solidi A **201(11)**, 2462 (2004).

[39] C. Tavares, A. Tajani, C. Baron, F. Jomard, S. Koizumi, E. Gheeraert, and E. Bustarret, {111}-oriented diamond films and p/n junctions grown on B-doped type Ib substrates, Diamond and Related Mater. **14(3–7)**, 522 (2005).

[40] C. Saguy, R. Kalish, C. Cytermann, Z. Teukam, J. Chevallier, F. Jomard, A. Tromson-Carli, J. E. Butler, C. Baron, and A. Deneuville, n-type diamond with high room temperature electrical conductivity by deuteration of boron doped diamond layers, Diamond and Related Mater. **13(4–8)**, 700 (2004).

[41] Z. Teukam *et al.*, Shallow donors with high n-type electrical conductivity in homoepitaxial deuterated boron-doped diamond layers, Nature Mater. **2**, 482 (2003).

[42] J. P. Goss, P. R. Briddon, S. J. Sque, and R. Jones, Boron-hydrogen complexes in diamond, Phys. Rev. B **69(16)**, 165215 (2004).

[43] Y. Dai, C. X. Yan, A. Y. Li, Y. Zhang, and S. H. Han, Effects of hydrogen on electronic properties of doped diamond, Carbon **43(5)**, 1009 (2005).

[44] S. Gupta, B. R. Weiner, and G. Morell, Room-temperature electrical conductivity studies of sulfur-modified microcrystalline diamond thin films, Appl. Phys. Lett. **83(3)**, 491 (2003).

[45] R. Kalish, A. Reznik, C. Uzan-Saguy, and C. Cytermann, Is sulfur a donor in diamond?, Appl. Phys. Lett. **76(6)**, 757 (2000).

[46] T. Miyazaki and H. Okushi, A theoretical study of a sulfur impurity in diamond, Diamond and Related Mater. **10**, 449 (2001).

[47] T. Miyazaki and H. Okushi, Theoretical modeling of sulfur-hydrogen complexes in diamond, Diamond and Related Mater. **11(3–6)**, 323 (2002).

[48] T. Miyazaki, Theoretical studies of sulfur and sulfur-hydrogen complexes in diamond, Phys. Status Solidi A **193(3)**, 395 (2002).

[49] T. Nishimatsu, H. Katayama-Yoshida, and N. Orita, Ab initio study of donor-hydrogen complexes for low-resistivity n-type diamond semiconductor, Jpn. J. Appl. Phys. Part 1 **41(4A)**, 1952 (2002).

[50] D. Saada, J. Adler, and R. Kalish, Sulfur: a potential donor in diamond, Appl. Phys. Lett. **77(6)**, 878 (2000).

[51] I. Sakaguchi, M. N.-Gamo, Y. Kikuchi, E. Yasu, H. Haneda, T. Suzuki, and T. Ando, Sulfur: a donor dopant for *n*-type diamond semiconductors, Phys. Rev. B **60(4)**, R2139 (1999).

[52] E. Trajkov, S. Prawer, J. E. Butler, and S. M. Hearne, Charge trap levels in sulfur-doped chemical-vapor-deposited diamond with applications to ultraviolet dosimetry, J. Appl. Phys. **98(2)**, 023704 (2005).

[53] L. G. Wang and A. Zunger, Phosphorus and sulphur doping of diamond, Phys. Rev. B **66(16)**, 161202 (2002).

[54] J. B. Cui, J. Ristein, and L. Ley, Electron affinity of the bare and hydrogen covered single crystal diamond (111) surface, Phys. Rev. Lett. **81(2)**, 429 (1998).

[55] F. Maier, J. Ristein, and L. Ley, Electron affinity of plasma-hydrogenated and chemically oxidized diamond (100) surfaces, Phys. Rev. B **64(16)**, 165411 (2001).

[56] J. Robertson and M. J. Rutter, Band diagram of diamond and diamond-like carbon surfaces, Diamond and Related Mater. **7**, 620 (1998).

[57] F. Maier, M. Riedel, B. Mantel, J. Ristein, and L. Ley, Origin of surface conductivity in diamond, Phys. Rev. Lett. **85(16)**, 3472 (2000).

[58] C. E. Nebel, F. Ertl, C. Sauerer, M. Stutzmann, C. F. O. Graeff, P. Bergonzo, O. A. Williams, and R. B. Jackman, Low temperature properties of the p-type surface conductivity of diamond, Diamond and Related Mater. **11(3–6)**, 351 (2002).

[59] J. Ristein, F. Maier, M. Riedel, M. Stammer, and L. Ley., Diamond surface conductivity experiments and photoelectron spectroscopy, Diamond and Related Mater. **10(3–7)**, 416 (2001).

[60] M. I. Landstrass and K. V. Ravi, Resistivity of chemical vapor deposited diamond films, Appl. Phys. Lett. **55(10)**, 975 (1989).

[61] J. S. Foord, C. H. Lau, M. Hiramatsu, R. B. Jackman, C. E. Nebel, and P. Bergonzo, Influence of the environment on the surface conductivity of chemical vapor deposition diamond, Diamond and Related Mater. **11(3–6)**, 856 (2002).

[62] M. Riedel, J. Ristein, and L. Ley, The impact of ozone on the surface conductivity of single crystal diamond, Diamond and Related Mater. **13(4–8)**, 746 (2004).

[63] M. Born and J. R. Oppenheimer, Ann. Physik (Leipzig) **84**, 457 (1927).

[64] J. K. L. MacDonald, Successive approximations by the Rayleigh-Ritz variation method, Phys. Rev. **43(10)**, 830 (1933).

[65] V. Fock, Z. Phys. **61**, 126 (1930).

[66] C. C. J. Roothaan, New developments in molecular orbital theory, Rev. Mod. Phys. **23(2)**, 69 (1951).

[67] J. C. Slater, Quantum Theory of Molecules and Solids (McGraw-Hill, New York, 1963–1974), Vol. 2: Symmetry and Energy Bands in Crystals.

[68] A. M. Stoneham, Theory of Defects in Solids: Electronic Structure of Defects in Insulators and Semiconductors, Oxford Classic Texts in the Physical Sciences (Oxford University Press, Oxford, 2001).

[69] J. C. Slater, The theory of complex spectra, Phys. Rev. **34(10)**, 1293 (1929).

[70] R. McWeeny, Methods of Molecular Quantum Mechanics (Academic Press, New York, 1992).

[71] J. M. Thijssen, Computational Physics (Cambridge University Press, Cambridge, 1999).

[72] T. Koopmans, Über die zuordnung von wellenfunktionen und eigenwerten zu den einzelnen elektronen eines atoms, Physica **1**, 104 (1934).

[73] P. Hohenberg and W. Kohn, Inhomogeneous electron gas, Phys. Rev. **136(3B)**, B864 (1964).

[74] W. Kohn and L. J. Sham, Self-consistent equations including exchange and correlation effects, Phys. Rev. **140(4A)**, A1133 (1965).

[75] R. G. Parr and W. Yang, Density-functional theory of atoms and molecules (Oxford University Press, Oxford, 1989).

[76] J. P. Perdew and A. Zunger, Self-interaction correction to density-functional approximations for many-electron systems, Phys. Rev. B **23(10)**, 5048 (1981).

[77] U. von Barth and L. Hedin, A local exchange-correlation potential for the spin polarized case, J. Phys. C **5(13)**, 1629 (1972).

[78] D. Ceperley, Ground state of the fermion one-component plasma: a Monte Carlo study in two and three dimensions, Phys. Rev. B **18(7)**, 3126 (1978).

[79] D. M. Ceperley and B. J. Alder, Ground state of the electron gas by a stochastic method, Phys. Rev. Lett. **45(7)**, 566 (1980).

[80] S. J. Vosko, L. Wilk, and M. Nusair, Accurate spin-dependent electron liquid correlation energy for local spin density calculations: a critical analysis, Chinese J. Phys. **58**, 1200 (1980).

[81] J. P. Perdew and Y. Wang, Accurate and simple analytic representation of the electron-gas correlation-energy, Phys. Rev. B **45(23)**, 13244 (1992).

[82] J. P. Perdew, in Electronic Structure of Solids '91, edited by P. Ziesche and H. Eschrig (Akademie Verlag, Berlin, 1991).

[83] J. P. Perdew, K. Burke, and M. Ernzerhof, Generalized gradient approximation made simple, Phys. Rev. Lett. **77(18)**, 3865 (1996).

[84] J. P. Perdew, K. Burke, and Y. Wang, Generalized gradient approximation for the exchange-correlation hole of a many-electron system, Phys. Rev. B **54(23)**, 16533 (1996).

[85] W. A. Harrison, Pseudopotentials in the Theory of Metals (W. A. Benjamin, Inc., New York, 1966).

[86] D. Brust, Methods in Computational Physics (Academic Press, New York, 1968), Vol. 8, p. 33.

[87] V. Heine, in Solid State Physics (Academic Press, New York, 1970), Vol. 24, p. 1, the Pseudopotential Concept.

[88] W. E. Pickett, Pseudopotential methods in condensed matter applications, Comput. Phys. Rep. **9(3)**, 115 (1989).

[89] S. G. Louie, S. Froyen, and M. L. Cohen, Nonlinear ionic pseudopotentials in spin-density-functional calculations, Phys. Rev. B **26(4)**, 1738 (1982).

[90] D. R. Hamann, M. Schlüter, and C. Chiang, Norm-conserving pseudopotentials, Phys. Rev. Lett. **43(20)**, 1494 (1979).

[91] G. B. Bachelet, D. R. Hamann, and M. Schlüter, Pseudopotentials that work: from H to Pu, Phys. Rev. B **26(8)**, 4199 (1982).

[92] C. Hartwigsen, S. Goedecker, and J. Hutter, Relativistic separable dual-space Gaussian pseudopotentials from H to Rn, Phys. Rev. B **58(7)**, 3641 (1998).

[93] R. Jones and P. R. Briddon, in Identification of defects in semiconductors, Vol. 51A of Semiconductors and Semimetals, edited by M. Stavola (Academic Press, San Diego, 1998), Chap. 6, pp. 287–349.

[94] P. R. Briddon and R. Jones, LDA calculations using a basis of Gaussian orbitals, Phys. Status Solidi B **217(1)**, 131 (2000).

[95] R. Jones and P. R. Briddon, The *ab initio* cluster method and the dynamics of defects in semiconductors, Semiconductors and Semimetals **51(PtA)**, 287 (1998).

[96] J. Coutinho, R. Jones, P. R. Briddon, and S. Öberg, Oxygen and dioxygen centers in Si and Ge: density-functional calculations, Phys. Rev. B **62**, 10824 (2000).

[97] H. J. Monkhorst and J. D. Pack, Special points for Brillouin-zone integrations, Phys. Rev. B **13(12)**, 5188 (1976).

[98] J. D. Pack and H. J. Monkhorst, "Special points for Brillouin-zone integrations"—a reply, Phys. Rev. B **16(4)**, 1748 (1977).

[99] C.-O. Almbladh and U. von Barth, Exact results for the charge and spin densities, exchange-correlation potentials, and density-functional eigenvalues, Phys. Rev. B **31(6)**, 3231 (1985).

[100] S. T. Epstein, A. C. Hurley, R. E. Wyatt, and R. G. Parr, Integrated and integral Hellmann-Feynman formulas, J. Chem. Phys. **47(4)**, 1275 (1967).

[101] R. P. Feynman, Forces in molecules, Phys. Rev. **56**, 340 (1939).

[102] G. Davies, The Jahn-Teller effect and vibronic coupling at deep levels in diamond, Rep. Prog. Phys. **44(7)**, 787 (1981).

[103] C. P. Flynn, Point Defects and Diffusion (Clarendon Press (Oxford University Press), Oxford, 1972).

[104] F. Reif, Fundamentals of Statistical and Thermal Physics, Fundamentals of Physics, 1st ed. (McGraw-Hill, New York, 1965).

[105] G. Makov and M. C. Payne, Periodic boundary conditions in *ab initio* calculations, Phys. Rev. B **51(7)**, 4014 (1995).

[106] G. A. Baraff and M. Schlüter, Electronic structure, total energies, and abundances of the elementary point defects in GaAs, Phys. Rev. Lett. **55(12)**, 1327 (1985).

[107] J. E. Northrup, Energetics of GaAs island formation on Si(100), Phys. Rev. Lett. **62(21)**, 2487 (1989).

[108] G.-X. Qian, R. M. Martin, and D. J. Chadi, First-principles study of the atomic reconstructions and energies of Ga- and As-stabilized GaAs(100) surfaces, Phys. Rev. B **38(11)**, 7649 (1988).

[109] J. E. Northrup and S. B. Zhang, Dopant and defect energetics: Si in GaAs, Phys. Rev. B **47(11)**, 6791 (1993).

[110] J. Coutinho, R. Jones, P. R. Briddon, S. Öberg, L. I. Murin, V. P. Markevich, and J. L. Lindström, Interstitial carbon-oxygen center and hydrogen related shallow thermal donors in Si, Phys. Rev. B **65**, 014109 (2002).

[111] J. Coutinho, V. J. B. Torres, R. Jones, and P. R. Briddon, Electrical activity of chalcogen-hydrogen defects in silicon, Phys. Rev. B **67(3)**, 035205 (2003).

[112] T. A. G. Eberlein, C. J. Fall, R. Jones, P. R. Briddon, and S. Öberg, Alphabet luminescence lines in 4*H*-SiC, Phys. Rev. B **65**, 184108 (2002).

[113] A. Resende, R. Jones, S. Öberg, and P. R. Briddon, Calculation of electrical levels of deep centers: Application to Au–H and Ag–H defects in silicon, Phys. Rev. Lett. **82(10)**, 2111 (1999).

[114] J.-W. Jeong and A. Oshiyama, Atomic and electronic structures of a boron impurity and its diffusion pathways in crystalline Si, Phys. Rev. B **64(23)**, 235204 (2001).

[115] J. P. Goss, P. R. Briddon, R. Jones, and S. Sque, Donor and acceptor states in diamond, Diamond and Related Mater. **13(4–8)**, 684 (2004).

[116] J. P. Goss, P. R. Briddon, M. J. Rayson, S. J. Sque, and R. Jones, Vacancy-impurity complexes and limitations for implantation doping of diamond, Phys. Rev. B **72(3)**, 035214 (2005).

[117] J. A. Pople and D. L. Beveridge, Approximate Molecular Orbital Theory, McGraw-Hill series in advanced chemistry (McGraw-Hill, New York ; London, 1970).

[118] W. Low, Paramagnetic resonance in solid state physics – advances in research and applications (Academic Press, New York, 1960).

[119] G. D. Watkins, in Semiconductors and molecular crystals (Plenum, New York, 1975), Vol. 2, Chap. Point defects in solids.

[120] G. D. Watkins, in Identification of Defects in Semiconductors, Vol. 51A of Semiconductors and Semimetals, edited by M. Stavola (Academic Press, New York, 1999).

[121] N. Casanova, E. Gheeraert, A. Deneuville, C. Uzan-Saguy, and R. Kalish, Phosphorus site after CIRA implantation of type IIa diamond, Diamond and Related Mater. **10(3–7)**, 580 (2001).

[122] N. Casanova, E. Gheeraert, A. Deneuville, C. Uzan-Saguy, and R. Kalish, ESR study of phosphorus implanted type IIa diamond, Phys. Status Solidi A **181(1)**, 5 (2000).

[123] T. Graf, M. S. Brandt, C. E. Nebel, M. Stutzmann, and S. Koizumi, Electrically detected magnetic resonance studies of phosphorus doped diamond, Physica B **308–310**, 593 (2001).

[124] T. Graf, M. S. Brandt, C. E. Nebel, M. Stutzmann, and S. Koizumi, Electron spin resonance of phosphorus in n-type diamond, Phys. Status Solidi A **193(3)**, 434 (2002).

[125] M. Katagiri, J. Isoya, S. Koizumi, and H. Kanda, Electron spin resonance characterization of phosphorus-doped CVD diamond films, Phys. Status Solidi A **201(11)**, 2451 (2004).

[126] J. Isoya, H. Kanda, M. Akaishi, Y. Morita, and T. Ohshima, ESR studies of incorporation of phosphorus into high-pressure synthetic diamond, Diamond and Related Mater. **6(2–4)**, 356 (1997).

[127] J. Isoya, H. Kanda, I. Sakaguchi, Y. Morita, and T. Ohshima, ESR studies of high-energy phosphorus-ion implanted synthetic diamond crystals, Radiat. Phys. Chem. **50(4)**, 321 (1997).

[128] N. D. Samsonenko, V. V. Tokiĭ, and S. V. Gorban, Electron paramagnetic resonance of phosphorus in diamond, Sov. Phys. Solid State **33(8)**, 1409 (1991).

[129] M. E. Zvanut, W. E. Carlos, J. A. Freitas Jr., K. D. Jamison, and R. P. Hellmer, Identification of phosphorus in diamond thin films using electron paramagnetic-resonance spectroscopy, Appl. Phys. Lett. **65(18)**, 2287 (1994).

[130] M. Fanciulli, S. Jin, and T. D. Moustakas, Nitrogen in diamond thin films, Physica B **229(1)**, 27 (1996).

[131] R. Kalish, C. Uzan-Saguy, B. Philosoph, V. Richter, J. P. Lagrange, E. Gheeraert, A. Deneuville, and A. T. Collins, Nitrogen doping of diamond by ion implantation, Diamond and Related Mater. **6(2–4)**, 516 (1997).

[132] V. A. Nadolinny, A. P. Yelisseyev, A. G. Badalyan, J. M. Baker, D. J. Twitchen, M. E. Newton, A. Hofstaetter, and B. Feigelson, New EPR spectra in diamonds with a high concentration of nitrogen atoms, Diamond and Related Mater. **8(8–9)**, 1565 (1999).

[133] Y. Show, T. Matsukawa, M. Iwase, and T. Izumi, Effects of defects introduced by nitrogen doping on electron emission from diamond films, Mater. Chem. Phys. **72(2)**, 201 (2001).

[134] Y. Show, T. Matsukawa, H. Ito, M. Iwase, and T. Izumi, Structural changes in CVD diamond film by boron and nitrogen doping, Diamond and Related Mater. **9(3–6)**, 337 (2000).

[135] C. M. Welbourn, EPR studies of a two-nitrogen-atom centre in natural, plastically-deformed diamond, Solid State Commun. **26(4)**, 255 (1978).

[136] C.-S. Yan and Y. K. Vohra, Multiple twinning and nitrogen defect center in chemical vapor deposited homoepitaxial diamond, Diamond and Related Mater. **8(11)**, 2022 (1999).

[137] J. Harrison, M. J. Sellars, and N. B. Manson, Optical spin polarisation of the N-V centre in diamond, J. Luminescence **107(1–4)**, 245 (2004).

[138] N. B. Manson, X.-F. He, and P. T. H. Fisk, Raman heterodyne studies of the nitrogen-vacancy centre in diamond, J. Luminescence **53(1–6)**, 49 (1992).

[139] K. Iakoubovskii, S. Dannefaer, and A. Stesmans, Evidence for vacancy-interstitial pairs in Ib-type diamond, Phys. Rev. B **71**, 233201 (2005).

[140] A. T. Collins, H. Kanda, J. Isoya, C. A. J. Ammerlaan, and J. A. van Wyk, Correlation between optical absorption and EPR in high-pressure diamond grown from a nickel solvent catalyst, Diamond and Related Mater. **7(2–5)**, 333 (1998).

[141] A. R. Lang, A. P. Yelisseyev, N. P. Pokhilenko, J. W. Steeds, and A. Wotherspoon, Is dispersed nickel in natural diamonds associated with cuboid growth sectors in diamonds that exhibit a history of mixed-habit growth?, J. Cryst. Growth **263(1–4)**, 575 (2004).

[142] R. I. Mashkovtsev and Y. N. Pal'yanov, EPR of new nickel-nitrogen center in annealed synthetic diamond, Solid State Commun. **111(7)**, 397 (1999).

[143] V. A. Nadolinny, J. M. Baker, N. E. Newton, and H. Kanda, EPR studies of a nickel-boron center in synthetic diamond, Diamond and Related Mater. **11(3–6)**, 627 (2002).

[144] V. Nadolinny, A. Yelisseyev, O. Yurjeva, A. Hofstaetter, B. Meyer, and B. Feigelson, Relationship between electronic states of nickel-containing centres and donor nitrogen in synthetic and natural diamonds, Diamond and Related Mater. **7(10)**, 1558 (1998).

[145] A. J. Neves, R. Pereira, N. A. Sobolev, M. H. Nazaré, W. Gehlhoff, A. Näser, and H. Kanda, New paramagnetic defects in synthetic diamonds grown using nickel catalyst, Physica B **273–274**, 651 (1999).

[146] R. N. Pereira, W. Gehlhoff, N. A. Sobolev, A. J. Neves, and D. Bimberg, Photo-EPR studies on the AB3 and AB4 nickel-related defects in diamond, Physica B **308–310**, 589 (2001).

[147] E. Colineau, E. Gheeraert, A. Deneuville, J. Mambou, F. Brunet, and J. P. Lagrange, Minimization of the defects concentration from boron incorporation in polycrystalline diamond films, Diamond and Related Mater. **6(5–7)**, 778 (1997).

[148] F. Fontaine, E. Gheeraert, and A. Deneuville, Conduction mechanisms in boron implanted diamond films, Diamond and Related Mater. **5(6–8)**, 752 (1996).

[149] H. Kim, A. K. Ramdas, S. Rodriguez, Z. Barticevic, M. Grimsditch, and T. R. Anthony, Magnetospectroscopy of acceptors in "blue" diamonds, Physica B **302–303**, 88 (2001).

[150] Y. Show *et al.*, ESR characterization of defects produced in diamond surface by B ion implantation, Appl. Surf. Sci. **117–118**, 574 (1997).

[151] X. J. Hu, R. B. Li, H. S. Shen, Y. B. Dai, and X. C. He, Electrical and structural properties of boron and phosphorus co-doped diamond films, Carbon **42(8–9)**, 1501 (2004).

[152] N. Mizuochi, M. Ogura, H. Watanabe, J. Isoya, H. Okushi, and S. Yamasaki, EPR study of hydrogen-related defects in boron-doped *p*-type CVD homoepitaxial diamond films, Diamond and Related Mater. **13(11–12)**, 2096 (2004).

[153] N. Mizuochi, H. Watanabe, J. Isoya, H. Okushi, and S. Yamasaki, Hydrogen-related defects in single crystalline CVD homoepitaxial diamond film studied by EPR, Diamond and Related Mater. **13(4–8)**, 765 (2004).

[154] B. Campbell, W. Choudhury, A. Mainwood, M. Newton, and G. Davies, Lattice damage caused by the irradiation of diamond, Nucl. Instrum. Methods A **476(3)**, 680 (2002).

[155] D. P. Erchak, V. G. Efimov, A. M. Zaitsev, V. F. Stelmakh, N. M. Penina, V. S. Varichenko, and V. P. Tolstykh, Peculiarities of damage in diamond irradiated by high energy ions, Nucl. Instrum. Methods B **69(4)**, 443 (1992).

[156] K. Fabisiak, M. Maar-Stumm, and E. Blank, Defects in chemically vapour-deposited diamond films studied by electron spin resonance and Raman spectroscopy, Diamond and Related Mater. **2(5–7)**, 722 (1993).

[157] K. Fabisiak, A. Banaszak, M. Kaczmarski, and M. Kozanecki, Structural characterization of CVD diamond films using Raman and ESR spectroscopy methods, Optical Materials **28(1–2)**, 106 (2006).

[158] K. Iakoubovskii, A. Stesmans, K. Suzuki, J. Kuwabara, and A. Sawabe, Characterization of defects in monocrystalline CVD diamond films by electron spin resonance, Diamond and Related Mater. **12(3–7)**, 511 (2003).

[159] J. K. Kirui, J. A. van Wyk, and M. J. R. Hoch, ESR studies of the negative divacancy in irradiated type-I diamonds, Diamond and Related Mater. **8(8–9)**, 1569 (1999).

[160] P. F. Lai, S. Prawer, and C. Noble, Electron spin resonance investigation of ion-irradiated diamond, Diamond and Related Mater. **11(7)**, 1391 (2002).

[161] V. A. Nadolinny and A. P. Yelisseyev, New paramagnetic centres containing nickel ions in diamond, Diamond and Related Mater. **3(1–2)**, 17 (1994).

[162] V. Nadolinny and A. Yelisseyev, Structure and creation conditions of complex nitrogen-nickel defects in synthetic diamond, Diamond and Related Mater. **3**, 1196 (1994).

[163] M. Nesládek *et al.*, Characteristic defects in CVD diamond: optical and electron paramagnetic resonance study, Diamond and Related Mater. **8(8–9)**, 1480 (1999).

[164] M. E. Newton, B. A. Campbell, D. J. Twitchen, J. M. Baker, and T. R. Anthony, Recombination-enhanced diffusion of self-interstitial atoms and vacancy-interstitial recombination in diamond, Diamond and Related Mater. **11(3–6)**, 618 (2002).

[165] N. V. Novikov, T. A. Nachalna, S. A. Ivakhnenko, O. A. Zanevsky, I. S. Belousov, V. G. Malogolovets, G. A. Podzyarei, and L. A. Romanko, Properties of semiconducting diamonds grown by the temperature-gradient method, Diamond and Related Mater. **12(10–11)**, 1990 (2003).

[166] E. Rohrer, C. F. O. Graeff, C. E. Nebel, M. Stutzmann, H. Güttier, and R. Zachai, Subbandgap spectroscopy of chemical vapor deposition diamond, Mater. Sci. Eng. B **46(1–3)**, 115 (1997).

[167] J. Rosa, J. Pangrác, M. Vaněček, V. Vorlíček, M. Nesládek, K. Meykens, C. Quaeyhaegens, and L. M. Stals, Simultaneous characterization of defect states in CVD diamond by PDS, EPR, Raman and photocurrent spectroscopies, Diamond and Related Mater. **7(7)**, 1048 (1998).

[168] N. D. Samsonenko, V. V. Tokiy, S. V. Gorban, and V. I. Timchenko, Electron spin resonance spectroscopy of impure and pure structural defects in the diamond, Surf. Coat. Tech. **47(1–3)**, 618 (1991).

[169] Y. Show, T. Izumi, M. Deguchi, M. Kitabatake, T. Hirao, Y. Morid, A. Hatta, T. Ito, and A. Hiraki, Defects in ion implanted diamond films (ESR study), Nucl. Instrum. Methods B **127–128**, 217 (1997).

[170] Y. Show, Y. Nakamura, T. Izumi, M. Deguchi, M. Kitabatake, T. Hirao, Y. Mori, A. Hatta, T. Ito, and A. Hiraki, Formation of paramagnetic defects in CVD diamond films (ESR study), Thin Solid Films **281–282(1–2)**, 275 (1996).

[171] Y. Show, M. Iwase, and T. Izumi, Structural characterization of CVD diamond films using the ESR method, Thin Solid Films **274(1–2)**, 50 (1996).

[172] D. J. Twitchen, D. C. Hunt, M. E. Newton, J. M. Baker, T. R. Anthony, and W. F. Banholzer, Electron paramagnetic resonance (EPR) and optical absorption studies of defects created in diamond by electron irradiation damage at 100 and 350 K, Physica B **273–274**, 628 (1999).

[173] A. Yelisseyev, Y. Babich, V. Nadolinny, D. Fisher, and B. Feigelson, Spectroscopic study of HPHT synthetic diamonds, as grown at 1500 °C, Diamond and Related Mater. **11(1)**, 22 (2002).

[174] W. Zhang, F. Zhang, Q. Wu, and G. Chen, Study of influence of annealing on defects in diamond films with ESR and IR measurements, Mater. Lett. **15(4)**, 292 (1992).

[175] J. A. van Wyk, O. D. Tucker, M. E. Newton, J. M. Baker, G. S. Woods, and P. Spear, Magnetic-resonance measurements on the $^5A_2$ excited state of the neutral vacancy in diamond, Phys. Rev. B **52(17)**, 12657 (1995).

[176] M. E. Newton and J. S. Hyde, ENDOR at S-band (2–4 GHz) microwave frequencies, J. Magn. Res. **95(1)**, 80 (1991).

[177] N. B. Manson, X.-F. He, and P. T. H. Fisk, Raman heterodyne detected electron-nuclear double-resonance measurements of the nitrogen-vacancy center in diamond, Opt. Lett. **15(19)**, 1094 (1990).

[178] P. G. Dawber and R. J. Elliott, Theory of optical absorption by vibrations of defects in silicon, Proc. Phys. Soc. **81(3)**, 453 (1963).

[179] C. Kittel, Introduction to Solid State Physics, 8th ed. (John Wiley & Sons (WIE), New York, 2004).

[180] M. Stavola, in Identification of Defects in Semiconductors, Vol. 51B of Semiconductors and Semimetals, edited by M. Stavola (Academic Press, New York, 1999), p. 153.

[181] M. D. McCluskey, Local vibrational modes of impurities in semiconductors, J. Appl. Phys. **87(8)**, 3593 (2000).

[182] R. C. Newman, Infrared Studies of Crystal Defects (Taylor and Francis, London, 1973).

[183] W. Kohn and J. M. Luttinger, Theory of donor states in silicon, Phys. Rev. **98(4)**, 915 (1955).

[184] W. Kohn, in Solid State Physics, edited by F. Seitz and D. Turnbull (Academic Press, New York, 1957), Vol. 5, pp. 257–320, Shallow impurity states in silicon and germanium.

[185] A. K. Ramdas and S. Rodriguez, Spectroscopy of the solid-state analogues of the hydrogen atom: donors and acceptors in semiconductors, Rep. Prog. Phys. **44(12)**, 1297 (1981).

[186] E. Gheeraert, S. Koizumi, T. Teraji, and H. Kanda, Electronic transitions of electrons bound to phosphorus donors in diamond, Solid State Commun. **113(10)**, 577 (2000).

[187] P. Thongnopkun and S. Ekgasit, FTIR Spectra of faceted diamonds and diamond simulants, Diamond and Related Mater. **14(10)**, 1592 (2005).

[188] N. Casanova, A. Tajani, E. Gheeraert, E. Bustarret, J. A. Garrido, C. E. Nebel, and M. Stutzmann, Epitaxial growth of phosphorus doped diamond on {111} substrate, Diamond and Related Mater. **11(3–6)**, 328 (2002).

[189] E. Gheeraert, S. Koizumi, T. Teraji, H. Kanda, and M. Nesladek, Electronic states of phosphorus in diamond, Diamond and Related Mater. **9(3–6)**, 948 (2000).

[190] E. Gheeraert, N. Casanova, S. Koizumi, T. Teraji, and H. Kanda, Low temperature excitation spectrum of phosphorus in diamond, Diamond and Related Mater. **10(3–7)**, 444 (2001).

[191] E. Gheeraert, N. Casanova, T. A., A. Deneuville, E. Bustarret, J. A. Garrido, C. E. Nebel, and M. Stutzmann, n-Type doping of diamond by sulfur and phosphorus, Diamond and Related Mater. **11**, 289 (2002).

[192] Y. V. Babich, B. N. Feigelson, and A. P. Yelisseyev, Nitrogen aggregation and linear growth rate in HPHT synthetic diamonds, Diamond and Related Mater. **13(10)**, 1802 (2004).

[193] D. Fisher and S. C. Lawson, The effect of nickel and cobalt on the aggregation of nitrogen in diamond, Diamond and Related Mater. **7(2–5)**, 299 (1998).

[194] I. Kiflawi, H. Kanda, D. Fisher, and S. C. Lawson, The aggregation of nitrogen and the formation of A centres in diamonds, Diamond and Related Mater. **6(11)**, 1643 (1997).

[195] I. Kiflawi, H. Kanda, and A. Mainwood, The effect of nickel and the kinetics of the aggregation of nitrogen in diamond, Diamond and Related Mater. **7(2–5)**, 327 (1998).

[196] V. A. Nadolinny, A. P. Yelisseyev, J. M. Baker, D. J. Twitchen, M. E. Newton, B. N. Feigelson, and O. P. Yuryeva, Mechanisms of nitrogen aggregation in nickel- and cobalt-containing synthetic diamonds, Diamond and Related Mater. **9(3–6)**, 883 (2000).

[197] E. Gheeraert, A. Deneuville, and J. Mambou, Boron-related infra-red absorption in homoepitaxial diamond films, Diamond and Related Mater. **7(10)**, 1509 (1998).

[198] C. Piccirillo, G. Davies, A. Mainwood, and C. M. Penchina, Investigation on boron-doped CVD samples, Diamond and Related Mater. **11(3–6)**, 338 (2002).

[199] C. Piccirillo, G. Davies, A. Mainwood, and C. M. Penchina, The variation of optical absorption of CVD diamond as a function of temperature, Physica B **308–310**, 581 (2001).

[200] J. Chevallier, A. Lusson, B. Theys, A. Deneuville, and G. E., Evidence of hydrogen-boron interactions in diamond from deuterium diffusion and infrared spectroscopy experiments, Diamond and Related Mater. **8(2–5)**, 278 (1999).

[201] J. Chevallier, A. Lusson, D. Ballutaud, B. Theys, F. Jomard, A. Deneuville, M. Bernard, E. Gheeraert, and E. Bustarret, Hydrogen-acceptor interactions in diamond, Diamond and Related Mater. **10(3–7)**, 399 (2001).

[202] V. G. Vins, New radiation induced defects in HPHT synthetic diamonds, Diamond and Related Mater. **14(3–7)**, 364 (2005).

[203] K. M. McNamara, B. E. Scruggs, and K. K. Gleason, The effect of impurities on the IR absorption of chemically vapor deposited diamond, Thin Solid Films **253(1–2)**, 157 (1994).

[204] G. Davies, in Identification of Defects in Semiconductors, Vol. 51B of Semiconductors and Semimetals, edited by M. Stavola (Academic Press, New York, 1999), Chap. 1, p. 1.

[205] E. C. Lightowlers, in Growth and Characterisation of Semiconductors, edited by R. A. Stradling and P. C. Klipstein (Adam Hilger, Bristol, 1990), Chap. 5, p. 135.

[206] T. Shibata, T. Nakatsuji, K. Unno, and E. Makino, in Proceedings of SPIE — Volume 3891 — Electronics and Structures for MEMS, edited by N. W. Bergmann, O. Reinhold, and N. C. Tien (SPIE, Gold Coast, Australia, 1999), pp. 336–343.

[207] M. Tachiki, Y. Kaibara, Y. Sumikawa, M. Shigeno, H. Kanazawa, T. Banno, K. S. Song, H. Umezawa, and H. Kawarada, Characterization of locally modified diamond surface using Kelvin probe force microscope, Surface Sci. **581(2–3)**, 207 (2005).

[208] B. Rezek and C. E. Nebel, Kelvin force microscopy on diamond surfaces and devices, Diamond and Related Mater. **14(3–7)**, 466 (2005).

[209] P. Moriarty, Y. R. Ma, M. D. Upward, and P. H. Beton, Translation, rotation and removal of C_{60} on Si(100)-2×1 using anisotropic molecular manipulation, Surface Sci. **407(1–3)**, 27 (1998).

[210] J. Nakamura and T. Ito, Oxidization process of CVD diamond (1 0 0):H 2 × 1 surfaces, Appl. Surf. Sci. **244(1–4)**, 301 (2005).

[211] O. A. Williams and R. B. Jackman, Homoepitaxial growth for surface conductive device applications, Diamond and Related Mater. **13(2)**, 325 (2004).

[212] S.-Y. Chen, M.-Y. Lee, C.-S. Chen, and J.-T. Lue, The mechanism of field emission for diamond films studied by scanning tunneling microscopy, Phys. Lett. A **313(5–6)**, 436 (2003).

[213] A. Watanabe, M. Deguchi, and M. Kitabatake, Microscopic study of field emission from diamond particles, Diamond and Related Mater. **10(3–7)**, 818 (2001).

[214] J. Nakamura, S. Fukumoto, T. Teraji, H. Murakami, and T. Ito, Hydrogen-related structural changes on CVD diamond (1 0 0) surfaces by ultra-high-vacuum annealing, Appl. Surf. Sci. **216(1–4)**, 59 (2003).

[215] M. Cannaerts, M. Nesladek, K. Haenen, L. De Schepper, L. M. Stals, and C. Van Haesendonck, Influence of annealing on the electronic properties of chemical vapor deposited diamond films studied by high vacuum scanning tunneling microscopy and spectroscopy, Diamond and Related Mater. **11(2)**, 212 (2002).

[216] B. B. Li, V. Baranauskas, A. Peterlevitz, D. C. Chang, I. Doi, V. J. Trava-Airoldi, and E. J. Corat, Annealing-induced enhancement in the activation energy of heavily boron-doped polycrystalline diamond, Diamond and Related Mater. **7(9)**, 1259 (1998).

[217] K. Bobrov, A. J. Mayne, A. Hoffman, and G. Dujardin, Atomic-scale desorption of hydrogen from hydrogenated diamond surfaces using the STM, Surface Sci. **528(1–3)**, 138 (2003).

[218] H. Murakami, M. Yokoyama, S. M. Lee, and T. Ito, Photoemission properties and surface structures of homoepitaxially grown CVD diamond(1 0 0) surfaces, Appl. Surf. Sci. **175–176**, 474 (2001).

[219] M. A. Adawi, A. Y. Didyk, V. S. Varichenko, and A. M. Zaitsev, Radiation damage in dielectric and semiconductor single crystals (direct observation), Radiat. Phys. Chem. **53(5)**, 577 (1998).

[220] Y. D. Kim, W. Choi, H. Wakimoto, S. Usami, H. Tomokage, and T. Ando, Characterization of boron doped polycrystalline CVD diamond by ultra high vacuum scanning tunneling microscopy, Diamond and Related Mater. **9(3–6)**, 1096 (2000).

[221] B. Koslowski, S. Strobel, M. J. Wenig, R. Martschat, and P. Ziemann, On the roughness of hydrogen-plasma treated diamond(100) surfaces, Diamond and Related Mater. **7(2–5)**, 322 (1998).

[222] L. Y. Ostrovskaya, A. P. Dementiev, I. I. Kulakova, and V. G. Ralchenko, Chemical state and wettability of ion-irradiated diamond surfaces, Diamond and Related Mater. **14(3–7)**, 486 (2005).

[223] L. Ostrovskaya, V. Perevertailo, V. Ralchenko, A. Dementjev, and O. Loginova, Wettability and surface energy of oxidized and hydrogen plasma-treated diamond films, Diamond and Related Mater. **11(3–6)**, 845 (2002).

[224] S. C. H. Kowk, J. Wang, and P. K. Chu, Surface energy, wettability, and blood compatibility [of] phosphorus doped diamond-like carbon films, Diamond and Related Mater. **14(1)**, 78 (2005).

[225] M. Filippi, L. Calliari, G. Pucella, and G. Verona-Rinati, Temperature evolution of the surface region of CVD diamond: an electron spectroscopy study, Surface Sci. **573(2)**, 225 (2004).

[226] R. Li, X. Hu, H. Shen, and X. He, Co-doping of sulfur and boron in CVD-diamond, Mater. Lett. **58(12–13)**, 1835 (2004).

[227] P. I. Belobrov, L. A. Bursill, K. I. Maslakov, and A. P. Dementjev, Electron spectroscopy of nanodiamond surface states, Appl. Surf. Sci. **215(1–4)**, 169 (2003).

[228] S. Yoshida, M. Toyoshima, T. Urano, and S. Hongo, Cs adsorption on H-terminated CVD-diamond studied by thermal desorption spectroscopy, Surface Sci. **532–535**, 857 (2003).

[229] S. Kono, T. Takano, M. Shimomura, T. Goto, K. Sato, T. Abukawa, M. Tachiki, and H. Kawarada, Electron-spectroscopy and -diffraction study of the conductivity of CVD diamond (0 0 1)2×1 surface, Surface Sci. **529(1–2)**, 180 (2003).

[230] K. Bobrov, H. Shechter, A. Hoffman, and M. Folman, Molecular oxygen adsorption and desorption from single crystal diamond (1 1 1) and (1 1 0) surfaces, Appl. Surf. Sci. **196(1–4)**, 173 (2002).

[231] P. E. Pehrsson, T. W. Mercer, and J. A. Chaney, Thermal oxidation of the hydrogenated diamond (1 0 0) surface, Surface Sci. **497(1–3)**, 13 (2002).

[232] T. Ando, T. Aizawa, K. Yamamoto, Y. Sato, and M. Kamo, The chemisorption of hydrogen on diamond surfaces studied by high resolution electron energy-loss spectroscopy, Diamond and Related Mater. **3(4–6)**, 975 (1994).

[233] T. Aizawa, T. Ando, K. Yamamoto, M. Kamo, and Y. Sato, Surface vibrational studies of CVD diamond, Diamond and Related Mater. **4(5–6)**, 600 (1995).

[234] T. Aizawa, T. Ando, M. Kamo, and Y. Sato, High-resolution electron-energy-loss spectroscopic study of epitaxially grown diamond (111) and (100) surfaces, Phys. Rev. B **48(24)**, 18348 (1993).

[235] K. Bobrov, B. Fisgeer, H. Shechter, M. Folman, and A. Hoffman, Thermal-programmed desorption (TPD) of deuterium from Di(111) surface: presence of two adsorption states, Diamond and Related Mater. **6(5–7)**, 736 (1997).

[236] K. Bobrov, H. Shechter, M. Folman, and A. Hoffman, A study of deuterium interaction with diamond (110) single crystal surface by TPD, EELS and LEED, Diamond and Related Mater. **8(2–5)**, 705 (1999).

[237] A. Hoffman, K. Bobrov, B. Fisgeer, H. Shechter, and M. Folman, Effects of deuterium adsorption-desorption on the state of diamond: surface degradation and stabilization of sp^3 bonded carbon, Diamond and Related Mater. **5(9)**, 977 (1996).

[238] J. Kinsky, R. Graupner, M. Stammler, and L. Ley, Surface vibrations on clean, deuterated, and hydrogenated single crystal diamond(100) surfaces studied by high-resolution electron energy loss spectroscopy, Diamond and Related Mater. **11(3–6)**, 365 (2002).

[239] A. Laikhtman, A. Lafosse, Y. Le Coat, R. Azria, and A. Hoffman, Interaction of water vapor with bare and hydrogenated diamond film surfaces, Surface Sci. **551(1–2)**, 99 (2004).

[240] H. Okuyama, S. Thachepan, T. Aruga, T. Ando, and M. Nishijima, Overtones of the C–H stretch vibrations on C(0 0 1)(2 × 1)–H, Chem. Phys. Lett. **381(5–6)**, 535 (2003).

[241] B. D. Thoms and J. E. Butler, HREELS and LEED of H/C(100): the 2 × 1 monohydride dimer row reconstruction, Surface Sci. **328(3)**, 291 (1995).

[242] M. Z. Hossain, T. Miki, H. Okuyama, T. Aruga, T. Tsuno, N. Fujimori, T. Ando, and M. Nishijima, Chemisorption of O_2 and CO on the K-modified diamond (100)2×1 surface, Diamond and Related Mater. **10(11)**, 2049 (2001).

[243] M. Z. Hossain, T. Kubo, T. Aruga, N. Takagi, T. Tsuno, N. Fujimori, and M. Nishijima, Chemisorbed states of atomic oxygen and its replacement by atomic hydrogen on the diamond (100)-(2×1) surface, Surface Sci. **436(1–3)**, 63 (1999).

[244] P. E. Pehrsson and T. W. Mercer, Oxidation of the hydrogenated diamond (100) surface, Surface Sci. **460(1–3)**, 49 (2000).

[245] P. E. Pehrsson and T. W. Mercer, Oxidation of heated diamond C(100):H surfaces, Surface Sci. **460(1–3)**, 74 (2000).

[246] M. Z. Hossain, T. Kubo, T. Aruga, N. Takagi, T. Tsuno, N. Fujimori, and M. Nishijima, Surface phonons, electronic structure and chemical reactivity of diamond (100)(2×1) surface, Jpn. J. Appl. Phys. Part 1 **38(12A)**, 6659 (1999).

[247] T. W. Mercer and P. E. Pehrsson, Surface state transitions on the reconstructed diamond C(100) surface, Surface Sci. **399(1)**, L327 (1998).

[248] H. Namba, M. Masuda, and H. Kuroda, Electronic states of 2×1 reconstructed surfaces of diamond(111) studied by UPS and EELS, Appl. Surf. Sci. **33–34**, 187 (1988).

[249] B. B. Pate, The diamond surface: atomic and electronic structure, Surface Sci. **165(1)**, 83 (1986).

[250] S. J. Sque, R. Jones, J. P. Goss, and P. R. Briddon, Shallow donors in diamond: pnictogen and chalcogen hydrogen defects, Physica B **340–342**, 80 (2003).

[251] S. J. Sque, R. Jones, J. P. Goss, and P. R. Briddon, Shallow donors in diamond: chalcogens, pnictogens, and their hydrogen complexes, Phys. Rev. Lett. **92(1)**, 017402 (2004).

[252] J. P. Goss, P. R. Briddon, R. Sachdeva, R. Jones, and S. J. Sque, Quantum mechanical modeling of the structure and doping properties of defects in diamond, AIP Conf. Proc. **772(1)**, 91 (2005), proceedings of the 27th International Conference on the Physics of Semiconductors, Flagstaff, Arizona, USA, 26–30 July 2004.

[253] J. P. Goss, R. Jones, M. I. Heggie, C. P. Ewels, P. R. Briddon, and S. Öberg, Theory of hydrogen in diamond, Phys. Rev. B **65(11)**, 115207 (2002).

[254] S. A. Kajihara, A. Antonelli, J. Bernholc, and R. Car, Nitrogen and potential n-type dopants in diamond, Phys. Rev. Lett. **66**, 2010 (1991).

[255] A. E. Alexenko and B. V. Spitsyn, Semiconducting diamonds made in the USSR, Diamond and Related Mater. **1(5–6)**, 705 (1992).

[256] S. Bohr, R. Haubner, and B. Lux, Influence of phosphorus addition on diamond CVD, Diamond and Related Mater. **4(2)**, 133 (1995).

[257] M. Kamo, H. Yurimoto, T. Ando, and Y. Sato, in Proceeding of the Second International Conference on New Diamond Science and Technology, edited by R. Messier, J. T. Glass, J. E. Butler, and R. Roy (Materials Research Society, Pittsburgh, 1991), pp. 637–641.

[258] K. Okano, H. Kiyota, T. Iwasaki, Y. Nakamura, Y. Akiba, T. Kurosu, M. Iida, and T. Nakamura, Synthesis of n-type semiconducting diamond film using diphosphorus pentaoxide as the doping source, Appl. Phys. A **51**, 344 (1990).

[259] S. Koizumi, M. Kamo, Y. Sato, H. Ozaki, and T. Inuzuka, Growth and characterization of phosphorous doped 111 homoepitaxial diamond thin films, Appl. Phys. Lett. **71(8)**, 1065 (1997).

[260] S. Koizumi, M. Kamo, Y. Sato, S. Mita, A. Sawabe, A. Reznik, C. Uzan-Saguy, and R. Kalish, Growth and characterization of phosphorus doped *n*-type diamond thin films, Diamond and Related Mater. **7(2–5)**, 540 (1998).

[261] S. Koizumi, Growth and characterization of phosphorus doped n-type diamond thin films, Phys. Status Solidi A **172(1)**, 71 (1999).

[262] S. Koizumi, T. Teraji, and H. Kanda, Phosphorus-doped chemical vapor deposition of diamond, Diamond and Related Mater. **9(3–6)**, 935 (2000).

[263] O. Gaudin, D. K. Troupis, R. B. Jackman, C. E. Nebel, S. Koizumi, and E. Gheeraert, Charge-based deep level transient spectroscopy of phosphorous-doped homoepitaxial diamond, J. Appl. Phys. **94(9)**, 5832 (2003).

[264] E. Gheeraert, S. Koizumi, T. Teraji, H. Kanda, and M. Nesládek, Electronic states of boron and phosphorus in diamond, Phys. Status Solidi A **174(1)**, 39 (1999).

[265] H. Kato, S. Yamasaki, and H. Okushi, *n*-type doping of (001)-orientated single-crystalline diamond by phosphorus, Appl. Phys. Lett. **86(22)**, 222111 (2005).

[266] Y. Koide, S. Koizumi, H. Kanda, M. Suzuki, H. Yoshida, N. Sakuma, T. Ono, and T. Sakai, Admittance spectroscopy for phosphorus-doped *n*-type diamond epilayer, Appl. Phys. Lett. **86**, 232105 (2005).

[267] M. Nesládek, K. Meykens, K. Haenen, L. M. Stals, T. Teraji, and S. Koizumi, Photocurrent and optical absorption spectroscopic study of *n*-type phosphorus-doped CVD diamond, Diamond and Related Mater. **8(2–5)**, 882 (1999).

[268] H. Sternschulte, K. Thonke, R. Sauer, and S. Koizumi, Optical evidence for 630-meV phosphorus donor in synthetic diamond, Phys. Rev. B **59(20)**, 12924 (1999).

[269] T. Miyazaki, H. Okushi, and T. Uda, Shallow donor state due to nitrogen-hydrogen complex in diamond, Phys. Rev. Lett. **88(6)**, 066402 (2002).

[270] E. B. Lombardi, A. Mainwood, and K. Osuch, Interaction of hydrogen with boron, phosphorus, and sulfur in diamond, Phys. Rev. B **70(20)**, 205201 (2004).

[271] D. Segev and S.-H. Wei, Design of shallow donor levels in diamond by isovalent-donor coupling, Phys. Rev. Lett. **91(12)**, 126406 (2003).

[272] R. Kalish, S. Dhar, and L. C. Feldman, Depth profiles, surface damage and lattice location of boron/deuterium co-doped diamond, Diamond and Related Mater. **14(10)**, 1600 (2005).

[273] R. Kalish *et al.*, Conversion of *p*-type to *n*-type diamond by exposure to a deuterium plasma, J. Appl. Phys. **96(12)**, 7060 (2004).

[274] J. P. Goss, P. R. Briddon, R. Jones, Z. Teukam, D. Ballutaud, F. Jomard, J. Chevallier, M. Bernard, and A. Deneuville, Deep hydrogen traps in heavily B-doped diamond, Phys. Rev. B **68(23)**, 235209 (2003).

[275] E. B. Lombardi, A. Mainwood, and K. Osuch, Ab initio study of the passivation and interaction of substitutional impurities with hydrogen in diamond, Diamond and Related Mater. **12(3–7)**, 490 (2003).

[276] S. P. Mehandru and A. B. Anderson, The migration of interstitial H in diamond and its pairing with substitutional B and N: molecular orbital theory, J. Mater. Res. **9(2)**, 383 (1994).

[277] F. Birch, Finite elastic strain of cubic crystals, Phys. Rev. **71(11)**, 809 (1947).

[278] R. W. Godby, M. Schlüter, and L. J. Sham, Self-energy operators and exchange-correlation potentials in semiconductors, Phys. Rev. B **37(17)**, 10159 (1988).

[279] D. A. Liberman, Slater transition-state band-structure calculations, Phys. Rev. B **62(11)**, 6851 (2000).

[280] F. J. Himpsel, J. F. van der Veen, and D. E. Eastman, Experimental bulk energy bands for diamond using $h\nu$-dependent photoemission, Phys. Rev. B **22(4)**, 1967 (1980).

[281] M. Nesladek, Conventional n-type doping in diamond: state of the art and recent progress, Semicond. Sci. Technol. **20(2)**, R19 (2005).

[282] M. Hasegawa, T. Teraji, and S. Koizumi, Lattice location of phosphorus in n-type homoepitaxial diamond films grown by chemical-vapor deposition, Appl. Phys. Lett. **79(19)**, 3068 (2001).

[283] K. Larsson, Substitutional n-type doping of diamond during growth. A theoretical approach using extremes in surface chemistry, Phys. Status Solidi A **193(3)**, 409 (2002).

[284] Y. Yan, S. B. Zhang, and M. M. Al-Jassim, Graphite-like surface reconstructions on C{111} and their implication for n-type diamond, Phys. Rev. B **66**, 201401 (2003).

[285] E. Borchi, M. Bruzzi, S. Pirollo, and S. Sciortino, Current-temperature analysis of DC glow discharge CVD diamond films, Solid-State Electron. **42(3)**, 429 (1998).

[286] A. T. Collins, The electrical and optical properties of thin film diamond, Ceram. Int. **22(4)**, 321 (1996).

[287] R. G. Farrer, On the substitutional nitrogen donor in diamond, Solid State Commun. **7(9)**, 685 (1969).

[288] B. B. Li, M. C. Tosin, A. C. Peterlevitz, and V. Baranauskas, Measurement of the substitutional nitrogen activation energy in diamond films, Appl. Phys. Lett. **73(6)**, 812 (1998).

[289] E. Rohrer, C. F. O. Graeff, R. Janssen, C. E. Nebel, M. Stutzmann, H. Güttler, and R. Zachai, Nitrogen-related dopant and defect states in CVD diamond, Phys. Rev. B **54(11)**, 7874 (1996).

[290] J. Walker, Optical absorption and luminescence in diamond, Rep. Prog. Phys. **42(10)**, 1605 (1979).

[291] I. S. Zevenbergen, T. Gregorkiewicz, and C. A. J. Ammerlaan, Electron-paramagnetic-resonance identification of hydrogen-passivated sulfur centers in silicon, Phys. Rev. B **51(23)**, 16746 (1995).

[292] P. T. Huy, C. A. J. Ammerlaan, T. Gregorkiewicz, and D. T. Don, Hydrogen passivation of the selenium double donor in silicon: a study by magnetic resonance, Phys. Rev. B **61(11)**, 7448 (2000).

[293] R. E. Peale, K. Muro, and A. J. Sievers, Sulfur-Hydrogen Donor Complexes in Silicon, Mater. Sci. Forum **65–66**, 151 (1990).

[294] G. Pensl, G. Roos, C. Holm, E. Sirtl, and N. M. Johnson, Hydrogen neutralization of chalcogen double donors in silicon, Appl. Phys. Lett. **51(6)**, 451 (1987).

[295] G. Roos, G. Pensl, N. M. Johnson, and C. Holm, Hydrogen neutralization and reactivation of chalcogen double-donor centers in silicon, J. Appl. Phys. **67(4)**, 1897 (1990).

[296] Z. N. Liang and L. Niesen, Evidence for the formation of tellurium-hydrogen complexes in crystalline silicon, Phys. Rev. B **51(16)**, 11120 (1995).

[297] J. P. Goss, Theory of hydrogen in diamond, J. Phys.: Condens. Matter **15**, R551 (2003).

[298] G. B. Bachelet, G. A. Baraff, and M. Schlüter, Defects in diamond: the unrelaxed vacancy and substitutional nitrogen, Phys. Rev. B **24(8)**, 4736 (1981).

[299] P. R. Briddon and R. Jones, Theory of impurities in diamond, Physica B **185(1–4)**, 179 (1993).

[300] S. A. Kajihara, A. Antonelli, and J. Bernholc, Impurity incorporation and doping of diamond, Physica B **185(1–4)**, 144 (1993).

[301] A. Cox, M. E. Newton, and J. M. Baker, ^{13}C, ^{14}N and ^{15}N ENDOR measurements on the single substitutional nitrogen centre (P1) in diamond, J. Phys.: Condens. Matter **6(2)**, 551 (1994).

[302] J. H. N. Loubser and J. A. van Wyk, Electron spin resonance in the study of diamond, Rep. Prog. Phys. **41(8)**, 1201 (1978).

[303] W. V. Smith, P. P. Sorokin, I. L. Gelles, and G. J. Lasher, Electron-Spin Resonance of Nitrogen Donors in Diamond, Phys. Rev. **115(6)**, 1546 (1959).

[304] J. Bernholc, S. A. Kajihara, C. Wang, A. Antonelli, and R. F. Davis, Theory of native defects, doping and diffusion in diamond and silicon carbide, Mater. Sci. Eng. B **11(1–4)**, 265 (1992).

[305] J. Koppitz, O. F. Schirmer, and M. Seal, Pseudo-Jahn-Teller optical absorption of isolated nitrogen in diamond, J. Phys. C **19(8)**, 1123 (1986).

[306] H. Katayama-Yoshida, T. Nishimatsu, T. Yamamoto, and N. Orita, Codoping method for the fabrication of low-resistivity wide band-gap semiconductors in p-type GaN, p-type AlN and n-type diamond; prediction versus experiment, J. Phys.: Condens. Matter **13**, 8901 (2001).

[307] T. Nishimatsu, H. Katayama-Yoshida, and N. Orita, Theoretical study of hydrogen-related complexes in diamond for low-resistive *n*-type semiconductor, Physica B **302–303**, 149 (2001).

[308] K. Jackson, M. R. Pederson, and J. G. Harrison, Donor levels and impurity-atom relaxation in nitrogen- and phosphorus-doped diamond, Phys. Rev. B **41(18)**, 12641 (1990).

[309] R. J. Eyre, J. P. Goss, P. R. Briddon, and J. P. Hagon, Theory of Jahn-Teller distortions of the P donor in diamond, J. Phys.: Condens. Matter **17(37)**, 5831 (2005).

[310] J. Isoya, H. Kanda, J. R. Norris, J. Tang, and M. K. Bowman, Fourier-transform and continuous-wave EPR studies of nickel in synthetic diamond: site and spin multiplicity, Phys. Rev. B **41(7)**, 3905 (1990).

[311] K. Bharuth-Ram, H. Quintel, H. Hofsäss, M. Restle, and C. Ronning, Emission channeling study of annealing of radiation damage in heavy-ion implanted diamond, Nucl. Instrum. Methods B **118(1–4)**, 72 (1996).

[312] J. G. Correia, J. G. Marques, E. Alves, D. Forkel-Wirth, S. G. Jahn, M. Restle, M. Dalmer, H. Hofsäss, K. Bharuth-Ram, and I. Collaboration, Microscopic studies of implanted ^{73}As in diamond, Nucl. Instrum. Methods B **127–128**, 723 (1997).

[313] S. M. Gorbatkin, R. A. Zuhr, J. Roth, and H. Naramoto, Damage formation and substitutionality in $^{75}As^{++}$ -implanted diamond, J. Appl. Phys. **70(6)**, 2986 (1991).

[314] H. Hofsaess, M. Dalmer, M. Restle, C. Ronning, K. Bharuth-ram, and H. Quintel, Behavior of the potential n-type dopants P and As in diamond after low dose ion implantation, MRS Symp. Proc. **442**, 675 (1997).

[315] R. Q. Hood, P. R. C. Kent, R. J. Needs, and P. R. Briddon, Quantum Monte Carlo study of the optical and diffusive properties of the vacancy defect in diamond, Phys. Rev. Lett. **91(7)**, 076403 (2003).

[316] J. P. Goss, R. Jones, M. I. Heggie, C. P. Ewels, P. R. Briddon, and S. Öberg, First principles study of H in diamond, Phys. Status Solidi A **186(2)**, 263 (2001).

[317] S. P. Mehandru, A. B. Anderson, and J. C. Angus, Hydrogen binding and diffusion in diamond, J. Mater. Res. **7(3)**, 689 (1992).

[318] M. Ogura, N. Mizuochi, S. Yamasaki, and H. Okushi, Passivation effects of deuterium exposure on boron-doped CVD homoepitaxial diamond, Diamond and Related Mater. **14(11–12)**, 2023 (2005).

[319] J. Chevallier, B. Theys, A. Lusson, C. Grattepain, A. Deneuville, and E. Gheeraert, Hydrogen-boron interactions in *p*-type diamond, Phys. Rev. B **58(12)**, 7966 (1998).

[320] R. Zeisel, C. E. Nebel, and M. Stutzmann, Passivation of boron in diamond by deuterium, Appl. Phys. Lett. **74(13)**, 1875 (1999).

[321] S. J. Breuer and P. R. Briddon, *Ab initio* study of substitutional boron and the boron-hydrogen complex in diamond, Phys. Rev. B **49(15)**, 10332 (1994).

[322] B. D. Yu, Y. Miyamoto, and O. Sugino, Efficient *n*-type doping of diamond using surfactant-mediated epitaxial growth, Appl. Phys. Lett. **76(8)**, 976 (2000).

[323] T. V. Albu, A. B. Anderson, and J. C. Angus, dopants in diamond nanoparticles and bulk diamond: density functional study of substitutional B, N, P, SB, S, PN, O, NN, and interstitial H, J. Electrochemical Soc. **149(5)**, E143 (2002).

[324] Y. Dai, D. Dai, D. Liu, S. Han, and B. Huang, Mechanism of *p*-type-to-*n*-type conductivity conversion in boron-doped diamond, Appl. Phys. Lett. **84(11)**, 1895 (2004).

[325] M. I. Heggie, C. P. Ewels, N. Martsinovich, S. Scarle, R. Jones, J. P. Goss, B. Hourahine, and P. R. Briddon, Glide dislocations in diamond: first-principles calculations of similarities with and differences from silicon and the effects of hydrogen, J. Phys.: Condens. Matter **14(48)**, 12689 (2002).

[326] W. Götz, A. Schöner, G. Pensl, W. Suttrop, W. J. Choyke, R. Stein, and S. Leibenzeder, Nitrogen donors in 4*H*-silicon carbide, J. Appl. Phys. **73(7)**, 3332 (1993).

[327] S. J. Sque, R. Jones, and P. R. Briddon, Structure, electronics, and interaction of hydrogen and oxygen on diamond surfaces, Phys. Rev. B **73(8)**, 085313 (2006).

[328] S. J. Sque, R. Jones, and P. R. Briddon, Hydrogenation and oxygenation of the (100) diamond surface and the consequences for transfer doping, Phys. Status Solidi A **202(11)**, 2091 (2005).

[329] C. B. Duke, Surface structures of tetrahedrally coordinated semiconductors: principles, practice, and universality, Appl. Surf. Sci. **65**, 543 (1993).

[330] R. J. Needs, Comment on "Should all surfaces be reconstructed?", Phys. Rev. Lett. **71(3)**, 460 (1993).

[331] G. P. Srivastava, Theory of semiconductor surface reconstruction, Rep. Prog. Phys. **60(5)**, 561 (1997).

[332] D. Wolf, Should all surfaces be reconstructed?, Phys. Rev. Lett. **70(5)**, 627 (1993).

[333] J. C. Angus and C. C. Hayman, Low-pressure, metastable growth of diamond and "diamondlike" phases, Science **241(4868)**, 913 (1988).

[334] C. J. Chu, M. P. D'Evelyn, R. H. Hauge, and J. L. Margrave, Mechanism of diamond growth by chemical vapor deposition on diamond (100), (111), and (110) surfaces: carbon-13 studies, J. Appl. Phys. **70(3)**, 1695 (1991).

[335] F. J. Himpsel, J. A. Knapp, J. A. VanVechten, and D. E. Eastman, Quantum photoyield of diamond(111)—A stable negative-affinity emitter, Phys. Rev. B **20(2)**, 624 (1979).

[336] J. van der Weide, Z. Zhang, P. K. Baumann, M. G. Wensell, J. Bernholc, and R. J. Nemanich, Negative-electron-affinity effects on the diamond (100) surface, Phys. Rev. B **50(8)**, 5803 (1994).

[337] P. K. Baumann and R. J. Nemanich, Negative electron affinity effects on H plasma exposed diamond (100) surfaces, Diamond and Related Mater. **4(5–6)**, 802 (1995).

[338] N. Eimori, Y. Mori, A. Hatta, T. Ito, and A. Hiraki, Photoyield measurements of CVD diamond, Diamond and Related Mater. **4(5–6)**, 806 (1995).

[339] S. G. Ri, K. Tashiro, S. Tanaka, T. Fujisawa, H. Kimura, T. Kurosu, and M. Iida, Hall effect measurements of surface conductive layer on undoped diamond films in NO_2 and NH_3 atmospheres, Japan J. Appl. Phys. **38(6A)**, 3492 (1999).

[340] S. G. Ri, T. Mizumasa, Y. Akiba, Y. Hirose, T. Kurosu, and M. Iida, Formation mechanism of *p*-type surface conductive layer on deposited diamond films, Japan J. Appl. Phys. **34**, 5550 (1995).

[341] J. Ristein, M. Riedel, and L. Ley, Electrochemical surface transfer doping — the mechanism behind the surface conductivity of hydrogen-terminated diamond, J. Electrochemical Soc. **151(10)**, E315 (2004).

[342] K. Bobrov, G. Comtet, L. Hellner, G. Dujardin, and A. Hoffman, Molecular oxygen adsorption on partially hydrogenated diamond (100) surfaces, Appl. Phys. Lett. **85(2)**, 296 (2004).

[343] G. Kern, J. Hafner, and G. Kresse, Atomic and electronic structure of diamond (111) surfaces I. Reconstruction and hydrogen-induced de-reconstruction of the one dangling-bond surface, Surface Sci. **366(3)**, 445 (1996).

[344] K. C. Pandey, New dimerized-chain model for the reconstruction of the diamond (111)-(2×1) surface, Phys. Rev. B **25(6)**, 4338 (1982).

[345] G. Kern, J. Hafner, and G. Kresse, Atomic and electronic structure of diamond (111) surfaces II. (2×1) and $(\sqrt{3} \times \sqrt{3})$ reconstructions of the clean and hydrogen-covered three dangling-bond surfaces, Surface Sci. **366(3)**, 464 (1996).

[346] A. Scholze, W. G. Schmidt, and F. Bechstedt, Structure of the diamond (111) surface: single-dangling-bond versus triple-dangling-bond face, Phys. Rev. B **53(20)**, 13725 (1996).

[347] R. Graupner, M. Hollering, A. Ziegler, J. Ristein, L. Ley, and A. Stampfl, Dispersions of surface states on diamond (100) and (111), Phys. Rev. B **55(16)**, 10841 (1997).

[348] J. Ristein, Electronic properties of diamond surfaces – blessing or curse for devices?, Diamond and Related Mater. **9(3–6)**, 1129 (2000).

[349] Y. M. Wang, K. W. Wong, S. T. Lee, M. Nishitani-Gamo, I. Sakaguchi, K. P. Loh, and T. Ando, Recent studies on diamond surfaces, Diamond and Related Mater. **9**, 1582 (2000).

[350] R. Boukherroub, X. Wallart, S. Szunerits, B. Marcus, P. Bouvier, and M. Mermoux, Photochemical oxidation of hydrogenated boron-doped diamond surfaces, Electrochem. Commun. **7(9)**, 937 (2005).

[351] M. J. Rutter and J. Robertson, *Ab initio* calculation of electron affinities of diamond surfaces, Phys. Rev. B **57(15)**, 9241 (1998).

[352] D. R. Alfonso, D. A. Drabold, and S. E. Ulloa, Structural, electronic, and vibrational properties of diamond (100), (111), and (110) surfaces from *ab initio* calculations, Phys. Rev. B **51(20)**, 14669 (1995).

[353] M. Araidai and K. Watanabe, Field emission of diamond surfaces by time-dependent density-functional calculations, Jpn. J. Appl. Phys. Part 2 **42(6B)**, L666 (2003).

[354] J. Furthmüller, J. Hafner, and G. Kresse, Dimer reconstruction and electric surface states on clean and hydrogenated diamond (100) surfaces, Phys. Rev. B **53(11)**, 7334 (1996).

[355] G. Kern and J. Hafner, *Ab initio* calculations of the atomic and electronic structure of clean and hydrogenated diamond (110) surfaces, Phys. Rev. B **56(7)**, 4203 (1997).

[356] Y. Yu, C. Z. Gu, L. F. Xu, and S. B. Zhang, *Ab initio* structural characterization of a hydrogen-covered diamond (001) surface, Phys. Rev. B **70(12)**, 125423 (2004).

[357] G. Kern, J. Hafner, J. Furthmüller, and G. Kresse, (2×1) reconstruction and hydrogen-induced de-reconstruction of the diamond (100) and (111) surfaces, Surface Sci. **352–354**, 745 (1996).

[358] W. G. Schmidt, A. Scholze, and F. Bechstedt, Dimerized, buckled, or ideal chains on the diamond (111)2×1 surface?, Surface Sci. **351(1–3)**, 183 (1996).

[359] D. Vanderbilt and S. G. Louie, Total energies of diamond (111) surface reconstructions by a linear combination of atomic orbitals method, Phys. Rev. B **30(10)**, 6118 (1984).

[360] W. J. Huisman, M. Lohmeier, H. A. van der Vegt, J. F. Peters, S. A. de Vries, E. Vlieg, V. H. Etgens, T. E. Derry, and J. F. van der Veen, Evidence for tilted chains on the diamond (111)-(2 $\times$ 1) surface, Surface Sci. **396(1–3)**, 241 (1998).

[361] L. Diederich, P. Aebi, O. M. Küttel, and L. Schlapbach, Electron affinity of the diamond (100) surface changed by adsorption of C_{60}, Diamond and Related Mater. **8(7)**, 1324 (1999).

[362] A. V. Hamza, G. D. Kubiak, and R. H. Stulen, The role of hydrogen on the diamond C(111)–(2 $\times$ 1) reconstruction, Surface Sci. **206(1–2)**, L833 (1988).

[363] G. Henkelman and H. Jónsson, Improved tangent estimate in the nudged elastic band method for finding minimum energy paths and saddle points, J. Chem. Phys. **113(22)**, 9978 (2000).

[364] N. Fujita, R. Jones, J. P. Goss, P. R. Briddon, T. Frauenheim, and S. Öberg, Diffusion of nitrogen in silicon, Appl. Phys. Lett. **87(2)**, 021902 (2005).

[365] J. C. Zheng, X. N. Xie, A. T. S. Wee, and K. P. Loh, Oxygen-induced surface state on diamond (100), Diamond and Related Mater. **10**, 500 (2001).

[366] A. Denisenko, A. Aleksov, and E. Kohn, pH sensing by surface-doped diamond and effect of the diamond surface termination, Diamond and Related Mater. **10(3–7)**, 667 (2001).

[367] B. S. Jursic, Computational study of water and ammonia dimers with density functional theory methods, J. Mol. Struct. (Theochem) **434(1–3)**, 29 (1998).

[368] X. P. Long, J. B. Nicholas, M. F. Guest, and R. L. Ornstein, A combined density functional theory/molecular mechanics formalism and its application to small water clusters, J. Mol. Struct. **412(1–2)**, 121 (1997).

[369] F. Sim, A. St-Amant, I. Papai, and D. R. Salahub, Gaussian density functional calculations on hydrogen-bonded systems, J. Am. Chem. Soc. **114(11)**, 4391 (1992).

[370] Y.-H. Kim, I.-H. Lee, and R. M. Martin, Density-functional study of the hydrogen-bonded water cluster $H_5O_2^+$, AIP Conf. Proc. **501(1)**, 366 (2000).

[371] K. Laasonen, M. Parrinello, R. Car, C. Lee, and D. Vanderbilt, Structures of small water clusters using gradient-corrected density functional theory, Chem. Phys. Lett. **207(2–3)**, 208 (1993).

[372] S. S. Xantheas, *Ab initio* studies of cyclic water clusters $(H_2O)_n$, $n = 1$–6. III. Comparison of density functional with MP2 results, J. Chem. Phys. **102(11)**, 4505 (1995).

[373] D. Takeuchi, H. Kato, G. S. Ri, T. Yamada, P. R. Vinod, D. Hwang, C. E. Nebel, H. Okushi, and S. Yamasaki, Direct observation of negative electron affinity in hydrogen-terminated diamond surfaces, Appl. Phys. Lett. **86**, 152103 (2005).

[374] D. Takeuchi, M. Riedel, J. Ristein, and L. Ley, Surface band bending and surface conductivity of hydrogenated diamond, Phys. Rev. B **68**, 041304 (2003).

[375] S. J. Sque, R. Jones, S. Öberg, and P. R. Briddon, Transfer doping of diamond: buckminsterfullerene on hydrogenated, hydroxylated, and oxygenated diamond surfaces, J. Mater. Sci. – Materials in Electronics, (2005), submitted.

[376] S. J. Sque, R. Jones, J. P. Goss, P. R. Briddon, and S. Öberg, First-principles study of C_{60} and $C_{60}F_{36}$ as transfer dopants for p-type diamond, J. Phys.: Condens. Matter **17(2)**, L21 (2005).

[377] S. J. Sque, R. Jones, S. Öberg, and P. R. Briddon, Transfer doping of diamond: the use of C_{60} and $C_{60}F_{36}$ to effect *p*-type surface conductivity, Physica B, (2006), in press.

[378] T. Maki, S. Shikama, M. Komori, Y. Sakaguchi, K. Sakuta, and T. Kobayashi, Hydrogenating effect of single-crystal diamond surface, Jpn. J. Appl. Phys. Part 2 **31**, L1446 (1992).

[379] J. A. Garrido, C. E. Nebel, M. Stutzmann, E. Snidero, and P. Bergonzo, Capacitance-voltage studies of Al-Schottky contacts on hydrogen-terminated diamond, Appl. Phys. Lett. **81(4)**, 637 (2002).

[380] H. J. Looi, R. B. Jackman, and J. S. Foord, High carrier mobility in polycrystalline thin film diamond, Appl. Phys. Lett. **72(3)**, 353 (1998).

[381] H. Umezawa, K. Tsugawa, S. Yamanaka, D. Takeuchi, H. Okushi, and H. Kawarada, High-performance diamond metal-semiconductor field-effect transistor with 1 μm gate length, Japan J. Appl. Phys. **38**, L1222 (1999).

[382] A. Aleksov, A. Denisenko, U. Spitzberg, T. Jenkins, W. Ebert, and E. Kohn, RF performance of surface channel diamond FETs with sub-micron gate length, Diamond and Related Mater. **11**, 382 (2002).

[383] H. J. Looi, L. Y. S. Pang, Y. Wang, M. D. Whitfield, and R. B. Jackman, High-performance metal-semiconductor field effect transistors from thin-film polycrystalline diamond, Diamond and Related Mater. **7**, 565 (1998).

[384] K. Kitatani, H. Umezawa, K. Tsugawa, K. Ueyama, T. Ishikura, S. Yamashita, and H. Kawarada, MOSFETs on polished surfaces of polycrystalline diamond, Diamond and Related Mater. **8(10)**, 1831 (1999).

[385] T. Banno, M. Tachiki, H. Seo, H. Umezawa, and H. Kawarada, Fabrication of diamond single-hole transistors using AFM anodization process, Diamond and Related Mater. **11**, 387 (2002).

[386] K. Tsugawa, K. Kitatani, H. Noda, A. Hokazono, K. Hirose, M. Tajima, and H. Kawarada, High-performance diamond surface-channel field-effect transistors and their operation mechanism, Diamond and Related Mater. **8(2)**, 927 (1999).

[387] B. F. Mantel, M. Stammler, J. Ristein, and L. Ley, The correlation between surface conductivity and adsorbate coverage on diamond as studied by infrared spectroscopy, Diamond and Related Mater. **10**, 429 (2001).

[388] B. Baral, S. S. M. Chan, and R. B. Jackman, Cleaning thin-film diamond surfaces for device fabrication: An Auger electron spectroscopic study, J. Vac. Sci. and Technol. A **14(4)**, 2303 (1996).

[389] K. Hayashi, S. Yamanaka, H. Okushi, and K. Kajimura, Study of the effect of hydrogen on transport properties in chemical vapor deposited diamond films by Hall measurements, Appl. Phys. Lett. **68(3)**, 376 (1996).

[390] O. A. Williams, M. D. Whitfield, R. B. Jackman, J. S. Foord, J. E. Butler, and C. E. Nebel, Formation of shallow acceptor states in the surface region of thin film diamond, Appl. Phys. Lett. **78(22)**, 3460 (2001).

[391] C. E. Nebel, C. Saurer, F. Ertl, and M. Stutzmann, Hydrogen-induced transport properties of holes in diamond surface layers, Appl. Phys. Lett. **79(27)**, 4541 (2001).

[392] H. Kawarada, Hydrogen-terminated diamond surfaces and interfaces, Surface Sci. Reports **26**, 205 (1996).

[393] M. I. Landstrass and K. V. Ravi, Hydrogen passivation of electrically active defects in diamond, Appl. Phys. Lett. **55(14)**, 1391 (1989).

[394] K. Hayashi, H. Watanabe, S. Yamanaka, H. Okushi, K. Kajimura, and T. Sekiguchi, Hydrogen-related gap states in the near surface of chemical vapor deposited homoepitaxial diamond films, Diamond and Related Mater. **6**, 303 (1997).

[395] K. Hayashi, S. Yamanaka, H. Watanabe, T. Sekiguchi, H. Okushi, and K. Kajiura, Investigation of the effect of hydrogen on electrical and optical properties in chemical vapor deposited on homoepitaxial diamond films, J. Appl. Phys. **61(2)**, 744 (1997).

[396] A. Denisenko, A. Aleksov, A. Pribil, P. Gluche, W. Ebert, and E. Kohn, Hypothesis on the conductivity mechanism in hydrogen terminated diamond films, Diamond and Related Mater. **9(3)**, 1138 (2000).

[397] J. P. Goss, B. Hourahine, R. Jones, M. I. Heggie, and P. R. Briddon, *p*-type surface doping of diamond: a first-principles study, J. Phys.: Condens. Matter **13(40)**, 8973 (2001).

[398] M. Szaneitat, X. Jiang, and W. Beyer, Influence of adsorbates on the surface conductivity of chemical vapor deposition diamond, Appl. Phys. Lett. **77(10)**, 1554 (2000).

[399] Y. Zhang, S. Yoshihara, T. Shirakashi, and T. Kyomen, Electrochemical characteristics of boron-doped, undoped and nitrogen-doped diamond films, Diamond and Related Mater. **14(2)**, 213 (2005).

[400] N. Matsuzawa, T. Fukunaga, and D. A. Dixon, Electronic structures of 1, 2- and 1, 4-$C_{60}X_{2n}$ derivatives with $n = 1, 2, 4, 6, 8, 10, 12, 18, 24,$ and 30, J. Phys. C **96**, 10747 (1992).

[401] N. Liu, Y. Morio, F. Okino, and H. Touhara, Electrochemical properties of $C_{60}F_{36}$, Synth. Metals **86(1–3)**, 2289 (1997).

[402] S. Kawasaki, F. Okino, H. Touhara, and T. Sonoda, Discrete-variational $X\alpha$ calculations of $C_{60}F_x$ with $x = 0$, 36, and 48, Phys. Rev. B **53(24)**, 16652 (1996).

[403] H. Selig, C. Lifshitz, T. Peres, J. E. Fischer, A. B. Smith, A. R. McGhie, W. J. Romanow, and J. P. McCauley, Fluorinated fullerenes, J. Fluorine Chem. **54(1–3)**, 359 (1991).

[404] O. V. Boltalina, A. Y. Borschevskii, L. N. Sidorov, J. M. Street, and R. Taylor, Preparation of $C_{60}F_{36}$ and $C_{70}F_{36/38/40}$, Chem. Commun., 529 (1996).

[405] N. S. Chilingarov, A. V. Nikitin, J. V. Rau, I. V. Golyshevsky, A. V. Kepman, F. M. Spiridonov, and L. N. Sidorov, Selective formation of $C_{60}F_{18}$(g) and $C_{60}F_{36}$(g) by reaction of [60]fullerene with molecular fluorine, J. Fluorine Chem. **113(2)**, 219 (2002).

[406] A. A. Gakh and A. A. Tuinman, The structure of $C_{60}F_{36}$, Tetrahedron Lett. **42(41)**, 7133 (2001).

[407] J. V. Rau, S. N. Cesaro, O. V. Boltalina, V. Agafonov, A. A. Popov, and L. N. Sidorov, Raman and infrared spectroscopic study of $C_{60}F_{18}$, $C_{60}F_{36}$ and $C_{60}F_{48}$, Vib. Spectrosc. **34(1)**, 137 (2004).

[408] A. G. Avent, B. W. Clare, P. B. Hitchcock, D. L. Kepert, and R. Taylor, $C_{60}F_{36}$: there is a third isomer and it has C_1 symmetry, Chem. Commun., 2370 (2002).

[409] B. W. Clare and D. L. Kepert, Structures, stabilities and isomerism in $C_{60}H_{36}$ and $C_{60}F_{36}$. A comparison of the AM1 Hamiltonian and density functional techniques, J. Mol. Struct. (Theochem) **589–590**, 195 (2002).

[410] Z. Slanina and F. Uhlík, Energy–entropy interplay of $C_{60}F_{36}$ isomers, Chem. Phys. Lett. **374(1–2)**, 100 (2003).

[411] C. M. Sayes *et al.*, The differential cytotoxicity of water-soluble fullerenes, Nano Lett. **4(10)**, 1881 (2004).

[412] R. Taylor, Why fluorinate fullerenes?, J. Fluorine Chem. **125(3)**, 359 (2004).

[413] G. Gensterblum *et al.*, Growth mode and electronic structure of the epitaxial C_{60}(111)/GeS(001) interface, Phys. Rev. B **50(16)**, 11981 (1994).

[414] L. Shebanovs, J. Maniks, and J. Kalnacs, X-ray diffraction study of crystallographic parameters and Debye temperature of C_{60} single crystals, J. Cryst. Growth **234(1)**, 202 (2002).

[415] A. J. Maxwell, P. A. Brühwiler, D. Arvanitis, J. Hasselström, M. K.-J. Johansson, and N. Mårtensson, Electronic and geometric structure of C_{60} on Al(111) and Al(110), Phys. Rev. B **57(12)**, 7312 (1998).

[416] P. Rudolf, G. Gensterblum, and R. Caudano, Growth and characterization of fullerene interfaces on metallic and semiconductor substrates, J. de Physique IV **7(C6)**, 137 (1997).

[417] S. H. Yang, C. L. Pettiette, J. Conceicao, O. Cheshnovsky, and R. E. Smalley, UPS of buckminsterfullerene and other large clusters of carbon, Chem. Phys. Lett. **139(3–4)**, 233 (1987).

[418] P. Rudolf, M. S. Golden, and P. A. Brühwiler, Studies of fullerenes by the excitation, emission, and scattering of electrons, J. Electron Spectroscopy and Related Phenomena **100**, 409 (1999).

[419] C. Brink, L. H. Andersen, P. Hvelplund, D. Mathur, and J. D. Voldstad, Laser photodetachment of C_{60}^- and C_{70}^- ions cooled in a storage ring, Chem. Phys. Lett. **233(1–2)**, 52 (1995).

[420] L. Wang, J. Conceicao, C. Jin, and R. E. Smalley, Threshold photodetachment of cold C_{60}^-, Chem. Phys. Lett. **182(1)**, 5 (1991).

[421] S. Saito and A. Oshiyama, Cohesive mechanism end energy bands of solid C_{60}, Phys. Rev. Lett. **66(20)**, 2637 (1991).

[422] P. Strobel, M. Riedel, J. Ristein, and L. Ley, Surface transfer doping of diamond, Nature **430**, 439 (2004).

[423] P. Strobel, M. Riedel, J. Ristein, L. Ley, and O. Boltalina, Surface transfer doping of diamond by fullerene, Diamond and Related Mater. **14(3–7)**, 451 (2005).

[424] S. F. Boys and F. Bernardi, The calculation of small molecular interactions by the differences of separate total energies: some procedures with reduced errors, Molecular Phys. **19(4)**, 553 (1970).

[425] M. Gutowski and G. Chałasiński, Critical evaluation of some computational approaches to the problem of basis set superposition error, J. Chem. Phys. **98(7)**, 5540 (1993).

[426] G. Van Lier, M. C. Amat, C. P. Ewels, R. Taylor, and P. Geerlings, Theoretical analysis of the addition patterns of C_{60} fluorination: $C_{60}F_n$ ($n = 1$–60), J. Org. Chem **70**, 1565 (2005).

[427] S. Iijima, Helical microtubules of graphitic carbon, Nature **354**, 56 (1991).

[428] R. H. Miwa, W. Orellana, and A. Fazzio, Substrate-dependent electronic properties of an armchair carbon nanotube adsorbed on H/Si(001), Appl. Phys. Lett. **86(21)**, 213111 (2005).

[429] W. Orellana, R. H. Miwa, and A. Fazzio, First-principles calculations of carbon nanotubes adsorbed on Si(001), Phys. Rev. Lett. **91(16)**, 166802 (2003).

Colophon

This thesis has been produced using the LaTeX 2_ε document preparation system (for the TeX typesetting program), running on various AMD- and Intel-based IBM-PC–compatible machines using the Red Hat, Fedora Core, and Ubuntu distributions of Linux-based operating systems. Copies of the thesis were kept current across the different computers using `rsync`. The bibliography was generated using BibTeX and a customised version of the *Physical Review* style file. The text and equations are set in the Palatino font family of Hermann Zapf, through the use of the `mathpple` LaTeX package, with all content entered and manipulated using the `vim` text editor.

Graphs of numerical data were produced using `gnuplot`, while schematic graphs and other vector diagrams were created in `Skencil` (*née* `Sketch`). Ray-traced ball-and-stick atomic geometry diagrams were rendered using `POV-Ray`, while those containing wavefunction plots were created by AIMview. Raster images were retouched using `The GIMP` and converted to Encapsulated PostScript via `sam2p`.